UNIVERSITY OF MESSINA

DOCTORAL THESIS

Applications of Monte Carlo simulation in internal dosimetry of radiopharmaceuticals employed in nuclear medicine

S.S.D. FIS/07 - FIS/04

Author:
Daniele PISTONE

Supervisor:
Prof. Giuseppe MANDAGLIO

Co-Supervisor:
Prof. Ernesto AMATO

Coordinator:
Prof. Vincenza CRUPI

A thesis submitted in fulfillment of the requirements
for the degree of Doctor of Philosophy

in the

Department of Mathematical and Computer Sciences, Physical Sciences and Earth Sciences (MIFT)
Ph.D Programme in Physics, Cycle XXXIV

Academic Year 2020/2021

Good, better, best.
Never let it rest.
Until your good is your better
and your better is your best.

Abstract

Internal dosimetry (ID) is acquiring a fundamental role in nuclear medicine for the planning, optimization and monitoring of radiopharmaceutical therapies and diagnostics. Direct Monte Carlo (MC) simulation of radiation transport, using morphological and functional tomographic imaging as input data to model, respectively, patient's body and radiopharmaceutical biodistribution, is the gold standard approach for ID. Despite being the most accurate and patient-specific method available, MC-ID is not routinely employed in clinics, because of its relevant requirements in terms of computational resources and times, and thus other simplified approaches - such as MIRD formalism - are usually preferred instead. Anyhow, it is MC which enables to validate the applicability of simplified methods within specific conditions, and is the most reliable method for research in the field of ID.

The research studies presented in this dissertation had the common denominator of taking advantage of voxel-level patient-specific MC simulation to obtain new results in ID for some nuclear medicine therapies and diagnostic exams. In parallel, focus was put in investigating the limits of such MC methodology, in developing viable corrections to overcome them, and in trying to optimize the computational times of these MC calculations, carried out with the GEANT4-based toolkits GATE and GAMOS.

A first topic concerned MC ID of ^{18}F-choline PET diagnostics cases and ^{90}Y-microspheres TARE therapy cases, focused on the effect on dosimetric outcomes of reconstruction noise, background noise and motion blurring affecting the functional scans used as input data for the simulations. From these studies emerged the non-negligible influence of the mentioned noise effects, highlighted by implementing threshold-based and segmentation-based filtering techniques of the functional scans, which appeared an effective tool for the correction of absorbed dose artefacts caused by noise.

A second topic regarding MC ^{90}Y TARE dosimetry was addressed in a study aimed at reducing computational times while maintaining high dosimetric accuracy, which was carried out by investigating the effect of different simulation parameters, as the production cuts on secondary particles and the resolution of CT scans, and finding the best combinations of them. In addition, the *OpenDose Dosimetry 3D* module of the software 3D Slicer, developed by the *OpenDose* collaboration for the user-friendly implementation of voxel ID workflows, was tested and validated for ^{90}Y TARE cases, comparing the results of the multiple algorithms offered, including MC, with literature results.

Finally, an original simplified renal dosimetry method for ^{177}Lu PRRT therapies, based on a single SPECT/CT scan and multiple external detector measurements, was designed and tested with the help of MC simulations. A proof-of-concept study for this protocol was indeed developed performing phantom experiments, reproducing them with MC simulations, and testing the proposed method on patient data. In the last step, simulating external measurements performed with collimated probe that would be used to deduce information on the radiopharmecautical biokinetics in kidneys, an estimate of the renal absorbed dose was retrieved adopting the simplified protocol and was compared to the estimate obtained with a full imaging-based MC voxel dosimetry, showing promising agreement. The proposed protocol would reduce the needed tomographic imaging to a single scan, minimizing machine occupation time and improving patient comfort.

Acknowledgements

I will probably be a little verbose, but nevertheless the words I will employ will be insufficient to appropriately thank all the people that contributed to my path during the PhD programme and to the realization of the present dissertation.

I would like to start thanking Prof. Giuseppe Mandaglio, which for the third time I had the honor of having as supervisor for a thesis, after bachelor's and master's degrees. In these years spent collaborating with him, he has never stopped supporting me, giving me countless teachings, and guiding me in conducting my research activity in areas for which I had and developed more and more passion. I owe to him a signficant part of my interest for nuclear and particle physics, radiation physics and their applications, Monte Carlo simulation and programming in general. Among the many things I learned – or at least I am trying to learn - from him, I would like to mention the drive in working with authentic passion and utmost commitment, "*probando et reprobando*", always keeping alive the scientific curiosity and in the constant tension in trying to satisfy it.

I am enormously thankful to Prof. Ernesto Amato, who accepted being my co-supervisor for my PhD course and enthusiastically involved me in his research activities. He guided me in the fields of nuclear medicine, internal dosimetry, radiation therapies and medical physics in general, for which I have always had a strong interest, and in which, accompanied by his precious teachings and advice, I had the pleasure to do research. I want to thank him for the many formative dialogues, the continuous collaboration and exchange of ideas, the friendly encouragement and the enlightening recommended readings, scientific and not. Among the aspects that I most appreciated and that I tried to absorb while working with him, there are the constancy and poise in conducting the research work, and the way of conceiving research as physicist in the medical field, without distorting the mindset and knowledge proper of our mother discipline, but learning how to put them at the service of medical purposes, interacting profitably with all the professionals - physicians *in primis* - involved in the process of improving the health and quality of life of patients, which is the final and common goal of all the professionals working in this area.

I would like to warmly thank Dr. Lucrezia Auditore for the kind and constant collaboration. With her great willingness and availability in instructing me in many aspects of my research field, in working together and in confronting ideas and results, she provided an irreplaceable help to my activities and she has been a huge example of work ethic and professionalism for me.

I am greatly thankful to Dr. Antonio Italiano, who has contributed in a fundamental way to my growth as a doctoral student and to most of the results of this dissertation. I tried to treasure at my best his wise and polite advice, our stimulating discussions on scientific topics, both strictly inherent to our research and also beyond it, and the time spent working together, during which he always inspired me in keeping vivid the thirst for knowledge.

I am also very thankful to Dr. Silvano Gnesin for the fruitful collaboration and the many experimental data shared with me; in particular, limiting to the studies that converged into this thesis, the one regarding simplified kidney dosimetry (that will be described in Chapter 7) would have not existed without him. I very much appreciated his lively and proactive approach to research, the *brainstormings* done and the always brilliant ideas shared, while at the same time listening with attention and sincere interest to those of others, and always stimulating new ones.

I would like to point out that the people mentioned so far have been very important for me in these three years also on an extra-academic level, as I have always been able to count on them for advice and support regarding life outside work; therefore, my deep esteem for them does not limit to the scientific level, but extends equally to the human level. I think I am not exaggerating by saying that in them I have found not only peerless scientific mentors, but almost a second family, and I am infinitely grateful to have had the fortune to meet them in my life.

Sincere and dutiful thanks to Prof. Lorenzo Torrisi and Prof. Vincenza Crupi, that have succeeded as the Coordinators of the PhD programme in Physics at University of Messina during the course of my doctoral cycle, guiding us students with wisdom and maximum support. I also thank all the professors and researchers of the MIFT department, whose doctoral lectures and seminars I attended with pleasure, and whith whom I have always had pleasant and enriching conversations.

Many thanks to the staff of the Nuclear Medicine U.O.C. of the University Hospital "G. Martino" in Messina, in which I conducted a significant part of my work, unfortunately with less material presence than I would have liked, due to the COVID-19 pandemics. In the given time I learned a lot, benefiting of the unique possibility of observing almost from the perspective of nuclear medicine physicians and radiology technicians the diagnostics and clinical procedures. I tried to make the best of any interaction, dialogue and experience done there, and in this respect I would like to thank especially Prof. Sergio Baldari, director of the aformentioned U.O.C., Prof. Fabio Minutoli and Dr. Alfredo Campennì, for the precious teachings and the fruitful dialogues.

Sincere thanks to all the members of the *OpenDose* collaboration, which I had the opportunity to join and in which I was warmly welcomed, with special thanks to Alex Vergara Gil for the big help given to me in using and testing the *OpenDose Dosimetry 3D* module, developed by him (and that will be detailed in Chapter 5).

Particular thanks also to Thomas Ligonnet, for the collaboration and work done toghether for the simplified kidney dosimetry method, especially concerning the data analysis of both experimental and simulated results.

I wish to thank all the other colleagues, professors, researchers, medical physicists, physicians, technicians, trainees, students and other professionals of various countries and institutions I had the chance to meet, collaborate with, dialogue with and learn from.

Aside from the people from the academic and scientific world, I want to thank from my heart for their immense love and support my family: my mother Alessandra, my father Angelo and my sister Cristina. Together we faced countless adversities, but thanks to our bond we managed to always move forward, finding serenity in the mutual affection and determination from never stopping trusting each other and believing in each other. They have been an anchor, a safe haven for me.

Last but not least, I thank my other relatives and all my friends and dear ones, from the ones who are also physicist colleagues or colleagues of other disciplines - with whom on one hand I had extremely stimulating discussions, and on the other hand I shared many moments of leisure and fun - to all my other friends; in particular, I thank the closest friends of a lifetime, with whom I have always been able to confide and in which I have always been able to rely. They often motivated me and gave me precious advice, while living amusing experiences together.

Thanks to all the other people not explicitly mentioned here who have had a place in my life in recent years, and therefore have indirectly contributed to the completion of this thesis.

Daniele Pistone

Messina, September 2021

Contents

Abstract **v**

Acknowledgements **vii**

List of Figures **xix**

List of Tables **xxii**

List of Abbreviations, Acronyms and Symbols **xxiii**

General introduction **1**

1 Foundamentals of internal dosimetry **3**

1.1 Introduction . . . 3
1.2 Dosimetric quantities . . . 3
1.2.1 Absorbed Dose . . . 3
1.2.2 Stopping power and linear energy transfer (LET) . . . 4
1.2.3 Quantities characterizing radionuclides . . . 5
1.3 Elements of radiobiology . . . 6
1.3.1 Radiation effects . . . 6
Classification of radiation damages . . . 6
Classification of radiation effects . . . 8
1.3.2 Radiobiological models of the radiation effects . . . 8
Cell survival curves . . . 8
Dose-response curves . . . 11
1.3.3 Quantities relevant to the risk of deterministic effects . . . 11
Relative biological effectiveness (RBE) . . . 11
Biologically effective dose (BED) . . . 12
Equivalent uniform dose (EUD) . . . 13
Isoeffective and Equieffective dose . . . 14
1.3.4 Quantities relevant to the risk of stochastic effects . . . 14
Equivalent dose . . . 14
Effective dose . . . 15
1.4 Principles of radionuclide therapies . . . 15
1.4.1 Radiation therapies . . . 15
1.4.2 Radionuclide therapies . . . 16
1.5 Imaging techniques in nuclear medicine . . . 17
1.5.1 Single-Photon Emission Computed Tomography (SPECT) . . . 18
1.5.2 Positron Emission Tomography (PET) . . . 18
1.5.3 Computed Tomography (CT) and hybrid imaging . . . 18
1.6 Internal dosimetry . . . 22
1.6.1 Organ-level dosimetry . . . 22
MIRD time-dependent formulation . . . 23

MIRD time-independent formulation 25
Organ S-factors calculations 25
1.6.2 Three-dimensional voxel-level dosimetry 26
Local energy deposition approach 26
Dose point-kernel convolution 27
Voxel S-factors approach 27
Direct Monte Carlo simulation 28

2 Monte Carlo simulation in Nuclear Medicine 31
2.1 Introduction 31
2.2 General information on Monte Carlo methods 31
2.2.1 Historical background 31
2.2.2 Basic concepts 32
2.2.3 Random Number Generators (RNGs) 33
2.2.4 Sampling methods 33
Direct sampling 33
Rejection sampling 33
Mixed sampling 34
2.3 Monte Carlo of radiation-matter interaction and its applications in Nuclear Medicine 34
2.4 GEANT4 35
2.4.1 General concepts 35
2.4.2 Suitable *Physics Lists* for Nuclear Medicine dosimetry simulations 36
EM Opt3 36
EM Opt4 37
Decays 37
2.4.3 Particle transport in GEANT4 38
2.5 GATE 40
2.5.1 General concepts 40
2.5.2 GATE simulation architecture for dosimetry applications 41
2.6 GAMOS 45
2.6.1 General concepts 45
2.6.2 User requirements 46
2.6.3 Framework design 46

3 Monte Carlo internal dosimetry in ^{18}F-choline PET diagnostics 49
3.1 Introduction 49
3.2 ^{18}F-choline PET exam 49
3.3 Aim of the study 50
3.4 Simulations settings 51
3.4.1 Softwares employed 51
3.4.2 Input data 51
3.4.3 Organ segmentations 52
3.4.4 Patient-specific phantom implementation 52
GATE procedure 53
GAMOS procedure 53
3.4.5 Radionuclide decays spatial distribution 54
3.4.6 Implementation of physical phenomena 55
3.4.7 Absorbed dose scoring settings 55
3.5 Post-simulation absorbed dose rate calculation 56

Absorbed dose rate maps . . . 56
Average absorbed dose rates in VOIs and DRVHs . . . 56
GATE - GAMOS comparison . . . 56
3.6 Background noise effects and absorbed dose artefacts study . . . 57
3.6.1 PET-filtering procedure . . . 57
Cuts . . . 57
Filtered-PET - native-PET simulations comparison . . . 58
3.7 Results . . . 58
3.8 Discussion . . . 62
3.8.1 GATE-GAMOS comparison . . . 62
3.8.2 PET background noise effects . . . 64

4 ^{90}Y-TARE Monte Carlo internal dosimetry: optimization of GATE simulation times 67
4.1 Introduction . . . 67
4.2 Trans-Arterial Radio-Embolization (TARE) of HepatoCellular Carcinoma (HCC) . . . 67
4.3 Aim of the study . . . 69
4.4 Simulations implementation . . . 70
4.4.1 Input data . . . 70
4.4.2 CT resamplings . . . 70
4.4.3 VOIs segmentations . . . 70
4.4.4 Phantoms, source definition and other settings . . . 71
4.4.5 Production cuts . . . 73
4.5 Dosimetric calculations and comparisons . . . 74
4.6 Results . . . 76
4.6.1 Average absorbed doses and DVHs . . . 76
4.6.2 Statistical uncertainties . . . 79
4.6.3 Simulation times . . . 81
4.7 Discussion . . . 81

5 ^{90}Y-TARE internal dosimetry with *OpenDose Dosimetry 3D* 85
5.1 Introduction . . . 85
5.2 Internal dosimetry with the *OpenDose Dosimetry 3D* module . . . 85
5.2.1 The *OpenDose* collaboration . . . 85
5.2.2 The *OpenDose3D* Slicer module . . . 86
5.3 Aims and calculations settings . . . 88
5.3.1 TARE imaging input data . . . 88
5.3.2 VOIs segmentations . . . 90
5.3.3 Dose calculation methods settings and outputs comparison . . . 90
5.4 Results and discussion . . . 95

6 Effects of SPECT artefacts and noise on Monte Carlo ^{90}Y-TARE dosimetry 101
6.1 Introduction . . . 101
6.2 Aim of the study . . . 101
6.3 Pre-simulation settings . . . 102
6.3.1 Input scans and VOIs segmentations . . . 102
6.3.2 SPECT filtering techniques . . . 104
6.3.3 Geometry and physics settings . . . 104
6.4 Post-simulation dosimetric calculations . . . 106
6.5 Results and discussion . . . 107

6.5.1 Liver-related VOIs 107
6.5.2 Lungs-related VOIs 108

7 A simplified kidney dosimetry protocol for ^{177}Lu-PRRT 121
7.1 Introduction 121
7.2 ^{177}Lu Peptide Receptor Radionuclide Therapy (PRRT) for NeuroEndocrine Tumors (NETs) 121
7.3 Motivations and aims 123
7.4 Phantom-based experimental study 124
7.5 Monte Carlo simulations of the phantom set-up 126
7.5.1 Geometry of the phantom set-up 126
Voxelized phantom volume 126
Geometrical-shaped volumes 128
7.5.2 Primary sources and simulations settings 129
7.5.3 Simulations output analysis and kidney half-life estimation . . 131
7.6 Monte Carlo test on a ^{177}Lu-DOTATATE PRRT clinical case 132
7.6.1 Simulations settings 133
7.6.2 Kidney half-life estimation and dosimetric calculations 134
Full image-based MC dosimetry 135
Simplified MC dosimetry 135
7.7 Results 136
7.7.1 Phantom study: experimental results 136
7.7.2 Phantom study: MC simulations results 136
7.7.3 Dosimetry workflows on ^{177}Lu-DOTATATE PRRT clinical case: MC simulations results 138
7.8 Discussion 140

General conclusion 145

A ^{90}Y-TARE MC dosimetry: optimization of simulation times 149
A.1 Average absorbed doses tables 149
A.2 DVHs 149

B ^{90}Y-TARE MC dosimetry: effects of SPECT artefacts and noise 167
B.1 DVHs 167

C ^{177}Lu-PRRT simplified kidney dosimetry protocol: uncertainties analysis 175
C.1 Statistics and uncertainties evaluation in experimental measurements 175
C.2 Statistics and uncertainties evaluation for MC simulations 176
C.2.1 Uncertainties on half-lives 176
C.2.2 Uncertainties on absorbed dose rates 177
C.2.3 Uncertainties on total absorbed doses 178

List of Figures

1.3 (a) Schema of the basic components of a modern gamma camera [40]. (b) Picture of a dual-headed SPECT system (Siemens Symbia Evo Excel `https://www.siemens-healthineers.com/en-eg/molecular-imaging/spect-and-spect-ct/symbia-evo`) 19
1.4 (a) Scheme of the detection of simultaneously emitted annihilation photons by a pair of opposite PET detectors [40]. (b) Scheme of PET detectors operating in electronic coincidence with detectors on the opposite side of the ring, allowing simultaneous acquisition of projection views from many different angles. Solid and dotted lines illustrate two simultaneously acquired projection views. [40]. (c) Picture of a PET/CT scanner (Siemens Biograph mCT Sim edition `https://www.siemens-healthineers.com/en-ae/molecular-imaging/pet-ct/biograph-mct-sim`). 20
1.6 (a) MIRD-based representation of target and source organs of interest for three types of radiopharmaceuticals (`https://humanhealth.iaea.org/HHW/NuclearMedicine/Webinars/Basic_Nuclear_Medicine/Basic_Radiopharmaceutical_Dosimetry/index.html`). (b) Illustrative representation of voxel-level targets and sources (`https://www.medphys.it/res_svoxel.htm`). 23

2.3 (a) A GATE's *World* geometry (the large cube with light-blue borders) and a cubic *daughter* volume (white); (b) a patient-specific voxelized phantom geometry (N.B. GATE visualization is not optimized for voxelized volumes); (c) a set of detector volumes reproducing an OPET scanner [104], with colors indicating different sections of the array. 43

3.1 Positron-emission energy spectrum of ^{18}F [111]. 50
3.2 Chemical structural formula of choline (left) and ^{18}F-choline (right) molecules. 50
3.3 Coronal slices of the resampled CT (a), the native PET (b) and of the fusion of the two (c). 52
3.4 Liver (green), right lung (blue) and left lung (orange) VOIs segmentations, reported on a coronal view superimposed to the CT (a) and in a 3D representation (b). 52
3.5 HU-density calibration points and their bi-linear fit, whose parameters are reported in Tab. 3.4. 54
3.6 Coronal slices of the native PET (a) and filtered PET (b) fused with CT (for visual morphological reference), and the logical difference between the two (c). 58
3.7 Coronal slices of absorbed dose rate maps estimated with GATE and GAMOS native-PET and filtered-PET simulations. 59

3.8 Distributions of absorbed dose rate relative percent differences at voxel level (ε^{ijk}) inside VOIs for unfiltered-PET (a, c, e) and filtered-PET (b, d, f) simulations. 61
3.9 Axial, sagittal and coronal slices of the absorbed dose rate maps (fused with CT) estimated with GATE using native PET (a1, b1, c1) and filtered PET (a2, b2, c2), and the corresponding slices obtained by subtraction of the filtered-PET absorbed dose map from the native-PET one (a3, b3, c3). 62
3.10 DRVHs in liver (a), right lung (b) and left lung (c) VOIs, obtained with native-PET (solid lines) and filtered-PET (dotted lines) simulations. . . 63

4.1 Schematic graphical representation of a TARE treatment, with detail, on the right, of the injection of microspheres that deposit into the capillaries supplying the tumour. 68
4.2 Beta-emission energy spectrum of ^{90}Y [111]. 69
4.3 Axial views of the native CT (a), of the various resampled CTs - R2 (b), R8 (c), R64 (d), RS (e) -, and of the Tc-MAA SPECT (f). All the images have no graphical smoothing of the actual slice pixels, in order to appreciate as much as possible the different resolutions. 72
4.4 Representation of the defined VOIs on axial (a,b) and coronal (c) native CT slices and in 3D view (d, e, f). The color-VOI key is: green = liver, yellow = liver perfused, orange = lesions, red = healthy liver perfused, violet = healthy liver, pink = right lung, magenta = left lung, blue = right kidney, light blue = left kidney. 73
4.5 Axial slices of the fusion images of CTs and corresponding absorbed dose maps obtained from simulations setting 0.01 mm as production cut. The resamplings shown are: (a) N - the reference simulation -, (b) R2, (c) R8, (d) R64, (e) RS. No graphical smoothing was applied to appreciate as much as possible the different resolutions. 77
4.6 $\langle D\rangle_{VOI}$ and ε_{VOI} in liver-related VOIs, for all the production cuts and CT resampling volumes used (N, R2, R8, R64, RS, as indicated in Table 4.1, denoted with different colors). 78
4.7 $\langle D\rangle_{VOI}$ and ε_{VOI} in lungs- and kidneys-related VOIs, for all the production cuts and CT resampling volumes used (N, R2, R8, R64, RS, as indicated in Table 4.1, denoted with different colors). 79
4.8 Δ_{VOI} values (Eq. 4.6) in VOIs as a function of voxel volume ratio with respect to N CT voxel volume. Full circles refer to simulations employing N, R2, R8 and R64 CTs, fitted with bi-exponential function; open circles refer to simulations employing RS CT, not considered in the fits but reported for completeness. 80
4.9 Simulation time ratios with respect to reference simulation time (which lasted 139.5 h), as a function of production range cut length (a) and of voxel volume ratio (b). Full triangles in (b) represent simulations using N, R2, R8 and R64 CTs, taken into account for fits; open triangles represent simulations using RS CT, not considered for fits. 82

5.1 World map showing the universities and institutes involved in the *OpenDose* collaboration [129]. 86
5.2 Flow chart of a clinical dosimetry workflow as followed by *OpenDose3D*, which requires the first 3 steps as input, and can manage the last 3 steps. 86

5.3 View of the utilities panels of the *OpenDose3D* module of 3D Slicer. . . 89
5.4 Coronal fusion slices of the input CT and SPECT for patient 1 (a), 2 (c) and 3 (e), and coronal fusion slices of resampled density maps and activity maps calculated during the D3D workflow for patient 1 (b), 2 (d), 3 (f). 91
5.5 Coronal slices on native CTs and 3D representations of the VOIs segmentations for patient 1 (a, b, c, d), 2 (e, f, g, h) and 3 (i, j, k, l). Color-VOI key is: yellow = liver, light blue = liver perfused, red = lesions, orange = healthy liver, blue = healthy liver perfused. 92
5.6 Average absorbed dose values in VOIs obtained with all the adopted D3D methods and relative percent differences with respect to MC GAMOS results ([48]) for patient 1. 98
5.7 Average absorbed dose values in VOIs obtained with all the adopted D3D methods and relative percent differences with respect to MC GAMOS results ([48]) for patient 2. 99
5.8 Average absorbed dose values in VOIs obtained with all the adopted D3D methods and relative percent differences with respect to MC GAMOS results ([48]) for patient 3. 100

6.1 Depictions of right lung (green) and left lung (magenta) segmentations for the three examined cases. The first row (a, b, c, d) refers to patient 1, 2nd row to pat. 2, 3rd row to pat. 3. For each row, starting from left, it is reported a 3D representation of the "standard" segmentations, and coronal slices of the "standard" segmentations, of the segmentations with air removal using -900 HU threshold, and of the segmentation with air removal using -855 HU threshold. 103
6.2 Pat. 2 coronal fusion slices of CT and SPECTs (counts), native (a) and filtered via A (b), B (d), C (f) and D (h) (Sec. 6.3.2), each accompanied on its right by the corresponding difference image between native and filtered SPECTs (e.g., (c) = (a) - (b)). 105
6.3 GATE average absorbed doses $\langle D \rangle_{VOI}$ in liver-related VOIs and corresponding relative percent differences κ_{VOI} with respect native-SPECT simulation for patient 1; the error bars are the average values of standard deviation of mean absorbed dose within VOIs, $\langle \delta \rangle_{VOI}$ (Eq. 4.5). 111
6.4 GATE average absorbed doses $\langle D \rangle_{VOI}$ in lungs-related VOIs and corresponding relative percent differences κ_{VOI} with respect native-SPECT simulation for patient 1; the error bars are the average values of standard deviation of mean absorbed dose within VOIs, $\langle \delta \rangle_{VOI}$ (Eq. 4.5). . 112
6.5 GATE average absorbed doses $\langle D \rangle_{VOI}$ in liver-related VOIs and corresponding relative percent differences κ_{VOI} with respect native-SPECT simulation for patient 2; the error bars are the average values of standard deviation of mean absorbed dose within VOIs, $\langle \delta \rangle_{VOI}$ (Eq. 4.5). . 113
6.6 GATE average absorbed doses $\langle D \rangle_{VOI}$ in lungs-related VOIs and corresponding relative percent differences κ_{VOI} with respect native-SPECT simulation for patient 2; the error bars are the average values of standard deviation of mean absorbed dose within VOIs, $\langle \delta \rangle_{VOI}$ (Eq. 4.5). . 114
6.7 GATE average absorbed doses $\langle D \rangle_{VOI}$ in liver-related VOIs and corresponding relative percent differences κ_{VOI} with respect native-SPECT simulation for patient 3; the error bars are the average values of standard deviation of mean absorbed dose within VOIs, $\langle \delta \rangle_{VOI}$ (Eq. 4.5). . 115

6.8 GATE average absorbed doses $\langle D\rangle_{VOI}$ in lungs-related VOIs and corresponding relative percent differences κ_{VOI} with respect native-SPECT simulation for patient 3; the error bars are the average values of standard deviation of mean absorbed dose within VOIs, $\langle\delta\rangle_{VOI}$ (Eq. 4.5). . 116
6.9 GATE average values of relative percent differences $\langle\kappa_{VOI}\rangle$ (Eq. 6.2) over the three patients in each type of VOI; the error bars here represent the standard deviations of the averages, σ_{VOI}. 117
6.10 Comparison between GATE and GAMOS simulations average absorbed dose results for patient 2, in terms of relative percent differences ε_{VOI} (Eq. 6.3). 118
6.11 Coronal fusion slices for patient 2 of CT and GATE absorbed dose maps (Gy) obtained with native- (a) and filtered-SPECT A (b), B (d), C (f) and D (h) (Sec. 6.3.2), each accompanied on its right by the corresponding difference image (Gy) between native- and filtered-SPECT absorbed dose maps. 119

7.1 β^--emission energy spectrum of ^{177}Lu [111]. 122
7.2 (a) The abdominal phantom employed for the study, with depicted the positions (red circles) for both left kidney and background subtraction measurements. (b) Voxelized phantom defined for MC simulations, with segmentations of the regions of interest for this study: left kidney (orange), right kidney (blue) and liver (green). The positions of the simulated measurements are depicted with full red circles; dashed circles are the experimental positions as shown in panel (a) . . 126
7.3 Axial (a), coronal (b) and sagittal (c) views of the phantom CT scan (the phantom was positioned standing on the CT bed), resampled and resized as described in Sec. 7.5.1. 127
7.4 Bi-linear fit (solid blue line) of the calibration points (red circles) in Tab. 7.2, whose parameters are reported in Tab. 7.3. 128
7.5 Axial view of L (a) and M (b) configurations implemented in the MC geometry, sagittal view (c) referred to both configurations, and a 3D representation of the system in L configuration (d). In MC, A = 62 mm for L, A = 0 mm for M; B = 90 mm for both M and L, since in the experiment L-UP and M-UP had B = 110 mm, L-DN and M-DN had B = 70 mm; C = 55 mm in MC for both L and M. 130
7.6 Coronal fusion slices of the resampled and corrected CTs and SPECTs at t = 2 hrs (a), 20 hrs (b) and 70 hrs (c); green lines represent the left kidney VOIs borders at the different time-points, magenta circles indicate the L and M positions of the detector in the simulations (pointing at the body from the posterior side) 133
7.7 Box-plots of the left kidney half-lives T_{eff} estimated from MC simulations employing $^{99\text{m}}$Tc and ^{177}Lu, deduced from four-time-points fit combinations as explained in Sec. 7.5.3 and Appendix C. In (a) and (b) the results from fits performed on with count-rates corrected for the background, in (c) and (d) without background correction. 138
7.8 Coronal slices of the absorbed dose rate maps estimated with MC simulations, fused with respective CTs, at t = 2 hrs (a), 20 hrs (b) and 70 hrs (c); green lines represent the left kidney VOIs borders at each time point. 139

7.9 In (a), the red points are the $\langle \dot{D}(t) \rangle$s, the solid blue line is the mono-exponential fit function integrated in Eq. 7.11 for the full image-based MC dosimetry. In (b), (c) and (d), the single red point is the average absorbed dose rate evaluated at time $T = 2$, 20, and 70 hrs, respectively, employed for the simplified dosimetry; the solid green line is the analytical mono-exponential function integrated in Eq. 7.12; the orange shaded region represents the absolute uncertainties on the function's values; the dashed blue line is the same function represented as solid blue line in a), plotted to compare full and simplified dosimetry functions. 140

A.1 DVHs and σs (%) in liver VOI for N, R2, R8 and R64 CTs, relative to Chapter 4. 155
A.2 DVHs and σs (%) in liver VOI for RS CT, and in lesions VOI for N, R2 and R8 CTs, relative to Chapter 4. 156
A.3 DVHs and σs (%) in lesions VOI for R64 and RS CTs, and in liver perfused VOI for N and R2 CTs, relative to Chapter 4. 157
A.4 DVHs and σs (%) in liver perfused VOIs for R8, R64 and RS CTs, and in healthy liver VOI for N CT, relative to Chapter 4. 158
A.5 DVHs and σs (%) in healthy liver VOI for R2, R8, R64 and RS CTs, relative to Chapter 4. 159
A.6 DVHs and σs (%) in healthy liver perfused VOI for N, R2, R8 and R64 CTs, relative to Chapter 4. 160
A.7 DVHs and σs (%) in healthy liver perfused VOI for RS CT, and in right lung VOI for N, R2 and R8 CTs, relative to Chapter 4. 161
A.8 DVHs and σs (%) in right lung VOI for R64 and RS CTs, and in left lung VOI for N and R2 CTs, relative to Chapter 4. 162
A.9 DVHs and σs (%) in left lung VOI for R8, R64 and RS CT, and in right kidney VOI for N CT, relative to Chapter 4. 163
A.10 DVHs and σs (%) in right kidney VOI for R2, R8, R64 and RS CTs, relative to Chapter 4. 164
A.11 DVHs and σs (%) in left kidney VOI for N, R2, R8 and R64 CTs, relative to Chapter 4. 165
A.12 DVHs and σs (%) in left kidney VOI for RS CT, relative to Chapter 4. . 166

B.1 DVHs in liver-related VOIs of patient 1 obtained with all the types of GATE simulations described in Chapter 6. 168
B.2 DVHs in lungs-related VOIs of patient 1 obtained with all the types of GATE simulations described in Chapter 6; the color key is the same as in Fig. B.1 169
B.3 DVHs in liver-related VOIs of patient 2 obtained with all the types of GATE and GAMOS simulations described in Chapter 6. 170
B.4 DVHs in lungs-related VOIs of patient 2 obtained with all the types of GATE and GAMOS simulations described in Chapter 6; the color key is the same as in Fig. B.3 171
B.5 DVHs in liver-related VOIs of patient 3 obtained with all the types of GATE simulations described in Chapter 6. 172
B.6 DVHs in lungs-related VOIs of patient 3 obtained with all the types of GATE simulations described in Chapter 6; the color key is the same as in Fig. B.5 173

List of Tables

3.1 Resolution and voxel dimensions for the resampled CT scan and PET scan used as input data for the study; for the PET scan are also reported the administered activity to the patient, $A(t_0)$, and the interval of time between the administration and the scan acquisition, Δt. 51
3.2 HU intervals and corresponding density (ρ) intervals set to identify the materials used in the simulations, whose compositions were taken from the GEANT4 database [115]. 53
3.3 HU-density calibration values used for the density values assignment to phantom's voxels. 54
3.4 Fit parameters (defined in Eq. 3.2.) and χ^2 of the bi-linear fit in Fig. 3.5, performed on the HU-density calibration values of Tab. 3.3. 54
3.5 $\langle \dot{D}(t_s) \rangle$s, $\langle \sigma^{ijk} \rangle$s, εs, $\langle \varepsilon_{ijk} \rangle$s and κs deduced from GATE and GAMOS filtered- and native-PET simulations for the three VOIs, as defined in Sec.s 3.5 and 3.6. 60

4.1 Resolution and voxel dimensions of the CT resamplings (R), compared to native (N) CT in terms of voxel volume ratio $\mathrm{v_R}/\mathrm{v_N}$. 71
4.2 Production range cuts on secondary particles produced for e^-, e^+ and photons set in the simulations in correspondence of the different resamplings of the CT. 74
4.3 VOI volumes (cm^3) for each absorbed dose CT resampling (and thus for each corresponding absorbed dose map). 75

5.1 Resolution and voxel dimensions of the input CTs and Tc-MAA SPECTs of the three patient cases of this study. 90
5.2 Masses m (g) of the VOI segmentations used in [48] and imported in 3D Slicer for this work (D3D). 91
5.3 Input parameters for the D3D workflow: injected activity $A(0)$(MBq), camera factor C.F. (Bq/counts), acquisition time A.T. (s) 93
5.4 Computation times required for the average absorbed dose calculations with the various D3D methods employed. HeC calculations were performed with 30.0 mm kernel limit, GATE MC calculations were obtained simulating $2 \cdot 10^8$ primary events. 97

7.1 Experimentally set total activities TA (MBq) and activity concentrations AC (kBq/mL) in the different compartments, and experimental effective half-lives ($T_{\mathrm{eff\,exp}}$) characterizing their time evolution reproduced through ERs, deduced by fitting the TA (or AC) points. 125
7.2 HU-density calibration values used for the density assignment to phantom's voxels, as described in Sec. 7.5.1. 127
7.3 Fit parameters (defined in Eq. 3.2) and χ^2 of the bi-linear fit in Fig. 7.4 performed on HU-density calibration values of Tab. 7.2. 128

7.4 HU intervals and corresponding density (ρ) intervals set to identify the materials used for the phantom study simulations (Sec. 7.5.1); materials compositions were taken from the GEANT4 database [115], except for PMMA (not present), defined with the following elements and mass fractions, according to its chemical formula $(C_5O_2H_8)_n$: H 8.0541 %, C 59.9846 %, O 31.9613 %. 129
7.5 HU intervals and corresponding density (ρ) intervals (through the fit in Fig. 7.4) set to identify the materials used for the clinical test simulations (Sec. 7.6); materials compositions were taken from the GEANT4 database, using ICRP compounds for tissues [115]. 134
7.6 Effective kidney half-lives T_{eff} calculated in the experimental phantom study from four-time-points fits of the average of the consecutive count-rates, their corresponding standard errors and the relative differences κ (%) with respect to reference (54.9 hrs) in Tab. 7.1. 136
7.7 Average effective kidney half-lives $\langle T_{\text{eff}} \rangle$ for the phantom study MC simulations, evaluated for the reported nuclides, CRs types, time-points choice (TP) and simulated sources, as explained in Sec. 7.5.3 and Appendix C. 137
7.8 Effective kidney half-lives for the PRRT patient study obtained for the full image-based and simplified dosimetry workflows, as described in Sec. 7.6. 139
7.9 Left kidney average absorbed doses $\langle D \rangle$, also expressed per unit of administered activity as $\langle D \rangle / A_{\text{adm}}$, evaluated with the full and simplified dosimetry protocols, and the relative percent differences δ (%) with respect to the full dosimetry value. 141

A.1 $\langle D \rangle_{VOI}$ (Gy), $\langle \delta \rangle_{VOI}$ (%) and ε_{VOI} (Eq. 4.7 in Chapter 4) for N CT in the considered VOIs, respectively reported as the upper, middle and lower value in column for each box, i.e. for each combination of range cut and VOI. 150
A.2 $\langle D \rangle_{VOI}$ (Gy), $\langle \delta \rangle_{VOI}$ (%) and ε_{VOI} (Eq. 4.7 in Chapter 4) for R2 CT in the considered VOIs, respectively reported as the upper, middle and lower value in column for each box, i.e. for each combination of range cut and VOI. 151
A.3 $\langle D \rangle_{VOI}$ (Gy), $\langle \delta \rangle_{VOI}$ (%) and ε_{VOI} (Eq. 4.7 in Chapter 4) for R8 CT in the considered VOIs, respectively reported as the upper, middle and lower value in column for each box, i.e. for each combination of range cut and VOI. 152
A.4 $\langle D \rangle_{VOI}$ (Gy), $\langle \delta \rangle_{VOI}$ (%) and ε_{VOI} (Eq. 4.7 in Chapter 4) for R64 CT in the considered VOIs, respectively reported as the upper, middle and lower value in column for each box, i.e. for each combination of range cut and VOI. 153
A.5 $\langle D \rangle_{VOI}$ (Gy), $\langle \delta \rangle_{VOI}$ (%) and ε_{VOI} (Eq. 4.7 in Chapter 4) for RS CT in the considered VOIs, respectively reported as the upper, middle and lower value in column for each box, i.e. for each combination of range cut and VOI. 154

List of Abbreviations, Acronyms and Symbols

A

A	Activity
$\tilde{A}$	Time-integrated (or "cumulated") activity
AC	Activity Concentration
ACTM	ACTivity Map
ATI	Activity Time-Integration

B

BED	Biologically Effective Dose
Bq	Becquerel (s $^{-1}$)

C

CPU	Central Processing Unit
CR	Count Rate
CT	Computed Tomography

D

D	Absorbed dose
$\dot{D}$	Absorbed dose rate
DNA	DeoxyriboNucleic Acid
DPK	Dose Point-Kernel
DRVH	Dose Rate - Volume Histogram
DVH	Dose-Volume Histogram
D3D	OpenDose Dosimetry 3D (module)

E

EBRT	External Beam RadioTherapy
EM	ElectroMagnetic
ENSDF	Evaluated Nuclear Structure Data File
ER	Experimental Realization
EUD	Equivalent Uniform Dose

F

FFT	Fast Fourier Transform
FOV	Field Of View

G

GAMOS	Geant4-based Architecture for Medicine-Oriented Simulations
GATE	Geant4 Application for Tomographic Emission
GEANT4	GEometry ANd Tracking (4)

GEP	GastroEnteroPancreatic
GPU	Graphics Processing Unit
Gy	Gray (J kg^{-1})

H

HCC	HepatoCellular Carcinoma
HeC	Heterogeneous Convolution
HoC	Homogeneous Convolution
HU	Hounsfield Unit

I

IAEA	International Atomic Energy Agency
ICRP	International Commission on Radiological Protection
ICRU	International Commission on Radiation Units

J

K

L

LED	Local Energy Deposition
LET	Linear Energy Transfer
LLN	Law of Large Numbers
LQ	Linear Quadratic (model)

M

MAA	MacroAggregated Albumin
MC	Monte Carlo
MIRD	(Committee on) Medical Internal Radiation Dose
MRI	Magnetic Resonance Imaging

N

NCRP	National Council on Radiation Protection and Measurements
NET	NeuroEndocrine Tumor
NM	Nuclear Medicine

O

P

PC	Prostate Cancer
PDF	Probability Density Function
PET	Positron Emission Tomography
PRRT	Peptide Receptor Radionuclide Therapy
PSA	Prostate-Specific Antigen

Q

R

RBE	Relative Biological Effectiveness
RNG	Random Number Generator
RPT	RadioPharmaceutical Therapy

S

SAF	Specific Absorbed Fraction
SF	Surviving Fraction
SI	International System (of Units)
SIRT	Selective Internal Radiation Therapy
SPECT	Single-Photon Emission Computed Tomography
SSA	Somatostatin Analog
SSTR	Somatostatin Receptor
Sv	Sievert (J kg^{-1})

T

TAC	Time-Activity Curve
TACE	Trans-Arterial Chemo-Embolization
TARE	Trans-Arterial Radio-Embolization

U

V

VSV	Voxel S-Value

W

X

Y

Z

Dedicated to my parents and my sister

General introduction

This very short initial chapter introduces schematically the scientific context in which the present dissertation was developed, which is internal dosimetry performed with the use of Monte Carlo methods, and summarizes the main contents that will be treated in detail in the different chapters.

Internal dosimetry in nuclear medicine aims to estimate the radiation absorbed doses to tissues and organs following diagnostic and therapeutic procedures employing radionuclides and radiopharmaceuticals. It has a growing role in planning and monitoring molecular radiotherapy treatments, and also in characterizing the diagnostic imaging procedures. Among the calculation methods adoptable for internal dosimetry, the gold standard is the direct Monte Carlo (MC) simulation of radiation transport and interaction in living matter, in particular when applied to voxelized geometries built from morphological (CT) and functional (SPECT or PET) scans, representing, respectively, patient's body and radionuclide spatial distribution. Even if not routinely employed in clinics because of its demanding computational resources and complexity of implementation, the high level of accuracy and patient-specificity of MC calculations makes it an excellent approach for research in internal dosimetry; for example to investigate via simulation new treatments, protocols or radiopharmaceuticals, to better characterize and improve already established procedures, to validate simplified dosimetric methods.

As anticipated, this work of thesis develops precisely in the field of MC internal dosimetry in nuclear medicine, and in it converge the results of research activities regarding original voxel-level dosimetry studies for some diagnostic imaging procedures and radionuclide therapy treatments, the optimization of simulation times required for such calculations, the investigation and correction of absorbed dose artefacts caused by different kinds of noise present in functional scans, the development of novel simplified dosimetric methods.

In particular, Chapter 1 describes the fundamental definitions, units and models of radiobiological effects, radionuclide therapies, nuclear medicine imaging and internal dosimetry.

Chapter 2 introduces the basic concepts of Monte Carlo methods, with particular emphasis on their applications in nuclear medicine dosimetry and on the main software packages used for these purposes in this work of thesis: GEANT4 and the interface toolkits GATE and GAMOS.

In Chapter 3 a comparative MC internal dosimetry study of GATE and GAMOS applied to a ^{18}F-choline PET procedure is reported. This work has also focused on the effect on dosimetric outcomes, in particular in lungs and other air-rich regions, of background noise affecting PET scan. For this purpose, it was taken advantage of an implemented filtering technique of the functional scan, which appeared promising as a reasonable correction method for noise-induced absorbed dose artefacts.

Chapter 4 reports a MC internal dosimetry study of ^{90}Y TARE cases, aimed at optimizing computation times by varying two main simulations parameters: CT scan resolution – via resampling of the native images – and production cuts on secondary particles. The behavior of computation time as a function of them was characterized

and the best combinations of parameters, maintaining good dosimetric accuracy, were found.
In Chapter 5 it is described the testing and validation for ^{90}Y TARE cases of the *OpenDose Dosimetry 3D* module of the software 3D Slicer, developed by the *OpenDose* collaboration for the user-friendly implementation of voxel-level internal dosimetry workflows. The results produced by the different algorithms available in the module were successfully compared with literature results obtained using the same input imaging data, testifying the correct functioning of *OpenDose Dosimetry 3D* for this kind of nuclear medicine procedure.
Chapter 6 deals with MC dosimetry of ^{90}Y TARE cases, focusing in particular on the identification and possible correction of absorbed dose artefacts caused especially in lungs by reconstruction noise and motion blurring present in SPECT scans. Similarly to what was done in Chapter 3, different threshold-based and segmentation-based filtering techniques were developed to achieve this goal.
Finally, in Chapter 7 it is presented and proposed an original simplified method for renal dosimetry in ^{177}Lu PRRT therapies, relying on a single SPECT/CT and multiple external collimated probe measurements directed on kidneys. A proof of concept of this novel method was carried out though an abdominal phantom experiment and related MC simulations and a MC test conducted on a patient imaging dataset, simulating probe measurements on them and comparing the simplified dosimetry workflow to a complete imaging-based workflow employing multiple SPECT/CTs.
A brief concluding chapter, entitled "General conclusion", summarizes all the main findings of this thesis and outlines some future perspectives.

Chapter 1

Foundamentals of internal dosimetry

1.1 Introduction

This chapter serves as an overview on the research macro-area in which this doctoral dissertation develops, which is internal dosimetry. Starting from the definition of the main quantities employed in dosimetry in general, the principal concepts regarding radiobiological effects of ionizing radiations are presented, outlining the most diffused models and quantities aimed at their description and quantification. Follows a brief introduction to the basic aspects of radiation therapies, in particular radionuclide therapies in nuclear medicine, and to the tomographic imaging techniques employed in this field to acquire information on patient's body morphology and radiopharmaceutical biodistribution. Finally, the different existing models of internal dosimetry are discussed, starting from organ-level MIRD formalism and arriving to three-dimensional Monte Carlo voxel-level dosimetry.

1.2 Dosimetric quantities

Radiation dosimetry deals with the quantification of the amount and of the spatial and temporal distribution of energy deposited in matter by ionizing radiation. For this purpose, dosimetric quantities are defined, which can have a "stochastic" or a "deterministic" (i.e., non-stochastic) nature. Quantities whose values occur randomly, subject to statistical fluctuations and hence not predictable except in probabilistic terms, are termed stochastic. Quantities which are the mean, or expectation value, of a large number of determinations of a stochastic quantity, are defined deterministic.

1.2.1 Absorbed Dose

The most widely used deterministic quantity in dosimetry is the absorbed dose (D), defined as the expectation value of the energy imparted to matter by any type of ionizing radiation, per unit mass of the considered volume [1, 2]:

$$D = \frac{d\bar{\epsilon}}{dm} \tag{1.1}$$

where $\bar{\epsilon}$ is the expectation value of the energy imparted to a the finite volume V during some time interval, $d\bar{\epsilon}$ is that for an infinitesimal volume dv, and dm is the mass of matter in dv. The "energy imparted" $\bar{\epsilon}$ can be expressed as:

$$\bar{\epsilon} = R_{in} - R_{out} + \sum Q \tag{1.2}$$

where R_{in} is the radiant energy of particles, both charged and uncharged, entering V, R_{out} is the radiant energy of particles leaving V, and $\sum Q$ is the net energy derived from rest mass in V (positive for $m \to E$ conversions, negative for $E \to m$).

The stochastic quantity related to the deterministic absorbed dose is the so called "specfic energy" (z_1):

$$z_1 = \frac{\epsilon_1}{m} \tag{1.3}$$

where ϵ_1 is the energy imparted to matter by a single energy deposition event and m is the mass of matter in volume V.

In the SI system, absorbed dose is expressed in gray (1 Gy = 1 J/kg). The older conventional unit was the rad (1 Rad = 1 erg/g), related to gray by the conversion: 1 Gy = 100 rad.

The deterministic quantity absorbed dose rate ($\dot{D}(t)$) at time t is defined as:

$$\dot{D}(t) = \frac{dD(t)}{dt} = \frac{d}{dt}\left(\frac{d\bar{\epsilon}(t)}{dm}\right) \tag{1.4}$$

1.2.2 Stopping power and linear energy transfer (LET)

The deterministic quantity linear stopping power (S) of a charged particle (or the secondary charged particle produced by the primary radiation) in a material is defined as the expectation value of the energy loss dE per unit path length dl transversed in that material [3, 4]:

$$S = \frac{dE}{dl} \tag{1.5}$$

Its SI units are J/m, and it may be expressed in eV/m or some other convenient multiples or submultiples, such as MeV/cm.

A mass stopping power (S/ρ) can be also defined as the quotient of the linear stopping power S by the mass density ρ of the absorbing material. It results in energy loss per unit of surface mass density of the medium, having J·m^2/kg as SI units. Dividing by the density of the absorbing material almost eliminates the dependence of the mass stopping power on density [4].

Stopping power can be expressed as a sum of independent contributing terms:

$$S = S_{el} + S_{rad} + S_{nucl} \tag{1.6}$$

S_{el} is the electronic (or collision) stopping power, due to interactions of charged particles with atomic orbital electrons resulting in ionization or excitation; S_{rad} is the radiative stopping power, due to emission of bremsstrahlung photons in the electric field of atomic nuclei or atomic electrons; S_{nucl} is the nuclear stopping power, due to elastic Coulomb interactions with atomic nuclei. In addition, energy losses due to nonelastic nuclear interactions could be considered, but such processes are not usually described by a stopping power.

Stopping powers are widely used in radiation dosimetry, but they are rarely measured and must be calculated from theory. For electrons and positrons the Bethe theory is usually used to calculate stopping powers [3].

Notably, in medical radiation dosimetry the quantity linear energy transfer (LET) - or restricted linear electronic stopping power - is used, indicated as L_Δ or LET_Δ. The

L_Δ of a material for charged particles of a given type and energy is defined as the energy loss dE per unit path length dl due to those electronic interactions in which the energy loss is less than the energy cut-off Δ; in other words, considering the electronic energy loss minus the mean sum of kinetic energies in excess of Δ of all the secondary electrons released by the charged particles ($dE_{ke,\Delta}$) [4]:

$$L_\Delta = \left(\frac{dE}{dl}\right)_\Delta = S_{el} - \frac{dE_{ke,\Delta}}{dl} \tag{1.7}$$

LET SI units are the same as stopping power, and it is often expressed in keV/μm. The concept of LET is introduced to calculate the energy transferred to a localized region of interest, since by "limiting" the energy transfer to secondary electrons to a threshold Δ, they are "allowed" to escape the region of interest, basically considering their energy deposition events as separate from those along the track of the primary radiation.

If the threshold Δ is disregarded, setting the energy cut-off equal to infinity, the 'unrestricted linear energy transfer', L_∞ (or LET_∞) is retrieved, which coincides simply to the electronic stopping power S_{el} [2].

LET is usually used to quantitatively characterize the "quality" of radiation, which is related to the characteristics of the microscopic spatial distribution of energy-deposition events, determined by the mass, charge and energy of the charged particles composing the radiation or, in the case of neutral particles, the secondary charged particles produced by the radiation. In fact, besides the quantity of radiation, estimated through the absorbed dose, the quality of radiation is as well important to determine the frequency and severity of radiogenic biologic effects. For the same absorbed dose, biologic effects are generally less for sparsely ionizing radiations (i.e., low-LET and thus "low-quality" radiations), such as X-rays, γ-rays and intermediate-to-high-energy electrons and β-particles, than densely ionizing radiations (i.e., high-LET and thus "high-quality" radiations) such as low-energy electrons (e.g., Auger electrons), protons, neutrons and α-particles.

1.2.3 Quantities characterizing radionuclides

In the case of internal dosimetry (Section 1.6), dealing with the energy deposition in tissues due to radionuclide decays within the body of patients, physical quantities characterizing the employed radionuclides are involved in the evaluations. The main ones of interest for these purposes are reassumed below.

Considering a large number N of identical radioactive atoms, the total radioactive decay constant λ is defined as the probability per unit time, considering a time interval very short in comparison to $1/\lambda$, that an individual atomic nucleus will decay during that time interval [1]; consequently λ has dimensions of reciprocal time (s^{-1} in SI).

The expectation value of the total number of atoms in the sample that disintegrate per unit of time (in an interval $\ll 1/\lambda$) is called the activity (A) of the sample, given by the product of λ and N. As long as the original sample is not replenished by a source of more radioactive nuclei, A is equal to the rate of change in N at any time t:

$$A(t) = -\frac{dN(t)}{dt} = \lambda N(t) \tag{1.8}$$

The SI unit of activity is the becquerel (Bq), defined as one disintegration per second (1 Bq = 1 dis/s), while the old unit was the curie (Ci, with: 1 Ci = 3.7×10^{10} Bq).

Separating variables and integrating from $t = 0$ to a generic time t in Eq. 1.8, the exponential decay law of radioactive nuclei present at time t in the considered sample is obtained:

$$N(t) = N(0)e^{-\lambda t} \tag{1.9}$$

The decay constant λ is related to the quantities decay time τ and half-life $T_{\frac{1}{2}}$, representing the time required to reduce the original sample $N(0)$ to $N(\tau) = N(0)/e$ and to $N(T_{\frac{1}{2}}) = N(0)/2$, respectively, by the relationships:

$$\lambda = \frac{1}{\tau} = \frac{ln(2)}{T_{\frac{1}{2}}} \tag{1.10}$$

λ, τ and $T_{\frac{1}{2}}$ are specific for the radioisotope considered, and describe at a glance the rapidity of its decay.

1.3 Elements of radiobiology

The branch of science concerned with the action of ionizing radiation on biological tissues and living organisms is radiobiology, combining the knowledge from radiation physics and biology. All living beings are made up of protoplasm, which essentially consists of inorganic and organic compounds dissolved or suspended in water. The smallest unit of protoplasm capable of independent existence is the cell. The two main constituents of a cell are the cytoplasm, which supports all the metabolic functions, and the nucleus, which contains the genetic information, i.e., the DNA. A group of cells that together perform one or more functions is referred to as tissue. A group of tissues that together perform one or more functions is called an organ. A group of organs that perform one or more functions is a system of organs or an organism [3].

Cells propagate through division, with somatic cells and stem cells (i.e., undifferentiated cells with capacity to self-renew, or as well to differentiate into any other cell type) dividing through mitosis, while germ cells (i.e., the cells dedicated to reproduction) dividing through meiosis. The cell proliferation cycle is defined by two well defined time periods, mitosis (M) and DNA synthesis (S), separated by two gap periods, G_1 and G_2; in sequence: M, G_1, S, G_2, repeated cyclically.

When cells are exposed to ionizing radiation, the standard physical effects following the interaction of radiation with the atoms or molecules of the cells occur first, and the possible biological damage to cell functions follows later. The biological effects of radiation result mainly from damage to the DNA, which is the most critical target within the cell, but also other sites, when damaged, may lead to cell death.

1.3.1 Radiation effects

Classification of radiation damages

When directly ionizing radiation is absorbed in biological material, the damage to the cell may occur in direct or indirect way.

- In direct action, the radiation interacts directly with the critical target inside the cell, with its atoms that may be ionized or excited through Coulomb interactions. This leads to the chain of physical and chemical events, such as the breaking of bonds, that eventually produce the biological damage. Direct action is the dominant one for high-LET particles.

- In indirect action the radiation interacts with molecules and atoms within the cell different from the critical targets, mainly water molecules - since about 80% of a cell is composed of water -, and produce free radicals that diffusing in the cell can cause damage to its critical targets. Free radicals produced in water, such as H_2O^+ (water ion) and $OH\cdot$ (hydroxyl radical), are short lived yet highly reactive molecules because they have an unpaired valence electron, thus they can break chemical bonds and produce chemical changes that lead to biological damage. About two thirds of the biological damage by low-LET radiations is due to indirect action [3].

A wide range of types of lesions can be created following both direct and indirect interactions with DNA, but they can be broadly separated into two categories: base damage and strand breaks. Base damage represents structural changes to the DNA base pairs that make up the genetic code, e.g. the attachment of an OH molecule to the base, or its complete removal. Strand breaks refer to damages to the sugarphosphate backbone which disrupts the structure of the DNA helix. These are furtherly sub-divided into single-strand breaks (SSBs) - in which only one strand is damaged - and double-strand breaks (DSBs), where opposite strands are damaged in close proximity, typically with separations of less than ten base pairs (corresponding approximately to 4 nm), which can lead to a complete separation of the DNA molecule. The exposure of a cell to 1 Gy of X-rays typically creates an amount of damaged bases and SSBs of the order of 10^3, while the yield of DSBs is on the order of 30-40 per gray [5].

Radiation damage to mammalian cells can be divided into three categories in terms of immediate severity:

- Lethal damage, which is irreversible, irreparable and leads to cell death;
- Sub-lethal damage, which can be repaired in hours unless additional sub-lethal damage is added, eventually leading to lethal damage;
- Potentially lethal damage, which can be manipulated by repair when cells are allowed to remain in a non-dividing state.

The entity at longer term of the radiation damage, both in tumours and in healthy tissues, can vary due to the difference in possible irradiation regimes (type and energy of the radiation, absorbed dose rate, repetition or fractionation of irradiation) and due to the different tissue properties, reassumed by the "five Rs of radiobiology": *repair*, *repopulation*, *reoxigenation*, *redistribution* and *intrinsic radiosensitivity* [6]. Cells are able to *repair* a sub-lethal damage, taking a repair time T_{rep}, though mechanisms that counteract all the natural damages to the DNA. The cells surviving to a radiation exposure will continue to proliferate, with a *repopulation* effect on the considered sample. On the other hand, cells death, in particular tumour cells death, leads to a neighboring tissue shrinkage, and consequently can improve the *reoxigenation* of the residual hypoxic cells, which are more radio-resistant than the oxygenated ones. In addition, radiobiology studies demonstrated that cells are most radiosensitive in the M and G_2 phases, and most resistant in the late S phase; therefore, after an irradiation, cells originally in the G1 or S phases have more probability to have survived,

and a *redistribution* of population is initiated, with a synchronization of cell life cycles.
Overall, the irradiation of a cell will result in one of the following possible outcomes: no effect, division delay, apoptosis, reproductive failure, genomic instability, mutation, transformation, bystander effect, adaptive responses.

Classification of radiation effects

The effects of radiation on the human population can be classified as either somatic or genetic:

- Somatic effects are harm that exposed individuals suffer in first person, during their lifetime, such as radiation induced cancers (carcinogenesis), sterility, opacification of the eye lens and life shortening.
- Genetic (or hereditary) effects are radiation induced mutations to an individual's genes and DNA that can contribute to harm his offspring.

The harmful effects of radiation may be classified into two general categories on the basis of their probability to occur and cause severe harm, following the definitions of the National Council on Radiation Protection and Measurements (NCRP): stochastic and deterministic.

- A stochastic effect is one whose probability of occurrence has no absorbed dose threshold (i.e., it has non-zero probability even at very small absorbed doses), increases with increasing absorbed dose but the severity does not depend on the absorbed dose, and arises in single cells. Examples of stochastic effects are induction of cancer, radiation carcinogenesis, genetic effects.
- A deterministic effect is one that occurs above a threshold absorbed dose and increases in severity with increasing absorbed dose. It is caused by damage to populations of cells, therefore it is also called "tissue reaction". Examples of deterministic effects are organ dysfunction, fibrosis, lens opacification, blood changes.

Stochastic and deterministic effects can be both somatic and genetic.

1.3.2 Radiobiological models of the radiation effects

Radiobiological effect modeling is the use of mathematical models – not necessarily mechanistic – in an attempt to link absorbed dose to the incidence of a specific biological effect attributable to the irradiation. Such models often involve converting the absorbed dose into a scalar quantity monotonically linked to the incidence of the specific biological effect or endpoint (i.e., a direct marker of a disease progression - e.g. disease symptoms or death - used to describe a health effect, or the probability of its occurrence, resulting from exposure) of interest through a mathematical link, a dose–response function.

Cell survival curves

A fundamental index of the radiobiologic effect of irradiation is the cell Surviving Fraction (SF), i.e., the fraction of irradiated cells of a sample surviving an imparted absorbed dose, and maintaing their reproductive integrity (remaining clonogenic cells). In particular, the relationships between SF and absorbed dose, called cell survival curves, are of interest in order to predict cell survival probabilities - and complementarily cell kill probabilities - for practical uses, for example in radiotherapy. Experimental cell SFs are determined with *in vitro* or *in vivo* techniques, and several mathematical models of varying degrees of complexity have been developed to describe and reproduce cell survival curves.

The Linear Quadratic (LQ) model has become the preferred one over the last fifty years, and remains the most widely used to date, in both laboratory and clinics [7]. It assumes that the survival fraction after irradiation is described by the formula:

$$SF(D) = e^{-\alpha D - \beta D^2} \tag{1.11}$$

or, adopting the diffused symbolism whereby the negative of the logarithm of the surviving fraction is written as E (effect) [6, 8]:

$$E = -log(SF(D)) = \alpha D + \beta D^2 \tag{1.12}$$

where α (Gy^{-1}) and β (Gy^{-2}) are parameters called radiosensitivity coefficients, and D is the absorbed dose to which the cells sample is exposed. From Eq. 1.12 appears evident the reason of the name "linear quadratic", since, when SF is typically plotted on a logarithmic scale, this gives a linear α term, dominating at low absorbed doses, and a quadratic β term, that becomes more and more significant as the absorbed dose increases, changing the low-dose linear behaviour into a "shoulder" with increasing curvature. The degree of curvature is frequently defined in terms of the α/β ratio (Gy), that corresponds to the absorbed dose at which the linear α and quadratic β contributions are equal. Cells types with high α/β ratios see a relatively constant rate of cell killing with increasing absorbed dose, while those with a low α/β ratio show a pronounced curvature, as depicted in Fig. 1.1.

The simplest interpretation of the LQ model is the empirical one approximating in Taylor series the absorbed dose response using a polynomial, and acknowledging that experimental survival fraction curves suggest that for practical absorbed doses only the D and D^2 terms are significant. An intuitive but more mechanistic interpretation is that the α term reflects death from 'single hit' events, i.e. lethal damage caused by a single incident particle, producing for example double-strand breaks of the DNA helix, while the β term represents 'multiple hit' cell death, resulting from the interaction of damage from two or more radiation tracks, which scales in proportion to the square of the absorbed dose. This concept is illustrated in Fig. 1.1.

The generally good agreement with the majority of preclinical *in vitro* cell survival data and with a number of different *in vivo* measures of normal tissue and tumour responses, together with its mathematical simplicity, led the standard LQ model to become the dominant tool in preclinical radiobiological modelling [7].

However, there remain questions about the mechanistic interpretability of the parameters α and β, as they reflect the very complex combined contributions of different biological processes. Therefore there is interest in the development of more mechanistically-informed interpretations or new mechanistic models. Such interpretations include revisiting approaches based on misrepair processes and damage severity classification (as defined in Sec. 1.3.1), such as repair-misrepair (RMR) model [9], lethal-potentially lethal (LPL) model [10] and saturable repair model [11], to place modified LQ curves on a stronger theoretical footing [12, 13]; the development of updated target-theory approaches [14]; or the development of mechanistic

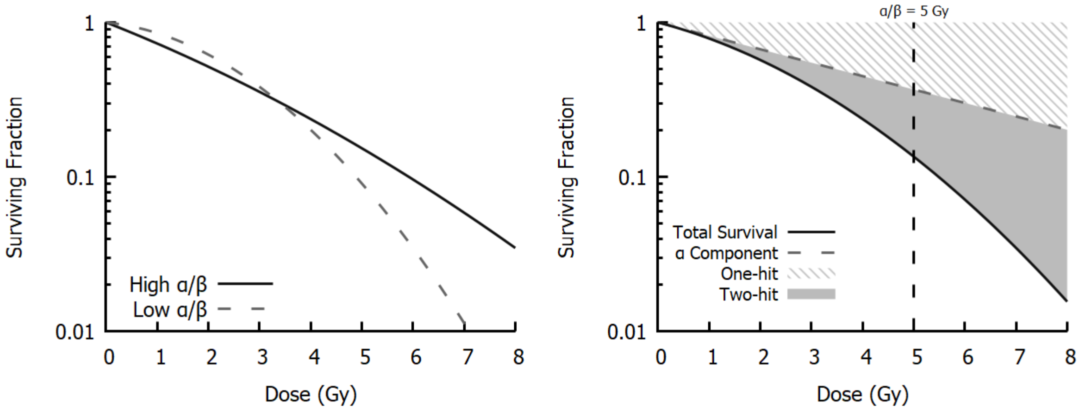

FIGURE 1.1: Examples of LQ SF curves [7]. Left: SF for cell lines with high and low α/β ratios. Right: Separation into one- and two-hit kinetics.

models characterising particular aspects of the DNA repair process, such as the involvement of ATM [15].

On the other hand LQ-based empirical models are also developed, to describe effects alterating the standard LQ behaviour, e.g. models including the contribution of LET by appropriately correcting the α and β parameters expressions [16].

In addition, the range of applicability and the validity of the LQ model for predictions of tissue-level responses remain subject of some debate. Growing evidence indicates that the LQ model may not be a perfect description of all cellular responses, especially for very-low or very-high absorbed doses. For example the phenomenon of low-dose hypersensitivity, in which some cells show dramatic sensitivity for absorbed doses typically lower than 0.5 Gy, can move away the SF from LQ behaviour before plateauing and “returning” to an LQ-like response at higher absorbed doses [17]. Conversely, some investigators reported *in vitro* cases in which the dose-response curve begins to straighten at high absorbed doses, with significant discrepancies with respect to LQ expectations at values larger than 5 Gy. These evidence is leading interest in the formulation of new response models, for example models proposing simple modifications of the original LQ formulation, adding an additional resiosensitivity parameter, such a "linear-quadratic-linear" model, and a "linear-quadratic-cubic" model [18]. Alternative approaches have attempted to introduce more mechanistic rationale for the alteration of the LQ parameters, by moving smoothly between linear-quadratic and multi-target models [19], or incorporating corrections for absorbed dose protraction and lesion interaction [20].

Finally, the LQ model can be corrected for temporal effect, having non-negligible impact when the irradiation time T is comparable or even longer than the repair time of the sub-lethal damage, T_{rep}. In fact, in the standard formulation of the LQ model it is assumed that absorbed dose fractions are delivered instantaneously, or are sufficiently well separated that sub-lethal damage is fully repaired between exposures. However, for low absorbed dose-rate exposures or closely-spaced fractions, this may not be the case. Thus Eq. 1.12 can be corrected to account for the competition between radiation-induced damage and cell repair rate by incorporating a "dose protraction factor" $g(T)$ [6, 7]:

$$E(D,T) = -log(SF(D,T)) = \alpha D + g(T)\beta D^2 \tag{1.13}$$

For an exposure due to a varying absorbed dose rate $\dot{D}(t)$, $g(T)$ is given by:

$$g(T) = \frac{2}{D^2} \int_o^{\infty} \dot{D}(t)dt \int_0^T e^{-T_{rep}(t-t')} \dot{D}(t')dt' \tag{1.14}$$

This expression indicates that the 'multiple-hit' damage done by an absorbed dose $\dot{D}(t)dt$ is proportional to the total amount of remaining unrepaired sub-lethal damage from all the exposures up to time T . This has the effect of reducing the value of the β component, and can provide correction factors for protracted exposures to arbitrary absorbed dose rates [21].

Dose-response curves

Other indices of radiobiological effect can be studied as a function of the imparted absorbed dose, for example tumour induction or tissue response; plots of this kind are called dose-response curves. Three types of dose-response relationship are known - linear, linar-quadratic and sigmoid - and each of them may or may not have a threshold absorbed dose below which that particular effect will not be observed. Linear-quadratic relationships with no threshold are usually assumed for stochastic effects, for example carcinogenesis; instead sigmoid relationships with threshold are common for deterministic effects in tissues, for example tumour control or treatment morbidity [3]. Examples of the various dose-response curves are shown in Fig. 1.2.

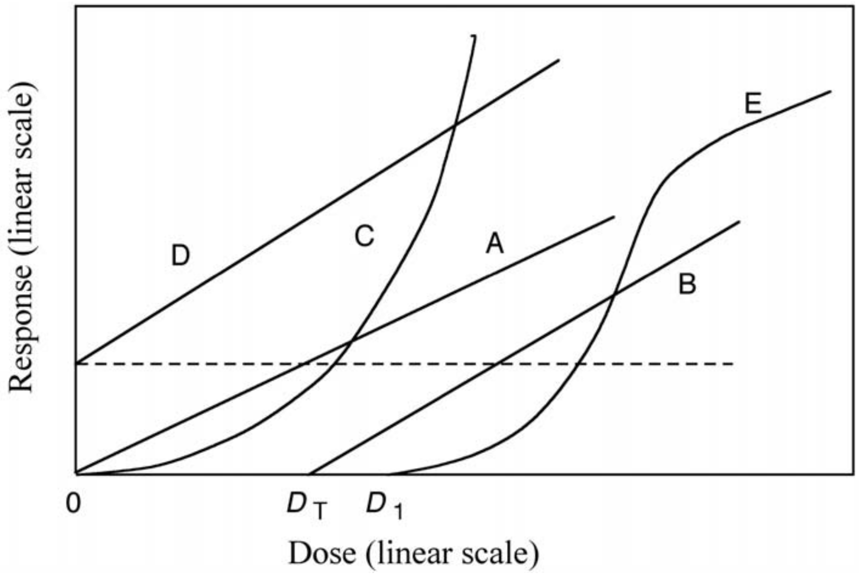

FIGURE 1.2: Typical dose-response curves for cancer induction (A, B, C and D) and for tissue response (E) [3]. A = linear with no threshold; B = linear with threshold D_T ; C = linear-quadratic with no threshold; D = linear with no threshold but with non-zero natural incidence of the effect even at zero absorbed dose; E = sigmoid with threshold D_1.

1.3.3 Quantities relevant to the risk of deterministic effects

Relative biological effectiveness (RBE)

As the LET of radiation increases, the ability of the radiation to produce deterministic biological damage also increases. The influence of LET on the frequency and severity of deterministic biological effects can be quantified by the Relative Biological Effectiveness (RBE), which compares the absorbed dose of a test radiation A to the absorbed dose of a *reference* radiation to produce the same biological effect:

$$RBE = \frac{D_{ref}}{D_A} \tag{1.15}$$

where D_{ref} is the absorbed dose of the selected reference radiation required to produce a specific, quantitatively expressed biologic effect, and D_A is the absorbed dose of radiation A required to produce the same frequency or severity of the same specific biologic effect, with all pertinent parameters maintained as nearly identical as possible. A widely available sparsely ionizing radiation should be typically chosen as the reference, such as ^{60}Co γ-rays, which currently is the recommended reference [3].
The RBE varies not only with the type of radiation A, but also with the type of cell or tissue, biologic effect under investigation, absorbed dose, absorbed dose rate and fractionation. In general, the RBE increases with the LET to reach a maximum value of 3–8 (depending on the level of cell kill) at LET = 200 keV/m, and then decreases because of energy overkill.
When assessing the potential for deterministic effects, the ICRP recommends that the mean absorbed dose to an organ or tissue of interest should be weighted by an appropriate value of the RBE for the specified biologic endpoint [22].

Biologically effective dose (BED)

As anticipated earlier, among the factors influencing the biologic response to irradiation figures the absorbed dose rate. If cells are allowed sufficient time (on the order of 6–24 h) to recover after a single irradiation, sub-lethal damage from the initial exposure will be fully repaired, and cells will respond as if they had not previously been irradiated. In the context of the LQ model of cell survival fraction, for an exposure subdivided into n well-separated fractions of absorbed dose d, such that the total exposure absorbed dose D is given given by $D = nd$, the predicted effect (Eq. 1.12) is given by n times the effect of a single exposure of absorbed dose d:

$$E = -log(SF(D)) = n(\alpha d + \beta d^2) = D(\alpha + \beta d) \tag{1.16}$$

It can be seen that, for equal total absorbed dose D, higher fractionation increases cell survival by reducing the magnitude of the quadratic contribution, as $Dd < D^2$.
"Biological effective dose" (BED) is defined as the total physical absorbed dose required for a given biologic effect to happen if the absorbed dose is delivered by infinitely small absorbed doses per fraction or, in the case of continuous radiation rates, at a very low absorbed dose rate [23]. In fact, considering progressively smaller values of d, such that it approaches zero, while accordingly increasing the number of fractions n to maintain the same effect, βd^2 will be nevertheless very small in comparison with αd (since d will greatly exceed d^2 for very small values and α always exceeds β). Therefore, for very small values of d, Equation 1.16 can be approximated as:

$$E = n\alpha d = \alpha D \tag{1.17}$$

The total absorbed dose required in these conditions coincides with the definition of BED, and constitutes the highest total absorbed dose required to obtain a specific effect, which emerged being equal to the quotient of the effect level E by the linear radiosensitivity α:

$$BED = \frac{E}{\alpha} \tag{1.18}$$

The BED for any irradiation fractionation regime, e.g. a practical radiotherapy schedule, can be therefore found, assuming the LQ model, as:

$$BED = \frac{n(\alpha d + \beta d^2)}{\alpha} = D\left[1 + \frac{d}{\alpha/\beta}\right] \tag{1.19}$$

BED is regarded as a measure of the true biological absorbed dose delivered by a particular combination of dose per fraction and total dose to a given tissue characterized by a specific α/β ratio. It follows from equation 1.19 that, even if the total absorbed dose D is kept constant, the BED will increase if the absorbed dose per fraction is increased, the increment being greater for tissues with a low, rather than a high, α/β ratio. The bracketed term in equation 1.19 is called the "relative effectiveness" (RE) per unit absorbed dose, so that:

$$BED = D \cdot RE \tag{1.20}$$

Two adjacent tissues with different α/β ratios, each receiving the same absorbed dose and fractionation, will be associated with different BEDs, but this does not necessarily mean that one tissue sustains more biological damage than the other; the BED for each tissue is simply a measure of the extent to which the absorbed dose can be escalated (while maintaining isoeffect on that tissue) if treating with very small fraction sizes. The knowledge of the α/β ratio and the employment of a cell survival model, as the LQ model, enables to evaluate the relative level of cell killing in different populations and consequently adjusting the fractionation schedule, an observation which proved to be extremely important in the development of clinical radiotherapy, where it remains a key predictive tool.

Equivalent uniform dose (EUD)

One of the most useful concepts for assessing the radiobiological impact of the non-uniform absorbed dose distribution in a tissue is the Equivalent Uniform Dose (EUD). EUD is defined as the absorbed dose that, if homogeneously delivered to a tissue (generally a tumor), would yield the same cell survival fraction as the one of the actual non-homogeneous absorbed dose distribution [24]. The underlying assumption in the definition of EUD, that for an inhomogeneous absorbed dose distribution delivered to a tissue volume via a fractionated regime there is an equivalent uniform absorbed dose distribution that will yield the same surviving cell fraction, is mathematically expressed by [25]:

$$SF(EUD) = \sum_{i}^{N} v_i \cdot SF(D_i) \tag{1.21}$$

where D_i is the total absorbed dose to the tissue subvolume v_i, and N is the number of subvolumes. The following empirical parametrized formula for the EUD expression found widespread applications, despite it is not derived from cell survival models [26]:

$$EUD = \left(\sum_{i} v_i \cdot D_i^a\right)^{\frac{1}{a}} \tag{1.22}$$

with the parameter a to be fitted depending on the tissue and the irradiation characteristics. This expression has sometimes been referred to as "generalized EUD (gEUD)".

Isoeffective and Equieffective dose

The International Commission on Radiation Units (ICRU) and the International Atomic Energy Agency (IAEA) have proposed the *isoeffective* dose (D_{IsoE}) for use in high-LET radiation therapy applications. This quantity is given as the product of the absorbed dose D and a weighting factor w_{IsoE} that includes the effects of multiple variables such as the absorbed dose, absorbed dose rate, absorbed dose per fraction, radiation quality, and other irradiation conditions known to affect the clinical outcome [27]:

$$D_{IsoE} = w_{IsoE} \cdot D \tag{1.23}$$

Recently the concept of *equieffective* dose ($EQDX$) was introduced to reduce confusion with past suggested terminologies and to try furnishing a general definition, accounting for the fact that bioeffect modeling presently is applied in different areas of radiation oncology as well as in other medical fields using ionizing radiation, with absorbed dose fractionations that can be very dissimilar between their schedules [28]. In the $EQDX$ formalism, two radiation treatment regimens having different dose–time–fractionation schedules or absorbed dose rate patterns, and/or different spatial distributions and/or different radiation qualities, are said to be *equieffective* with respect to a specific clinical (biological) endpoint, if they produce the same probability of reaching this endpoint when delivered under the carefully specified conditions.
$EQDX$ is defined as the total absorbed dose delivered by the reference treatment plan (with fraction size X) that leads to the same biological effect as a test treatment plan that is conducted with absorbed dose per fraction d and total absorbed dose D, according to the following relation adapted from the Withers formula [29]:

$$EQDX_{\alpha/\beta} = D \cdot \frac{d + \alpha/\beta}{X + \alpha/\beta} \tag{1.24}$$

where α/β is an endpoint- and radiation quality-specific parameter that describes the effect of changes in absorbed dose per fraction. Any value can be selected for the reference absorbed dose per fraction X in Eq. 1.24, but two choices dominate the published literature: X = 2 Gy or X = 0 Gy [30]. In this context the BED coincides with $EQD0_{\alpha/\beta}$, i.e. the case in which X = 0 Gy.

1.3.4 Quantities relevant to the risk of stochastic effects

Equivalent dose

The equivalent dose H_T is a radiation protection quantity introduced by the ICRP to relate absorbed dose to the probability of stochastic health effect in a population exposed to radiation fields or radionuclides, which include a mixture of radiation types of varying LET [22]. It is defined as:

$$H_T = \sum_R w_R D_{R,T} \tag{1.25}$$

where $D_{R,T}$ is the contribution to the mean absorbed dose in the target organ or tissue T coming from radiation of type R, and w_R is the so-called "radiation-weighting factor" for radiation of type R, a dimensionless factor based on representative values of the RBE of that radiation type for causing a stochastic effect, concieved to appropriately reflect the higher biological effectiveness of an high-LET radiation compared with a low-LET radiation. Note that the w_R values are not intended for use in predicting deterministic effects and, if used as such, may result in an overestimation of their occurrence and severity to irradiated tissues. Current ICRP-recommended values of w_R are 1.0 for photons, positrons and electrons including β-particles, 2.0 for protons, 20.0 for α-particles, and between 2.5 and 20.7 for neutrons, depending on the neutron energy [31].

The SI unit of equivalent dose is J/kg, with the special name sievert (Sv), given to distinguish it from the gray, referring to “common” absorbed dose. The old unit was the rem, and the relationship between the two units is 1 Sv = 100 rem. w_R and H_T are similar, respectively, to the older quantities "quality factor" (Q) and "dose equivalent" (H), with the key difference that the former ones are related to the mean absorbed dose to a tissue or organ, whereas the latter were related to the absorbed dose at a point, and thus are often less useful.

Effective dose

The effective dose E is a radiation protection quantity defined by the ICRP for establishing annual limits of exposure to workers and members of the general public [22]. This quantity takes into account external radiation fields and internal radionuclide sources that both contribute to low-dose irradiation of tissues and organs, and it is intended to provide a single value estimate of the overall stochastic risk of a given irradiation, whether received by the whole body, part of the body, or one or more individual organs:

$$E = \sum_T w_T H_T = \sum_T \sum_R w_T w_R D_{R,T} \tag{1.26}$$

where w_T is the weighting factor for tissue or organ T, a dimensionless quantity representing the fraction contributed by T to the total stochastic risk as result of a uniform total-body irradiation. The weighting factors are therefore defined normalized such that:

$$\sum_{r_T} w_T = 1 \tag{1.27}$$

w_Ts values for the different organs and tissues of the human body are reported in [22].

The effective dose is similar in concept to the "effective dose equivalent" (H_E), that was instead based on the absorbed dose at a point in tissue weighted by the LET-dependent distribution of quality factors Q at that point [32]. The equivalent dose, in contrast, is based on the average absorbed doses in the tissue or organ weighted by the radiation weighting factor w_R for the radiation actually impinging on that tissue or organ. The unit of equivalent dose is the same of effective dose, the sievert.

1.4 Principles of radionuclide therapies

1.4.1 Radiation therapies

Radiation therapy is a type of disease treatment using ionizing radiations to kill pathologic cells, especially used to treat some types of cancer. The principle of all radiation therapies is to cause maximum damage to a pathologic tissue, delivering to it an high-enough amount of absorbed dose through the irradiation with primary or secondary ionizing radiation, while preserving healthy organs and tissues from unnecessary exposure, by minimizing as much as possible their irradiation [33]. Several sources of radiation with different features and clinical applications are available. External beam radiation therapy (EBRT) – often called simply “radiotherapy” - delivers high-energy ionising radiation from outside the body. In standard EBRT, X-ray or electron beams generated by a linear accelerator are generally used, but therapies using beams of protons, ions and neutrons, eventually accelerated through cyclotrons or synchrotrons, are increasingly used and developed, constituting the branch of EBRT referred to as hadron-therapy (or also ion-therapy or particle-therapy) [34]. Brachytherapy (also known as Curietherapy) instead involves sealed sources internally inserted in an anatomic location in proximity to the target lesion [35]. Finally, the third main type of radiation therapy is radionuclide therapy, which employs high-LET-emitting isotopes administered inside patient’s body, usually in the form of radiopharmaceuticals [36].

1.4.2 Radionuclide therapies

Radionuclide therapies are characterized by the systemic or selective loco-regional delivery of radioactive atoms to lesion-associated targets. The first case can be also classified as systemic radiation therapy (SRT), while the second case includes specific treatments such as selective internal radiation therapy (SIRT) for liver tumors [37]. The radionuclide delivery - with the exception of some nuclides which by themselves exhibit a natural uptake in target organs, e.g. radioiodine in the thyroid [38] - is usually achieved by administering to the patient the radioisotope in the form of a radiopharmaceutical, i.e., attaching the radioisotope to an appropriate molecular complex acting as delivery vehicle ("carrier"), having a specific biodistribution in the organism. In such radiopharmaceutical therapies (RPT), also called molecular radiation therapies (MRT) or targeted radiotherapies, binding to specific endogenous targets and accumulating in them by a wide variety of physiological mechanisms characteristic of the lesion, the radiopharmecautical exploits a targeted therapeutic function. Another way of administration, adopted in some radionuclide therapies, is via radiolabeled implants, such as resin or glass microspheres loaded with yttrium-90 in the case of the above mentioned SIRT.

By selecting adequate selective administration procedures for radiolabeled implants or, in the case of RPTs, by choosing proper pharmaceuticals whose biodistribution is narrowly targeted on the considered pathologic tissues, and labelling them with a suitable radionuclide as radiation source, it can be achieved the aim of maximizing energy deposition in the target tissues during the desired treatment time while preserving as much as possible healthy organs and tissues. β-emitters are the best choice in most cases, guaranteeing a localized energy deposition thanks to the relatively small mean range of electrons in tissue, ranging from few millimeters to few centimeters. α- and Auger-emitters are also increasingly used, for millimeter and sub-millimeter ranges [6]. In addition, therapeutic radioisotopes are chosen among the ones having half-lives of the order of days, in order to provide activities - and respective absorbed dose rates - adequate for lesion damage, and consequently have treatment cycles with these extents of duration. The most widely used radioisotopes in radionuclide therapy clinics over the last forty years are the β-emitters iodine-131, lutetium-177, yttrium-90 and samarium-153, and the α-emitters astatine-211, bismuth-212, lead-212, bismuth-213, actinium-225, radium-223 and thorium-227. A review of the radiopharmaceuticals currently used or under development in radionuclide therapy practice can be found in [36].

Radionuclide therapy is emerging as a safe and effective approach for treating many types of diseases, for example the radiometabolic therapy of hyperthyroidism, the radioimmunologic therapy of lymphomas, the radio-receptorial therapy of neuroendocrine tumors and the trans-arterial radio-embolization of liver carcinomas with radio-labelled microspheres, to cite the most classical ones [39]. Compared with almost all other systemic cancer treatment options, like chemotherapy and biologic therapy, radionuclide therapy has shown efficacy with minimal toxicity. In addition, since almost all the radionuclides used in clinics have also decay channels emitting detectable gamma photons, or annihilation photons in case of positron-emitters, they enable the non-invasive visualization of the biodistribution of radioactivity – and thus of the therapeutic agent - via nuclear medicine imaging techniques [36]. Besides assessing the targeting of the agent, in the case of quantitative activity samplings performed several times post-administration, imaging opens the possibility to assess absorbed dose in target tissues and in healthy organs of interest (as it will be detailed in Sec. 1.6).

1.5 Imaging techniques in nuclear medicine

Nuclear nedicine (NM) is the medical speciality employing radionuclides administered to patients for diagnostic an therapeutic purposes. Radionuclide theraphy, introduced in Sec. 1.4.2, constitutes the therapeutic branch of NM, while functional imaging constitutes its diagnostic branch, having almost a century of history. With functional imaging it is intended the series of detection and reconstruction techniques that permit to deduce the distribution of a radinuclide administered to a patient; this distribution reflects certain biological processes taking place at cellular and subcellular level, expression of a body function or of metabolism. Since in presence of disease the functional pharmaceutical distribution is altered, reconstructing it enables the diagnosis of eventual pathologies.

The base principle of functional imaging is administering to the patient a radiopharmaceutical labeled with a γ-emitting or β^+-emitting radionuclide and detecting the emitted photonic radiation with an external detector device.

In planar functional imaging two-dimensional (2D) projections of the three-dimensional (3D) source distributions are obtained. The projections starting from anatomical structures at certain depths in the patient are obviously "obscured" by superimposed projections of overlying and underlying structures. One solution is to acquire projection images from different angles around the body (e.g., posterior, anterior, lateral) and interpret the structures from the different views trying to deduce the true 3-D nature of the distribution.

An alternative approach is tomographic imaging, which furnishes 2D representations of structures lying within a selected plane in a 3D object. In tomography, from multiple 2D projections acquired during a scan, a so-called sinogram is obtained, and applying matematical algorithms, such as filtered backprojection, 2D cross-sectional images of selected planes (usually transaxial, sagittal, coronal, but potentially also oblique slices) within the analyzed object are reconstructed [40]. Functional tomography, using the detected emissions from radionuclides within the body, is known as Emission Computed Tomography (ECT); tomography using transmitted emissions from an external source (e.g., an X-ray tube) is known

as Transmission Computed Tomography (TCT) or, usually, just Computed Tomography (CT).
There are two main classes of ECT in nuclear medicine imaging: Single Photon Emission Computed Tomography and Positron Emission Tomography.

1.5.1 Single-Photon Emission Computed Tomography (SPECT)

Single-photon emission computed tomography (SPECT) is a functional tomographic imaging technique detecting the gamma-rays emitted from radiopharmaceuticals labelled with γ-emitting radionuclides. In SPECT systems the acquisition of a series of planar projections at equally spaced angular intervals around the patient is performed by a gamma camera mounted on a special gantry rotating around the patient through 180° or 360° [41]. The gamma camera is the photon-detecting device of SPECT systems, and its major components - schematized in Fig. 1.3(a) - are: a collimator, a large-area scintillation crystal (usually NaI(Tl)), a light guide and an array of PhotoMultiplier Tubes (PMTs) fed to electronic or digital position logic circuits, which determine the X-Y location of each scintillation event occurring. The most common type of SPECT gamma camera is the single-headed system, but dual-headed (Fig. 1.3(b)) or even three-headed systems are becoming increasingly popular.
Typically, clinical SPECT images are reconstructed on a matrix of 64 × 64 or 128 × 128 pixels; such reconstructed cross-sectional slices are produced for all the axial locations covered by the field of view (FOV) of the gamma camera, resulting in a stack of contiguous 2D images that form a 3D image volume representing the spatial distribution of the radionuclide concentration [40].

1.5.2 Positron Emission Tomography (PET)

Positron Emission Tomography (PET) is based on the detection of 511-keV "back-to-back" photons pairs produced by the annihilation of a positron and an electron in the considered volume, with positrons emitted within it from radiopharmaceuticals labelled with β^+-emitters. A PET scanner is provided with a ring-shaped detector device made of thousands of scintillating crystals (e.g. BGO, LSO, LYSO, GSO) coupled with an array of PMTs and coincidence electronics circuitry, enabling the detection in coincidence of the two photons in opposite direction within a limited time window [42]. This allows the deduction of a line of response (LOR), i.e. a line along which the positron annihilation was located, as depicted is in Fig. 1.4(a). By acquiring a large number of LORs (of the order of 10^8-10^9), it is possible to reconstruct the distribution of the radionuclide inside the examined volume. The coincidence detection permits to obviate the need for collimators to determine the direction of emission of photons, and yields a superior sensitivity with respect to SPECT. In addition, the use of a ring array that completely surrounds the patient enables to acquire data for all projection angles simultaneously, as shown in 1.4(b), and consequently allows relatively fast dynamic studies with a reduction of artifacts caused by patient motion [40].

1.5.3 Computed Tomography (CT) and hybrid imaging

Computed Tomography (CT) is a non-destructive radiographic process producing a 3D photon attenuation map of the patient's body based on the variable attenuation of a beam of X-rays as it passes through patient's body. In contrast to ECTs, which employ internally biodistributed radionuclide sources, in CT an external source,

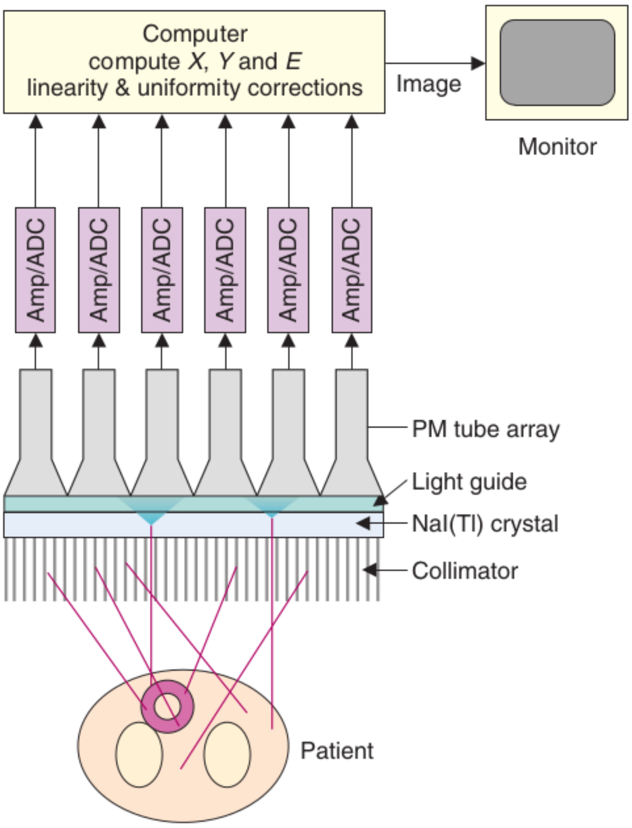
Computer
compute X, Y and E
linearity & uniformity corrections
Image
Monitor
Amp/ADC
Amp/ADC
Amp/ADC
Amp/ADC
Amp/ADC
Amp/ADC
PM tube array
Light guide
NaI(Tl) crystal
Collimator
Patient

(a)

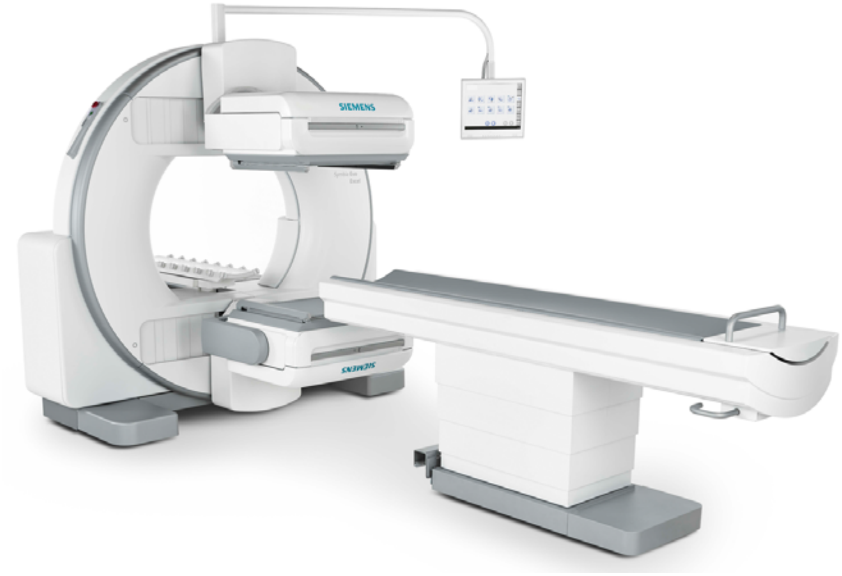

(b)

FIGURE 1.3: (a) Schema of the basic components of a modern gamma camera [40]. (b) Picture of a dual-headed SPECT system (Siemens Symbia Evo Excel `https://www.siemens-healthineers.com/en-eg/molecular-imaging/spect-and-spect-ct/symbia-evo`)

constituted by an X-ray tube, is used to obtain projections through the patient and form a transmitted attenuation profile at the detectors. To retrieve a cross-sectional

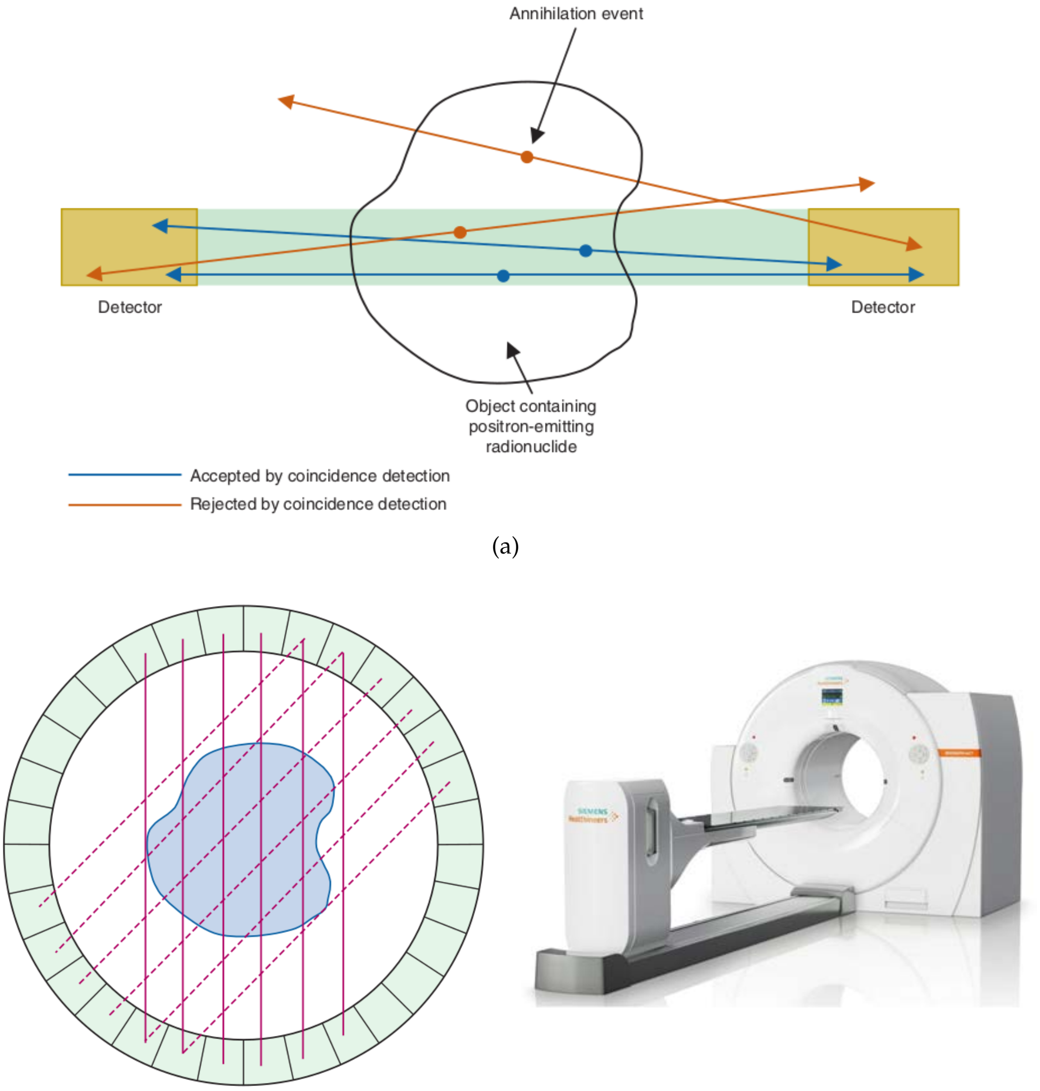
Annihilation event
Detector
Detector
Object containing positron-emitting radionuclide
Accepted by coincidence detection
Rejected by coincidence detection

(a)

(b) (c)

FIGURE 1.4: (a) Scheme of the detection of simultaneously emitted annihilation photons by a pair of opposite PET detectors [40]. (b) Scheme of PET detectors operating in electronic coincidence with detectors on the opposite side of the ring, allowing simultaneous acquisition of projection views from many different angles. Solid and dotted lines illustrate two simultaneously acquired projection views. [40]. (c) Picture of a PET/CT scanner (Siemens Biograph mCT Sim edition `https://www.siemens-healthineers.com/en-ae/molecular-imaging/pet-ct/biograph-mct-sim`).

image, the employed beam is restricted to a thin fan across the patient (in the X–Y direction) of thickness between 0.5 and 10 mm for a single slice in the axial (z) direction [42]. In CT scanners, an X-ray tube operating between 80 and 140 kV, mounted on a suitable gantry, rotates around the patient, and many hundreds of attenuation profiles are created in each revolution, by detecting the transmitted photons with an arc detector array jointed to the gantry in opposite direction with respect to the X-ray tube (Fig. 1.5). The CT detectors were typically ionization chambers using high-pressure xenon, nowadays replaced by scintillation detectors (e.g. CsI(Tl) or ceramic scintillators such as Gd_2O_2 S, YGdO and $CdWO_4$) read out by silicon photodiodes. The projection data are generally collected as the scanner performs a helical trajectory, where the patient bed is translated through the scanner while the X-ray tube and detector rotate. The attenuation profiles are then reconstructed to form the required transverse image.

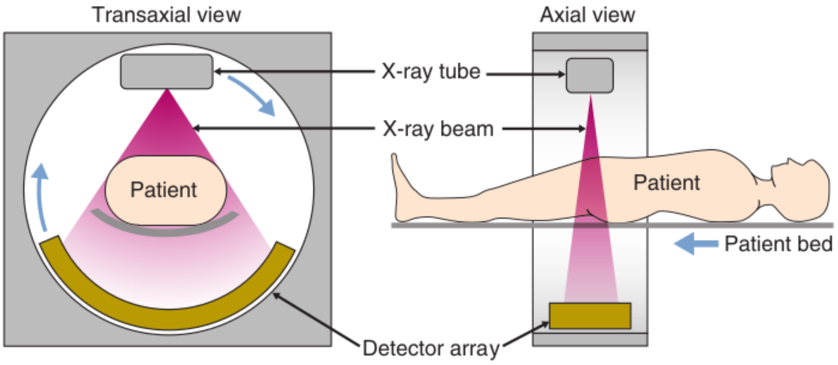

FIGURE 1.5: Scheme showing the components and geometry of a CT scanner [40].

CT images are morphological, meaning that they give information about the anatomy of the patient, showing the shapes of organs and tissues, and also their densities, them being roughly proportional to the photon-attenuation coefficient for the X-ray energies used and the relatively low atomic number of most tissue constituents [43]; in fact, the majority of X-ray interactions in the body are Compton scatters, which depend primarily on tissue density.
Pixel values in CT slices usually are expressed on a normalized scale with respect to the values for water, called Hounsfield Units (HU) scale, defined as follows [40]:

$$HU(x,y) = 1000 \cdot \frac{\mu(x,y) - \mu_{water}}{\mu_{water}} \tag{1.28}$$

Since SPECT and PET provide functional information, but not much anatomic information, it has been common practice for several decades to complement nuclear medicine tomography with CT or Magnetic Resonance Imaging (MRI) scans, typically acquired on separate instruments and possibly days apart. As a consequence, correlating information in the two studies was hampered by the difficulty of spatially registering the images and the effect of any changes in the patient's condition during the elapsed time between the two procedures. Many modern PET scanners and an increasing number of SPECT scanners are now integrated with a CT scanner. These hybrid PET/CT [44] (Fig. 1.4(c)) and SPECT/CT [45] imaging systems are capable of acquiring PET or SPECT images along with spatially automatically coregistered CT images, in quick succession. Such integrated CT scans not only provide anatomic context to improve the diagnostic interpretation, but can also be used to perform corrections for photon attenuation and scatter in the functional scans [40, 42], permitting an accurate and high-resolution quantification of activity concentrations and thus opening the way to dosimetry.

1.6 Internal dosimetry

Internal dosimetry in nuclear medicine practice aims at estimating the radiation absorbed dose to tissues and organs due to the irradiation occurring during diagnostic and therapeutic procedures employing radionuclides. It has an increasingly growing role in planning and monitoring molecular radiotherapies, and also in characterizing the diagnostic imaging procedures. In fact, since the absorbed dose causes biological effects in living matter (as detailed in Section 1.3), dose-response correlations in tumors and dose-toxicity correlations in all the irradiated tissues exist. Therefore it is fundamental to accurately quantify the absorbed dose to deduce these correlations, and consequently verify the effectiveness of an applied treatment, as well as evaluating the risk to which healthy tissues are exposed [39].

The absorbed dose spatial and time distribution within the patient's body depends on the physical decay scheme of the employed radionuclide and on the bio-kinetics of the radiopharmaceutical (or of the radiolabelled implant, or of the bare radionuclide in the case of iodine). While the physical properties of each radioactive isotope are well known from experimental data and nuclear physics theoretical models, the dynamic biodistribution of the radionuclide depends on the physio-pathologic behaviour of the carrier molecule (or of the implant), on the type and stage of the disease, on the route of administration and on the specific characteristics of the patient, which influence all the mentioned aspects [6]. Tomographic imaging (Sec. 1.5) enables to deduce patient's morphology (employing CT) and the functional radioactivity distribution (using SPECT and PET) at certain times after the radionuclide administration, but given the experimental impossibility to directly measure absorbed dose or absorbed dose rate within patient's body, models are needed for its quantification, eventually using precisely CT and SPECT or PET scans as input data.

First of all the geometry of patient's anatomy must be modeled, and depending on the dimensions scale of the volumes considered it is possible to perform dosimetry at different levels: whole organs, sub-organ regions, small-scale tissue regions, multi-cellular clusters, single cells and even sub-cellular regions [46]. For clincal applications organ- and region- level schemes or sub-organ voxel-level schemes are usually employed. Computational phantoms representing standard human morphology types can be modeled from cohort data, or, on the other hand, patient-specific phantoms can be built. Secondly, a mathematical calculation scheme has to be chosen for absorbed dose evaluation.

1.6.1 Organ-level dosimetry

In organ- or region- level internal dosimetry it is assumed a uniform distribution of the radionuclide in some up-taking volumes representing the "source organs" (or regions), and the aim is the calculation of the absorbed doses imparted by the radiations emitted from these sources to surrounding volumes of interest, representing "target organs" (or regions). Examples of target and source organs for some radiopharmaceuticals are depicted in Fig. 1.6(a). The Medical Internal Radiation Dose (MIRD) committee has developed through the years a well-established procedure for the evaluation of absorbed dose based on the previously described assumptions, nowadays known as MIRD formalism [31].

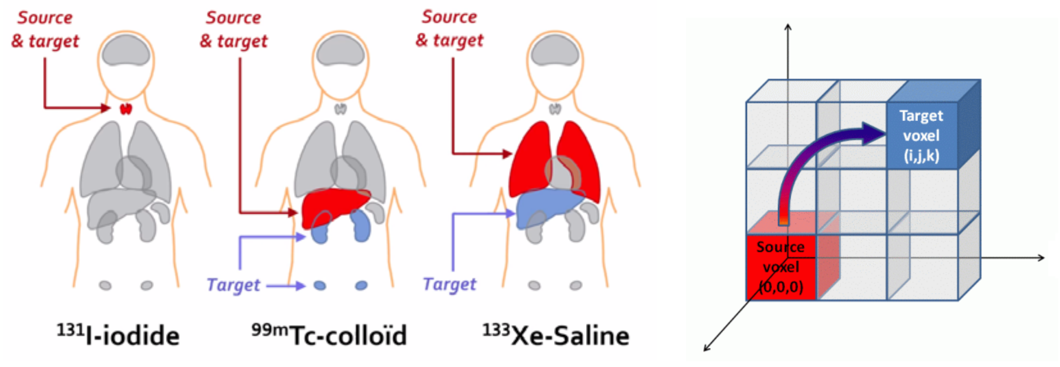

(a) (b)

FIGURE 1.6: (a) MIRD-based representation of target and source organs of interest for three types of radiopharmaceuticals (`https://humanhealth.iaea.org/HHW/NuclearMedicine/Webinars/Basic_Nuclear_Medicine/Basic_Radiopharmaceutical_Dosimetry/index.html`). (b) Illustrative representation of voxel-level targets and sources (`https://www.medphys.it/res_svoxel.htm`).

MIRD time-dependent formulation

In the context of MIRD formalism, the time-dependent absorbed dose rate $\dot{D}(r_T \leftarrow r_S, t)$ imparted to a target volume r_T by the radiations emitted by a single source volume r_S, with radioactive material uniformly distributed within it, is calculated as:

$$\dot{D}(r_T \leftarrow r_S, t) = A(r_S, t) S(r_T \leftarrow r_S, t) \tag{1.29}$$

where $A(r_S, t)$ is the time-dependent activity in the source volume r_S, and $S(r_T \leftarrow r_S, t)$ is the so called S-factor, which is the average absorbed dose rate imparted to the target per unit of activity in the source.
In the general case of several organs accumulating the radionuclide, and therefore having non-zero activity inside them, the overall absorbed dose rate $\dot{D}(r_T, t)$ in a target r_T is obtained by summing over all the source volumes:

$$\dot{D}(r_T, t) = \sum_{r_S} A(r_S, t) S(r_T \leftarrow r_S, t) \tag{1.30}$$

S is specific of the radionuclide and of the anatomic model chosen to represent the patient's body (or some specific region of interest), through the spatial relationship and tissue compositions of r_S and r_T, and is given as:

$$S(r_T \leftarrow r_S, t) = \frac{1}{M(r_T, t)} \sum_i E_i Y_i \phi(r_T \leftarrow r_S, E_i, t) \tag{1.31}$$

where E_i is the mean (or individual) energy emitted as i-th radiation following from the i-th available nuclear transition, Y_i is the number of i-th nuclear transitions per nuclear decay, $\phi(r_T \leftarrow r_S, E_i, t)$ is the "absorbed fraction", defined as the fraction of radiation energy E_i emitted by the source r_S at time t which is absorbed in the target r_T, and $M(r_T, t)$ is the mass of the target volume at time t.
We can define as Δ_i the product of E_i and Y_i, that therefore is the average energy emitted per decay in the form of i-th radiation:

$$\Delta_i = E_i Y_i \tag{1.32}$$

In addition we can define the quantity “specific absorbed fraction” (SAF), indicating it as $\Phi(r_T \leftarrow r_S, E_i, t)$, as the quotient of $\phi(r_T \leftarrow r_S, E_i, t)$ and $M(r_T, t)$, which thus is the absorbed fraction per unit mass of the target:

$$\Phi(r_T \leftarrow r_S, E_i, t) = \frac{\phi(r_T \leftarrow r_S, E_i, t)}{M(r_T, t)} \tag{1.33}$$

such that we can rewrite the S-factor of Eq. 1.31 as:

$$S(r_T \leftarrow r_S, t) = \sum_i \Delta_i \Phi(r_T \leftarrow r_S, E_i, t) \tag{1.34}$$

The mean absorbed dose $D(r_T)$ to the target volume r_T over a defined time period after the radionuclide administration, commonly taken to be infinity, is obtained as:

$$\begin{aligned} D(r_T) &= \int_0^\infty \dot{D}(r_T, t)dt = \\ &= \sum_{r_S} \int_0^\infty A(r_S, t) S(r_T \leftarrow r_S, t)dt \end{aligned} \tag{1.35}$$

In the MIRD schema, the time-dependent activity in the source r_S, $A(r_S, t)$, is obtained by numeric solution of a set of first-order coupled differential equations defined by compartment models for all the volumes of interest [31]. Alternatively, the individualized time-dependent activity in source tissues of the patient may be obtained directly via quantitative imaging, (planar imaging, SPECT or PET), external probe measurements (e.g. scintillation probe for iodine thyroid uptake) or by tissue sampling (e.g., biopsy, blood, or urine collection).

The number and timing of the acquisitions are optimized, depending on the biokinetics of the radionuclide (or radiopharmaceutical) in the organs of interest expected from previous clinical studies, in order to accurately fit the Time-Activity Curve (TAC) $A = A(t)$, within the limits set by the detecting devices use time and by the logistical problems for the patients (as they must remain or come back to the nuclear medicine department for each measurement) [6]. Most of the pharmacokinetic data in radionuclide therapy applications can be described with sums of exponentials [47]. In general two pharmacokinetic phases can be distinguished: an uptake phase, i.e. the phase in which the radionuclide (or radiopharmaceutical) is accumulating in the organ and its activity concentration rises with time; and a washout phase, in which activity concentration diminishes following biological clearance and radioactive decays.

The simplest model applies when the uptake phase is short enough to be considered instantaneous, and the washout phase can be described with a mono-exponential function:

$$A(r_S, t) = A(r_S, t_0)e^{-\lambda_{eff} t} \tag{1.36}$$

where $\lambda_{eff} = \lambda + \lambda_{bio}$ is the effective decay constant in the organ r_S for the considered radionuclide (or radiopharmaceutical), given by the sum of the physical radioactive decay constant (Section 1.2.3) and the biological decay constant, characteristic of the biological wash-out from that organ. Similarly to Eq. 1.10, an effective (biological) decay time τ_{eff} (τ_{bio}) and an effective (biological) half life T_{eff} (T_{bio}) can be defined. An even simpler model, in which only physical wash-out is present, describes well some radionuclide treatments such as trans-arterial radio-embolization with radiolabelled microspheres, for which no biological clearance happens since the microspheres remain permanently attached to the capillaries of the patient [48].

In more complex cases, the uptake phase requires a certain amount of time and can be usually described by an exponential growth. Furthermore, the washout phase may be better described by a bi-exponential curve, characterized by a first phase of rapid clearance with biologic half-life much smaller than the physical half-life, followed by a slower retention phase in which, conversely, the physical half-life is smaller and governs the overall effective half-life. An overview of further TAC fit functions used to model pharmacokinetics in nuclear medicine can be found in [47].

MIRD time-independent formulation

The general time-dependent formulation described in the previous subparagraph enables to take into account possible variations of mass of volumes, an important aspect in cases of tumor regions whose mass increases or decreases over the period of irradiation, or in lifetime mean organ absorbed dose assessments for subjects exposed to long-lived radionuclides. By the way, in most cases the source and target masses remain constant during the period of irradiation, and under these conditions the time dependency of S can be neglected, enabling to reduce Eq. 1.35 to the following time-independent form:

$$D(r_T) = \sum_{r_S} \tilde{A}(r_S) S(r_T \leftarrow r_S) \tag{1.37}$$

where $\tilde{A}(r_S)$ is the time-integrated activity in source volume r_S (commonly referred to also as "cumulated activity"), which represents the total number of decays of the radionuclide happening in r_S:

$$\tilde{A}(r_S) = \int_0^\infty A(r_S, t)dt \tag{1.38}$$

while S is now defined in terms of time-independent quantities:

$$S(r_T \leftarrow r_S) = \frac{1}{M(r_T)} \sum_i \Delta_i \phi(r_T \leftarrow r_S, E_i) \tag{1.39}$$

Organ S-factors calculations

For organ-level dosimetry, S-factors are commonly calculated by means of Monte Carlo simulations using reference antrophomorphic computational phantoms with organs and anatomical districts defined as mathematical volume shapes [49]. These phantom geometries were refined over the years to represent reference standards for individuals of given age, sex, body mass and standing height, accounting for basic differences in human morphology [50]. Reference models are effective to compute absorbed doses to normal organs, but when the volume of interest is a lesion or nodule, other models must be assumed, such as spherical [51] or ellipsoidal models [52]. In these cases, a uniform uptake of the radionuclide is considered in the source, modeled as a sphere or ellipsoid of appropriate size, generally immersed in an indefinite medium of water or unit-density soft tissue, identical to the material constituent the source volume; then the self-dose is evaluated, i.e., the absorbed dose imparted to the same volume in which radioactive decays occur, thus considering the target coinciding with the source.

Given an anatomical model and its respective organ S-factors for the radionuclide of interest (available in tabular form in various works, e.g., [53]), and calculating the time-integrated activity (or time-dependent activities) in the source organs of interest, the absorbed dose to target organs is deduced through Eq. 1.37 (or Eq. 1.35 in the time-dependent case).

1.6.2 Three-dimensional voxel-level dosimetry

With the diffusion of three-dimensional (3D) voxelized functional imaging, i.e. SPECT and PET tomography, in conjunction with 3D voxelized morphological imaging (CT) - automatically integrated in SPECT/CT and PET/CT scanners – a boost in the development of 3D internal dosimetry methods took place. With voxelized image it is intended an image in a 3D space discretized into a regular grid whose smallest volume entity is the voxel, generally with parallelepipedic or cubic shape, constituting the equivalent in three dimensions of the pixel (in Fig. 1.6(b) an illustrative representation). A value representing a physical or mathematical quantity is associated to each voxel, such that a voxelized image is in effect a 3D matrix representing a distribution map of the considered quantity. By defining voxelized computational anthropomorphic phantoms, i.e. 3D density and chemical composition maps of the patient's body, together with the 3D non-uniform activity distributions of a radiopharmaceutical/radionuclide, it is possible to derive the 3D absorbed dose distributions at sub-organ level [39]. In particular, if a phantom is defined from a CT scan of the specific patient considered – through the conversion of its Hounsfield Units (HU) through the appropriate calibration –, and if the activity distributions are deduced from quantitative SPECT or PET scans of the same patient, with attenuation and scatter correction applied, a fully patient-specific dosimetry is obtainable. Otherwise, reference anthropomorphic computational phantoms can be used, representing some standard human morphological types, such as male and female adult, pregnant woman and various stages of pediatric ages. More and more refined models were developed through the years, in the form of 3D voxel or mesh structures derived from tomographic data on patient cohorts, with certain models offering also some degree of patient-specificity by adapting the dimensions of some organs and anatomic regions [50].

For both cases of patient-specific or standardized data, four main schemes are currently available for the calculation of the 3D absorbed dose distribution: local energy deposition approach, dose point-kernel convolution, voxel S-factors approach and direct Monte Carlo simulation. In all the approaches the absorbed dose calculation can be carried out following one of two alternative ways; in the first one, a time-integrated activity map is evaluated, and starting from it the absorbed dose map is deduced; in the second one, for each activity map available an absorbed dose-rate map relative to that scan time is calculated, and the overall absorbed dose map is retrieved from the time integration of absorbed dose-rate maps. For simplicity and to synthesize, in the following the calculation approaches will be described referring to the first way, bearing in mind that the second way is in principle equally viable.

Local energy deposition approach

Local Energy Deposition (LED) approach, also called Normalized Average Absorbed Dose (NAAD) method, assumes that all the energy emitted by a voxel is completely absorbed in that same voxel [54]. Within this hypothesis, the absorbed dose is calculated by simply multiplying, for each voxel, the time-integrated activity for the average emission energy of the radionuclide spectrum, and dividing for the mass of that voxel, deducible from the CT scan or standardized phantom used. This approximation scheme is acceptable for certain α and β particles or Auger electrons, but is not suitable for γ-rays or secondary photons, due to their longer penetration depth. LED method is fairly accurate for a quick analysis in toxicity studies in cases when the interest is in assessing absorbed dose for specific parts of the radionuclide emission spectrum, and within its physical assumptions is potentially patient-specific [33, 55].

Dose point-kernel convolution

The Dose Point-Kernel (DPK) is defined as the distribution of absorbed dose per decay event as a function of distance from an isotropic point source located inside a virtually infinite and homogeneous absorbing medium. DPKs depend on the type and energy of the radiation and on the medium, and can be determined via Monte Carlo calculations, by simulating the considered radiation generated from a point source and scoring the energy deposition in concentric shells. Wide DPKs databases for various radionuclide spectra, materials (mainly tissue and tissue-equivalent materials, such as water) and voxel dimensions are available to date, either in tabular form or as analytical functions retrieved by fitting the simulative data [56, 57].
Through the discrete convolution sum of the DPKs relative to the radionuclide and material of interest with a 3D distribution of time-integrated activity, derived from SPECT or PET imaging, the corresponding 3D voxel-level map of absorbed dose is obtained [58]:

$$D[r_n] = (\tilde{A} * k)[r_n] = \sum_{r_m} \tilde{A}[r_m]k[r_n - r_m] \tag{1.40}$$

where $D[r_n]$ is the absorbed dose in the voxel at r_n position, $\tilde{A}[r_m]$ is the time-integrated activity in the voxel at r_m position, and $k[r_n]$ is the DPK at position r_n.
Favourable aspects of the DPK convolution method are the capability of handling patient-specific inhomogeneous activity distributions and the rapidity of its implementation, with fast Fourier transforms and fast Hartley transformations profitably used to speed up this kind of calculations; as a consequence, its clinical use for patient-specific voxel-based tumour and normal tissue dosimetry is feasible. Nevertheless, it has to be noticed that this approach lacks in reliability when relevant differences of tissue densities, and thus inter-voxel heterogeneities, are present. Effort is being put in research precisely in the aspect of density corrections for DPK method [33, 39, 59].

Voxel S-factors approach

The application of MIRD schema to voxel geometries, instead of mathematical volumes representing entire organs, constitutes the so called voxel S-factor approach, also referred to as Voxel S Value (VSV) approach [46]. In this framework, the voxelized 3D distribution of absorbed dose can be assessed starting from a voxelized geometry, the knowledge of the VSVs characteristic of that geometry, matter composition and of a radionuclide of interest, and a voxelized map of time-integrated activity having the same resolution. Each generic n-th voxel is considered as an individual uniform radiation source, while all the surrounding voxels - from time to time - as uniform targets (see Fig. 1.6(b)), and the average absorbed dose $\bar{D}_m$ imparted to the m-th voxel is calculated as follows:

$$\bar{D}_m = \sum_{n} \tilde{A}_n \cdot S_{m \leftarrow n} \tag{1.41}$$

where $\tilde{A}_n$ is the time-integrated activity in the n-th voxel and $S_{m\leftarrow n}$ is the VSV, defined as:

$$S_{m\leftarrow n} = \sum_i \Delta_i \frac{\phi_i(m \leftarrow n)}{M_m} \tag{1.42}$$

in which Δ_i is the mean energy per decay emitted by the i-th radiation, $\phi_i(m \leftarrow n)$ is the absorbed fraction by the m-th voxel of the i-th radiation emitted in the n-th voxel, and M_m is the mass of the m-th voxel.
VSVs are calculated by means of Monte Carlo simulations, scoring energy deposition in each voxel of the implemented geometry, separately for each i-th radiation present for the considered radioisotope. Over the last two decades many studies contributed to the extension of VSVs calculation for photons, electrons and numerous radionuclide spectra [60–62], for different materials and geometries characterized by various voxel sizes, including specific calculations for computational anthropomorphic phantoms [63–67].
If in the traditional organ-level MIRD schema S-factors are appliable in clinics to simplified mathematical humanoid models, VSVs schema is appliable to reference voxel-based anthropomorphic phantoms, such as the latest MIRD/ICRP phantoms [31, 68, 69]. Although patient-specific organ masses, positions and shapes can be derived from tomographic imaging, personalized adjustments are not routinely appliable in these type of phantoms [63, 70]. Nevertheless, the VSV approach is nowadays widely diffused and is considered a standard method in clinical dosimetry, with the favourable aspects of being fast and easy to implement [71].

Direct Monte Carlo simulation

Monte Carlo (MC) methods are a set of computational methods based on statistical algorithms taking advantage of iterative (pseudo-)random sampling to perform simulations aiming at solving problems in various fields. In the field of radiation-matter interaction, MC can be employed to estimate random pathways and interactions of particles in 3D geometries, allowing the voxel-level scoring of energy depositions, and thus absorbed dose estimations [2, 72].
In internal dosimetry, the direct MC simulation of radionuclide decays and the interaction of the emitted daughters with patient's body, appropriately modeled in voxelized geometries, is the gold standard approach. It ensures the highest accuracy and patient-specificity among the available dosimetric methods if the body geometry is appropriately derived from CT imaging and if the radionuclide spatial distribution is modeled from functional 3D imaging of the considered patient [71, 73, 74]. In fact, it permits to accurately take into account for the patient-specific inhomogeneous radioactivity distribution, variations in tissue density and composition between voxels, and the shapes and extent of organs and lesions. At the same time it allows to simulate all the main possible physical processes involved, including secondary particles such as delta-rays and bremsstrahlung photons, enabling a reliable "cross-fire" absorbed dose estimation, relevant especially for isotopes exhibiting γ-emissions [75]. Generating a certain number of decay events, statistically distributed in space according to emission tomography data within the patient's body modeled from CT, and tracking all primary and secondary particles to calculate the geometrical distribution of energy depositions, the 3D voxelized map of absorbed dose is finally retrieved rescaling the results to the actual values of time-integrated activity and mass of the voxels.
On the other hand, MC simulations have the drawback of being in general quite demanding with respect to the other internal dosimetry methods, because of the more

complex implementation of calculations, requiring numerous input parameters, the relatively long computational times and the requirements in terms of storage memory [33, 76, 77]. As a consequence, it is not currently used in clinical routine, but has an established role in internal dosimetry research, in particular in comparative studies with the other dosimetric methods, validations of new faster algorithms studied for specific assumptions and in retrospective studies on clinical data [48, 59, 70].

Chapter 2

Monte Carlo simulation in Nuclear Medicine

2.1 Introduction

The last paragraph of Chapter 1 introduced the technique of Monte Carlo simulation, in particular applied for internal dosimetry. Monte Carlo simulation was the principal calculation technique employed in the research works that will be described in this dissertation. In the present Chapter will be presented an overview on Monte Carlo methods and their usefulness in nuclear medicine, starting from their most basic and general concepts, and then detailing their use for simulations of radiation-matter interaction and particle transport. Afterwards, the main simulation software packages devoted to these purposes will be presented, describing especially the main characteristics of the ones employed for this thesis: GEANT4, one of the most widely used and validated frameworks for the simulation of particles interactions in matter, and GATE and GAMOS, two toolkits acting as user-friendly interfaces to GEANT4 and more oriented on medical applications of such simulations.

2.2 General information on Monte Carlo methods

Monte Carlo methods indicate a broad class of statistical methods applied via computational algorithms relying on repeated random sampling, that are used to perform simulations whose aim is obtaining numerical solutions to problems. In particular, problems that do not admit analytical solution, or whose analytical or numerical solution is difficult to calculate, primarily benefit from these methods. Thanks to the ever increasing development in computing power, with high CPU performances and large mass memory, Monte Carlo methods are nowadays profitably employed for this kind of problems in various fields of human knowledge: from mathematical, physical, chemical and biological sciences to economy, from computer graphics to social sciences, to mention the main ones [78].

2.2.1 Historical background

Usually the experience of "Buffon's needle", dating back to 18th century by Georges-Louis Leclerc, Comte de Buffon, is regarded as the archetype of the Monte Carlo method; it consists in randomly tossing needles on to a table on which parallel lines were drawn, in order to determine experimentally the value of π [79]. However, the "official" appearance of Monte Carlo techniques is dated back to the 1940s, when some members of the Manhattan Project working at the Los Alamos laboratories,

namely the physicists Stanislaw Ulam and John von Neumann, begun to study neutron diffusion adopting a statistical approach to simulate neutrons' trajectories. In this approach they chose the successive velocities of neutrons by selecting from the experimentally determined probability distributions at each impact [80]. Ulam and von Neumann themselves, around 1944, coined the name "Monte Carlo" as a code name for this method, emphasizing the gaming aspect of such random sampling calculations. Their reference was precisely to the Monte Carlo casino in the Principality of Monaco, where Ulam's uncle would borrow money from relatives to gamble [1].
Thereafter, the Monte Carlo method began to be used more and more in the scientific community, at first in particular for nuclear physics. In 1948 Enrico Fermi, Nicholas Metropolis and Ulam obtained Monte Carlo estimates for the eigenvalues of the Schrödinger equation. In the same period Spencer performed the earliest application of the Monte Carlo method to radiation transport problems, concerning the effects of polarization on multiple successive Compton scatterings. In 1949 Kahn published a work in which he employed Monte Carlo for predicting neutron fluxes associated with nuclear reactors. In the same year Mayer reported in a symposium his use of one of the first digital electronics computers, the ENIAC, for neutron transport Monte Carlo calculations [2]. In parallel Fermi designed the analog computer FERMIAC to substitute ENIAC in a period of interruption of operations, and used it to study the variation in time of the neutron number, giving an additional stimulus to the work started by the Los Alamos group [81]. Since then, as anticipated, Monte Carlo techniques have been used and are currently used in the most diverse fields of human activities.

2.2.2 Basic concepts

The general idea behind Monte Carlo simulations can be synthesized into three points:

1. Adopt or develop a model reproducing as better as possible the real system of interest, and define input variables for it;
2. Generate inputs within the modeled system, based on known probabilities of occurrence, through random sampling of Probability Density Functions (PDFs), and score output variables;
3. Iterate the computation of step 2. to fulfill the Law of Large Numbers (LLN) [82], and aggregate the results.

In probability theory and statistics, a PDF of a continuous random variable X is a function that describes the relative likelihood for this random variable to take on a given value. The probability of X falling within a particular range of values is given by the integral of this X's density over that range. A PDF is non-negative everywhere in its domain and must be integrable within the domain; its integral over the entire domain in which it is defined is equal to one (since PDFs are normalized to 1, to respect the definition of probability).
PDFs furnish the *a priori* needed information about the processes to be simulated, that will be practically used by sampling a stochastic variable from them. As the number of individual events simulated (called 'histories') is increased, the quality of the reported average behaviour of the selected output variables of the system improve following the LLN, in the sense that the associated statistical uncertainty decreases [2].

---

[1] `https://permalink.lanl.gov/object/tr?what=info:lanl-repo/lareport/LA-UR-88-9067`

2.2.3 Random Number Generators (RNGs)

A fundamental part of any Monte Carlo calculation is the Random Number Generator (RNG), i.e., the part of code providing a stream of - seemingly - uncorrelated random numbers, in order to imitate the stochastic nature of a process to be simulated. It must be underlined that it is intrinsically impossible to produce true random numbers, since by definition they are randomly distributed and, as a consequence, unpredictable. Given that the codes aimed to get random numbers rely on deterministic and repeatable algorithms, we actually deal with so-called "pseudo-random numbers", having the appearance of randomness, but nevertheless exhibiting a specific, repeatable pattern [78]. For simplicity we will refer to pseudo-random numbers as just 'random' numbers.
The mathematically desired properties of a sequence of random numbers used for a Monte Carlo simulation are: high uncorrelation, long period, uniformity, reproducibility, parallelization [83]. The most commonly used type of generator is the linear congruential RNG (LCRNG), in particular the multiplicative linear congruential RNG (MLCRNG). Lagged-Fibonacci series (LFRNG) acquired attention in the Monte Carlo scientific community, for the advantages of extremely long periods and superior speed than LCRNG [2]. Other popular and high-quality RNGs are the RANMAR and RANLUX algorithms [78].

2.2.4 Sampling methods

Given a PDF $f(x)$ of the variable x (that for example can be a physical quantity), defined in the interval $[x_{inf}, x_{sup}]$ and that, by definition, is normalized to unit area, the corresponding cumulative distribution function $F(x)$ is defined as:

$$F(x) \equiv \int_{x_{inf}}^{x} f(\tau) d\tau \tag{2.1}$$

$F(x)$ gives the probability that the random variable τ is less than or equal to x. Uniformly distributed random numbers R in the range $[0, 1]$ can be used to sample a stochastic variable that follows the PDF $f(x)$, according to three different available sampling methods, briefly described below [2].

Direct sampling

The variable x is sampled replacing $F(x)$ in Eq. 2.1 with the uniform random number R and solving for $x : x = F^{-1}(R)$. This method is used when the inverse of $F(x)$ can be easily calculated.

Rejection sampling

When the inverse of $F(x)$ is impractical to be calculated, an alternative method is the rejection method, which consists in the following steps:

1. Define a normalized function $f'(x) = f(x)/f_{max}(x)$, with $f_{max}(x)$ being the maximum value of $f(x)$, and consequently with $f'_{max}(x) = 1$.

2. Sample an uniformly distributed random number in the interval $[0, 1]$, R_1, and calculate x with the following equation, given that it is uniform in the PDF's range $[x_{inf}, x_{sup}]$:

$$x = x_{inf} + R_1(x_{sup} - x_{inf}) \tag{2.2}$$

3. Sample another uniformly distributed random number in the interval $[0,1]$, R_2, and if $R_2 < f'(x)$ accept x as a sampled value, otherwise reject it and go back to step 2.

The rejection method works provided that $f(x)$ is not infinite anywhere.

Mixed sampling

When the two previous methods are not applicable individually, a combination of the two can be used. Assuming that the PDF can be factored in the product of two PDFs, $f(x) = f_a(x) \cdot f_b(x)$, with $f_b(x)$ acting as a rejection function, it is determined an x value using the direct sampling method on $f_a(x)$ and then it is applied the rejection method with that x to $f_b(x)$.

2.3 Monte Carlo of radiation-matter interaction and its applications in Nuclear Medicine

Monte Carlo methods can be applied to simulate physical processes in a straightforward way, defining the system of interest and the PDFs from the known models or experimental data describing the interactions to be simulated. If the specific interest is in the simulation of radiation-matter interactions, meaning in a broad sense the transport and interaction of particle or wave radiations with other particles, atoms, nuclei and fields of a medium, the ingredients to build such simulations are: the definition of the medium's geometry, composition and density; the choice of the theoretical models - or parametrizations of experimental data - for electromagnetic, weak and hadronic interactions to be simulated, including de-excitations and radioactive decays; the definition of the primary radiation source and of the quantities to be scored within the simulation geometry; and last but not least, a code that enables to implement all of this.
Among the general-purpose softwares designed for the simulation of particle transport and interaction with matter, the most widely used and validated to date are GEANT4 [84], FLUKA [85], MCNP with its latest version MCNP6 [86], EGS with its latest versions EGS5 [87] and EGSnrc [88], PENELOPE [89]. Such Monte Carlo softwares in general enable to simulate individual particles, following them from their emission by a source, through to their loss by absorption or leakage, and recording aspects of their behavior along their path, such as kinetic energy and direction. The trajectory of each simulated particle can be thought as broken down into sequences comprising free flight and, at given steps, collisions. The nature of collisions is randomly selected from a set of possible phenomena in the material, with respective assigned probabilities being related to the cross sections in the specific material. The statistical averaged behavior of real particles within the considered physical system is predicted by the accumulated data on a large number of simulated particles [72].
The Monte Carlo simulation of particle transport and interaction in matter finds growing applications in medical radiation physics. Multiple areas of research and clinical development where the interaction of ionizing radiation with matter is of highest importance benefit of MC simulations: x-ray diagnostics, imaging instrumentation design and optimization, dosimetry and consequent treatment planning of external beam radiotherapy with photons, electrons or fast heavy ions, radioprotection of hospital workers and spaces, radionuclide production, nuclear medicine

diagnostics and therapies. The aforementioned general-purpose MC codes are profitably used in all of these domains, but also exist simulation codes dedicated in particular to nuclear medicine imaging (such as SimSET, PETSIM and SIMIND [78]) and modules or interfaces of the general-purpose codes that are specifically developed for medical radiation physics and nuclear medicine applications, such as the GEANT4-DNA project [90, 91], focusing on the biological damage induced by ionizing radiation at the DNA scale, and the interface toolkits GATE [92] and GAMOS [93] for GEANT4, enabling the user-friendly configuration of simulations for various kinds of medical physics applications.

Historically, nuclear medicine is the field in which Monte Carlo calculation found its early applications in medical radiation physics, and today its use continues to increase, especially in internal dosimetry for radionuclide therapies [72]. For this purpose, MC simulations can be set defining geometries and materials representing patient's body (or organs/tissues of interest) and simulating as primary radiation source the decay of radionuclides – or directly their daughters according to the corresponding emission spectra – distributed within the body. In these simulations the primary interest is scoring the deposited energies along the particle tracks inside volumes of interest, which can be macroscopic shapes representing entire organs or on the other hand voxels, and retrieve the corresponding absorbed doses.

2.4 GEANT4

2.4.1 General concepts

GEANT4 (acronym for "GEometry ANd Tracking") is a software for the simulation of the interaction and transport of radiation through matter [84, 94–96]. It enables to define geometry and materials of a setup - including detectors -, navigate inside them, simulate physical interactions using a choice of physics engines, underlying physics cross sections and models, visualize and store results. GEANT4 is implemented in C++ language, utilizing Object Oriented programming to create a structure of class categories that provide key capabilities. Its code can be seen as the combination of three sets of modules [97]:

- The 'kernel', which initializes and manages geometry and 'run' configurations, handles particles, tracking, field propagation and materials, and enables the simulation of processes. Each of the mentioned aspects is governed by corresponding objects that permit the user to configure the various settings.
- The 'Physics processes', the largest module, which includes the cross sections and Physics models used to perform the simulations.
- The 'Interfaces', providing visualization, input/output and the facility for the user to steer the application.

Several Physics models are provided, taking advantage of cross sectional theoretical functions, experimental data or parametrizations, describing with different precision and performance a large number of electromagnetic processes from $\sim$10 eV to PeV energy range and hadronic processes from sub-eV scale to PeV, as well as decays and processes for optical photons [95, 98].

GEANT4 includes coherent physics model configurations, called "*Physics Lists*", that merge sets of the available Physics models useful for specific purposes. The *Physics List* is a mandatory user class in the last versions of GEANT4, in which all the

GEANT4 particles and their interaction processes should be instantiated (by inheriting from the `G4VUserPhysicsList` GEANT4 class). The user can choose among many existing reference *Physics Lists*, or create its own at will, depending on his requirements and the application area [99].
Apart from the *Physics List*, other two objects are mandatory in GEANT4 to describe the simulation setup and decide the physics of its application: the *geometry*, defined by instantiating a C++ class inheriting from the `G4VUserDetectorConstruction` class, and the *primary generator*, which contains the initial particles of each event, by instantiating a class inheriting from the `G4VUserPrimaryGeneratorAction` class.
Thanks to the flexible kernel and the availability of different physics modeling choices, GEANT4 finds a wide range of application areas, including high energy physics and nuclear physics, detectors design, accelerator engineering, medical physics and space science [96].

2.4.2 Suitable *Physics Lists* for Nuclear Medicine dosimetry simulations

Since in Monte Carlo nuclear medicine dosimetry the aim is simulating the interaction of radionuclide decay daughters with living matter, the physics of interest must include the electromagnetic processes involving photons, electrons and positrons (and eventually α-particles in case of alpha emitters). The most suitable reference *Physics List* for this purpose is the "Standard GEANT4 electromagnetic" *Physics List*, built by the `G4EmStandardPhysics` constructor. It is implemented for gammas, all leptons, and all stable charged hadrons/ion, with no treatment of optical photons, that in case should be added on top of any reference or user custom physics [99]. In particular, the configurations recommended for accurate internal dosimetry results are the ones built by the `G4EmStandardPhysics_option3` (EM Opt3) and `G4EmStandardPhysics_option4` (EM Opt4) constructors.

EM Opt3

The standard EM Opt3 *Physics List* uses a set of electromagnetic (EM) processes with accurate simulation of gamma and charged particle transport. Its Processes cover physics from 0 to 100 TeV for gammas, electrons and positrons, up to 1 PeV for muons, and EM interactions of charged hadrons and ions from 0 to 100 TeV, with all the mentioned intervals being abundantly beyond the energy range of interest for internal dosimetry, that goes approximately from 10 keV to 10 MeV. Though the operational energy ranges go down to zero, below 1 keV the accuracy of the used models is substantially lower.
The processes of major interest for dosimetry implemented by the EM Opt3 *Physics List* are the ones indicated below, according to the reported models [99] for the following types of particles:

- Photons
  - e^-/e^+ pair production is implemented by the BetheHeitler model with the Landau–Pomeranchuk–Migdal (LPM) effect at high energies.
  - Compton scattering is implemented by the Klein-Nishina model.
  - Photo-electric effect and Rayleigh scattering are both handled by the Livermore models.
- Electrons and positrons

  - Multiple Coulomb scattering is handled by the Urban model from 0 to 100 TeV. UseDistance-ToBoundary step limitation is used for multiple scattering.
  - Bremsstrahlung is implemented by the eBremSB model and the eBremLPM model, which takes into account the LPM effect at high energies.
  - Ionization is modeled by the Moller-Bhabha formulation.
  - Positron annihilation is implemented by the eplus2gg model.

- Alpha particles and G4GenericIon(s)
  - Multiple Coulomb scattering in implemented by the Urban model at all energies.
  - For alphas, Bragg ionization is performed below 7.9 MeV and BetheBloch ionization above.
  - For generic ions, Bragg is used below 2 MeV and BetheBloch above.
  - Nuclear stopping model is used below 1 MeV.

EM Opt4

The standard EM Opt4 *Physics List* uses a set of EM physics models selected from the low energy and standard packages. As a consequence it is the slowest among the standard EM constructors, but in principle is the most accurate. The processes of interest are implemented according to the following models [99]:

- Photons
  Same as EM Opt3 except for Monarsh University model (G4LowEPComptonModel) used for Compton scattering Below 20 MeV and Penelope model for pair production.

- Electrons and positrons
  Same as EM Opt3 except for multiple Coulomb scattering, which is handled by the Goudsmit-Sounderson model from 0 to 100 MeV and by the WentzelVI model from 100 MeV to 100 TeV, combined with the single Coulomb scattering model, applied for large angle scattering. UseSafetyPlus step limitation with error free approach near geometry boundaries is used for multiple scattering.

- Alpha particles and G4GenericIon(s)
  Same as EM Opt3 except that for ion ionisation of ions below 1 GeV/u ICRU73 model (G4IonParametrisedLossModel) is used, while above 1 GeV/u the Bethe-Bloch model is applied.

Decays

Besides all the reported processes and models, in the EM Standard *Physics Lists* the decay of all long-lived hadrons and leptons is handled by the `G4Decay` process, which by the way does not handle the decay of hadronic resonances like deltas, heavy-flavor particles like D and B mesons or charmed hyperons. In addition, they invoke the `G4RadioactiveDecay` process in order to activate the simulation of the radioactive decay of unstable nuclei. `G4RadioactiveDecay` and associated classes are used to simulate the decay, either in-flight or at rest, of radioactive nuclei by α, β^+ , β^- and γ emission and by electron capture (EC). The simulation model employed depends on data taken from the Evaluated Nuclear Structure Data File (ENSDF) [100], which provides information on nuclear half-lives, nuclear level structure for the parent or daughter nuclide, decay branching ratios, and the energy of the decay process [99]. If the daughter of a nuclear decay is an excited isomer, its prompt nuclear de-excitation is treated using the `G4PhotoEvaporation` class.

2.4.3 Particle transport in GEANT4

Four classes define the structure of any GEANT4 simulation:

- *run*: a set of events sharing the exact same conditions in terms of geometry and physics.
- *event*: the set of tracks that include the primary particles created by the primary generator and all the secondary tracks formed as they are transported through the geometry.
- *track*: a snapshot of a particle as it is being tracked through the geometry, containing only information about the initial state and the current state.
- *step*: the information about the change of a track as it is being propagated, containing initial and final points plus the differential information (energy loss on the step, time of flight spent by the step, etc.). From a geometrical point of view, it corresponds to the distance between two successive interaction positions.

The simulation of particle transport is performed tracking each considered particle in a discretized way, by creating a track object sequentially numbered by a trackID and placed on a stack, and moving it through the defined geometry step by step. A step ends when the particle changes volume, or an interaction occurs, or the user limits it after a certain length with a cut.

Particle transport in GEANT4 is carried out as the result of the combined actions of the GEANT4 kernel's Stepping Manager class and Physics processes which it invokes, and the Transportation 'process', responsible for determining the geometrical limits of a step and identifying the next volume in which the track enters in case of volume boundary crossing.

At the beginning of each step a particle, depending on its identity, energy, and the medium in which travels, is subject to different competing possible processes, each with specific relative probability – or in other terms, cross section - of happening. The next physics interaction and the successive point of interaction are sampled in terms of 'number of mean free paths' or by various step limitations. To describe this procedure, first of all it is useful to remind that it is possible to express the mean free path λ for a given process - also called the "interaction length" - in terms of the total cross section $\sigma(Z, E)$ of that process, depending on the atomic number Z of the medium and on the energy E of the particle

$$\lambda(E) = \left(\sum_i [n_i \cdot \sigma(Z_i, E)] \right)^{-1} \tag{2.3}$$

where i runs over all the elements composing the material and n_i is number of atoms per volume of the i-th element. λ cannot be used directly to sample the probability of an interaction in an heterogeneous medium, since it depends on the medium composition. Therefore the number of mean free paths n_λ is used, which is independent of the material traversed and - it can be shown - intervenes into the probability of interacting along a path l for a given process, $P(l) = 1 - e^{-n_\lambda \cdot l}$:

$$n_\lambda = \int_{x_1}^{x_2} \frac{dx}{\lambda(x)} \tag{2.4}$$

n_λ is sampled at the beginning of the step, using direct sampling method to extract a random number η uniformly distributed in the range $(0, 1)$, by setting n_λ as:

$$n_\lambda = -log(\eta) \tag{2.5}$$

The lowest among the sampled n_λs is chosen as the actual step over which the particle will be transported, and determines which is the selected process, unless the step is limited by geometric boundaries or thresholds, such as energy cuts and maximum step limits.
In the case of boundary crossing into a new medium, the number of mean free paths is adjusted as follows:

$$n'_\lambda = n_\lambda - \frac{\Delta x}{\lambda} \tag{2.6}$$

where Δx is the step length. The tracking is continued in the new medium until an interaction point is reached, selecting the shortest step originating from $s(x) = n_\lambda \lambda(x)$ and its corresponding process.
In summary, each new interaction and corresponding "true step length" is chosen by polling all processes applicable at that step and selecting the ones returning the minimum step length from the random extraction.
The particle is then transported along a straight line in case it has neutral electric charge or, if its charged, if electromagnetic fields are absent; otherwise the transport is carried out along a curved line according to the equation of motion taking into account the EM fields in play. The final state of the interaction is then generated for the selected process, which can include the generation of secondary particles. If the "original" particle survived the interaction, its transport is continued with a further step and so on. In this approach, besides the discrete processes, the continuous energy loss and multiple scattering impose a limit on the step-size too, because the cross sections of different processes depend on the energy of the particle. Thus it is assumed that the step is small enough to maintain cross sections approximately constant during the step. The energy of the particle is updated through the steps in case of continuous energy loss.
In view of what was described above, considering a primary particle starting from the beginning of its history in the simulation, its track in the defined system is simulated step by step, recording the physical quantities of interest along it, including energy losses in each traversed region. Obviously various processes generate secondary particles, and for each of them are also simulated their interactions and their tracks are followed, recording equally energy transfers and their other characteristic quantities. All the particles involved are tracked until they reach a cutoff energy, below which further simulation is stopped and the residual energy is considered absorbed in the point - or volume region - where the particle was in its final position.
A visual example of the simulation of a run, with the tracks and steps of the primary particle and of the secondary particles generated by its interactions, is illustrated in Fig. 2.1.
At the end of such "cascade", constituting a single event or "history", a new one

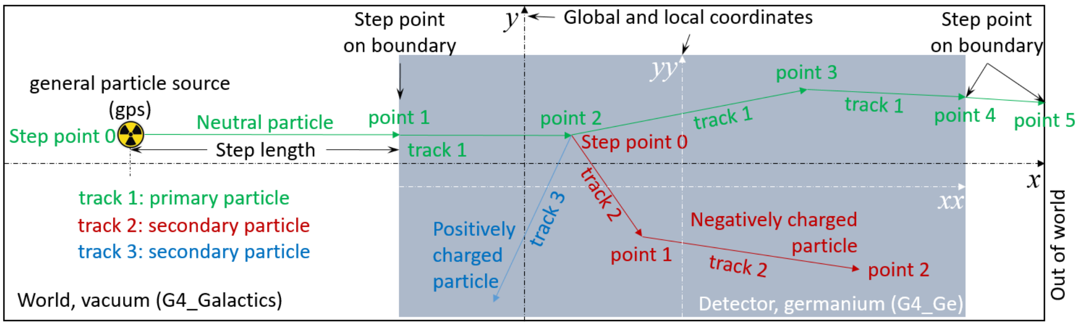
Step point
on boundary
y
Global and local coordinates
Step point
on boundary
general particle source
(gps)
yy
point 3
Step point 0
Neutral particle
point 1
point 2
track 1
track 1
point 4
point 5
Step length
track 1
Step point 0
x
track 1: primary particle
track 2: secondary particle
track 3: secondary particle
track 2
track 3
xx
Positively
charged
particle
Negatively charged
particle
point 1
track 2
point 2
Out of world
World, vacuum (G4_Galactics)
Detector, germanium (G4_Ge)

FIGURE 2.1: Schematic example of GEANT4 particle transport and tracking for a single simulation history (`http://physino.xyz/gears/examples/output/`): a neutral primary particle is generated in vacuum, enters in a germanium detector volume, interacts within it and produces secondary particles; all the particles are tracked until the end of their tracks within the *World* volume.

is started by generating and tracking a new primary and all the consequent secondaries. This algorithm is repeated until all the histories started by each primary event set in the designed simulation run have been simulated. After the entire run has been simulated, the averaged behaviours of physical quantities of interest can be evaluated from the aggregated results.

To modify the running conditions and to extract information out of simulations, the mechanism offered by GEANT4 is by means of so called *user action* classes. These are user-defined C++ classes invoked by the GEANT4 code at the beginning/end of a run (G4UserRunAction), at the beginning/end of an event (G4UserEventAction), at the creation/destruction of a track (G4UserTrackingAction), at each step (G4UserSteppingAction), to modify the stack of tracks to be processed (G4User StackingAction).

2.5 GATE

2.5.1 General concepts

GATE (Geant4 Application for Tomographic Emission) is a general-purpose free open-source software dedicated to numerical simulations of radiation transport in medical imaging and radiation therapies [101]. It is developed by the international OpenGATE collaboration and it is based on GEANT4, encapsulating its libraries, physics models, geometry description tools, visualization and 3D rendering tools, and combining them with original features to achieve a modular, versatile, scripted simulation "interface" toolkit specific to emission tomography and dosimetry [92, 102, 103].

GATE can be seen as an *application* or an "interface" to GEANT4, since GEANT4 manages the kernel that simulates the interactions between particles and matter, while GATE provides additional high-level features to facilitate the design of the GEANT4-based simulations. GATE consists of several hundred C++ classes, among which those dedicated to the management of time, geometry, particle tracking and radioactive sources, which are base classes or even mandatory classes, form a *core layer* close to the GEANT4 kernel. An *application layer* provides for the implementation of user classes derived from the core layer classes to model specific objects or processes, e.g. building specific geometrical volume shapes and specifying operations on them, like translations and rotations. Finally, a *user layer* provides the user the simple mechanisms to set up and run a Monte Carlo simulation, allowing for script-based input without requiring C++ programming, differently form direct GEANT4; a dedicated easy-to-learn scripting mechanism - referred to as *macro language* – indeed extends the native command interpreter of GEANT4, enabling an user-friendly configuration of simple or highly sophisticated experimental settings [104]. A graphic schematization of GATE's layered architecture is given in Fig. 2.2.

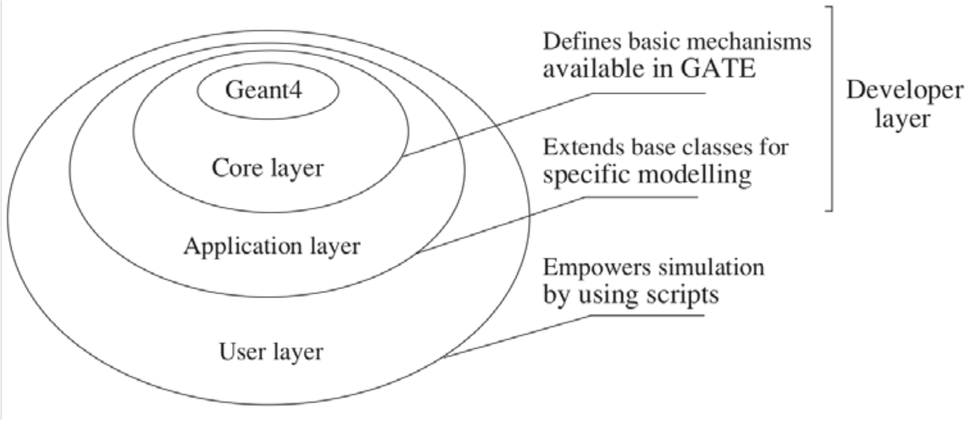
Geant4
Core layer
Application layer
User layer
Defines basic mechanisms available in GATE
Extends base classes for specific modelling
Empowers simulation by using scripts
Developer layer

FIGURE 2.2: Sketch of the layered architecture of GATE [92].

GATE currently supports simulations of emission tomography (PET and SPECT), computed tomography (CT), optical imaging (bioluminescence and fluorescence), external-beam radiotherapy treatments, molecular radiotherapy treatments and brachytherapy, but users can take advantage of it also for different and more particular applications. Nowadays it plays a key role in the design of new medical imaging devices, in the optimization of imaging protocols, in the development and assessment of image reconstruction algorithms and correction techniques. It can also be used for dosimetry calculations for the aforementioned radiation therapies or for any other related application (e.g., dose point kernel calculations, voxel S-factor calculations etc.) [102, 103].

A unique original feature of GATE is its capability for modeling time-dependent phenomena - for certain set-ups and input data -, enabling the movement of objects during a simulation. This permits to simulate, for example, detector movements or source decay kinetics, and thus the deduction of time curves under realistic acquisition conditions. This feature is a notable enhancement with respect to the GEANT4 architecture on which it is based, since GEANT4 is not thought for moving or transforming sources during a simulation. Two approaches for time-dependent simulations are available in GATE: a real-time dynamic phantom simulation approach, through which it is possible to define and manage some dynamic voxelized phantoms (via the functionalities `GateRTPhantom` and `GateRTPhantomMgr`), and a multiple static simulations approach [104].

2.5.2 GATE simulation architecture for dosimetry applications

GATE, just as GEANT4, is a program in which the user interface is based on scripts. To perform actions, the user can either enter commands in interactive mode, writing them sequentially on the `Idle>` prompt, or in batch-wise mode, building up

macro files (ASCII files with '.mac' extension) containing an ordered collection of commands. The GATE commands are organized in a "tree structure" with respect to the function they accomplish. For example, all geometry-control commands start with the string `geometry`, and they will all be found under the geometry branch of the tree structure.
The main steps a user must go through to perform a dosimetry or radiotherapy simulation are [104]:

1. **Definition of the phantom geometry**
   The first thing to be defined is the geometry of the simulation, based on volumes, each characterized by shape, size, position, and material composition. The list of available materials must be provided in a GateMaterials.db file, that has to be called at the beginning of simulations. Elements and densities are the building blocks of all the materials used in GATE simulations. Elements can be used alone as materials themselves, or can be mixed to form multi-element materials; multiple materials can also be mixed to define a new material given by their combination.
   The base of the geometry tree is represented by the *World* volume, which sets the experimental framework of the simulation, since it must include the entire simulation geometry. All the other volumes are defined as *daughters* or *grand-daughters* of the *World*, with sub-volumes of volumes defined as *daughters* of volumes, forming in this way a branched structure. A simple example is shown in Fig. 2.3(a).
   Many types of volumes can be defined, from simple geometrical shapes, that can be combined and/or repeated to set more complex shapes, to tessellated volumes, tetrahedral mesh volumes and voxelized volumes imported from external files. To define voxelized volumes it is necessary to import voxelized morphological input data, i.e., a digital anthropomorphic (or animal) phantom or a patient's CT scan. In order to do so, GATE uses special "navigator" algorithms that permit to quickly track particles from voxel to voxel. The recommended one for most uses is the "`ImageNestedParametrisedVolume`" algorithm, a parametrized approach that allows GATE storing a single voxel representation in memory and dynamically changing its location and composition at run-time during the navigation.
   To assign materials to voxels (and through materials their densities), a first method available is the *Range translator*, to be used with images providing label values as voxel values; the user must give as input a table with range intervals of labels and corresponding materials, and according to it a particular material will be assigned to each voxel whose value falls within that material's range.
   A second, basic method is the *Units to materials conversion*, which allows to associate a material to each label or Hounsfield Unit (HU) voxel value , according to a user defined input table.
   Finally, a more complex method called *Automated HU stoichiometric calibration*, described by Schneider et al. [105], can be used to generate a correspondence between HUs and materials in the case of input CT scans. This procedure is based on a user-defined mass *density tolerance* parameter and two calibration files describing the piecewise linear correspondence between HUs and mass density, and a list of material compositions. The tolerance parameter can be used to tune the number of materials depending on the accuracy required in

the simulation. The list of materials generated and the correspondence between materials and HU values are stored and can be used for converting any CT image into materials. A graphic representation of a voxelized phantom imported into GATE with the *Automated HU stoichiometric calibration* is shown in Fig. 2.3(b).

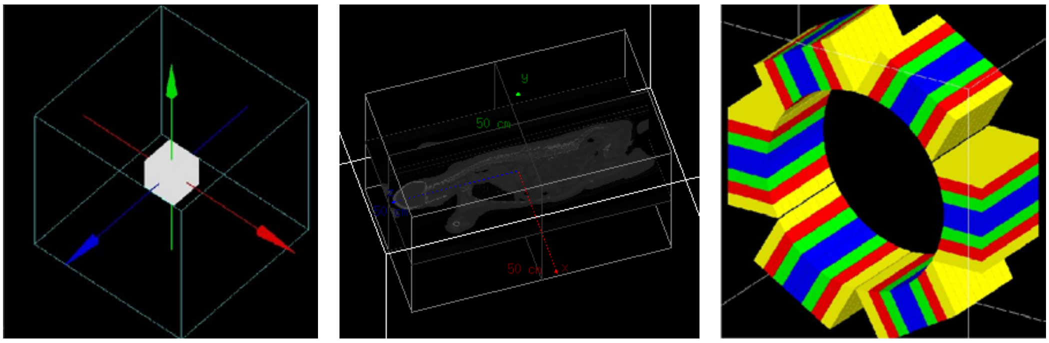

(a) (b) (c)

FIGURE 2.3: (a) A GATE's *World* geometry (the large cube with light-blue borders) and a cubic *daughter* volume (white); (b) a patient-specific voxelized phantom geometry (N.B. GATE visualization is not optimized for voxelized volumes); (c) a set of detector volumes reproducing an OPET scanner [104], with colors indicating different sections of the array.

2. **Outputs specification**
   By default, GATE's data output formats for all systems used are ASCII and ROOT [106]. An important feature introduced into GATE's core layer since the version 6.0 is the concept of "Actor". An Actor is similar to a sensitive detector (SD) in GEANT4, but has extended capabilities; it can store information at each step, but can also act on particles at each step, track, event or run. For instance, to mention some important actors, the `DoseActor` measures the energy deposited in a given volume, the `KillActor` stops the tracking of particles when they reach a given volume, the `SimulationStatisticsActor` gives the number of run, events, track, geometrical and physical steps of the simulation, the `PhaseSpaceActor` stores information related to incoming particles in output files that can successively be used as input files in subsequent GATE simulations. With the `Filter` feature the user can moreover modify the behaviour of actors. Filters perform tests on the particle properties (e.g., energy, type, or position) at the step track, event, or run level in order to trigger the actor only if the test output is true. Actors and filters can be combined to get new outputs.
   It is of particular interest for dosimetry, as it can be expected, the `DoseActor`, which can store 1D, 2D or 3D distributions of absorbed dose (in Gy) and/or energy (in MeV) deposited, with the associated statistical uncertainty in any volume [103]. A user-defined scoring matrix consisting of so-called "dosels" can be *attached to* any volume, including voxelized geometries. The user can provide the matrix size and the matrix position within the coordinate system of a monitored volume; the sizes of the dosels can be different from the geometry voxel sizes. Every time a particle interacts in the volume, the energy deposited and/or the absorbed dose are recorded in the corresponding dosel.

The `DoseActor` outputs can be stored in multiple formats, among them notably mhd image file format, composed of a header file ('.mhd') and a '.raw' data file; mhd format is useful since it can be handled by several open-source image processing toolkits, such as ITK [2], ImageJ [3] and 3D Slicer [107].

3. **Set up of physics processes**
   To predispose the interaction processes of interest that are enabled to occur in the defined volumes, GATE uses the GEANT4 models for physical processes. The user has to choose among these processes for each particle, and he can customize at will the simulation by setting production thresholds, cuts, electromagnetic options etc.
   As described in Sec. 2.4, in GEANT4 each physics process can be described by a model, generally among several models available, and corresponding cross-section tables. All the GEANT4 physics models and cross-sections below 10 GeV are available in GATE, including the ones describing transport of optical photons (useful for single detector response simulation) and hadronic interactions. New processes can be easily added thanks to the *auto-list* mechanism, which enables to manage lists of object types only requiring the inheritance from a GEANT4 base class and putting the new source file in the appropriate directory, with no change in other files [102].
   From GATE version 7.0 the recommended way to set physics processes is to use the "physics list builder" mechanism, called by the *addPhyslicsList* command, which basically loads GEANT4 *Physics Lists* seen in Sec. 2.4. Builders are already defined for all the main electromagnetic *Physics Lists* (emstandard, emstandard_opt1, emstandard_opt2, emstandard_opt3, emstandard_opt4, emlivermore, emlivermore_polar, empenelope) and hadronic *Physics Lists* (QGSP, QGSC, FTFP etc.). Further processes not included in the loaded *Physics List* can be anyways added and enabled singularly, and likewise it is possible to disable processes of the loaded *Physics List*.

4. **Initialization of the simulations**
   When the 3 steps described above are completed, the initialization, called by the line `/gate/run/initialize`, actually triggers the calculation of the cross section tables. After this step, the *Physics List* cannot be modified any more and new volumes cannot be inserted into the geometry.

5. **Definition of the radiation source**
   In GATE, a source is represented by a volume in which the primary particles of the simulations are emitted. The user can define the geometry of the source by simply defining a volume and *attaching* to it the 'status' of source. Besides its shape, the user has then to define other source's characteristics, such as specifying its type (GPS(General Particle Source), linacBeam, phaseSpace, PencilBeam, TPSPencilBeam, voxelized), its identity (simple particles, such as gammas, protons, electrons etc., or ion sources), the direction of emission, the energy distribution and, in case of radioactive ions, the activity. The lifetime of unstable sources is usually obtained from the GEANT4 database, but can also be set by the user. Voxelized geometries can be defined by importing patient datasets, tomographic scans among others, and enable to simulate realistic imaging acquisitions or radiation-therapies, through the conversion

---

[2] `https://itk.org/`

[3] `https://imagej.nih.gov/ij/`

of scan values into activity values (or equivalently into spatial probability of event occurrence).

6. **Start of the simulation**
   In this next and final step, the last acquisition characteristics are defined and the simulation run is triggered. If the sources involved in the simulation are not radioactive or if activity is not defined, user can fix the total number of events with the "`/gate/application/setTotalNumberOfPrimaries [N]`" command. The generator seed for RNG used for the simulation can be chosen in three ways: a 'default' option, which takes the default internal seed of the CLHEP C++ library; an 'auto' option, which automatically generates a new seed each time GATE is run, which is ensured to be different because it is selected taking the time in millisecond since January 1, 1970 and the process ID of the running GATE instance; a 'manual' option, to manually set the seed as an unsigned integer value to be included in the interval [0,900000000] [104].

In case of simulations for imaging applications and not for dosimetry-purpose only, besides a phantom geometry, a scanner geometry must be defined, by attaching volumes that have to act as detectors to a *system* and a *sensitive detector*; such detector volumes will therefore have the ability to record *Hits* (i.e. particle interactions) within them. *Hits* are then converted into physical observables by setting-up *digitizer* functions at the level of the detector pixels, which also permit to model readout schemes and trigger logics. An example of scanner geometry is shown in Fig. 2.3(c).

2.6 GAMOS

2.6.1 General concepts

GAMOS, acronym that stands for "Geant4-based Architecture for Medicine-Oriented Simulations", is another easy-to-use and flexible GEANT4-based Monte Carlo simulation software [108, 109]. It allows to perform simulations on top of the GEANT4 toolkit by using a simplified scripting language, without requiring the direct writing of C++ code. At the same time, its design allows the extension of its existing functionality through user-supplied C++ classes. In fact, though originally meant specifically for simulations in the medical physics field, as the acronym suggests, GAMOS has been developed to serve the widest possible range of users requirements by adopting three strategies. Firstly, maximizing the range of input and output options available through the scripting language, in order to cover most of the possibilities offered by GEANT4. Secondly, providing the users with direct access through the scripting language to a rich set of predefined applications for field specific simulations. For example, in the current version several applications for PET, SPECT, and Compton camera simulation are available, as well as for radiotherapy and shielding studies, and new applications are added by the GAMOS community at each new release. Thirdly, as anticipated, the possibility offered to users with minimum knowledge of C++ to easily extend and customize the framework by adding new code without modifying and re-compiling the GAMOS kernel. To achieve these features, GAMOS has been based on the plug-in technology and on a careful modular design [93].

2.6.2 User requirements

In GAMOS design, the following main input and output user requirements must be satisfied to implement a simulation [93, 110]:

- **Input requirements** include geometry, primary generator and physics list (exactly as in GEANT4, Sec. 2.4.1).
  Using external input text files with a specific format and a structure based on simple tags is the standard way of defining geometries. The order and meaning of parameters in each tag are the same as in the corresponding GEANT4 C++ geometry class.
  To define primary particles, a large number of different primary generator distributions are provided by GAMOS commands, extensible at will with new C++ code to cover new cases.
  Any of the *Physics lists* provided with the GEANT4 source code are selectable in GAMOS with simple user commands to define physics, and also them can be customized by the user.

- **Output requirements** include the choice among two macro-sets of mechanisms inherited from GEANT4 to extract information out of a simulation: the creation of a sensitive detector, that simulates the signals (hits) in a device, or the scoring, which counts a certain type of data within a certain volume during a run and prints a final score at the end of run. The main scoring applications provided by the GAMOS framework are: the energy (or absorbed dose) deposition in mathematical volumes or in voxelized phantoms, in this last case both evaluable in a real voxelized geometry or with only a voxelized scoring on a non-voxelized geometry; fluxes; currents; number of interactions.
  GAMOS provides easy access to a rich set of predefined GEANT4 *user actions* serving for these purposes, with also the possibility to attach to user actions or scorers different filters and/or 'classifiers'. The classifier is an original GAMOS concept with respect to GEANT4; it is a C++ class that receives a track or track step information and returns a different index (an unsigned integer) depending on some given criteria, classifying according to it the step or track examined.
  To maintain a good flexibility and leave to the user the freedom to analyze the results among a wide selection of external software, GAMOS can save table and histogram results with two simple text formats: comma-separated value (CVS) and a simpler text format that contains only the histogram limits and the list of histogram entries, one per column. In addition, it can provide histograms directly written in ROOT [106].

2.6.3 Framework design

The GAMOS C++ code is divided into a *core* and an *application code*. The *core* is a set of classes that “wrap” the GEANT4 kernel to make its functionality accessible to GAMOS users through commands and plug-ins, and to provide functionality not related to any specific application. The *application code* exploits the tools available in GEANT4 and those added by the GAMOS *core* to provide the user with predefined simulation setups optimized for a specific field. All the default tools of GAMOS are directly available through its scripting language, that operates as an interface between the user and the kernel. This is practically made possible by a *command interpreter*, that reads and and interprets the user-provided scripts (and input text files

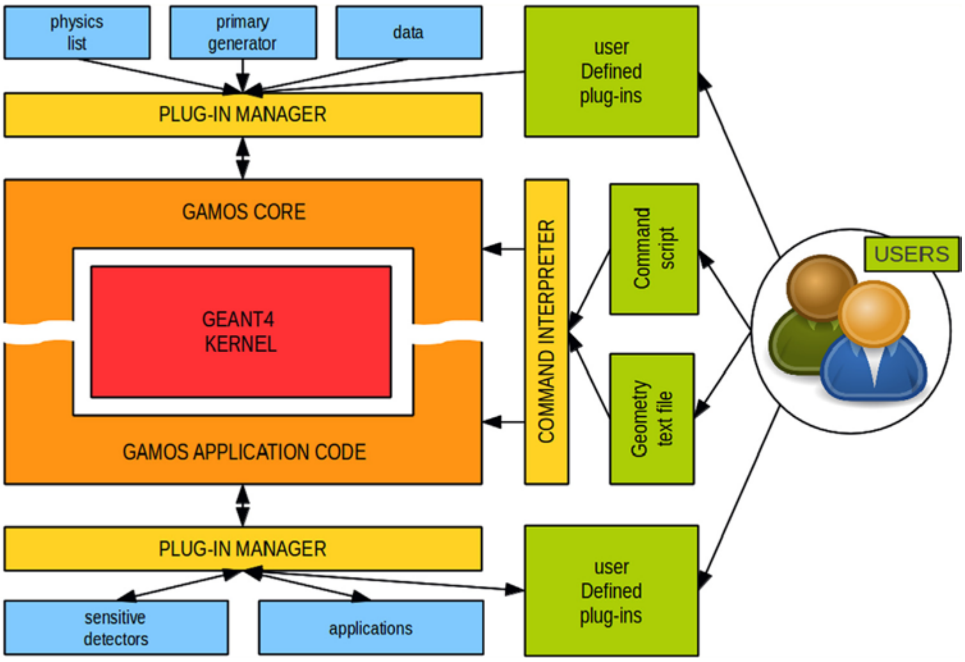
physics list
primary generator
data
user Defined plug-ins
PLUG-IN MANAGER
GAMOS CORE
GEANT4 KERNEL
GAMOS APPLICATION CODE
COMMAND INTERPRETER
Command script
Geometry text file
USERS
PLUG-IN MANAGER
user Defined plug-ins
sensitive detectors
applications

FIGURE 2.4: A schematic view of the GAMOS design structure [93].

for geometry) to initialize the required configuration. The interpretation is made once per job, since those parameters needed several times in a job are stored as private class members after their value is read a first and unique time. This is why there is virtually no difference between a GAMOS simulation and a direct GEANT4 one, with the only penalization in run-time being the initialization procedure, whose time is negligible.

As already anticipated, GAMOS plug-in mechanism enables customizing the functionality of an application via plug-ins, without modifying the GAMOS kernel or even knowing how the kernel works. This means that the "main" program runs without predefined components, and the user tells it which components are being loaded at run time, with no need for recompiling, by simply listing them in a text input file. This mechanism also lets the user define new components that were not foreseen by GAMOS developers and easily tell GAMOS to use them together with any other of his/her own components or GAMOS components.

An intuitive example to understand the plug-in logic is considering the case in which a user wants to use the default GAMOS geometry text format and one of the GAMOS physics lists, but wants to use a primary generator created by himself/herself and defined in a new C++ class named, let's say, `MyPrimaryGenerator`. The user only has to include this new file through the following line:

```
#DEFINE_GAMOS_GENERATOR(MyPrimaryGenerator);
```

and, after compiling the new user class alone, the new primary generator will be selectable in any job by simply adding in the GAMOS script the command:

```
"/gamos/generator MyPrimaryGenerator"
```

instead of the default GAMOS one [93]:

```
"/gamos/generator GmGenerator"
```

A schematic diagram summarizing the GAMOS code design described in this paragraph is shown in Fig. 2.4.

Chapter 3

Monte Carlo internal dosimetry in ^{18}F-choline PET diagnostics

3.1 Introduction

This Chapter describes our research on Monte Carlo (MC) internal dosimetry in PET diagnostics, carried out applying the concepts introduced in the previous chapters, about internal dosimetry and MC simulation of radiation interaction. Specifically, the direct MC voxel-level patient-specific dosimetry for a case of routinary ^{18}F-choline PET/CT exam was performed, with particular attention to liver and lungs. Both GATE and GAMOS toolkits, introduced in Chapter 2, were employed independently to run simulations, and their implementations will be detailed. Results showed a good agreement, with just some differences in low-density and poorly-perfused areas, imputable to the slightly different procedure adopted to assign density to voxels.

A further investigation was carried out to evidence eventual absorbed dose rate artefacts and overestimation caused in MC calculations because of PET background noise, since the PET is used to model the radiopharmaceutical distribution. At this scope, simulations employing a PET-filtering technique were executed and compared with native-PET ones. Absorbed dose rate decreases of about 40% were observed in lungs for filtered-PET simulations with respect to the unfiltered ones, and a general lowering of background absorbed dose rate outside the body and of high-dose-rate spots corresponding to air-rich regions was found, confirming the unrealistic generation - in the simulations - of spurious decays from air regions, caused by PET background noise. The PET-filtering produced in addition an improved, excellent agreement between GATE and GAMOS results, within 6% in lungs and 1% in liver, supporting the hypothesis that the differences in the density assignment procedures have more impact on low-density and poorly-perfused voxels.

3.2 ^{18}F-choline PET exam

^{18}F is a positron-emitting radioactive isotope of fluorine widely used in PET practice, characterized by an half-life of $T_{\frac{1}{2}} = 109.77$ min [111]. Its main decay channel, with a Branching Ratio of 96.73 %, is precisely β^+-decay, according to the following reaction:

$$^{18}_{9}\text{F} \rightarrow {}^{18}_{8}\text{O} + \beta^+ + \nu \tag{3.1}$$

where ν indicates the electronic neutrino. The average beta-emission energy of ^{18}F is $\langle E_{\beta^+} \rangle$ = 249.8 keV, its end-point $E_{\beta^+ max}$ = 632 keV, with the beta-emission spectrum reported in Fig. 3.1.

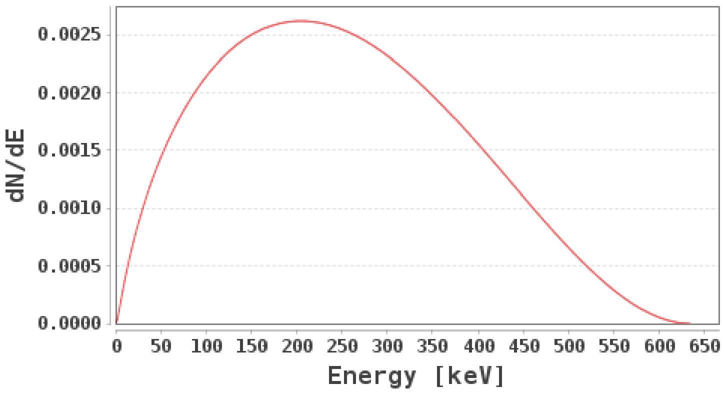

FIGURE 3.1: Positron-emission energy spectrum of ^{18}F [111].

Choline (whose chemical structural formula is reported in Fig. 3.2) is a water-soluble organic molecule, sometimes referred to as Vitamine J, classified as an essential nutrient. It is a precursor for the biosynthesis of phospholipids, the major components of the cellular membrane. Normal choline biodistribution shows relatively high uptake in pancreas, liver, kidneys, and salivary glands, variable uptake in bowels and little urinary excretion, the last feature being advantageous for the assessment of diseases in the prostate gland [112, 113]. Choline indeed accumulates in certain tumors, in particular prostate cancer, in part because of the overexpression of the choline kinease enzyme in support of the increased demand for cellular membrane synthesis induced by the malignancy. Choline kinase catalyzes the phosphorylation of choline to form phosphorylcholine, followed by generation of phosphatidylcholine in the tumor cell membrane [112].

Labelling choline with positron-emitting radioisotopes such as ^{11}C and ^{18}F, it is possible to perform PET or PET/CT examinations for the diagnosis and staging of prostate cancer (PC). In particular ^{18}F-choline (Fig. 3.2) is recently used for the detection of locally recurrent primary PC of for PC metastatic disease - especially in bones - for men with prostate-specific antigen (PSA) release, since its diagnostic performances proved to improve with increasing PSA level [112].

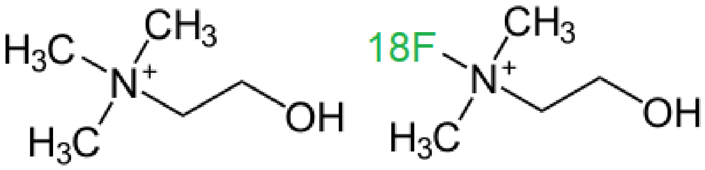

FIGURE 3.2: Chemical structural formula of choline (left) and ^{18}F-choline (right) molecules.

3.3 Aim of the study

We carried out a comparative study of the toolkits GATE and GAMOS applied to MC patient-specific internal dosimetry of ^{18}F-choline PET diagnostic examinations. Taking morphological and functional information on the patient from CT and PET scans, respectively, the aim was to evaluate three-dimensional absorbed dose rate distributions for a patient who underwent such type of PET, deduce the average absorbed dose rates and dose rate volume histograms (DRVHs) within volumes of interest (VOIs) representing liver and lungs, and compare the results obtained with the simulations performed by the two softwares. Focus was also put on the investigation of the influence of PET scan background noise on the dosimetric outcomes, applying a threshold-based filtering technique on the functional scan and comparing the results of filtered-PET simulations and native-PET ones.

3.4 Simulations settings

3.4.1 Softwares employed

GATE version 8.1, relying on GEANT4 version 10.04.p03, and GAMOS version 6.0.0, relying on GEANT4 10.02, were used to implement the simulations. For input and output images processing, the image computing software 3D Slicer [107, 114] version 4.10 was used.

3.4.2 Input data

The initial data of the study were the ^{18}F-choline PET/CT scans in Dicom format of a patient, performed at the Nuclear Medicine Unit of the University Hospital "G. Martino" in Messina (Italy) with a Philips Gemini TF 16 scanner [1]. The native CT scan had a resolution of 512 × 512 × 1019, with voxel dimensions of (1.17 × 1.17 × 1.00) mm^3. In order to shorten the simulation time and the demands in terms of storage memory of the output files, the native CT was first resampled via linear interpolation by means of the *Resample Scalar Volume* module of 3DSlicer; a resampling doubling each voxel dimension was adopted, to get the resolution reported also in Table 3.1. The PET scan employed had been corrected for decay, attenuation (with CT correction), non-uniform radial sampling, scatter, randoms, dead time and detector normalization. Other relevant acquisition parameters of both the CT and PET scans are reported in Table 3.1. Coronal views of resampled CT, native PET and fusion of the two are shown in Fig. 3.3.

TABLE 3.1: Resolution and voxel dimensions for the resampled CT scan and PET scan used as input data for the study; for the PET scan are also reported the administered activity to the patient, $A(t_0)$, and the interval of time between the administration and the scan acquisition, Δt.

CT	resolution	256 × 256 × 520
	voxel dimensions (mm)	2.34 × 2.34 × 2.00
PET	radiotracer	^{18}F-choline
	$A(t_0)$ (MBq)	296
	Δt (min)	84
	resolution	144 × 144 × 255
	voxel dimensions (mm)	4.00 × 4.00 × 4.00

---

[1] `https://www.clinicalimagingsystems.com/product/philips-gemini-tf-16-64-slice-pet-ct-scanner/`

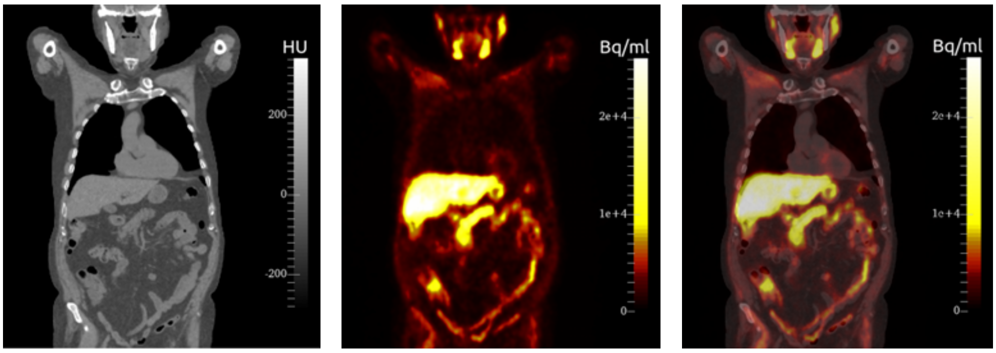

(a) (b) (c)

FIGURE 3.3: Coronal slices of the resampled CT (a), the native PET (b) and of the fusion of the two (c).

3.4.3 Organ segmentations

As mentioned in Sec. 3.2, liver is among the organs exhibiting the highest ^{18}F-choline uptake as a consequence of the normal choline biodistribution [112], and the considered patient case makes no exception, as it can be seen from the PET scan (Fig. 3.3(b)). Consequently liver, as a source organ for radiation, is expected to exhibit significant absorbed dose rates at the time point of the PET/CT scan acquisition. Lungs, especially the right one, above the liver, can be also expected to receive non-negligible absorbed dose rates. Therefore we decided to segment the following Volumes Of Interest (VOIs) for the quantification of average absorbed dose rates and DRVHs: liver, right lung, and left lung. The segmentations, shown in Fig. 3.4, were performed manually using 3D Slicer's *Segmentation* module on the resampled CT image.

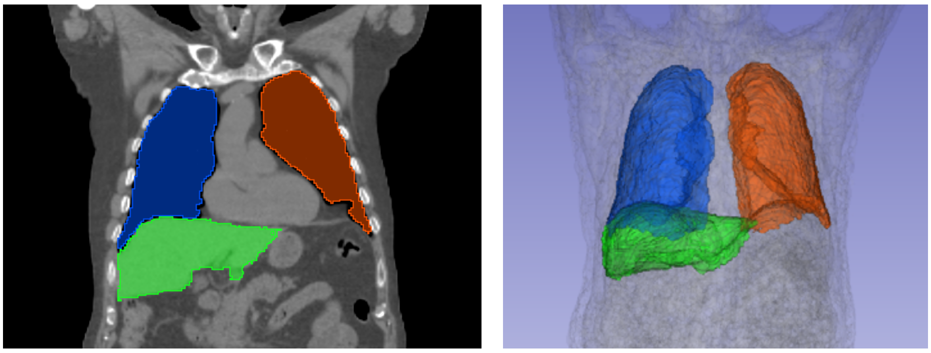

(a) (b)

FIGURE 3.4: Liver (green), right lung (blue) and left lung (orange) VOIs segmentations, reported on a coronal view superimposed to the CT (a) and in a 3D representation (b).

3.4.4 Patient-specific phantom implementation

Both in GATE and GAMOS, the resampled CT image was used to model a computational voxelized phantom reproducing the patient's body morphology. The phantom implementation procedure available differs a bit in the two toolkits.

GATE procedure

The CT Dicom image was imported to model a voxelized volume through the *ImageNestedParametrisedVolume* algorithm [104]. By means of the *Automated HU stoichiometric calibration* procedure it is possible firstly to assign to each CT voxel a material, i.e., a chemical composition, on the basis of user defined Hounsfield Units (HU) intervals. Then HU sub-intervals are defined and a density is assigned to each of them, through the interpolation of a HU-density calibration relation; the sub-intervals are defined in such a way that densities differ from each other for a user defined value, called "density tolerance" (described in Sec. 2.5.2). Thus to each voxel of the phantom is assigned one of this sub-materials, characterized by a given chemical composition and density.
The five intervals of HU reported in Table 3.2 were set to identify the materials to be assigned, namely: air, lung tissue, adipose tissue, soft tissue and cortical bone. Their chemical compositions were selected from the GEANT4 materials database [115], and the choice of materials was done to properly reproduce the main tissues characterizing the thoraco-abdominal region of the human body. The adopted HU intervals were deduced to reproduce the density intervals reported in Table 3.2, selected to have the best possible match with the designated materials. The conversion was performed through a bi-linear HU-density calibration relation, fitted with the following function: [116]

$$\begin{cases} y = ax + b & x < 0 \\ y = a'x + b' & x \geq 0 \end{cases} \tag{3.2}$$

In particular, the calibration data reported in Tab. 3.3 were used, with bi-linear fit reported in Fig. 3.5 and fit parameters listed in Tab. 3.4. The mentioned HU-density calibration was also used for the density assignment, setting a density tolerance of 0.1 $\mathrm{g/cm^3}$.

GAMOS procedure

GAMOS permits to assigns to each CT voxel a density directly converting through a HU-density relation, and assigns to them a material on the basis of user-defined density intervals. The same HU-density relation and density intervals used for GATE simulations (Tables 3.2 and 3.3 and Fig. 3.5) were adopted.

TABLE 3.2: HU intervals and corresponding density (ρ) intervals set to identify the materials used in the simulations, whose compositions were taken from the GEANT4 database [115].

Material	**HU intervals**	**ρ (g/cm^3)**
G4_AIR	HU $\leq$ -855.75	$\rho \leq 0.10$
G4_LUNG_ICRP	-855.75 $<$ HU $\leq$ -126.50	$0.10 < \rho \leq 0.85$
G4_ADIPOSE_TISSUE_ICRP	-126.50 $<$ HU $\leq$ -38.98	$0.85 < \rho \leq 0.94$
G4_TISSUE_SOFT_ICRP	-38.98 $<$ HU $\leq$ 343.61	$0.94 < \rho \leq 1.2$
G4_BONE_CORTICAL_ICRP	HU $>$ 343.61	$\rho > 1.2$

TABLE 3.3: HU-density calibration values used for the density values assignment to phantom's voxels.

HU	-1000	-700	-450	0	300	1000	1400	2500	3500
ρ (g/cm^3)	0.0012	0.187	0.521	1.0	1.169	1.594	1.837	2.506	3.113

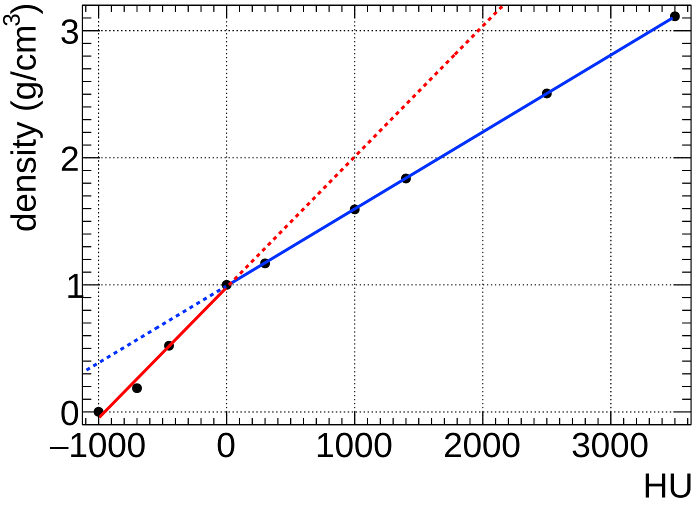

FIGURE 3.5: HU-density calibration points and their bi-linear fit, whose parameters are reported in Tab. 3.4.

TABLE 3.4: Fit parameters (defined in Eq. 3.2.) and χ^2 of the bi-linear fit in Fig. 3.5, performed on the HU-density calibration values of Tab. 3.3.

a	10.284e-04 $\pm$ 8.75e-05
b	0.9919 $\pm$ 0.0033
χ^2/ndf (x < 0)	0.00822096
a′	6.054e-04 $\pm$ 1.74e-06
b′	0.980 $\pm$ 0.057
χ^2/ndf (x $\geq$ 0)	0.000108113

3.4.5 Radionuclide decays spatial distribution

To model the spatial distribution of radionuclide inside the phantom, and consequently simulate radioactive decays happening with spatial probabilities proportional to the redionuclide concentration, the PET Dicom scan was imported in both GATE and GAMOS as a voxelized source volume. In correspondence to each of its voxels, a decay event generation probability (p) was assigned through a linear conversion of its PET values (v) - in our specific case in terms of activity concentrations, expressed in Bq/mL -, that normalizes the PET values to the sum of values of all the PET voxels:

$$p_{ijk} = \frac{v_{ijk}}{\sum_{ijk} v_{ijk}} \tag{3.3}$$

In particular, in GATE this is done by the *linear translator* command of the *imageReader* method, whereas in GAMOS by employing the generator class *GmGenerDistPositionInVoxelsFromFile* [110]. The voxelized source volume was placed in the spatial reference system by applying the proper translations, in order to have the correct relative position with respect to phantom, according to the information included in the Dicom files headers.

3.4.6 Implementation of physical phenomena

The primary events that we associated to the voxelized source were the radioactive decays of ^{18}F nuclei, simulated in both toolkits with the *G4RadioactiveDecay* GEANT4 module and related classes [115], setting the source as ion type. To account for all the possible electromagnetic interactions that can happen in the subsequent secondary interactions in the simulations, the GEANT4 physics list *G4EmStandardPhysics_option3* was used [115]. In order to sample with high spatial accuracy the distribution of energy depositions, we set a range cut of 50 μm on the production of secondary particles from the propagation of all the possible simulated particles (electrons, positrons, photons); in fact this value is significantly shorter than the voxel dimension, and in terms of energy corresponds to a cut of about 15 keV for electrons in soft tissue.

3.4.7 Absorbed dose scoring settings

We set up the scoring of absorbed doses and their related statistical uncertainties at voxel level with the *DoseActor* method in GATE, using the *MassWeighting* algorithm [104], and with *GmPSPrinter3ddose* scorer [110] in GAMOS. The adopted "dosel grid", i.e. the voxelized absorbed dose matrix to be sampled, was chosen to spatially coincide with the phantom matrix, so that we obtain an absorbed dose map having the same voxel dimensions and resolution as the input CT, indicated in Tab. 3.1. The absorbed doses are evaluated as the sum of all the energy depositions that took place within the considered voxel in the entire simulation run, divided by the mass of the voxel, calculated from the density assigned as detailed in Section 3.4.4. The statistical uncertainties for each absorbed dose voxel (σ^{ijk}) are evaluated as standard deviation of the mean absorbed dose on the total number of primary histories simulated [117]:

$$\sigma^{ijk} = \frac{1}{N-1}\sqrt{\frac{\sum_{n=1}^{N}\left(d_n^{ijk}\right)^2}{N} - \left(\frac{\sum_{n=1}^{N} d_n^{ijk}}{N}\right)^2} \tag{3.4}$$

where N is the total number of simulated primary events (and thus histories) and $d_n^{ijk} = \sum_m d_{n,m}^{ijk}$ is the deposited absorbed dose in the considered voxel during a single n-th primary simulated history, given by the sum of all the m-th absorbed dose depositions happening in that voxel because of particle interactions simulated in that history.

We simulated $N = 10^8$ histories, a setting which ensured an average value of σ^{ijk} below 6% within the liver VOI.

3.5 Post-simulation absorbed dose rate calculation

Absorbed dose rate maps

From Monte Carlo (MC) simulations outputs we obtained the 3D absorbed dose maps relative to N primary event histories, i.e, ^{18}F disintegrations in our study. To deduce the 3D absorbed dose rate maps at the time point of the PET/CT scan, we divided each MC absorbed dose voxel for the total number of histories N - giving absorbed dose-per-event - and then multiplied it for the total activity in the PET field of view (FOV) at the scan acquisition time $t = t_s$. Thus, indicating with D_{MC}^{ijk} (Gy) the MC output absorbed dose in a given voxel (i, j, k) and with $A(t_s)$ (MBq) the total activity measured in the PET FOV at the acquisition time, the absorbed dose rate $\dot{D}^{ijk}(t_s)$ $(\mathrm{Gy} \cdot \mathrm{s}^{-1})$ at the acquisition time in the voxel (i, j, k) was calculated as:

$$\dot{D}^{ijk}(t_s) = \frac{D_{MC}^{ijk}}{N} \cdot A(t_s) \tag{3.5}$$

$A(t_s)$ was deduced from the PET image and related Dicom information, by summing up the activity concentration values of all the PET voxels and multiplying them for the voxel volume:

$$A(t_s) = \sum_{ijk} A^{ijk}(t_s) = \sum_{ijk} c^{ijk}(t_s) \cdot V_{voxel} \tag{3.6}$$

where $A^{ijk}(t_s)$ (MBq) is the activity in a single PET voxel at the scan acquisition time, $c^{ijk}(t_s)$ (MBq/mm^3) is the activity concentration in a single PET voxel at the acquisition time and V_{voxel} (mm^3) is the volume of the PET voxel.
All the mentioned mathematical operations on voxelized images were performed with 3D Slicer.

Average absorbed dose rates in VOIs and DRVHs

We used 3D Slicer's *Segment statistics* module to evaluate as follows the absorbed dose rate average values in the segmented VOIs (Sec. 3.4.3), $\langle \dot{D}(t_s) \rangle_{VOI}$:

$$\langle \dot{D}(t_s) \rangle_{VOI} = \frac{1}{N_{vox \in VOI}} \sum_{ijk \in VOI} \dot{D}^{ijk}(t_s) \tag{3.7}$$

with $N_{vox \in VOI}$ indicating the number of absorbed dose rate voxels contained in the considered VOI, and the *Dose Volume Histogram* module to compute DRVHs, i.e., histograms whose columns' height indicates the volume percentage of the considered VOI receiving an absorbed dose rate given by the bin value.

GATE - GAMOS comparison

The average absorbed dose rate values in VOIs obtained with GATE and GAMOS were compared in terms of relative per cent difference ε (%), taking GAMOS as a reference:

$$\varepsilon_{VOI} = 100 \cdot \frac{\langle \dot{D}_{\,\mathrm{GATE}}(t_s) \rangle_{VOI} - \langle \dot{D}_{\,\mathrm{GAMOS}}(t_s) \rangle_{VOI}}{\langle \dot{D}_{\,\mathrm{GAMOS}}(t_s) \rangle_{VOI}} \tag{3.8}$$

In addition, the relative percent differences at voxel level ε_{ijk} (%) were evaluated:

$$\varepsilon^{ijk} = 100 \cdot \frac{\dot{D}^{ijk}_{\mathrm{GATE}}(t_s) - \dot{D}^{ijk}_{\mathrm{GAMOS}}(t_s)}{\dot{D}^{ijk}_{\mathrm{GAMOS}}(t_s)} \tag{3.9}$$

and their average values $\langle \varepsilon^{ijk} \rangle_{VOI}$ (%) in VOIs.

3.6 Background noise effects and absorbed dose artefacts study

One of the aims of the described work was to investigate the effect of PET image background noise on the absorbed dose rate outcomes. In fact, from the preliminary results obtained during this study, high-dose spots and distributions were observed in certain low-density regions, for example lungs and air outside of the patient's body, and we decided to analyze their origin and to introduce proper corrections. In particular, we focused on background noise due to the PET image reconstruction process, that inevitably affects tomographic scans, which depends on the reconstruction algorithms, and in principle survives the conventional corrections applied to the scans, such as attenuation and scatter corrections. No attempt has been made to correct specifically other sources of noise, e.g. misalignment in registration of PET and CT scans, motion blurring and positron-range blurring.

Since, as described in Sec. 3.4.5, the primary event generation probability distribution is built from the PET scan, a non-zero event generation probability will be assigned to source voxels having noise-induced non-zero activity concentration in the PET. As a consequence, radionuclide decays will be simulated happening also in these locations, and in these noisy areas erroneous absorbed dose rate background or artefacts may be produced in MC simulations results.

3.6.1 PET-filtering procedure

Cuts

To quantify the discussed contribution, we performed further simulations with both GATE and GAMOS, using as input data for the radionuclide source spatial distribution the PET scan filtered through the following threshold-based procedure:

(i) PET voxels corresponding to CT voxels having HU < -855, to whom air is assigned as material (Table 3.2), were set to zero.

(ii) PET voxels with activity concentrations smaller than 100 Bq/mL were set to zero; such low-value PET voxels (< 0.3% of the maximum activity concentration value of the scan) are mainly blurring-noise located in areas outside the patient's body but not identified as air - because of their slightly higher density -, in particular the PET/CT bed and some CT reconstruction artifacts near it.

These two cuts were applied using the *Mask volume* section of 3D Slicer's *Segment editor* module [114], which allows thresholding and logical operations on voxel sets, adopting a zero-order interpolation in case of operations between voxelized images with different voxel dimensions and resolutions.

The overall aim of the two cuts was to build a filtered-PET that, used as input for radioactive source distribution, minimizes the probability of generating decays in areas of the patient's body phantom where it is unrealistic to have decays, actually corresponding to air - inside and outside the body -, and materials outside the body.

The effect of the filter can be observed in Fig. 3.6, in particular in panel (c), showing the difference between native and filtered PET; the filter, as expectable, acts especially in lungs, in the oro-nasal cavity, in spots of the abdomen corresponding to bowels and in the air surrounding the patient's body.
The filtered-PET simulations were carried out using all the same settings adopted for the native-PET simulations except for the PET input image, and the same types of outputs were deduced: absorbed dose rate maps, dose-rate average values into VOIs, DRVHs. In particular, also in the case of filtered-PET, to deduce the absorbed dose rate as in Eq. 3.5, the total activity in the PET FOV, $A(t_s)$ (Eq. 3.6), was the one retrieved from the native PET, to ensure the conservation of the total rate of decays.

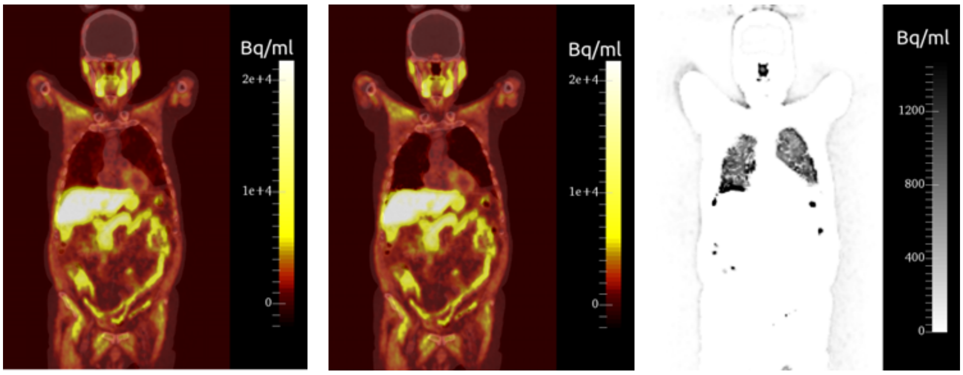

(a) (b) (c)

FIGURE 3.6: Coronal slices of the native PET (a) and filtered PET (b) fused with CT (for visual morphological reference), and the logical difference between the two (c).

Filtered-PET - native-PET simulations comparison

The native-PET and filtered-PET average absorbed dose rate values in VOIs were compared, both for GATE and GAMOS, in terms of their relative per cent difference κ (%), taking the native-PET results as a reference:

$$\kappa_{VOI} = 100 \cdot \frac{\langle \dot{D}_{\text{filtered}}(t_s)\rangle_{VOI} - \langle \dot{D}_{\text{native}}(t_s)\rangle_{VOI}}{\langle \dot{D}_{\text{native}}(t_s)\rangle_{VOI}} \tag{3.10}$$

Also for the filtered-PET simulations we compared the results of GATE and GAMOS, in the same way described in Sec. 3.5.

3.7 Results

Coronal slices of the absorbed dose rate maps obtained using native PET and filtered PET as input data for both GATE and GAMOS simulations are reported in Fig. 3.7. The average absorbed dose rates $\langle \dot{D}^{ijk}(t_s)\rangle$ in each considered VOI obtained for native-PET and filtered-PET simulations with both GATE and GAMOS are presented in Tab. 3.5, together with the corresponding average values of standard deviation of the mean absorbed dose rate in VOIs, $\langle \sigma^{ijk}\rangle$, the relative per cent difference ε between the average absorbed dose rate values obtained with GATE and GAMOS, the average value $\langle \varepsilon^{ijk}\rangle$ of the voxel-level relative per cent differences between GATE and GAMOS, and the relative per cent differences κ between the average absorbed

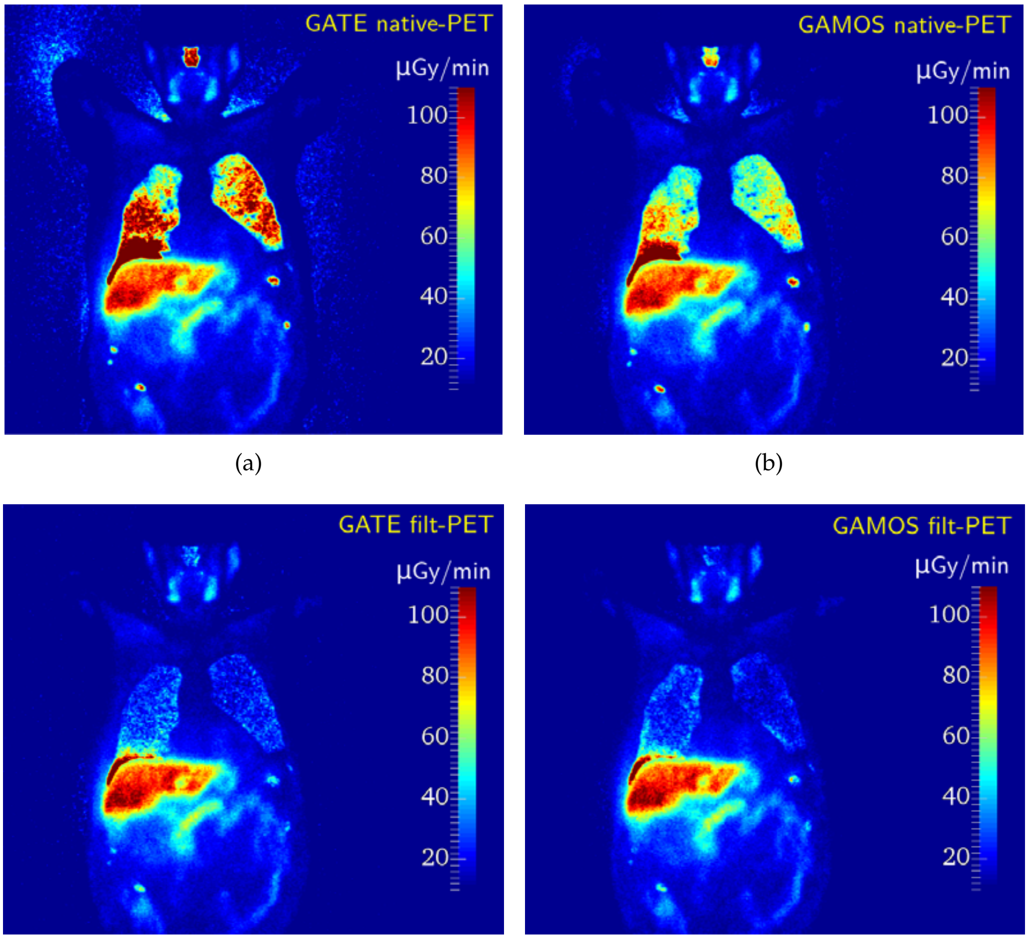

(a) (b) (c) (d)

FIGURE 3.7: Coronal slices of absorbed dose rate maps estimated with GATE and GAMOS native-PET and filtered-PET simulations.

dose rates obtained with filtered- and native-PET simulations.

Considering the results of the simulations employing the native PET, a very good agreement was found between GATE and GAMOS average absorbed dose rate in liver VOI, within about 1% in terms of both ε and $\langle \varepsilon^{ijk} \rangle$. Instead, for lungs-related VOIs wider differences were observed, with GATE overestimating their average absorbed dose rates with respect to GAMOS by about 13% in right lung and 18% in left lung (ε in Tab. 3.5). An almost identical situation is found in terms of local voxel-level absorbed dose rate differences ε^{ijk} between GATE and GAMOS, whose distributions within VOIs are reported in Fig. 3.8 (panels a, c and e) and whose average values within VOIs, $\langle \varepsilon^{ijk} \rangle$, are comparable with ε values. Such local differences in absorbed dose rates can be appreciated in Fig. 3.7 comparing panel (a) and (b), not only within lungs, but also in the nasal cavity and in the background outside body, more pronounced in GATE's absorbed dose rate map.

Considering the results of the filtered-PET simulations with respect to the native-PET ones, a slight increase, of about 3% in terms of κ, of the average absorbed dose rate in liver is observed with both GATE and GAMOS when using the filtered-PET. Instead, a decrease between about 40% and 50% of the average absorbed dose rate is observed in lungs, also in this case with both toolkits. This significant lowering of

TABLE 3.5: $\langle \dot{D}(t_s) \rangle$s, $\langle \sigma^{ijk} \rangle$s, εs, $\langle \varepsilon_{ijk} \rangle$s and κs deduced from GATE and GAMOS filtered- and native-PET simulations for the three VOIs, as defined in Sec.s 3.5 and 3.6.

	VOI	Liver	Right Lung	Left Lung
PET	Volume (cm^3)	1074	2091	1797
native	$\langle \dot{D}(t_s) \rangle$ GATE (μGy/min)	83.34	71.42	59.79
	$\langle \sigma^{ijk} \rangle$ GATE (%)	±5.55	±14.55	±15.60
	$\langle \dot{D}(t_s) \rangle$ GAMOS (μGy/min)	84.28	62.74	50.67
	$\langle \sigma^{ijk} \rangle$ GAMOS (%)	±5.55	±13.20	±14.28
	ε (%)	-1.11	+13.83	+18.01
	$\langle \varepsilon^{ijk} \rangle$ (%)	-0.44	+12.83	+17.26
filtered	$\langle \dot{D}(t_s) \rangle_{\text{GATE}}$ (μGy/min)	86.27	38.36	28.55
	$\langle \sigma^{ijk} \rangle$ GATE (%)	±5.63	±19.80	±22.21
	$\langle \dot{D}(t_s) \rangle_{\text{GAMOS}}$ (μGy/min)	86.82	37.38	26.96
	$\langle \sigma^{ijk} \rangle$ GAMOS (%)	±5.62	±17.72	±20.21
	ε (%)	-0.64	+2.60	+5.91
	$\langle \varepsilon^{ijk} \rangle$ (%)	-0.40	+9.40	+14.66
	κ_{GATE} (%)	+3.51	-46.29	-52.25
	κ_{GAMOS} (%)	+3.02	-40.42	-46.80

absorbed dose rate in lungs with respect to the native-PET simulations can be identified graphically in Fig. 3.7, comparing panels (c) and (d) with panels (a) and (b), and in Fig. 3.9, showing absorbed dose rate map slices (fused with CT slices for a clearer morphological reference) obtained with GATE simulations, comparing panels (a2), (b2), (c2) with (a1), (b1), (c1), and even more looking at panels (a3), (b3), (c3), showing the voxel-level differences between filtered-PET and native-PET absorbed dose maps. From both figures it can be also observed a reduction of absorbed dose rate, of about half and beyond with respect to native-PET values, of the background in the air outside the body and in air-rich spots of abdomen and oro-nasal cavity.

Comparing the results of GATE and GAMOS filtered-PET simulations, an excellent agreement in liver is maintained, with ε and $\langle \varepsilon^{ijk} \rangle$ below 1%, and the agreement for lungs improves significantly with respect to native-PET simulations, with ε going down below 3% in right lung and below 6% in left lung, and $\langle \varepsilon^{ijk} \rangle$ below 10% in right lung and below 15% in left lung; the distributions of ε^{ijk} within VOIs for filtered-PET simulations are reported in panels (b), (d) and (f) of Fig. 3.8.

In Fig. 3.10, the DRVHs in the defined VOIs are reported, giving the voxel-level information about the absorbed dose rate distribution. All the evidences observed in terms of averaged results can be further appreciated in terms of DRVHs. The excellent agreement between GATE and GAMOS in the estimation of liver absorbed dose rate is testified also at voxel-level by panel (a), with GATE and GAMOS histograms practically superimposed both in the case of native-PET and filtered-PET simulations. Moreover, comparing the latter histograms to the former ones, the significant decrease of absorbed dose rate within lungs for filtered-PET simulations with respect to the native-PET ones is observable, likewise the slight increase of liver absorbed dose rate in the filtered-PET simulations. For both lungs VOIs, as expected from averaged results, it can be seen some discrepancy between GATE and GAMOS histograms for the native-PET simulations, evident for volume percentages smaller

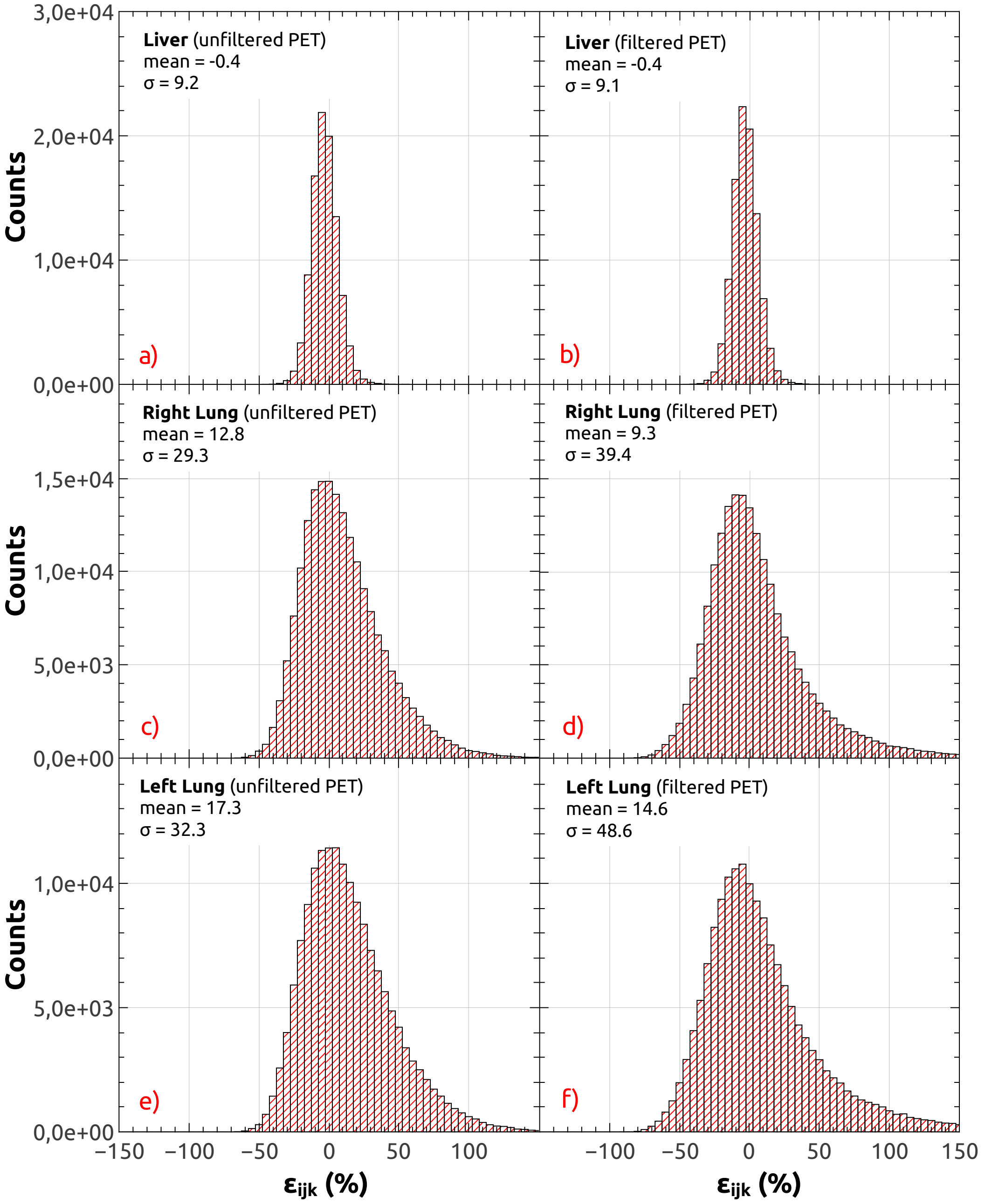

FIGURE 3.8: Distributions of absorbed dose rate relative percent differences at voxel level (ε^{ijk}) inside VOIs for unfiltered-PET (a, c, e) and filtered-PET (b, d, f) simulations.

than 60% of the total, while on the contrary with the filtered-PET simulations GATE and GAMOS gain a good agreement, with their respective histograms overlapped quite well.

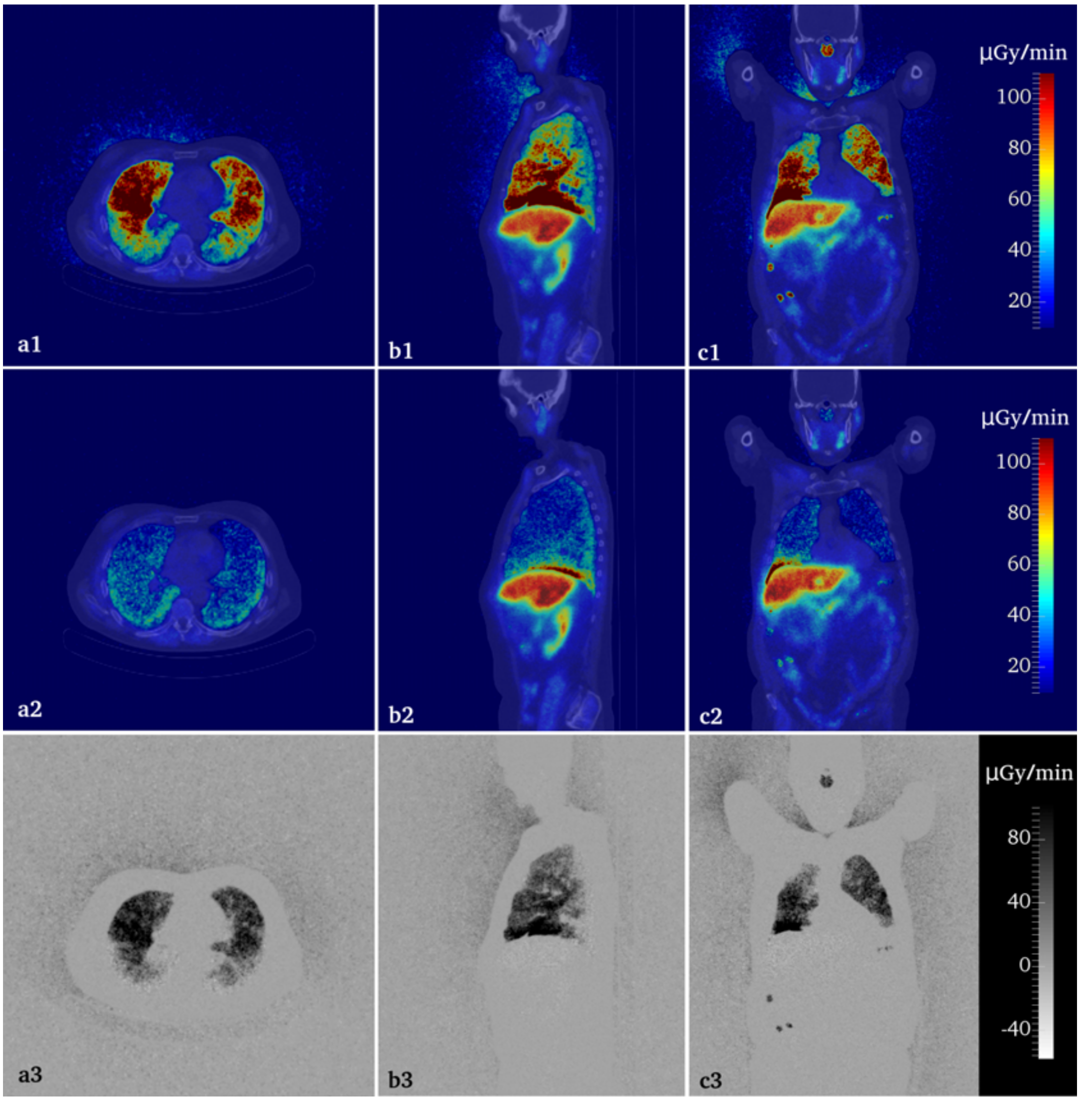

FIGURE 3.9: Axial, sagittal and coronal slices of the absorbed dose rate maps (fused with CT) estimated with GATE using native PET (a1, b1, c1) and filtered PET (a2, b2, c2), and the corresponding slices obtained by subtraction of the filtered-PET absorbed dose map from the native-PET one (a3, b3, c3).

3.8 Discussion

3.8.1 GATE-GAMOS comparison

The larger differences between absorbed dose rates in lungs calculated with GATE and GAMOS using native PET compared to the ones found in liver, are mainly attributable to the different density-assignment procedure employed by the two toolkits. This different assignment, as it can be reasonably expected, appears to have more impact for low density voxels, as in lungs, causing wider differences in their corresponding absorbed dose outcomes with respect to more dense voxels, as in liver. Moreover, lungs are heterogeneous districts, with densities of contiguous voxels that on average vary more than in liver, which usually is a fairly homogeneous organ.
In addition, in evaluating the significance of absorbed dose rate differences in lungs,

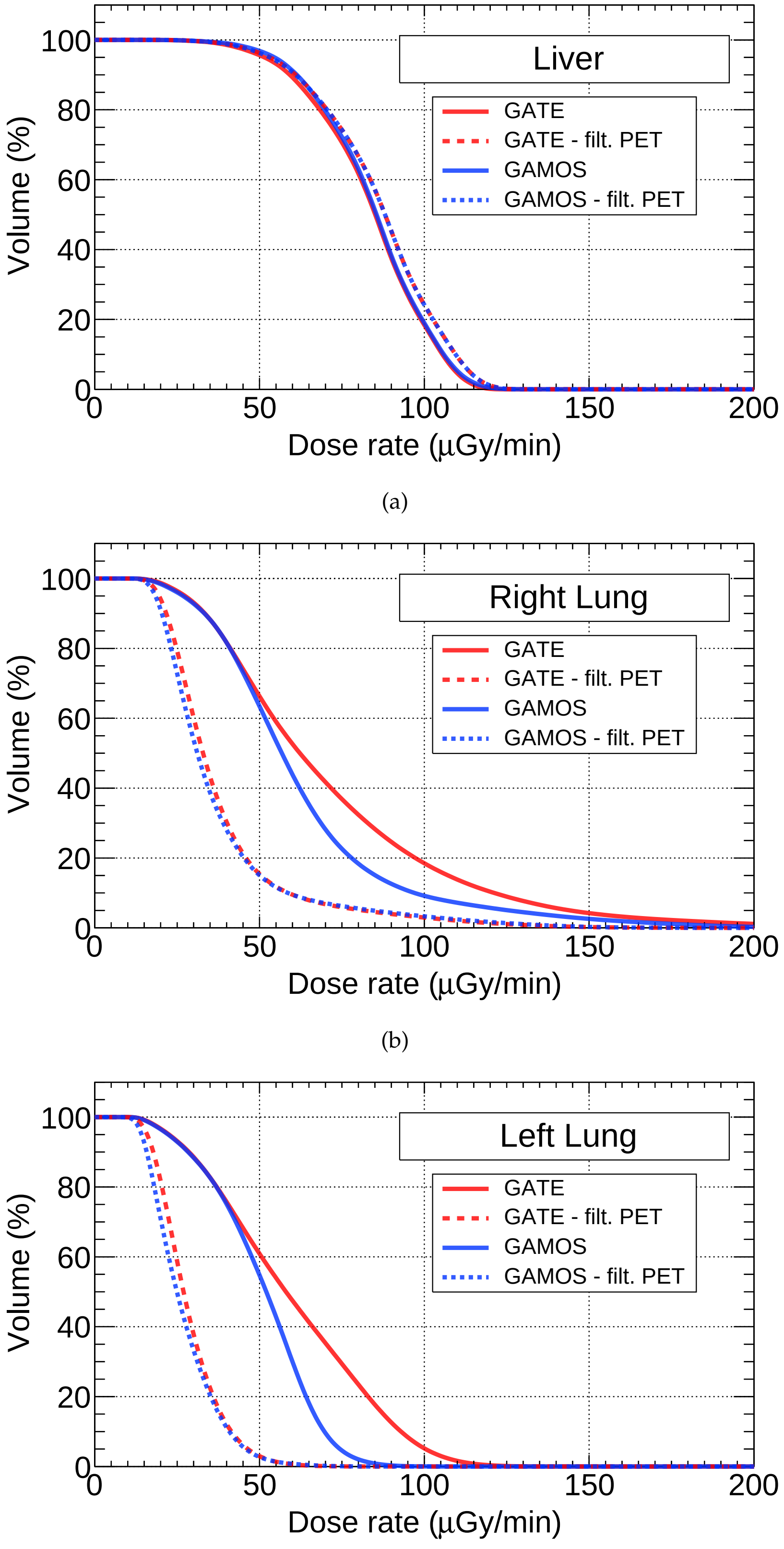

(a)

(b)

(c)

FIGURE 3.10: DRVHs in liver (a), right lung (b) and left lung (c) VOIs, obtained with native-PET (solid lines) and filtered-PET (dotted lines) simulations.

it has to be taken into account the entity of their respective statistical uncertainties at voxel level, with $\langle\sigma^{ijk}\rangle$ values in lungs about three times higher than in liver. Considering that lungs show lower ^{18}F-choline uptake and have lower density than liver, for a given number of total simulated histories, absorbed doses scored in lungs voxels will always exhibit larger statistical uncertainties than absorbed doses scored in liver, because of the smaller interaction probabilities in lungs voxels, and consequently the lower number of interactions happening within them. As a consequence of the described aspects, the poorer agreement between GATE and GAMOS lungs results could be partially enhanced by such uncertainties.

The agreement within 3% in right lung and within 6% in left lung emerging from the comparison of GATE and GAMOS filtered-PET average absorbed dose rate results (ε in Table 3.5), together with the closer agreement at voxel level for filtered-PET results showed by DRVHs (Fig. 3.10(b) and (c)), supports the previously presented supposition that the differences between GATE and GAMOS native-PET results could be due to the different density-assignment procedures, having a stronger effect on low-density voxels. The minimization of decay event generation in air-related low density voxels, obtained with the PET filtering, in fact causes a reduction of the contribution of low density voxels to the absorbed dose rate; their "exclusion" in the input filtered PET brings GATE and GAMOS results to find closer agreement.

Concerning liver, GATE and GAMOS results, both in terms of average absorbed dose rates and DVRHs, show excellent agreement irrespective of the use of native or filtered PET, in agreement with the hypothesis that higher-density voxels are less influenced by differences in the density-assignment procedures.

Summarizing, GATE and GAMOS showed to provide essentially equal results for soft tissue, as in liver, in the case of ^{18}F-choline PET dosimetry simulations, and that consequently they are expected to be usable equivalently for liver dosimetry for this kind of procedure; in fact, there is no specific aspect that suggests either of them to be better than the other, being both their slightly different density-assignment procedures robustly based on a documented HU-density conversion. In the case of lungs dosimetry, the mentioned difference can instead lead to discrepancies between the results of the two toolkits, but such discrepancies strongly reduce adopting PET-filtering procedures, which are advisable not only for this aspect, but especially for a more realistic setting of the simulations, as it will be commented in the following section.

3.8.2 PET background noise effects

Observing the native-PET simulations absorbed dose rate maps in panels (a) and (b) of Fig. 3.7 and panels (a1), (b1) and (c1) of Fig. 3.9, it is noticeable a certain amount of background absorbed dose rate present outside the patient body. It is reasonably partly due to the interactions of the annihilation photons with the air and other eventual materials outside the patient. However, given the results of PET-filtered simulations (panels (c) and (d) of Fig. 3.7 and panels (a2), (b2) and (c2) of Fig. 3.9), in which, removing the decay probability in air regions, the absorbed dose rates outside the body almost goes to zero, it must be concluded that the absorbed dose rate background is partly due also to the ^{18}F decays generated outside the patient's body because of noise-induced non-zero activity concentration outside the body in the native-PET data.

From the above mentioned figures, in the case of native-PET simulations, high absorbed dose rate distributions and spots are visible in correspondence of the following air-rich areas inside patient's body: oro-nasal cavity, larynx, trachea, esophagus, stomach and intestinal tracts, and especially lungs. Given the reported evidences, it can be hypothesized that decays generated "erroneously" in air regions, both outside and inside the computational phantom reproducing the patient's body, influence the absorbed dose rate evaluation, possibly causing absorbed dose artifacts and overestimation in certain anatomical regions. This appears in particular in lungs, with the 40-50% decrease of average absorbed dose rate when using filtered PET, for both GATE and GAMOS. It can be excluded that these differences would be merely imputable to statistical fluctuations, since their magnitude largely exceeds the - albeit significant - average standard deviation of the mean absorbed dose rates $\langle \sigma^{ijk} \rangle$, which can be thought as the maximum statistical uncertainty for the average absorbed dose rate values.

Always from Fig. 3.7 and Fig. 3.9, it can be seen that in the filtered-PET absorbed dose rate maps, despite an almost general decrease in the right lung with respect to native-PET maps, in the lower part of the organ an high absorbed dose rate distribution remains. Part of it is reasonably and realistically caused by the energy deposition coming from decays generated in the simulation in the perfused lower lung itself and in the contiguous perfused liver. At the same time, another part is likely caused by decays generated in the simulation in the lower part of the right lung because of event decay probability actually due to liver activity accidentally measured in the lower lung, as a consequence of the respiratory motion during the PET acquisition [118]. This blurring of the liver activity in the native PET can be seen in Fig. 3.3(b) and a little better in panel (c) with CT fused. From the absorbed dose maps obtained with filtered-PET emerges how the adopted filtering procedure was unable to correct for this kind of artifact.

Concerning the previously mentioned slight increase of liver absorbed dose rate in filtered-PET simulations with respect to native-PET ones, its cause is identifiable in the reduction of decay generation in air-associated areas produced by the filter that, being equal the number of generated histories in the two types of simulations, consequently enhances the number of decays in all the other non-zero activity areas. Therefore it can be deduced that realistically the PET background noise, in absence of filtering, can lead to underestimate a bit the liver absorbed dose rate.

Overall, from the obtained results it can be concluded that the native-PET simulations generate a significant amount of decays in the air inside lungs and some other anatomical districts, enough to cause a non-negligible overestimation of absorbed dose rate with respect to the filtered-PET simulations. Well designed filtering procedures of PET scans, and in general of functional scans used as input for MC simulations, could enable to reproduce more realistically the actual radionuclide distribution and improve the dosimetric assessment for organs like lungs, with a substantial presence of air inside them, by reducing the contribution of decays improperly simulated in non-perfused regions.

Chapter 4

^{90}Y-TARE Monte Carlo internal dosimetry: optimization of GATE simulation times

4.1 Introduction

In this Chapter will be presented a study concerning patient-specific voxel-level dosimetry for ^{90}Y Trans-Arterial Radio-Embolization (TARE), carried out though direct MC simulations implemented on GATE. The main focus of the study was to try optimizing simulation times by varying two parameters: the range cuts on the production of secondary particles, and the CT scan resolution, varied by resampling the 3D images. Employing as starting data the patient's pre-therapy CT and ^{99m}Tc-SPECT, simulations were carried out examining multiple CT resamplings, characterized by voxel volumes approximately equal to 2, 8, and 64 times the native one, and also a resampling with the SPECT resolution and dimensions; for each of them, different production cuts were set (0.01 mm, 0.05 mm, 0.1 mm, 0.5 mm and some more, specific for each resampling). It was observed that by increasing the cut length and in parallel reducing CT resolution, an early rapid decrease of simulation time followed by a late slow decrease as a function of this two parameters is obtained, with a maximum reduction up to the 30% of the reference simulation time, referred to the simulation using the most precise cut, of 0.01 mm, and the native CT resolution. Absorbed doses in liver, liver sections, lungs and kidneys were compared, and it emerged that the time saving is in general obtained preserving acceptable dosimetric accuracy, especially considering the estimates in liver-related volumes of interest (VOIs), which by the way are the perfused regions in TAREs. The best combination of settings among the examined ones resulted the choice of the CT resampling with 8 times the native voxel volume and a range cut of 0.1-0.5 mm, which ensured an agreement with reference results within 1% in liver-related VOIs, while reducing the simulation time to the 45% of the reference.

4.2 Trans-Arterial Radio-Embolization (TARE) of HepatoCellular Carcinoma (HCC)

HepatoCellular Carcinoma (HCC) is the most frequent primary liver cancer and the third responsible of worldwide cancer-related deaths, with more than 700 thousand annual deaths reported [119, 120]. Most often HCC patients are not surgically operable because of the extent of the lesions and/or the underlying cirrhosis. Therefore systemic chemotherapy with *sorafenib* has established as the conventional therapy for advanced HCC, while Trans-Arterial Chemo-Embolization (TACE) with the same pharmaceutical is recommended for the intermediate HCC stage [120]. However the tolerability to *sorafenib* therapies has shown sub-optimal results in some cases, a situation that opened the way to new therapies for the management of HCC, for example the combination of *bevacizumab* with *atezolizumab*, which showed a significant improvement of survival and is expected to become the new chemotherapy standard of care for this carcinoma [121].

In parallel, in the last two decades Trans-Arterial Radio-Embolization (TARE) - also referred to as Selective Internal Radiation Therapy (SIRT) - has given promising results in the treatment of HCC in intermediate or advanced stage, as well as for other liver malignancies such as intra-hepatic cholangiocarcinoma and liver metastasis from other cancers, with favourable outcomes in comparison to the conventional treatments both in terms of disease control and tolerability profile [122–124]. TARE consists in the selective intra-arterial administration of glass microspheres (TheraSphere©, Boston Scientific, Marlborough, MA, USA) or resin microspheres (SIR-Sphere©, Sirtex Medical, Australia) loaded with a radioactive compound, usually containing ^{90}Y [119]. The microspheres are injected through a catheter directly into the hepatic artery - eventually up to one of its branches that supplies the tumor masses, as depicted in Fig. 4.1 -, and embolize the capillaries in which they deposit; being a permanent implant, they settle definitively there and guarantee a radionuclide distribution fixed in time, that will provide the therapeutic effect by locally irradiating the surrounding pathologic tissue. In fact ^{90}Y is an high-energy β^--emitting isotope with no primary gamma emission, whose betas have a maximum range in tissue of about 11 mm and a mean range of 2.5 mm. With an half-life of $T_{\frac{1}{2}} = 64.05$ hours, ^{90}Y decays with Branching Ratio of 100 % through the following reaction [111]:

$$^{90}_{39}\mathrm{Y} \rightarrow {}^{90\mathrm{m}}_{40}\mathrm{Zr} + \beta^- + \bar{\nu} \tag{4.1}$$

where $\bar{\nu}$ indicates the electronic antineutrino. In Fig. 4.2 is reported the beta-emission spectrum of ^{90}Y, characterized by an average emission energy $\langle E_{\beta^-} \rangle$ = 932.40 keV and an end-point $E_{\beta^- max}$ = 2278.5 keV [111].

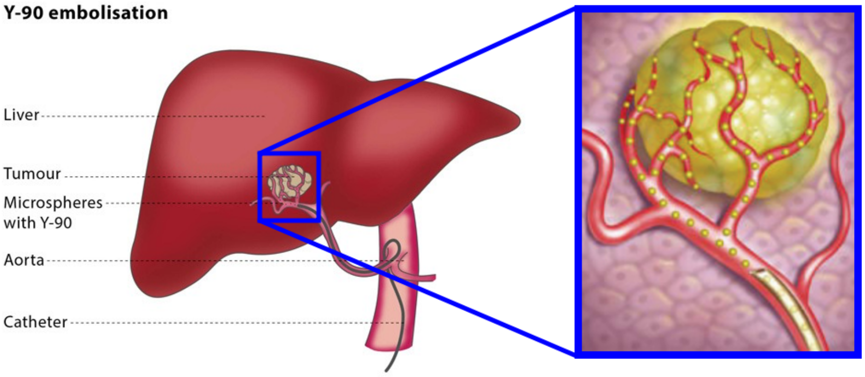

FIGURE 4.1: Schematic graphical representation of a TARE treatment, with detail, on the right, of the injection of microspheres that deposit into the capillaries supplying the tumour.

TARE therapies are preceded by a pre-treatment phase consisting in the intra-arterial injection under angiographic guidance of $^{99\mathrm{m}}$Tc Macro-Aggregated Albumin (Tc-MAA), delivered by placing the catheter in the same position as planned for the therapeutic administration of microspheres [119, 121]. Microspheres and MAA have

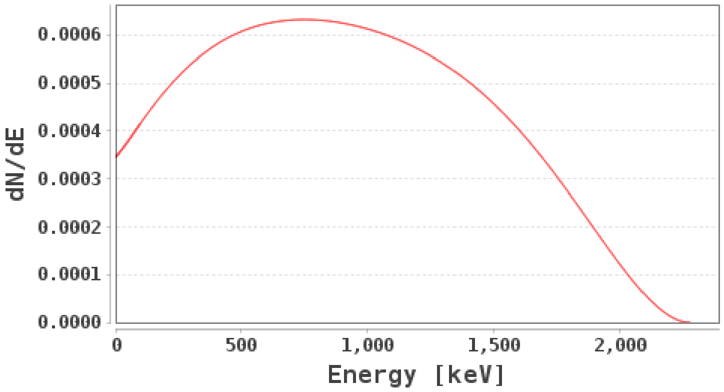

FIGURE 4.2: Beta-emission energy spectrum of ^{90}Y [111].

shown comparable biodistributions in retrospective studies including TARE post-therapy ^{90}Y-bremsstrahlung SPECT or ^{90}Y PET, thus radio-labelled MAA is used to predict the microspheres biodistribution in view of TARE [123]. The Tc-MAA administration enables a liver perfusion scintigraphy by means of planar imaging or, preferably, SPECT acquisitions, given that ^{99m}Tc is a gamma emitting isomer, de-exciting from its metastable state to its ground state with an half-life of 6.0072 hours by emitting gammas of 140.511 keV, with Branching Ratio of 89 % (and of 142.6836 keV with much smaller B.R.) [111]. These gamma radiations are suitable to be detected by a gamma camera and consequently ^{99m}Tc is used as a radioactive tracer for medical imaging.

The aforementioned Tc-MAA pre-therapy diagnostic imaging is executed for a meticulous selection of eligible patients, to exclude the ones with absolute contraindication to TARE, such as those showing significant lung shunts or gastrointestinal leakage [123]; in addition, as anticipated, they serve to correctly plan the microspheres injection procedure, in order to reduce the incidence of complications [119].

Quantitative Tc-MAA SPECT/CT imaging moreover opens the way for predictive internal dosimetry, including three-dimensional voxel-level dosimetry, that can be used to optimize the amount of activity to be administered on the basis of patient-specific pre-therapy data [121, 123, 124]. The most recent studies have described with favourable outcomes the aim of targeting HCC lesions with an absorbed dose larger than 205 Gy [121].

4.3 Aim of the study

Growing interest is recently arising in the use of three-dimensional internal dosimetry for the optimization of TARE therapy of HCC, particularly in retrospective studies taking advantage of the Monte Carlo (MC) method [48, 124, 125]. As explained in Sec. 1.6.2, direct MC simulation employing patient-specific functional and anatomic imaging as input data is the gold standard approach for internal dosimetry, but presents the drawback of requiring longer computational times with respect to the other dosimetric approaches, resulting in a limiting factor especially when dealing with voxelized geometries [33, 76, 77]. In the work presented in this Chapter the focus was put on trying to shorten the simulation time without loosing much dosimetric accuracy in voxelized MC internal dosimetry of ^{90}Y-loaded glass microspheres

TARE carried out from pre-therapy ^{99m}Tc-MAA SPECT and CT data. For this purpose, multiple simulations with different cuts on the production of secondary particles and different resolutions of the input CT images were carried out. The effect on dosimetric accuracy and on computational time produced by these two varying "parameters" was investigated, in order to find combinations of settings optimizing the computational time.

4.4 Simulations implementation

4.4.1 Input data

The pre-therapy tomographic images of a patient suffering from HCC enrolled for ^{90}Y-loaded glass microspheres TARE (and subsequently actually treated) were used as the starting data for the dosimetric study. They consisted of an abdominal contrast-enhanced CT scan, which is done in clinics for lesions localization, and an abdominal ^{99m}Tc-MAA SPECT, for the prediction of the therapeutic distribution of the ^{90}Y-microspheres and to identify eventual pulmonary shunts, that could lead to the ineligibility of the patient for this treatment.
The CT scan was performed with a Siemens SOMATOM Definition AS [1] and had a resolution of 512×512×146 voxels, with voxel dimensions of 0.89×0.89×2.0 mm^3. The SPECT scan was executed with a Philips BrightView Dual Head gamma camera SPECT system [2] and had a resolution of 128×128×105 voxels, with voxel dimensions of 4.66×4.66×4.66 mm^3. Axial views of the native CT (N from now on, for simplicity) and of the SPECT are shown in Figure 4.3(a) and (f) respectively.

4.4.2 CT resamplings

Resamplings of the N CT image characterized by different resolutions were performed using 3D Slicer [107, 114]. First of all resamplings leaving unchanged the overall volume of the N CT image were performed, characterized by voxel volume multiple by factors approximately equal to 2, 8 and 64 with respect to the N CT voxel; we will hereafter refer to them as R2, R8 and R64 respectively. In order to obtain them, 3D Slicer's *Resample Scalar Volume* module was used, adopting Lanczos interpolation [114, 126]. Secondly, a resampling of the CT having the same resolution, voxel volume and overall volume as the SPECT scan was produced with the *Resample Image (BRAINS)* module using also in this case Lanczos interpolation, and we will refer to it as RS in the following. Axial views of the various resamplings are shown in Figure 4.3, while in Table 4.1 are summarized the resolutions and voxel dimensions of all the resampled CTs.

4.4.3 VOIs segmentations

Segmentations were performed with the help of the *Segment Editor* module of 3D Slicer, defining VOIs corresponding to the following organs or organ regions: liver, lesions, liver perfused, healthy liver, healthy liver perfused, right and left kidney,

---

[1] `https://www.siemens-healthineers.com/it/computed-tomography/single-source-ct/somatom-definition-as#:~:text=SOMATOM%20Definition%20AS%20con%20gantry%20scorrevole%20consente%20un%20imaging%20TC,all'interno%20della%20sala%20operatoria.`

[2] `https://incenter.medical.philips.com/doclib/enc/10117823/452296296931_LR.pdf%3Ffunc%3Ddoc.Fetch%26nodeid%3D10117823`

TABLE 4.1: Resolution and voxel dimensions of the CT resamplings (R), compared to native (N) CT in terms of voxel volume ratio v_R/v_N.

CT name	v_R/v_N	Resolution	Voxel dimensions (mm^3)
N		512×512×146	0.89×0.89×2.00
R2	2.4	384×384×110	1.19×1.19×2.65
R8	8.0	256×256×73	1.79×1.79×4.00
R64	64.9	128×128×36	3.58×3.58×8.11
RS	63.4	128×128×105	4.66×4.66×4.66

visible parts of right and left lungs in the field of view of the CT (that will be referred to as simply right lung and left lung in the following). Liver (Li.), lesions (Le.) and kidneys (R.K., L.K.) were manually segmented on the native CT; lungs (R.L., L.L.) were segmented on native CT using a thresholding method; liver perfused (Li.P.) was segmented on the SPECT using a thresholding method; healthy liver (H.Li.) was obtained as volume subtraction of lesions from liver; healthy liver perfused (H.Li.P.) as volume subtraction of lesions from liver perfused. 2D Sections and 3D representations of all the VOIs are shown in Figure 4.4.

Liver-related VOIs are obviously of interest in TARE, since liver is the perfused organ. Lungs, especially the right lung, can receive a non-negligible amounts of absorbed dose in case of liver lesions located near them. Right kidney could in principle receive some absorbed dose, being near to the liver, but high values are not expected, and least of all in the left kidney; kidney VOIs were defined mainly to observe the dosimetric differences introduced by the different settings employed in this study in non-perfused regions.

4.4.4 Phantoms, source definition and other settings

Native and resampled CT images and the SPECT image were used as input data for GATE MC simulations, employing GATE version 9.0 [104] relying on GEANT4 version 10.05.p01.

The CTs have been imported into GATE to model voxelized phantoms reproducing patient's body morphology. The *Automated HU stoichiometric calibration* tool was employed to assign materials and densities to the voxels of the phantoms, in the same way as described in Sec. 3.4.4, and setting a density tolerance of 0.01 g/cm^3 for building the density intervals; the same Hounsfield Units intervals, materials and HU-density bi-linear calibration relation specified in Sec. 3.4.4 were used, reported in Tab. 3.2, Tab. 3.3 and Fig. 3.5.

The SPECT scan was imported into GATE to define a voxelized source reproducing the radionuclide spatial distribution, associating to each SPECT voxel a decay event probability through linear normalized conversion of its value, as explained more in detail in Sec. 3.4.5.

^{90}Y nuclei at rest were set as primary radiation, treating them as an ion type source and activating their decay with the *G4RadioactiveDecay* module; the physics models used to simulate the interactions of ^{90}Y daughters with phantoms' materials are the ones of the *G4EmStandardPhysics_option3* physics list.

For each simulation performed, the absorbed doses at voxel level D_{out}^{ijk} and their respective statistical uncertainties δ^{ijk} (intended as standard deviation of the mean evaluated over the number of primary histories, as described in Sec. 3.4.7 and in

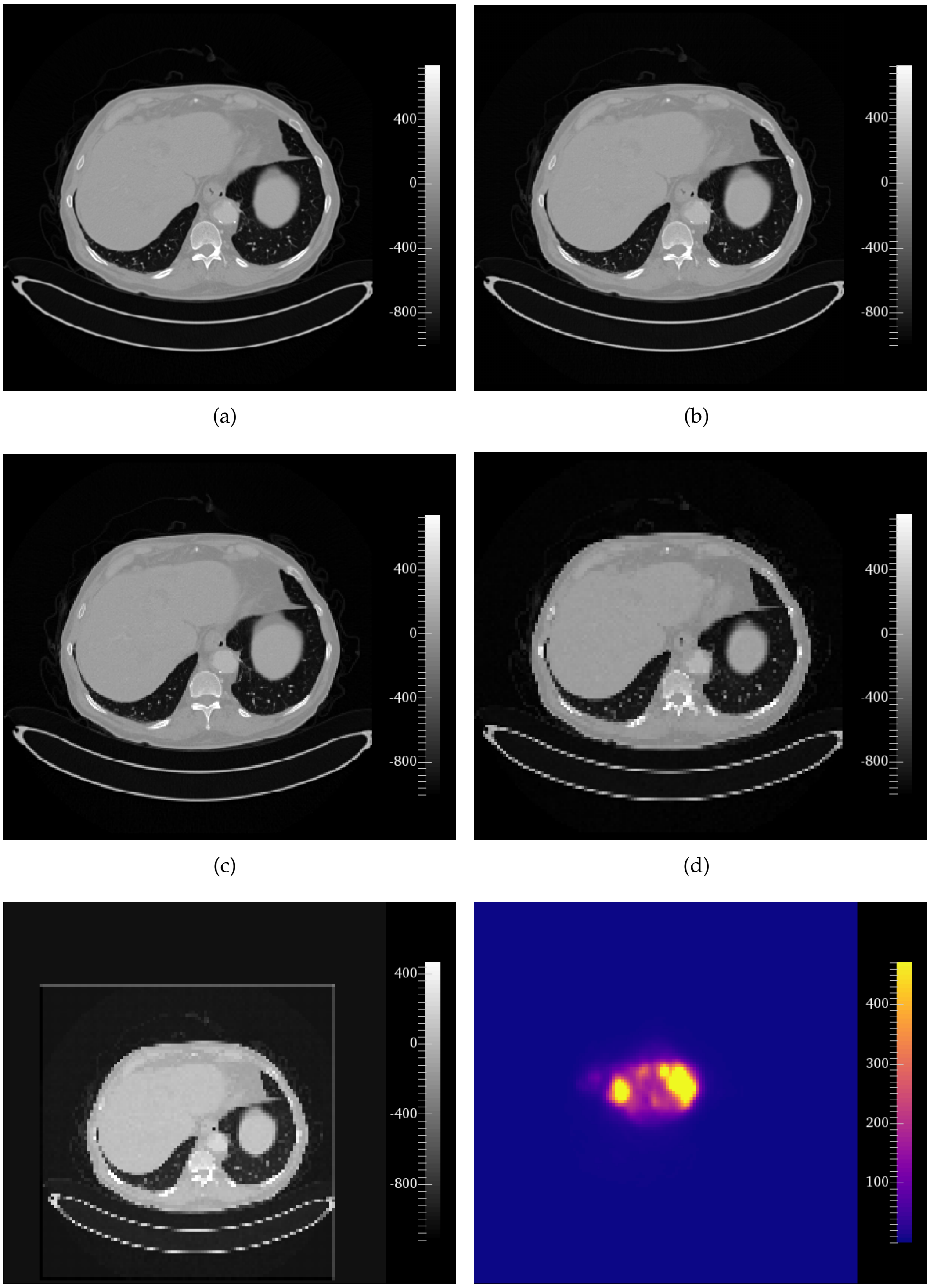
400
0
-400
-800
400
0
-400
-800
400
0
-400
-800
400
0
-400
-800
400
0
-400
-800
400
300
200
100

(a) (b)

(c) (d)

(e) (f)

FIGURE 4.3: Axial views of the native CT (a), of the various resampled CTs - R2 (b), R8 (c), R64 (d), RS (e) -, and of the Tc-MAA SPECT (f). All the images have no graphical smoothing of the actual slice pixels, in order to appreciate as much as possible the different resolutions.

[117]) were scored with GATE's *DoseActor*, employing the *MassWeighting* algorithm as setting scoring grid dimensions and resolutions equal to the ones of the phantom

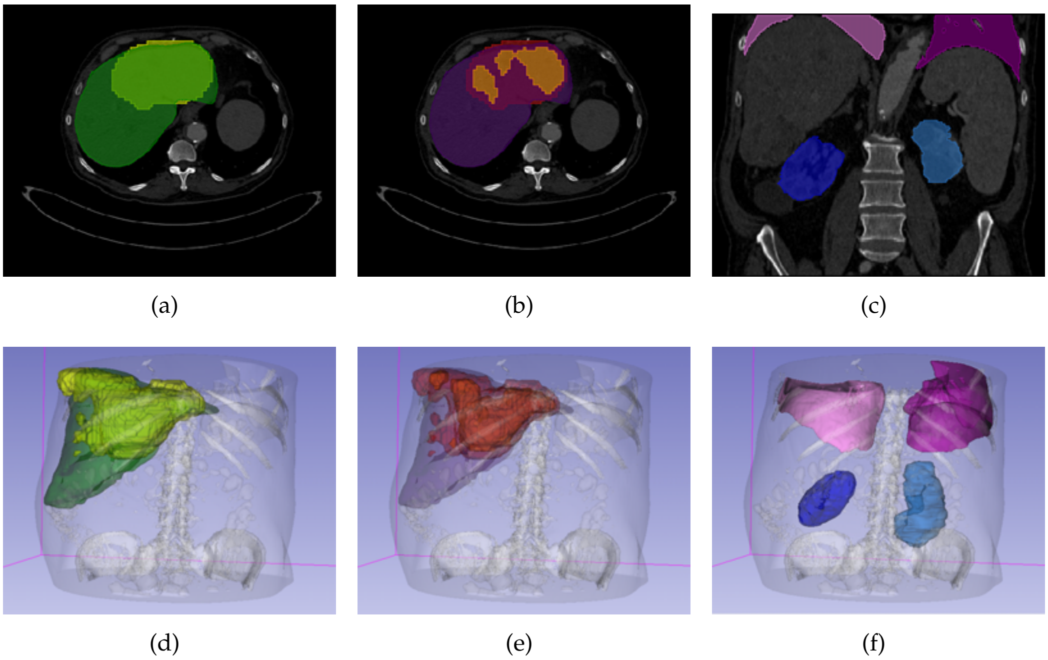

FIGURE 4.4: Representation of the defined VOIs on axial (a,b) and coronal (c) native CT slices and in 3D view (d, e, f). The color-VOI key is: green = liver, yellow = liver perfused, orange = lesions, red = healthy liver perfused, violet = healthy liver, pink = right lung, magenta = left lung, blue = right kidney, light blue = left kidney.

used in each specific simulation.
$2 \cdot 10^8$ was set as the number of primary events (N_{evts}) in all the simulations, a value which ensured an average value of standard deviation of the mean absorbed dose $\langle \delta^{ijk} \rangle$ below 3% in lesions, below 4% in liver perfused and below 5% in healthy liver perfused, when using native CT to build the patient's phantom.
The simulations were run on a computer equipped with Intel(R) Xeon(R) CPU E5-2620 v4 @ 2.10GHz processors, with each simulation run individually in a single CPU and without other processes running at the same time, in order to have the same CPU and RAM conditions for all of them. Simulation times were registered for each simulation in terms of the GATE variable *ElapsedTimeWoInit*.

4.4.5 Production cuts

In GEANT4 (and consequently in GATE) charged particles by default could be tracked until the end of their path, but if all the secondary particles were tracked infrared divergence would occur, since the differential cross sections of delta-electron production and bremsstrahlung rapidly grow when the energy of secondary particles decreases. This would result in poor CPU performances of the MC code in tracking all the secondary particles until they stop. The traditional solution to avoid that inconvenience is the use of *production cuts* for electrons, positrons, gammas (and protons if present), setting thresholds below which the production of further secondary particles is disabled and the residual energy is deposited locally [96, 115, 127]. The threshold cuts are set in terms of *range cuts*, thus they are given to the code as length dimensions, in order to use a coherent policy for different particles and materials. In a simulation run, at the beginning of the initialization of GEANT4 physics, these range cut values are internally converted into threshold energies for each material

and for each particle type. The definition of a certain value of range cut can be thought as a requirement for the degree of accuracy of the spatial distribution of energy (and consequently of absorbed dose) deposition and its sampling.
In this study several simulations were performed for each phantom, adopting different values of production cuts on secondary particles production from electrons, positrons and photons: 0.01 mm, 0.05 mm, 0.1 mm, 0.5 mm. These values are smaller or even much smaller than the voxel dimensions for all the phantoms obtained from the different resampling resolutions; this in principle ensures an accurate spatial energy sampling for all the cases. In addition, simulations were performed adopting range cuts of the order of voxel axial dimensions for each resampling, namely: 1.0 mm for N, 1.5 mm for R2, 2.0 mm for R8, 4.0 mm for R64 and RS. These wider cuts were set to investigate the effect on dosimetric outcomes of using range cuts producing, in principle, low spatial sampling accuracy. All the described production range cuts applied for the various resamplings of CT are summarized in Table 4.2, which thus represents all the combinations of settings adopted for the simulations of this study.

TABLE 4.2: Production range cuts on secondary particles produced for e^-, e^+ and photons set in the simulations in correspondence of the different resamplings of the CT.

Production cut (mm)	**CT**				
	N	R2	R8	R64	RS
0.01	✓	✓	✓	✓	✓
0.05	✓	✓	✓	✓	✓
0.1	✓	✓	✓	✓	✓
0.5	✓	✓	✓	✓	✓
1.0	✓				
1.5		✓			
2.0			✓		
4.0				✓	✓

4.5 Dosimetric calculations and comparisons

To deduce the correct 3D absorbed dose values D^{ijk}, the values of absorbed doses obtained as output from the GATE simulations were divided for the number of primary events simulated, N_{evts}, and multiplied for the cumulated activity, $\tilde{A}$:

$$D^{ijk} = \frac{D^{ijk}_{\text{out}}}{N_{evts}} \cdot \tilde{A} \tag{4.2}$$

$\tilde{A}$ was calculated analytically in the reasonable assumptions, for TARE treatments, of instantaneous uptake and of mono-exponential physical decay only, due to the absence of biological clearance:

$$\tilde{A} = A(0) \int_0^{\infty} e^{-t/\tau_{^{90}Y}} dt = A(0) \cdot \tau_{^{90}Y} \tag{4.3}$$

where $\tau_{^{90}\mathrm{Y}}$ is the exponential time constant of ^{90}Y ($\simeq$ 332916 s) and $A(0) = 2.49$ GBq is the actual administered activity to the patient in the TARE treatment he/she underwent.
With the help of 3D Slicer, average absorbed doses within the defined VOIs, $\langle D \rangle_{VOI}$, were evaluated with the *Segment Statistics* module, and Dose Volume Histograms (DVHs) within VOIs were evaluated using the *Dose Volume Histogram* module. When the resolution of a VOI's segmentation is different from the resolution of the absorbed dose map on which *Segment Statistics* are to be evaluated, 3D Slicer performs an automated adaptation via zero-order interpolation of the segment voxels to the image on which they are applied for calculations. The volumes of all the employed VOIs, adapted by 3D Slicer depending on the absorbed dose rate maps on which were applied (corresponding to the CTs in dimensions and resolution), are reported in Table 4.3.

TABLE 4.3: VOI volumes (cm^3) for each absorbed dose CT resampling (and thus for each corresponding absorbed dose map).

VOI	Li.	Le.	Li.P.	H.Li.	H.Li.P.	R.K.	L.K.	R.L.	L.L.
CT									
N	2770.2	359.5	892.6	2416.0	533.1	198.9	262.7	404.8	652.4
R2	2773.7	360.7	893.5	2418.7	532.8	197.9	262.8	400.9	647.7
R8	2770.2	359.5	892.6	2416.0	533.1	198.8	262.7	404.9	652.4
R64	2735.1	356.0	883.4	2383.1	527.4	201.8	262.5	377.6	627.9
RS	2767.9	358.5	893.1	2415.1	534.7	198.5	262.4	408.9	654.5

Each $\langle D \rangle_{VOI}$ was calculated averaging the absorbed doses in each voxel of the considered VOI over the number of voxels composing the VOI, N_{VOI}^{vox}:

$$\langle D \rangle_{VOI} = \frac{1}{N_{VOI}^{vox}} \sum_{i,j,k \in VOI} D^{ijk} \tag{4.4}$$

For each average absorbed dose evaluated, the average value of standard deviation of the mean absorbed dose $\langle \delta \rangle_{VOI}$ for the voxels within the considered VOI was also calculated:

$$\langle \delta \rangle_{VOI} = \frac{1}{N_{VOI}^{vox}} \sum_{i,j,k \in VOI} \delta^{ijk} \tag{4.5}$$

In addition, the average of standard deviations of the mean absorbed dose in VOIs over the production cuts, i.e. averaging them between the simulations employing CTs with same resolution, was evaluated, and will be indicated as Δ_{VOI}:

$$\Delta_{VOI} = \frac{1}{N_C} \sum_{C} \langle \delta \rangle_{VOI,C} \tag{4.6}$$

where the C label indicates the specific production cut and N_C is the number of different production cuts for each CT resolution employed.
The average absorbed doses in VOIs for the various resamplings (Table 4.1) and production range cuts (Table 4.2) were compared in terms of relative percent differences

ε_{VOI} (%), taking the average absorbed doses obtained in the simulation using the native (N) CT phantom and the shortest cut (0.01 mm) as the reference $\left(\langle D\rangle_{VOI}^{ref}\right)$:

$$\varepsilon_{VOI} = 100 \cdot \frac{\langle D\rangle_{VOI} - \langle D\rangle_{VOI}^{ref}}{\langle D\rangle_{VOI}^{ref}} \tag{4.7}$$

Concerning DVHs in VOIs, bearing in mind that they are histograms whose bins represent the volume percentage (v) of a VOI receiving a certain amount of absorbed dose, each DVH was compared with the one obtained from the reference simulation (v_{ref}) in terms of relative per cent difference σ between volume percentages, evaluated "dose bin by dose bin":

$$\sigma = 100 \cdot \frac{v - v_{ref}}{v_{ref}} \tag{4.8}$$

Finally, the computation times of all the performed simulation were compared as ratios with respect to the computation time of the reference simulation.

4.6 Results

4.6.1 Average absorbed doses and DVHs

Axial views of the absorbed dose map obtained from the reference simulation - employing native CT and 0.01 mm production cut -, and from simulations using 0.01 mm production cut and all the other CT resamplings, are shown in Figure 4.5, each represented fused with its respective CT slice for morphological reference.

The average absorbed doses $\langle D\rangle_{VOI}$ calculated in the defined VOIs and their relative percent differences ε_{VOI} with respect to the reference simulation are reported in histogram form, for all the simulations performed, in Fig. 4.6 and Fig. 4.7, respectively referring to liver and to lungs and kidneys. $\langle D\rangle_{VOI}$s and ε_{VOI}s are also reported in tabular form in Tab. A.1-A.5 in Appendix A, including average standard deviation of mean absorbed doses $\langle\delta\rangle_{VOI}$s.

Average absorbed doses in all the five considered liver-related VOIs show an agreement with reference simulation within 1% in terms of ε_{VOI} for all the resamplings except for R64 (and RS in the case of healthy liver), and independently from the production cuts. In the case of R64 resampling, εs are within 6% for all liver VOIs independently from cuts. For RS resampling, $\langle D\rangle$s in healthy liver VOI show εs within 4% for all the cuts. Considering a fixed resampling, no appreciable differences in average absorbed doses are observed in liver-related VOIs varying the production cuts, even when using the largest cuts having dimensions comparable with the voxel's one (Sec. 4.4.5).

Average absorbed doses in lung VOIs exhibit agreement with reference within 5% for R2 and R8 resamplings and within 13% for R64 and RS resamplings, irrespective of production cuts. Average absorbed doses in kidney VOIs show εs within 4% for R64 resampling and within 2% for all the other resamplings, with only minimal differences when varying the productions cuts.

DVHs and relative percent differences σ with respect to the DVHs calculated for the reference simulation are reported in Figures A.1-A.12 of Appendix A. In liver-related VOIs, DVHs show an excellent agreement in a wide range of absorbed dose values, in general from 0 Gy to 200-300 Gy, depending on the resampling adopted. Fluctuations in σ affect on average only high absorbed dose values, corresponding

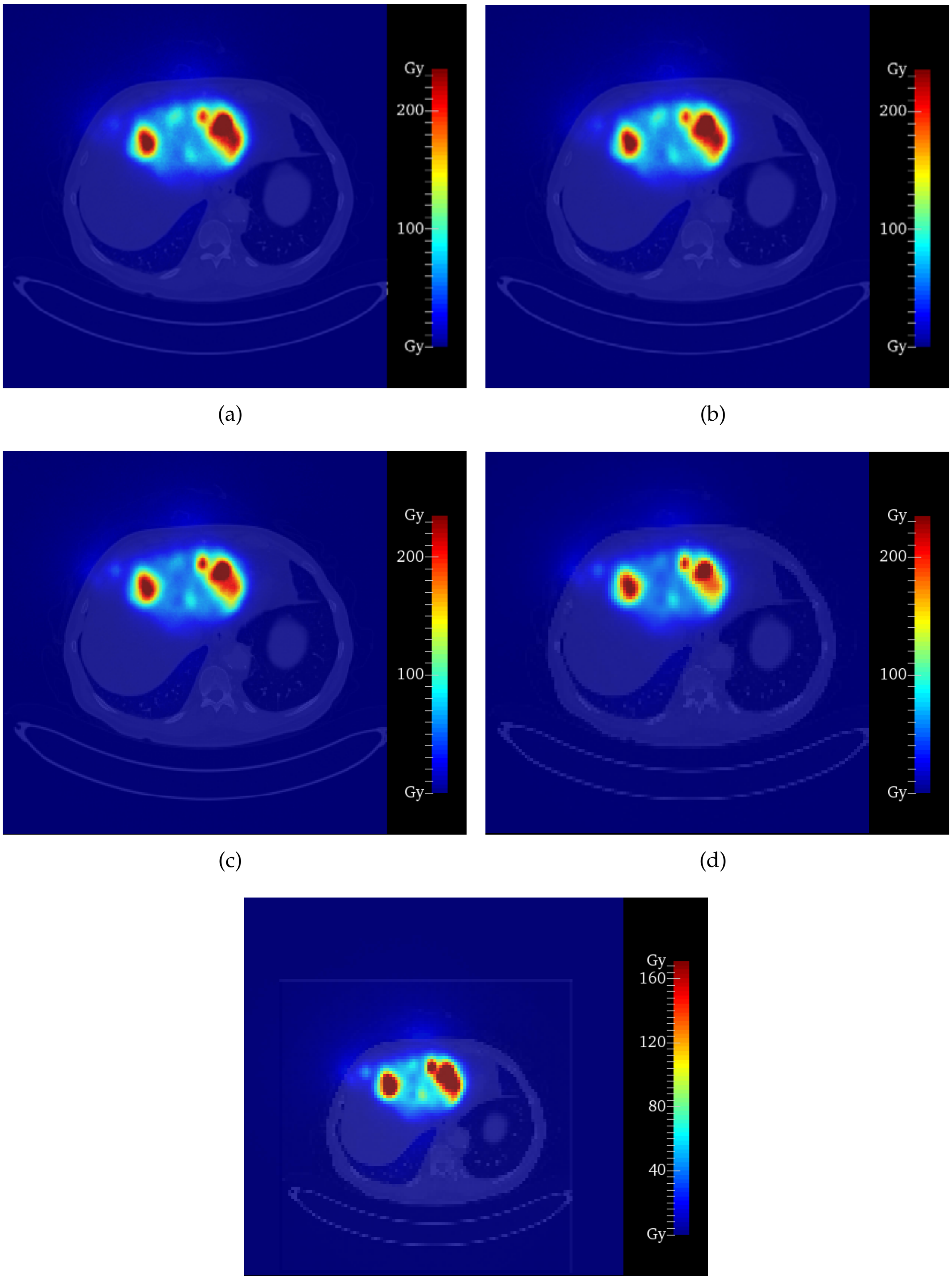
Gy
200
100
Gy
Gy
200
100
Gy
Gy
200
100
Gy
Gy
200
100
Gy
Gy
160
120
80
40
Gy

(a) (b) (c) (d) (e)

FIGURE 4.5: Axial slices of the fusion images of CTs and corresponding absorbed dose maps obtained from simulations setting 0.01 mm as production cut. The resamplings shown are: (a) N - the reference simulation -, (b) R2, (c) R8, (d) R64, (e) RS. No graphical smoothing was applied to appreciate as much as possible the different resolutions.

to volume percentages smaller than 1% and often close to exactly 0%; σ in healthy liver perfused VOI shows some fluctuations at lower absorbed dose values for R8,

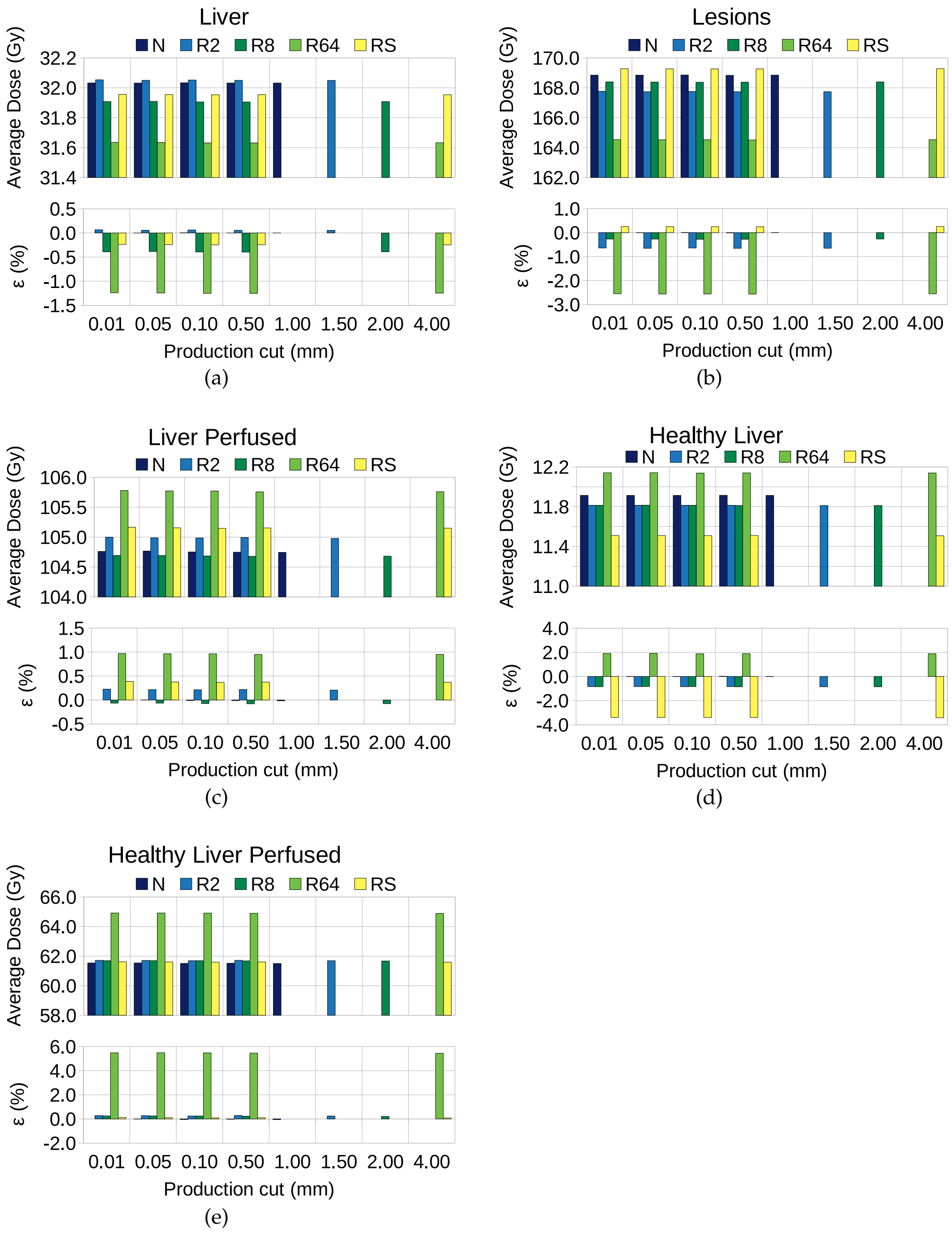

FIGURE 4.6: $\langle D \rangle_{VOI}$ and ε_{VOI} in liver-related VOIs, for all the production cuts and CT resampling volumes used (N, R2, R8, R64, RS, as indicated in Table 4.1, denoted with different colors).

R64 and RS resamplings. DVHs in lung and kidney VOIs show good agreement too, considering the absorbed dose intervals in which they assume significant volume percentage values, with fluctuations in σ starting to widen in correspondence of the lower part of the tails of DVHs. No noteworthy differences in DVHs and σs are observed among the different production cuts for a fixed CT resampling.

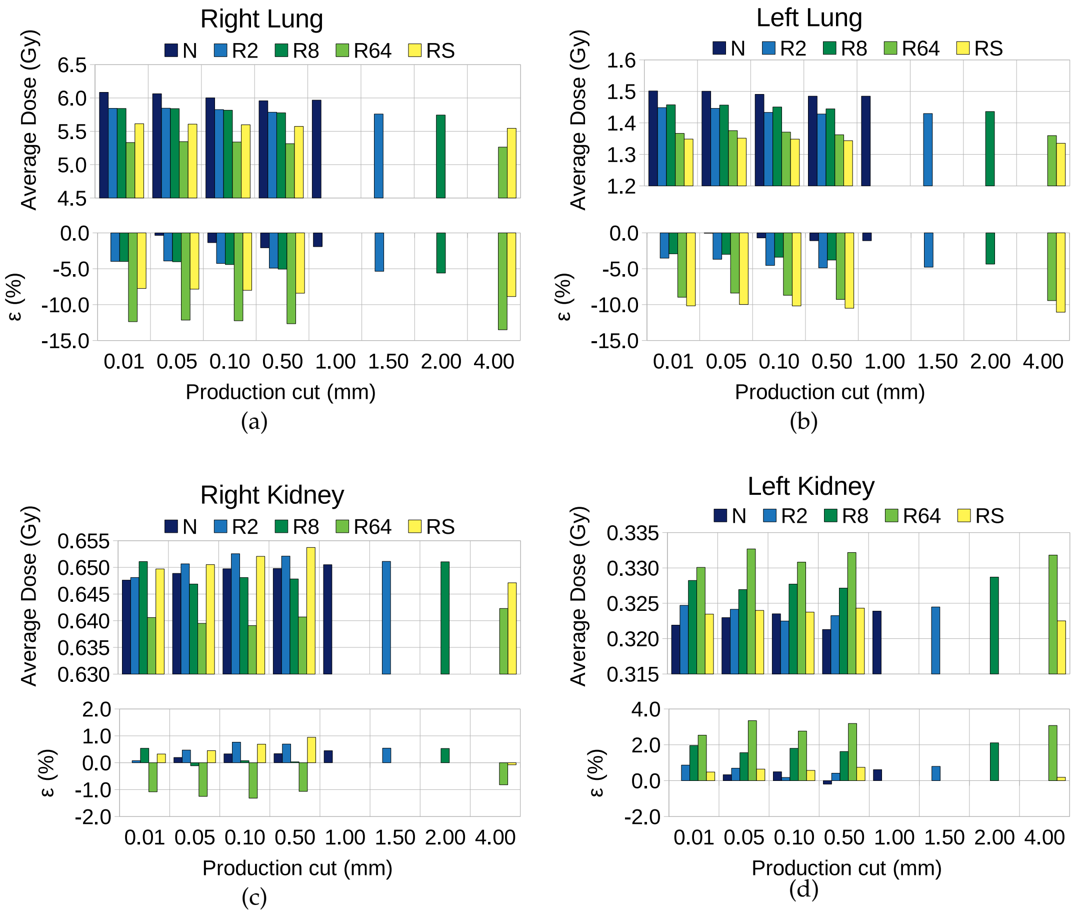

(a) (b) (c) (d)

FIGURE 4.7: $\langle D\rangle_{VOI}$ and ε_{VOI} in lungs- and kidneys-related VOIs, for all the production cuts and CT resampling volumes used (N, R2, R8, R64, RS, as indicated in Table 4.1, denoted with different colors).

4.6.2 Statistical uncertainties

Voxel-level average standard deviations of the mean absorbed dose ($\langle\delta\rangle_{VOI}$s in Tab. A.1-A.5 of Appendix A), considering a fixed resampling, do not show significant differences varying the production cuts. Instead, varying the resampling and consequently the voxel volumes, they rapidly decrease as voxel volume increases. This behaviour is understandable keeping in mind that δs are standard deviations of the mean evaluated on the number of primary events, and as a consequence, leaving equal the number of primary events but increasing the size of the volume in which absorbed doses are scored (in our case the voxels), more absorbed dose depositions are expected to be sampled in a single larger volume rather than in multiple smaller volumes. Therefore the estimate of the total absorbed dose sum or of the average absorbed dose in a larger volume tends to be accompanied by lower standard deviation with respect to the ones of the smaller volumes taken singularly.
In Figure 4.8 are shown Δ_{VOI} values (Eq. 4.6) for all the VOIs as a function of voxel volume ratio with respect to native CT. Δ_{VOI} values corresponding to the N CT and to the resamplings R2, R8 and R64, that conserve the overall volume of the CT image, exhibit a trend as a function of voxel volume ratio which is well described by a bi-exponential function of the form $f(x) = ae^{-bx} + ce^{-dx}$, with $x = \mathrm{v}_R/\mathrm{v}_N$ (Table 4.1) and a, b, c, d parameters. Δ_{VOI}s for the RS resampling, which has similar voxel

volume as the R64 resampling but different overall CT volume, do not differ much from R64 values, and consequently they neither depart from the described trend as a function of voxel volume ratio. It should be noted that the described decrease of uncertainty with increasing voxel volume concerns only statistical uncertainty of MC estimates, and the reported trends do not take into account systematic uncertainties coming from the resampling procedure applied on CT, whose evaluation is beyond the scope of this work.

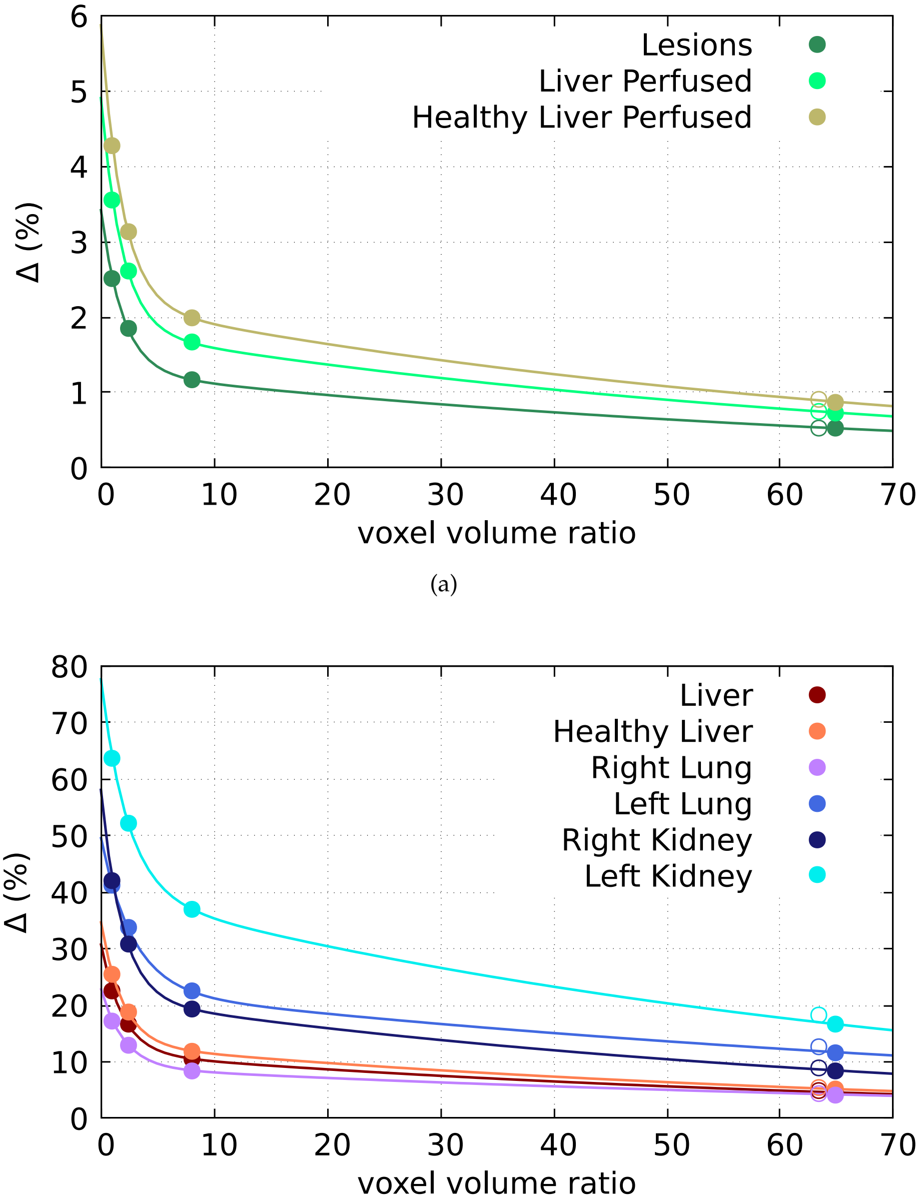

(a)

(b)

FIGURE 4.8: Δ_{VOI} values (Eq. 4.6) in VOIs as a function of voxel volume ratio with respect to N CT voxel volume. Full circles refer to simulations employing N, R2, R8 and R64 CTs, fitted with bi-exponential function; open circles refer to simulations employing RS CT, not considered in the fits but reported for completeness.

4.6.3 Simulation times

Last but not least, the behavior of simulation computation times for all the simulations is reported in Figure 4.9, in terms of simulation time ratios with respect to the reference simulation (which lasted 139.5 hours), as a function of production cut length in panel (a) and as a function of voxel volume ratio with respect to the reference simulation in panel (b). As observable from panel (a), for all the CT resolutions used a rapid decrease of simulation time is obtained increasing the length of production cuts up to about 0.1 mm. For higher length of cuts the decrease continues, but with lower slope. For each CT resolution the behaviour as a function of production cut length is well reproduced by a bi-exponential function, characterized by an early fast decaying term and a subsequent slow decaying term. Given a CT resolution, using cuts equal or larger than 0.1 mm, among the ones employed in this work, leads to a decrease of simulation time by about 25-35% with respect to the respective case with the smallest cut used of 0.01 mm.

Looking at panel (b) of Fig. 4.9 and considering a fixed production cut (i.e., a single color in the plot), by increasing the voxel size through CT resamplings conserving the overall volume of the CT, as done by the R2, R8 and R64 resamplings, a bi-exponential decrease of simulation times is observed. For each fixed cut, a reduction of simulation time by about 17%, 35% and 60% with respect to simulations using native CT is obtained with simulations using R2, R8 and R64 resamplings, respectively. In the case of the RS resampling, that does not conserve the total volume of the CT, despite it has a similar voxel volume as the R64 resampling, its simulation times are higher, comparable instead to the ones of the R8 resampling. Therefore RS results do not follow the bi-exponential trend shown considering N, R2, R8 and R64 resampling, as visible looking at the open triangles in Figure 4.9(b), which represent RS simulations.

4.7 Discussion

In order to determine the best combinations of the examined parameters varied in the simulations, i.e., voxel volume via CT resampling and secondary production cuts, we considered the behaviour of simulation time ratios as a function of both them, while taking as an index of the absorbed dose evaluation accuracy the relative percent differences with respect to the average absorbed dose of the reference simulation, ε_{VOI}s. Based on these premises, the use of the R8 resampling - which doubles voxel volume - with 0.1 mm production cuts appears as the optimal choice. This combination of parameters ensures an agreement within 1% in terms of ε_{VOI} in liver-related VOIs, within 4% in lungs and within 2% in kidneys, while reducing the simulation time to less than half of the reference simulation time. The use of 0.5 mm cut does not alter significantly the accuracy in terms of ε_{VOI} and can be equally considered, but the improvement in terms of simulation time saving is minimal (from ∼47% time ratio with 0.1 mm cut to ∼42% with 0.5 mm). 2.0 mm cuts, although they show still very good agreement, are not recommended, as well as all the cuts with length comparable or larger than the voxel dimensions, as a general rule to ensure an adequate absorbed dose spatial sampling with respect to the resolution of the grid used. In addition, the simulation time reduction for cuts larger than about 0.5 mm is slightest.

The combination of parameters giving the fastest simulation among the examined ones is the R64 resampling with 4.0 mm cuts, which reduces the simulation time to about 1/4 of the reference simulation time. Anyways, as motivated above, a smaller

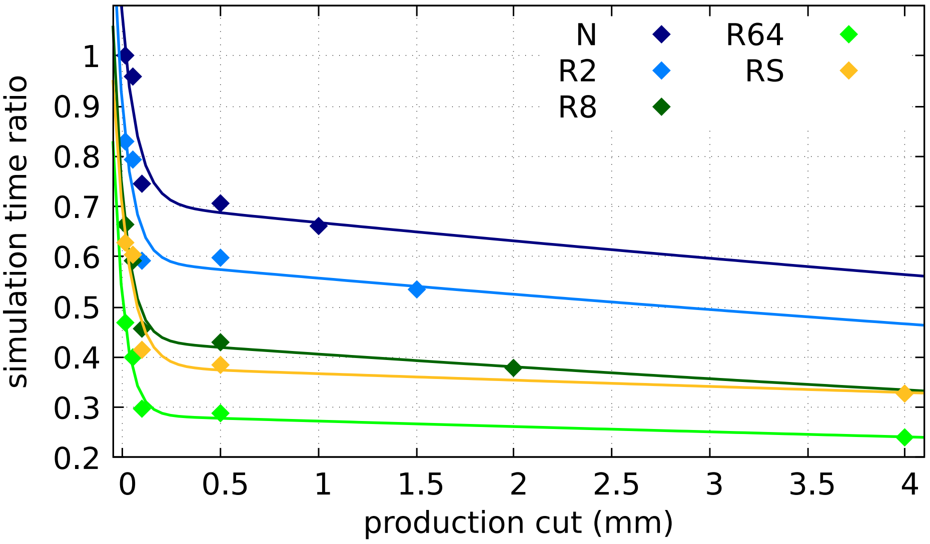

(a)

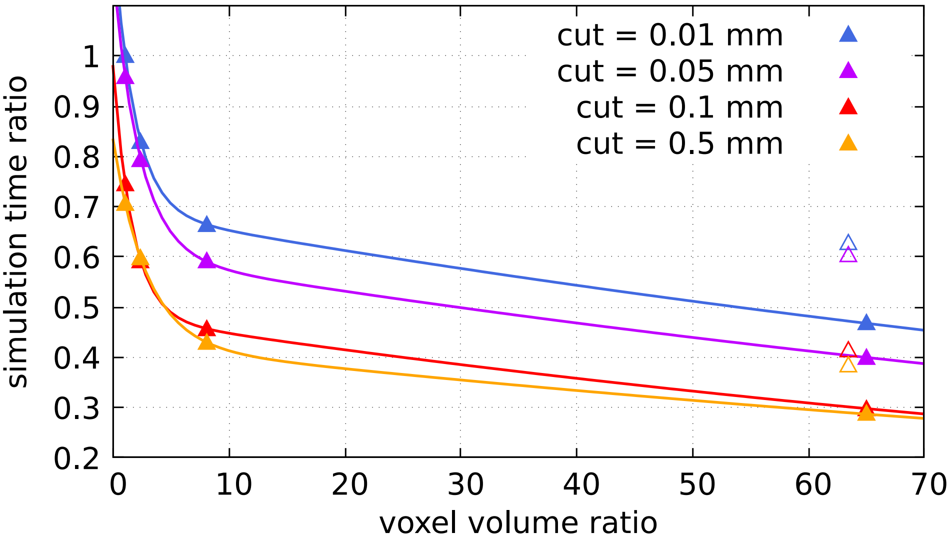

(b)

FIGURE 4.9: Simulation time ratios with respect to reference simulation time (which lasted 139.5 h), as a function of production range cut length (a) and of voxel volume ratio (b). Full triangles in (b) represent simulations using N, R2, R8 and R64 CTs, taken into account for fits; open triangles represent simulations using RS CT, not considered for fits.

cut, with a length of at least half the size of the voxel (3.58 mm of side in axial direction for the R64 resampling), would be suggested. Cuts of lengths between 0.5 and 1.5 mm would in any case give excellent time reduction, between 30% and 25%. Using the R64 resampling returns less accuracy with respect to R8, but its level of accuracy can be considered still acceptable especially for liver-related VOIs, with an agreement in terms of ε_{VOI} within 6% in healthy liver perfused and within 3% in all the other liver-related VOIs.

Lastly, it is worth mentioning the parameter combination using the RS resampling and the 0.1 mm or 0.5 mm cuts, which enable a time reduction to about 40% of reference simulation time, ensuring at the same time fair agreement in liver-related VOIs, with ε_{VOI} being within 4% in healthy liver and within 1% in all the other liver-related VOIs. This type of resampling, adopting the SPECT resolution and dimensions for the CT used as input for building the phantom, despite obviously lowering the resolution with respect to the native CT, offers some useful aspects. Regarding GATE's macros scripting, it enables a much easier deduction of volumes translations in GATE's *World* geometry [104]. Concerning a possible pre-simulation processing of the images, it brings to a more straightforward way of performing logical operations involving CT and SPECT (or PET) images (such as the ones performed in Sec. 3.6.1 of Chapter 3), avoiding the introduction of further interpolations between voxels, since CT and SPECT voxels have a one-to-one correspondence with this kind of resampling.

The results obtained can be helpful as a starting point guideline in selecting settings for speeding up MC voxel dosimetry in ^{90}Y-TARE planning or retrospective studies, avoiding significant loss of accuracy.

It could be argued that simplified voxel dosimetry methods, such as dose point-kernel (DPK) convolution, are much faster than MC simulations, even after the optimization of times presented, and that DPK convolution, for TARE, is reported in literature to ensure excellent agreement with MC for absorbed dose estimations in the abdomen, in particular when sources and targets are entirely included within liver - considered as a homogeneous medium -, or alternatively adopting density-corrections methods [59]. However, this does not undermine the relevance of MC for TARE and the interest in speeding up such simulations, since first of all MC is the reference method against whom simplified methods are compared to verify their reliability, and moreover it remains the most accurate method in case of relevant inhomogeneities; in this respect, beyond eventual cases of peculiar inhomogeneities within liver, a clear interest in MC dosimetry for TARE can be found in the estimation of absorbed dose gradients delivered to the lungs, given the intrinsically inhomogenoeous character of these organs and their possible close proximity to the radioactivity source in liver, as it is testified by works such as [128].

Chapter 5

^{90}Y-TARE internal dosimetry with *OpenDose Dosimetry 3D*

5.1 Introduction

In this Chapter will be described the functionalities of the *OpenDose Dosimetry 3D* module of the software 3D Slicer, developed by the *OpenDose* collaboration to offer to the scientific community a free user-friendly module for the easy implementation of personalized voxel-level internal dosimetry calculations with multiple algorithms. The testing and validation of the module for some ^{90}Y-TARE cases will be presented, carried out by completing full *OpenDose Dosimetry 3D* dosimetric workflows with all its available methods (time integration of activities and time integration of absorbed dose rates with local energy deposition, dose point kernel convolution, GATE-based direct MC simulations), and comparing the obtained average absorbed doses in liver compartments with the respective values published in literature for the same patient datasets, calculated via GAMOS direct MC simulations. Good agreement with published results was found for all the dosimetric algorithms, with some minor discrepancies due to the intrinsic differences between the employed algorithms; therefore the module can be considered satisfactorily validated for ^{90}Y-TAREs.

5.2 Internal dosimetry with the *OpenDose Dosimetry 3D* module

5.2.1 The *OpenDose* collaboration

The *OpenDose* international collaboration brings together resources and expertise to provide open access material for the benefit of the nuclear medicine dosimetry scientific community [69, 129]. Currently it includes members of 27 research teams from 13 countries around the world (Fig. 5.1), who are researchers, postdocs and PhD students with experience in nuclear medicine dosimetry, Monte Carlo methods, high performance computing, software development and education.

The activity of the collaboration is divided into the following main branches: production of model-based dosimetry data (SAFs and S-values) via Monte Carlo simulations on voxelized-phantoms, development of open-source software for model-based and patient-specific dosimetry, production and sharing of educational materials, such as lectures and recommended readings regarding nuclear medicine dosimetry. During the course of my PhD, I had the opportunity to join the *OpenDose* collaboration, and up to now I was mainly involved in the testing, validation and support to developers for the patient-specific dosimetry software, which was developed as an extension module of 3D Slicer [107], named *OpenDose Dosimetry*

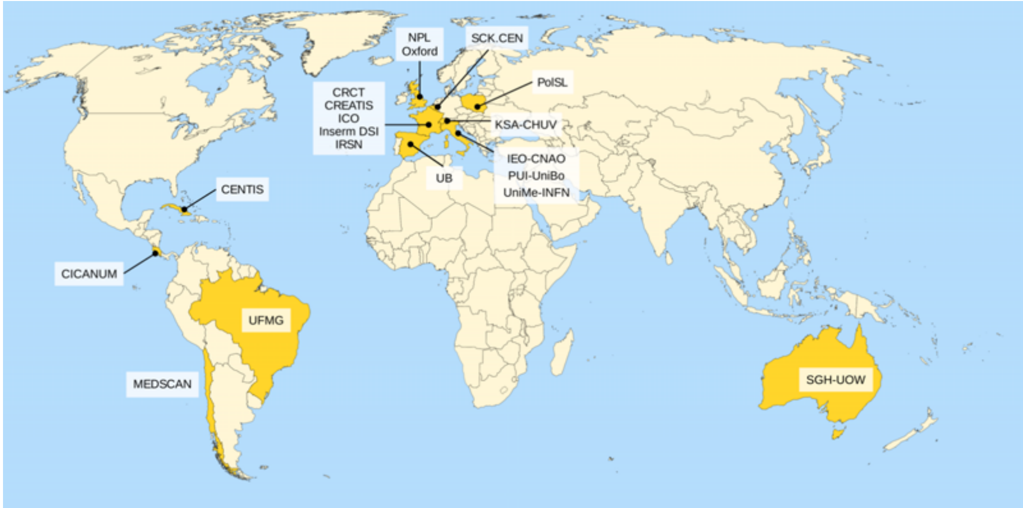
NPL
Oxford
SCK.CEN
PolSL
CRCT
CREATIS
ICO
Inserm DSI
IRSN
KSA-CHUV
IEO-CNAO
PUI-UniBo
UniMe-INFN
UB
CENTIS
CICANUM
UFMG
MEDSCAN
SGH-UOW

FIGURE 5.1: World map showing the universities and institutes involved in the *OpenDose* collaboration [129].

3D (or abbreviated *OpenDose3D* in the following). This module is currently in beta version but already working and publicly available, freely downloadable from 3D Slicer's Extension Manager [114] (or from the project's GitLab page [130]). It aims at being an open-source user-friendly graphic interface for performing voxel-level internal dosimetry with different approaches, at the moment intended for academic research purposes and not for clinical use.

5.2.2 The *OpenDose3D* Slicer module

The *OpenDose3D* module provides the possibility to perform internal dosimetry for molecular radiotherapy treatment cycles, being able to deal with CTs and SPECTs or PETs at multiple time points. It requires as input data tomographic images in Dicom format and respective organ segmentations in formats readable by 3D Slicer - which by the way can be performed by the user with 3D Slicer itself using its *Segment Editor* module [114] - . *OpenDose3D* follows a workflow mode, schematized in Fig. 5.2, to perform the dosimetry process from start to end, meaning that the user has to complete some steps to be able to access further ones, subdivided into several sequential utilities, represented in Fig. 5.3 and briefly explained below:

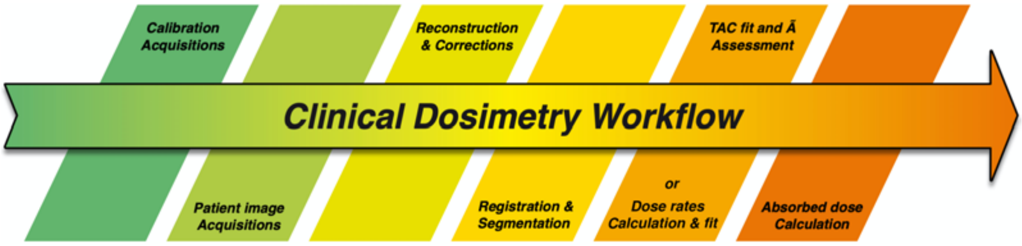
Calibration Acquisitions
Reconstruction & Corrections
TAC fit and Ã Assessment
Clinical Dosimetry Workflow
Patient image Acquisitions
Registration & Segmentation
or
Dose rates Calculation & fit
Absorbed dose Calculation

FIGURE 5.2: Flow chart of a clinical dosimetry workflow as followed by *OpenDose3D*, which requires the first 3 steps as input, and can manage the last 3 steps.

1. *Parameters* panel allows to enter input variables for the study: the isotope, the scanner camera factor (i.e. its sensitivity), the injected activity and the injection time.

2. *Preprocessing* panel allows to prepare the essential objects for the calculation:
    (a) *Rename files* button allows to create some required variables in the *Data* section of 3D Slicer, starting from the input Dicom CT and PET/SPECT files, group the files by time point and rename them using a convention.
    (b) *Resample CTs* button performs automatic resampling of the CT volumes to the dimensions and resolution of the associated SPECT or PET volumes, employing Lanczos interpolation [126] taking advantage of the *Resample Image (BRAINS)* module of 3D Slicer.
    (c) *Rescale* button deduces density volumes (in kg/m^3) from CT volumes using the well established Hounsfield Units conversion described in [105], and converts the SPECT volumes to activity map volumes (in MBq).
3. *Registration* panel allows an automatic spatial registration of all volumes, taking one of them as a reference. It uses the already available registration methods in 3D Slicer, specifically the *General Registration (BRAINS)* and the *Transforms* modules, using rigid + affine transforms. The user can then review the results and correct manually any broad misalignment using the *Transforms* module and repeating the registration.
4. *Absorbed Dose Rate Calculation* panel allows to select among different algorithms for the calculation of absorbed dose rate maps at the various time points:
    (a) *Local Energy Deposition (LED)* uses the procedure described in Section 1.6.2 to calculate the absorbed dose rates, employing the patient-specific density map in case of selecting the "Apply density correction" option, otherwise considering a density volume assumed as homogeneous and composed of a selectable material between: water, soft tissue, cortical bone, lung, adipose tissue.
    (b) *FFT convolution (homogeneous)* stands for voxelized dose point kernel convolution in homogeneous medium using Fast Fourier Transform, as described in Section 1.6.2; the DPKs available were pre-calculated for the materials mentioned for LED algorithm with GATE Monte Carlo simulations, for a number of voxel resolutions, but more can be added by request; also in this case an "Apply density correction" option is available in order to weight for the patient-specific density map.
    (c) *Convolution (heterogeneous)* is a modified voxelized dose point kernel convolution in which, for each multiplication intervening in the convolution, the average density of the couple of voxels considered is calculated and used as weight. Since this calculation is computationally more demanding than FFT convolution homogeneous, two options permit to set a kernel distance limit (in mm) and an activity threshold for the activity map (in terms of % with respect to the maximum available value) to reduce the memory burden and the computation time by slightly approximating the mentioned variables.
    (d) *Monte Carlo* generates a set of macros ready to be run on the GATE toolkit to perform simulations, whose results can be imported on *OpenDose3D* to continue the workflow, or alternatively can be analyzed separately with other 3D Slicer modules or with any other software capable of processing .mhd and .raw images (that are the formats of the output files).

5. *Segmentation* panel allows to import user defined segmentations to provide segment statistics in the next steps of the workflow. The *Propagate Segmentation* button is optional, and permits to handle volume variations per time point by replicating a single imported segmentation in each time point folder, that the user can then refine for each time point using the *Segment Editor* module.
6. *Segment Tables and Plots* panel produces the segment statistic tables for each time point, necessary to obtain absorbed doses in the provided segmentations, enabling to choose between the two alternative kind of workflows, as described in Section 1.6.2: time integration of the activity maps or time integration of the absorbed dose rate maps.
7. *Time Integration* panel produces the final output of the module, by integrating for each defined segment either the activity maps segment statistics or the absorbed dose rate maps segment statistics.
   (a) *Incorporation Mode* allows to select how to model the beginning of the treatment, from the injection (taken as the 0.0 hours time point) to the first acquisition: linear, constant or exponential behaviour.
   (b) *Integration Algorithm* allows to select the algorithm that will be used to perform the time integration from the first acquisition to the last acquisition: trapezoid, mono-exponential, bi-exponential, tri-exponential, x-exponential, auto-fit (using the most suitable among those listed above). In the case of trapezoid integration, it is possible to choose how to model the tail, i.e. the behaviour of the treatment after the last acquisition up to infinity, either with the Physical Decay of the radionuclide or with the Effective Decay of the treatment in that segment, deduced from the *Integration Algorithm* fit. For all the other algorithms, Effective Decay is by default used to model the tail (substantially prolonging the fit up to infinity).
8. *Utilities* panel allows to perform final optional tasks: export output files with results, cleaning the scene by erasing all non-conform volumes and all intermediate results.

5.3 Aims and calculations settings

The activity of testing and preliminary validation of the *OpenDose3D* (D3D in the following, for brevity) module for ^{90}Y-microspheres TARE clinical datasets will be described. The aim was carrying out the complete D3D dosimetry workflow for some ^{90}Y TARE cases whose results were already published in literature, starting from the same input data, and comparing the results obtained in order to ensure the correct functioning of the module, and in addition to give hints on pro and cons of the available D3D's calculation algorithms when applied to this kind of treatment cases. The methods described and the final results presented in this Chapter were obtained with *OpenDose Dosimetry 3D* module updated to July 2021 and running on 3D Slicer version 4.11.20210226 Linux release.

5.3.1 TARE imaging input data

Three clinical TARE cases studied in [48] were considered, for which the therapeutic absorbed dose distributions due to ^{90}Y-labelled glass microspheres in liver

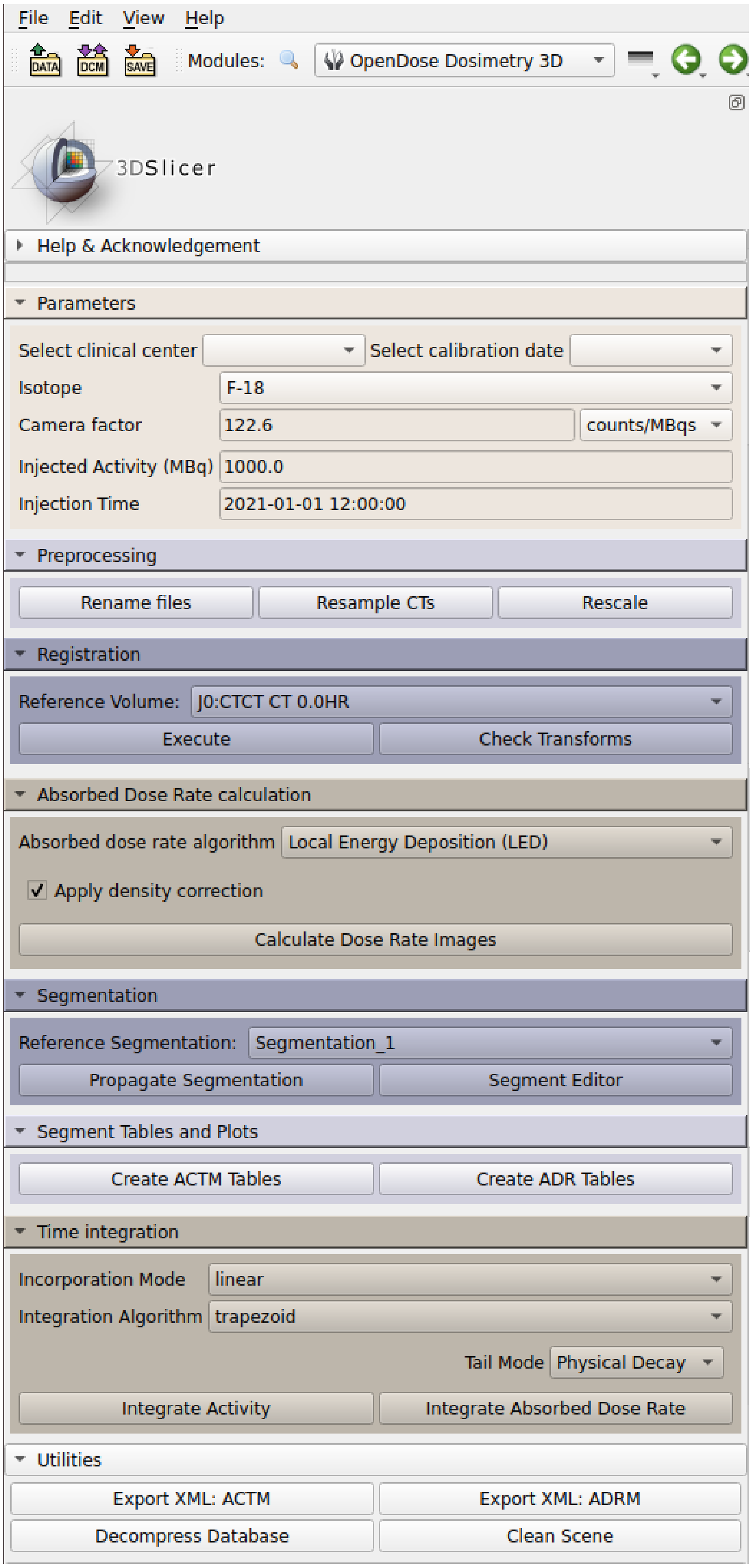
File
Edit
View
Help
DATA
DCM
SAVE
3DSlicer
Help & Acknowledgement
Parameters
Preprocessing
Rename files
Resample CTs
Rescale
Registration
Execute
Check Transforms
Absorbed Dose Rate calculation
Calculate Dose Rate Images
Segmentation
Propagate Segmentation
Segment Editor
Segment Tables and Plots
Create ACTM Tables
Create ADR Tables
Time integration
Integrate Activity
Integrate Absorbed Dose Rate
Utilities
Export XML: ACTM
Export XML: ADRM
Decompress Database
Clean Scene

Modules: OpenDose Dosimetry 3D

Select clinical center

Select calibration date

Isotope: F-18

Camera factor: 122.6 counts/MBqs

Injected Activity (MBq): 1000.0

Injection Time: 2021-01-01 12:00:00

Reference Volume: J0:CTCT CT 0.0HR

Absorbed dose rate algorithm: Local Energy Deposition (LED)

☑ Apply density correction

Reference Segmentation: Segmentation_1

Incorporation Mode: linear

Integration Algorithm: trapezoid

Tail Mode: Physical Decay

FIGURE 5.3: View of the utilities panels of the *OpenDose3D* module of 3D Slicer.

were retrospectively evaluated using as starting functional data the corresponding pre-therapeutic ^{99}Tc-macroaggregated albumin (Tc-MAA) scintigraphic images. For each patient the input Dicom imaging data used, both in [48] and in the present D3D calculations, were a multi-phase abdominal contrast-enhanced CT executed with a Siemens SOMATOM Definition AS scanner (footnote 1 in Chapter 4), and an abdominal Tc-MAA SPECT acquired using 120 projections (3 degrees angular step), each made of 128 x 128 pixels, resulting in cubic voxels with 4.664 mm side. Philips BrightView Dual Head gamma camera SPECT system (footnote 2 in Chapter 4) equipped with low energy general-purpose collimators had been used for SPECT acquisitions.

Resolutions and voxel dimensions of the input scans for the three examined cases, that will be referred to as patient 1, patient 2 and patient 3, are indicated in Tab. 5.1. Slices of the input images for the three patients are shown in panels (a), (c) and (e) of Fig. 5.4.

TABLE 5.1: Resolution and voxel dimensions of the input CTs and Tc-MAA SPECTs of the three patient cases of this study.

Patient	Scan	Resolution	Voxel dimensions (mm^3)
1	CT	512×512×227	0.96×0.96×1.00
	SPECT	128×128×128	4.66×4.66×4.66
2	CT	512×512×335	0.88×0.88×1.00
	SPECT	128×128×101	4.66×4.66×4.66
3	CT	512×512×146	0.89×0.89×2.00
	SPECT	128×128×105	4.66×4.66×4.66

5.3.2 VOIs segmentations

The same VOIs segmentations used in [48] were employed in this work. Images registrations and VOI segmentations were made by an experienced operator using the Philips IMALYTICS Research Workstation. Segmentations were imported into 3D Slicer and were converted from their native RTSTRUCT format into Binary labelmap format (needed for 3D Slicer's calculations) via the *Segmentation* module; eventual artefacts produced by the conversion have been corrected manually with 3D Slicer's *Segment Editor*, using the *Paint* tool. The segmentations correspond to VOIs representing the following anatomical structures: liver (Li.), liver perfused (Li.P.), healthy liver (H.Li.), healthy liver perfused (H.Li.P.), lesions (Le.). Liver and lesions had been manually segmented on the CT while liver perfused had been segmented on the SPECT using a thresholding method. Healthy liver had been obtained by subtracting lesions from liver, while healthy liver perfused by subtracting lesions from liver perfused. The masses of the segmentations reported in [48] and the ones returned by D3D after having imported and converted them in 3D Slicer are reported in Table 5.2.

5.3.3 Dose calculation methods settings and outputs comparison

To initialize the D3D workflow for the calculation of mean absorbed doses in the defined VOIs, the input parameters inserted in the *Parameters* panel were ^{90}Y as isotope and the injected activities, camera factors and acquisition times reported in

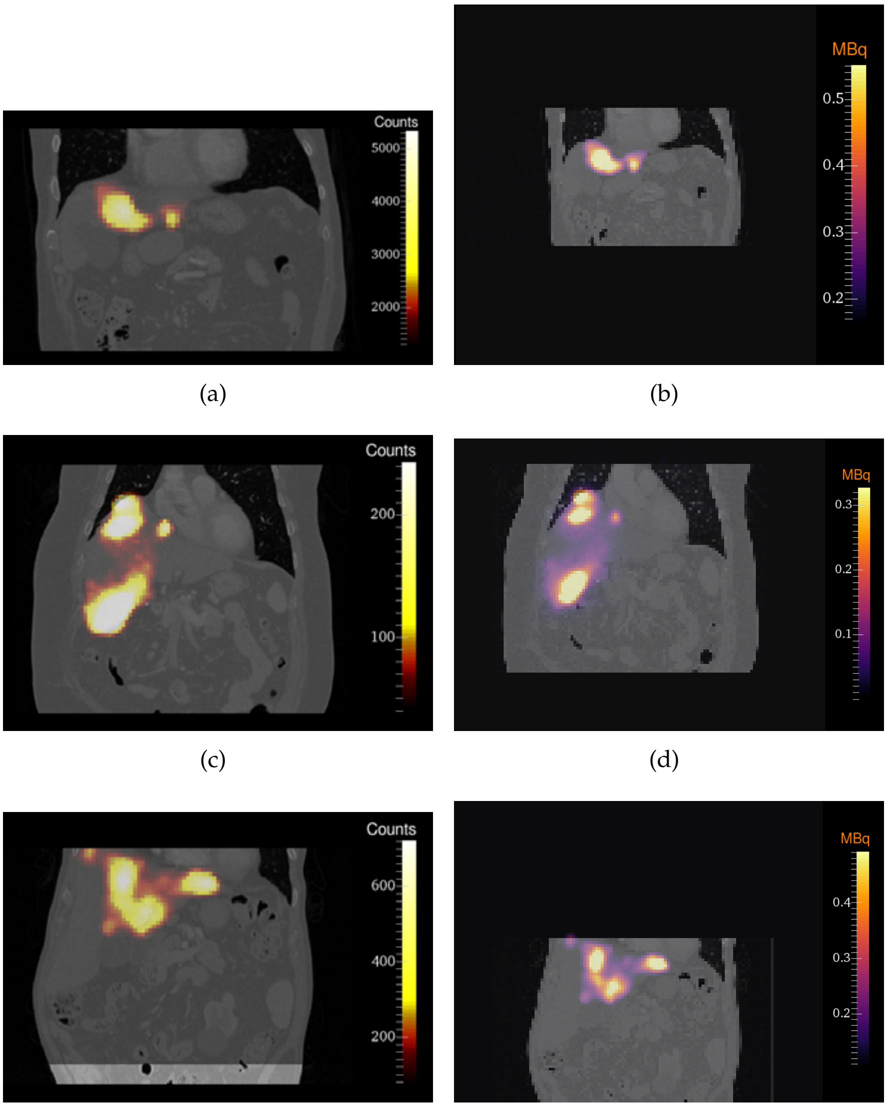
Counts
5000
4000
3000
2000
MBq
0.5
0.4
0.3
0.2
Counts
200
100
MBq
0.3
0.2
0.1
Counts
600
400
200
MBq
0.4
0.3
0.2

(a) (b)

(c) (d)

(e) (f)

FIGURE 5.4: Coronal fusion slices of the input CT and SPECT for patient 1 (a), 2 (c) and 3 (e), and coronal fusion slices of resampled density maps and activity maps calculated during the D3D workflow for patient 1 (b), 2 (d), 3 (f).

TABLE 5.2: Masses m (g) of the VOI segmentations used in [48] and imported in 3D Slicer for this work (D3D).

Patient	**VOI**	Li.	Li.P.	Le.	H.Li.	H.Li.P.
1	m [48]	1266.3	239.5	189.1	1074.4	51.1
	m **D3D**	1275.0	243.3	192.3	1086.0	51.6
2	m [48]	2425.7	1040.6	169.7	2063.9	879.9
	m **D3D**	2426.0	1039.0	169.3	2063.0	878.2
3	m [48]	2853.0	918.9	369.0	2479.4	542.5
	m **D3D**	2836.0	900.9	369.6	2467.0	531.2

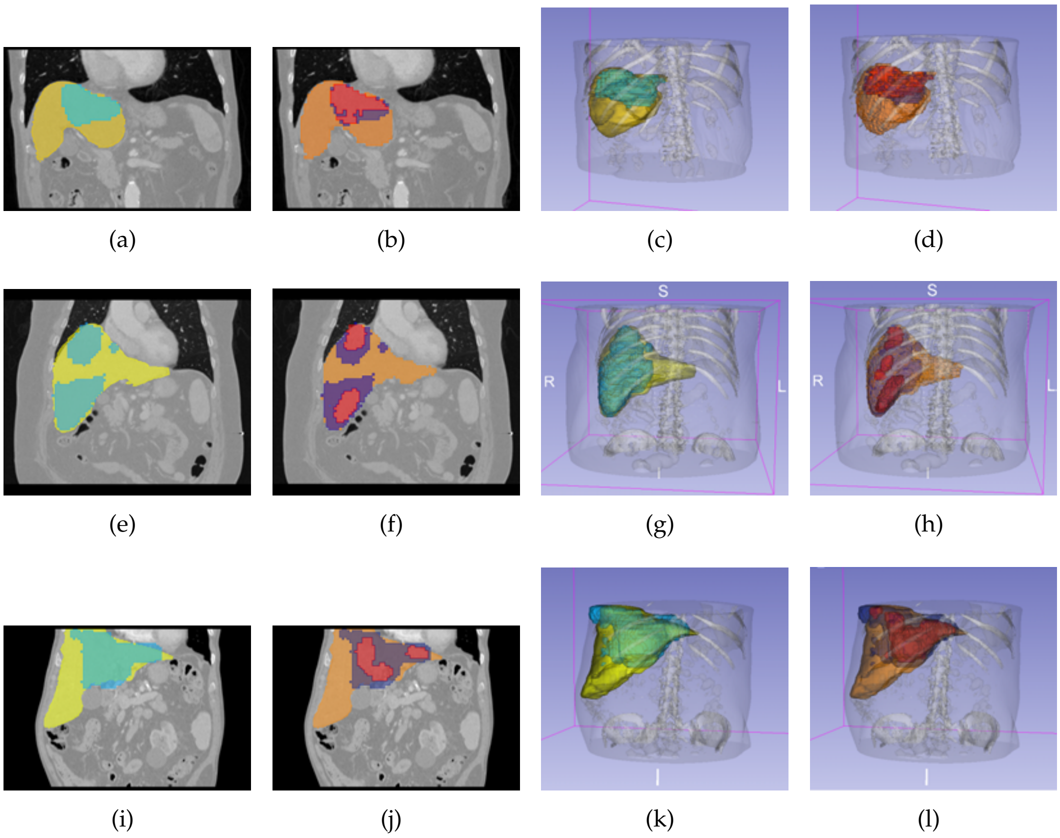

(a) (b) (c) (d)

(e) (f) (g) (h)

(i) (j) (k) (l)

FIGURE 5.5: Coronal slices on native CTs and 3D representations of the VOIs segmentations for patient 1 (a, b, c, d), 2 (e, f, g, h) and 3 (i, j, k, l). Color-VOI key is: yellow = liver, light blue = liver perfused, red = lesions, orange = healthy liver, blue = healthy liver perfused.

Tab. 5.3. The injected activities set were the ones actually used for the three considered ^{90}Y-labelled glass microspheres TARE treatments. Camera factor (C.F.) is the factor that enables to retrieve the correct activities ("ACTM" maps in D3D's jargon) starting from SPECT (or PET) numbers. SPECT (PET) numbers can be in different units, for example in quantitative SPECTs (PETs) they are already calibrated, usually expressed in Bq/ml, while in other cases their voxel values are merely counts. D3D enables to select the desired units units of C.F., that can be in principle calculated with a dedicated calibration scan, as indicated in D3D User manual at [130]. In our case, given that for the examined cases the SPECT numbers were counts in arbitrary units, the camera factor was deduced for each case as the ratio between the therapeutic ^{90}Y injected activity (in Bq) (Tab. 5.3) and the total number of counts inside the liver VOI in the ^{99m}Tc-MAA SPECT. This definition relies on the assumption that in TARE therapies, because of the embolization of liver capillaries where the spheres are delivered, the effective decay time of the radiopharmaceutical coincides with the physical nuclide decay time, without biological clearance. The indicated calculation gives a C.F. in Bq/counts, and when setting these units the formula used by D3D to deduce from native SPECT numbers the activity values (ACTM, expressed in MBq) in each voxel is:

$$\text{ACTM} = \frac{\text{C.F.} \cdot \text{SPECT number} \cdot \text{SPECT frame duration}}{10^6 \cdot \text{calibration scan frame duration}} \tag{5.1}$$

where "SPECT frame duration" is the duration of the considered SPECT scan in seconds, usually present as part of Dicom image metadata and automatically deduced by D3D, and "calibration scan frame duration" is the duration of the calibration scan as described in [130], also in this case in seconds. In our case, given how we deduced C.F., "calibration scan frame duration" corresponds to the acquisition time (A.T.) of the considered ^{99m}Tc-MAA SPECT itself. Note that if the functional scan of interest was a PET, the logic behind the calculations would have been exactly the same.

TABLE 5.3: Input parameters for the D3D workflow: injected activity $A(0)$(MBq), camera factor C.F. (Bq/counts), acquisition time A.T. (s)

Patient	***A*(0)** (MBq)	**C.F.** (Bq/counts)	**A.T.** (s)
1	739	201.38	2400
2	2720	852.50	2400
3	2490	997.80	2400

After receiving all the discussed input data, as described in Sec. 5.2.2 the D3D *Preprocessing* steps calculate CT maps resampled with resolution and dimension of the corresponding SPECT, activity maps and density maps (both calculated from resampled and native CTs); slices of the activity maps and density maps deduced for the three cases of this study are shown in panels (b), (d) and (f) of Fig. 5.4.

In addition to what already said, we manually modified the "*OpenDose3D.TimeStamp*" attribute in Slicer's *Data → MRML node information*, setting it to 0.0, so that the single evaluation time point of absorbed dose rate (or activity) is zero, corresponding to the radiopharmaceutical administration time.

In the D3D workflow, the average absorbed dose calculations within VOIs for each case were done according to the following methods:

1. D3D ATI: VOI activity time integration
   The total activity within VOIs was calculated through the *Create ACTM Tables* workflow and then integrated with respect to time via *Integrate Activity* button. Since in our cases there is a single data point, at $t = 0.0$ s, and in D3D by default the tail region after the last data point (the only data point, in our case) is integrated as mono-exponential physical decay ("Physical Decay" option), it does not matter the choice of *Incorporation Mode* and *Integration Algorithms*. Following ATI workflow, D3D evaluates the mean absorbed doses ($\langle D \rangle_{VOI}$) within VOIs via local energy deposition algorithm, considering the cumulated activities in each VOI.

2. D3D LED: Absorbed dose rate time integration using Local Energy Deposition
   Absorbed dose rates at voxel level were calculated via *Absorbed dose rate algorithm → Local Energy Deposition (LED)*, with the "apply density correction" option, and then integrated with respect to time via *Integrate Activity* button. Time integration was done as mono-exponential physical decay after the single data point, as stated in the previous point.

3. D3D FFT HoC: Absorbed dose rate integration using FFT convolution (homogeneous)
   Absorbed dose rates at voxel level were calculated via *Absorbed dose rate algorithm → FTT convolution (homogeneous)*, with the "apply density correction" option, and then integrated with respect to time via *Integrate Activity* button.

Time integration was done as mono-exponential physical decay after the single data point, as stated above.

4. D3D HeC: Absorbed dose rate integration using using convolution (heterogeneous)
   Absorbed dose rates at voxel level were calculated via *Absorbed dose rate algorithm → Convolution (heterogeneous)* , setting 0% "Activity threshold" and 30.0 mm "kernel limit", and then integrated with respect to time via *Integrate Activity* button. Time integration was done as mono-exponential physical decay after the single data point, as stated above.

5. D3D GATE MC: GATE Monte Carlo simulation
   Absorbed doses were calculated through Monte Carlo (MC) simulation of ^{90}Y decays and interaction of decay-products with matter using D3D-generated macros and files for GATE. Macros were generated via *Absorbed dose rate algorithm → Monte Carlo → Generate GATE*. Only the following change to the macros was applied by the user:

   - in file "`/mac/executor.mac`", at the row:
     `/gate/application/setTotalNumberOfPrimaries n`
     the D3D deduced number of primaries n was replaced with $m = 2 \cdot 10^8$, in order to shorten the simulation time.

   Macros were run using GATE version 9.0, and the folder with output results was returned as input to D3D via *Absorbed dose rate algorithm → Monte Carlo → Import GATE*, in order to resume and finish the average absorbed dose calculation in VOIs.
   Since we used m instead of n as number of primary events, before the time integration of the absorbed dose rate maps, we corrected the latter ones for the factor (n/m) using Slicer's *Filtering → Simple Filters → ShiftScaleImageFilter*. In addition, to be consistent with the procedure adopted for the GAMOS MC calculations in [48], we also evaluated the absorbed doses multiplying them for a corrective factor b, used in that paper for MC results in order to correct for the background noise-due activity present in the SPECT outside the liver VOI (since liver is the only source organ in TARE therapies); b is defined as the ratio between total activity (or SPECT counts, equivalently) in the whole SPECT scan and total activity (counts) in liver VOI.

   $$b = \frac{\text{activity} \in \text{whole SPECT}}{\text{activity} \in \text{liver VOI}} \tag{5.2}$$

   In formulas, indicating with $\langle \dot{D} \rangle_{VOI}^{out}$ the average absorbed dose rates deduced by the D3D workflow with n events, the two D3D Monte Carlo estimates of average absorbed dose rates were calculated as

   $$\langle \dot{D} \rangle_{VOI}^{\text{D3D GATE MC}} = \frac{n}{m} \left(\langle \dot{D} \rangle_{VOI}^{out} \right) \tag{5.3}$$

   in the case without SPECT background correction, and as

   $$\langle \dot{D} \rangle_{VOI}^{\text{D3D GATE MC bkg}} = \frac{n}{m} \left(\langle \dot{D} \rangle_{VOI}^{out} \right) \cdot b = \left(\langle \dot{D} \rangle_{VOI}^{\text{D3D GATE MC}} \right) \cdot b \tag{5.4}$$

   in the case applying the SPECT background correction factor.

All the average absorbed dose values ($\langle D \rangle_{VOI}$) within VOIs deduced with the five different D3D methods (X) were compared with the results obtained via GAMOS direct Monte Carlo simulation (MC GAMOS) published in [48] for the corresponding patients, in terms of relative per cent differences δ_{VOI} (%), taking MC GAMOS results as the reference:

$$\delta_{VOI}^{\text{D3D method } X} = 100 \cdot \frac{\langle D \rangle_{VOI}^{\text{D3D method } X} - \langle D \rangle_{VOI}^{\text{MC GAMOS}}}{\langle D \rangle_{VOI}^{\text{MC GAMOS}}} \tag{5.5}$$

5.4 Results and discussion

Histograms representing the average absorbed dose values within VOIs obtained with all the D3D methods used, and the relative percent differences δ_{VOI} with respect to the reference MC GAMOS, are reported in Fig. 5.6 for patient 1, in Fig. 5.7 for patient 2 and in Fig. 5.8 for patient 3.

First of all, the results obtained for all the three cases and all the D3D dosimetric methods reassure on the correct functioning of the D3D module for ^{90}Y TARE, given that, apart from some exceptions that will be discussed specifically, the agreement with the reference in terms of δ_{VOI} is within about 12% in all the examined VOIs.

The main exception is the D3D GATE MC method, which exhibits underestimation of results with respect to GAMOS MC reference between 20% and about 50% in all the VOIs, with the larger or lower differences depending on the specific patient. This behaviour is anyways expected, since the D3D GATE MC method, as performed by default by D3D, does not apply the background correction factor b described in the previous paragraph and included in GAMOS MC results. The "D3D GATE MC bkg" method indeed, as expected since applying to the D3D GATE MC results the b factor, finds close agreement with the GAMOS MC reference, with relative differences going from 1% to 6% in all VOIs of all patients, and of 10 % only for the healthy liver VOI of patient 3. Considering the comparisons between MC GAMOS and D3D GATE MC bkg results, it should be also taken into account that, though both are three-dimensional voxel-level MC simulation dosimetry methods, they have some different settings, the main ones being:

- The patient's phantom dimensions and resolution, being the ones of the native CT for GAMOS MC, while being the ones of resampled CT with the resolution and dimensions of SPECT for D3D GATE MC;
- The materials assigned to phantom voxels, being in both cases air, lung tissue, adipose tissue, soft tissue and bone, but defined slightly differently and associated to slightly different Hounsfield Units intervals (see [48] and [127] for GAMOS MC and the files in the `/opendose3d/OpenDose3D/Resources/Gate` folder at [130] for D3D GATE MC);
- The procedures assigning densities to phantom voxels in GATE and GAMOS, as also detailed in Chapter 3;
- The GEANT4's physics lists employed, *GmEMExtendedPhysics* for GAMOS MC, *G4EMStandardPhysics_opt4* for D3D GATE MC.
- The number of primary events simulated, 10^8 for GAMOS MC, $2 \cdot 10^8$ for D3D GATE MC, which consequently has results with statistical uncertainties lower by a factor $(1/\sqrt{2})$ with respect to GAMOS MC, since the statistical uncertainties in MC simulation decrease as $(1/\sqrt{N})$, with N the number of simulated histories [82].

The other exception showing a larger relative difference with respect to reference as compared to the average behaviour is the D3D HeC method in healthy liver perfused for patient 3, with an overestimation of about 35% with respect to GAMOS MC. To comment this isolated case, first of all it has to be considered that the heterogeneous dose point kernel convolution algorithm is obviously different from MC simulation, but the obtained difference can't be imputed trivially to the HeC algorithm alone, since for the other VOIs and also for the same type of VOI for the other patients the differences are smaller. The reason can be imputed to a combination with further factors, e.g. the fact that healthy liver perfused is a VOI obtained via subtraction from liver perfused VOI (segmented on SPECT) of lesions VOI (segmented on CT), the latter delimiting the highest-uptaking voxels of the patient; following furthermore from the Slicer conversion of original RTSTRUCT segmentations, some small geometrical discrepancies can arise, and can have more impact at "interface" areas with activity discontinuities or with density inhomogeneities. Another related factor can be some spill-out of activity distribution (SPECT) with respect to the morphological counterpart (CT), due to motion blurring, reconstruction background etc., that actually affects more or less all tomographic functional scans, but in the case of patient 3 can be seen a little more than in the other twos, and that could have had more impact for this specific "subtraction" VOI when using the HeC algorithm. With reference to this last aspect, it has to be noted that, in coherence with [48], no SPECT activity thresholding or masking has been used ("Activity threshold" option in D3D has been set to 0.0 %), a technique that would reduce absorbed dose artifacts inside and outside the body, as described in Chapter 3 for ^{18}F-choline PET and that will be detailed in Chapter 6 for ^{90}Y TARE.

Apart from this specific highest discrepancy, it can be noted that the healthy liver VOI results exhibit the largest relative differences with respect to GAMOS MC, that are the ones reaching δ_{VOI} values of about -12% for patient 1 and 3. This evidence can in part can be justified with the same consideration described for healthy liver perfused, regarding VOIs obtained as subtraction between other VOIs, with the additional issue that healthy liver VOI covers all the non-perfused areas of liver (remind that it is obtained as liver - lesions), and therefore has on average the highest statistical uncertainties and lowest absorbed dose values among the five examined VOIs of this study; as a consequence, the average absorbed dose results in this VOI are more sensible to eventual "fluctuations" in high-dose values. On the contrary, as thus expected, the VOI showing the best agreements is liver (intended as the entire liver), with δ_{VOI} well below 5% in all cases, often below 1%.

In Table 5.4 are reported the computation times of all the D3D dosimetry methods employed, intended as the times taken for the calculation of absorbed dose rates for LED, FFT HoC and HeC methods (after using *Calculate Dose Rates Images* button), the times taken for the calculation of time-integrated activities for ATI method (after using *Create ACTM Tables* button), and the time taken for the simulations for GATE MC method (in terms of the *ElapsedTime* variable of GATE); the time spent to treat the input images and parameters for D3D and the time employed to obtain average absorbed dose rates from time integration have been excluded, since they are in principle the same for all the methods.

Given the very fast computation times accompanied by the very good agreements with the reference results for all the three patient cases, especially for liver, liver perfused and lesions VOIs, the D3D FFT HoC method emerges as the most suitable choice in case of the need of rapid results in these VOIs. D3D ATI and D3D LED are also valid choices for the same purpose, being as fast as D3D FFT HoC with only a slightly less agreement on average. D3D HeC shows very similar accuracy as D3D

TABLE 5.4: Computation times required for the average absorbed dose calculations with the various D3D methods employed. HeC calculations were performed with 30.0 mm kernel limit, GATE MC calculations were obtained simulating $2 \cdot 10^8$ primary events.

Patient	**D3D dose calculation method**				
	ATI	LED	FFT HoC	HeC	GATE MC
1	1-5 sec	1-5 sec	1-5 sec	∼40 min	2966 min
2	1-5 sec	1-5 sec	1-5 sec	∼40 min	2302 min
3	1-5 sec	1-5 sec	1-5 sec	∼40 min	2691 min

FFT HoC, but its longer computation times (up to almost $2 \cdot 10^3$ times slower than D3D HoC using 30.0 mm kernel limit) makes its use less meaningful; even reducing the kernel limit the computation times remain much longer than D3D HoC, while in principle reducing in parallel the accuracy. GATE MC method is obviously the slowest (up to $1.8 \cdot 10^5$ times slower than D3D HoC, when simulating $2 \cdot 10^8$ events), and the performances get worse as the resolution of images is higher, but remains the most accurate choice, with on average the best agreements in terms of δ_{VOI} for all VOIs and all patient cases.

In conclusion, the *OpenDose Dosimetry 3D* module of 3D Slicer can be considered satisfactorily validated as regards ^{90}Y TARE cases, and it promises to become a very useful tool for the user-friendly implementation of internal dosimetry research calculations.

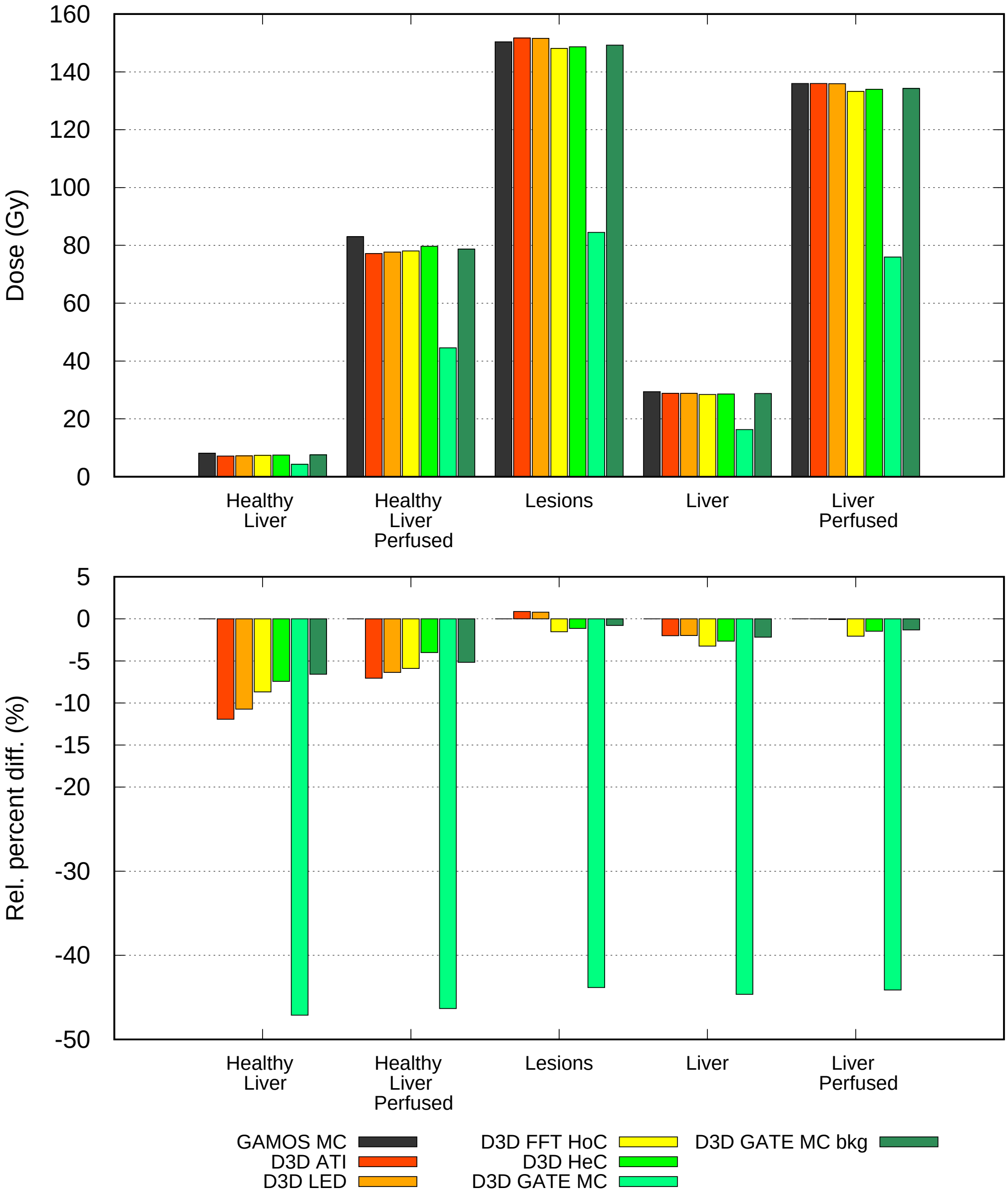

FIGURE 5.6: Average absorbed dose values in VOIs obtained with all the adopted D3D methods and relative percent differences with respect to MC GAMOS results ([48]) for patient 1.

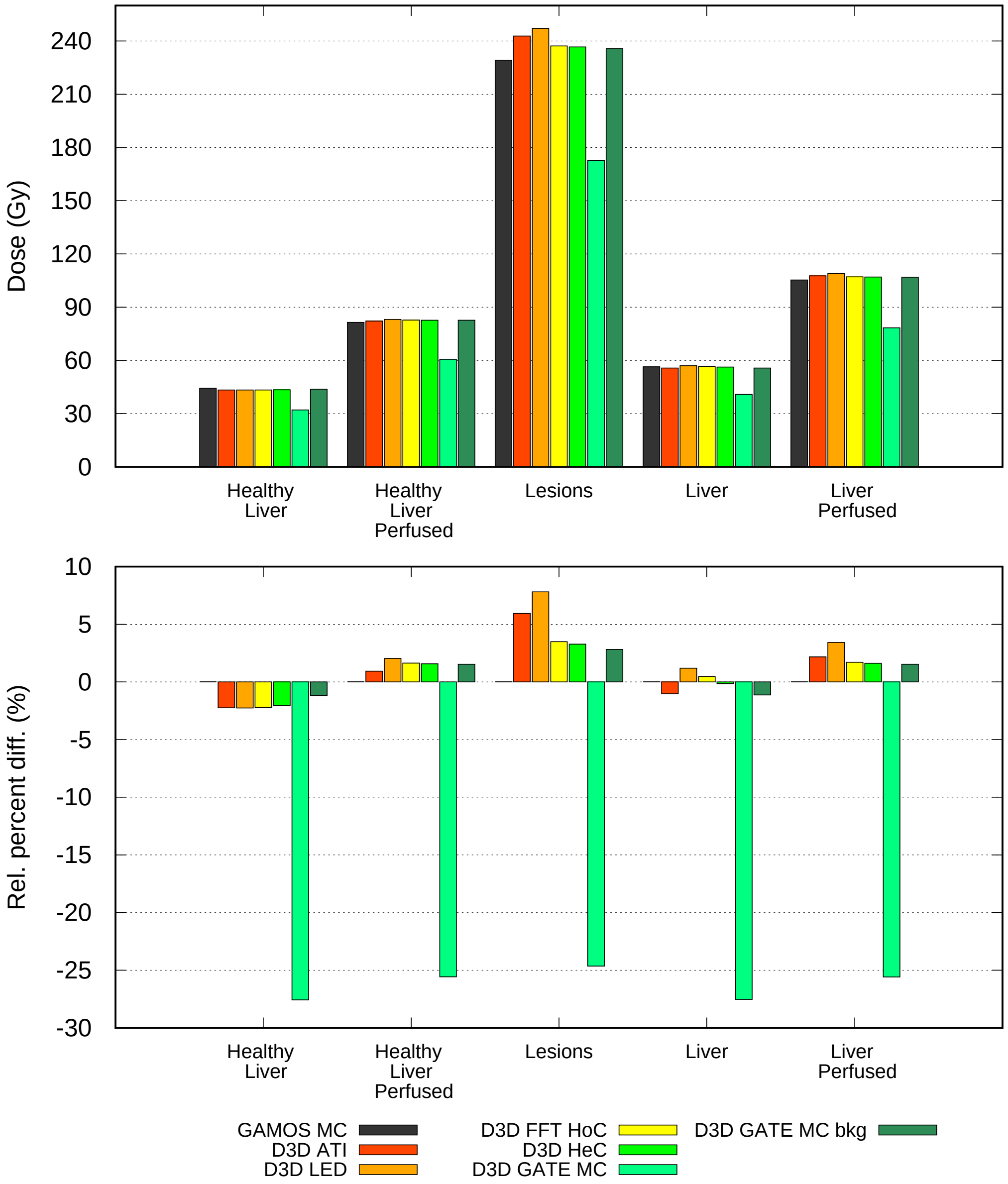

FIGURE 5.7: Average absorbed dose values in VOIs obtained with all the adopted D3D methods and relative percent differences with respect to MC GAMOS results ([48]) for patient 2.

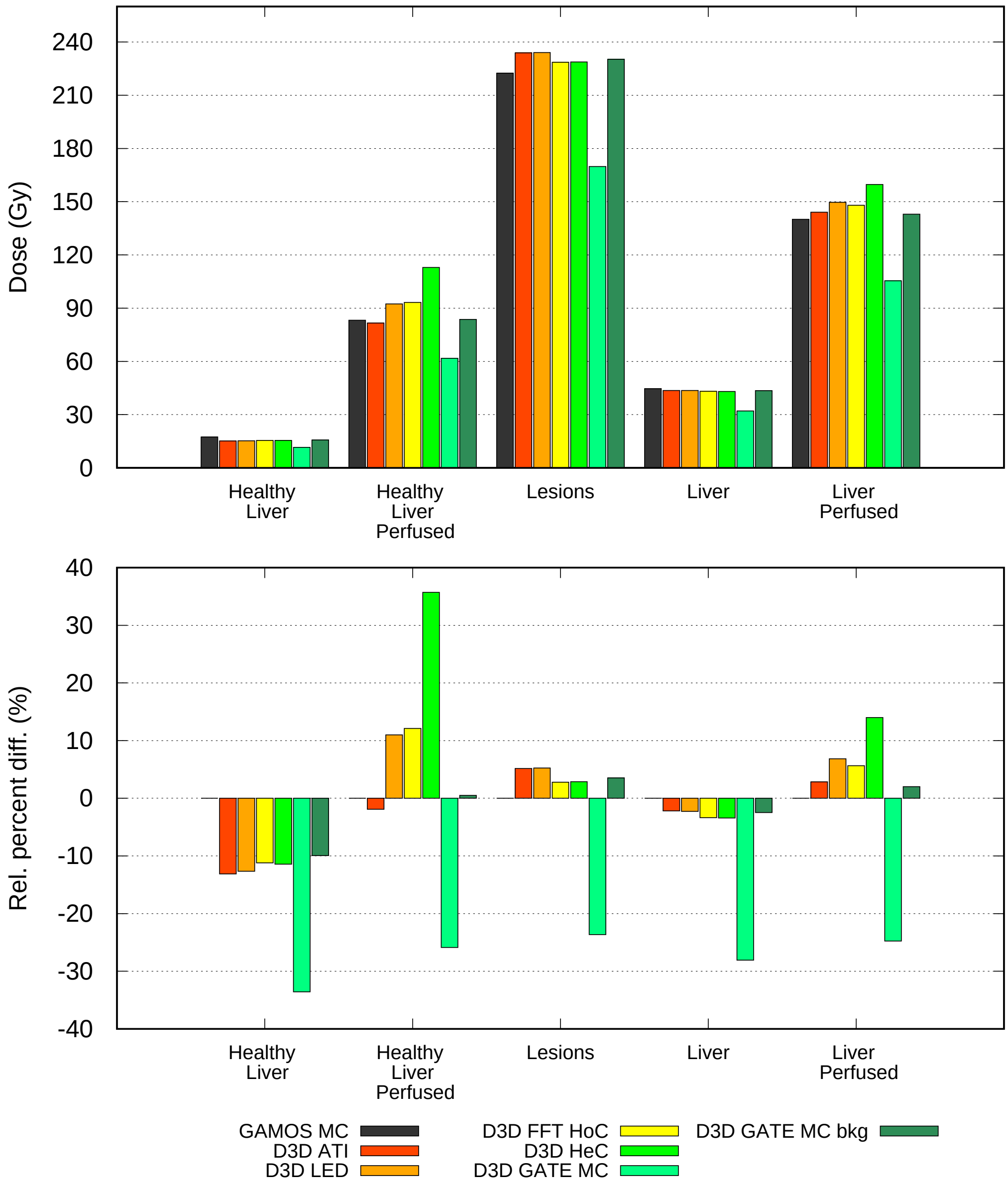

FIGURE 5.8: Average absorbed dose values in VOIs obtained with all the adopted D3D methods and relative percent differences with respect to MC GAMOS results ([48]) for patient 3.

Chapter 6

Effects of SPECT artefacts and noise on Monte Carlo ^{90}Y-TARE dosimetry

6.1 Introduction

As evidenced in Chapter 3 regarding ^{18}F-choline PET dosimetry, reconstruction noise, motion blurring and other noise effects affecting the functional scans, can be cause of non-negligible absorbed dose artefacts in MC dosimetric calculations. These artefacts can arise especially in low-density and lowly-perfused regions, such as lungs and other air-rich tissues. In this Chapter will be described the findings of a study aimed at investigating the presence of absorbed dose artefacts of this kind in ^{90}Y-microspheres TARE MC dosimetry. In order to verify that, MC simulations on ^{90}Y TARE patients data were implemented, developing and comparing different SPECT filtering techniques, aimed respectively at zeroing the activity concentration in air, lungs, or the whole volume outside liver, to consequently minimize in the simulations the decay probability in these "unrealistic" regions. Concerning liver-related volumes of interest (VOIs), increases of absorbed dose up to about 40% were found with respect to native-SPECT simulations, depending on the filter adopted. Regarding lungs-related VOIs, decreases of absorbed dose ranging from 20% to 90% - or even 99% in left lung - with respect to native-SPECT values were retrieved, strongly depending on the selected filter. These results highlight how functional imaging noises and subsequent geometrical mismatches with respect to the morphological imaging have a non-negligible effect on the absorbed dose estimations for ^{90}Y TARE cases, potentially causing overestimation of lung absorbed doses and underestimation of liver absorbed doses, if not properly treated. SPECT-filtering techniques to be applied before the dosimetric calculations could be a valid solution, but need to be implemented with extreme care with the help and opinion of physicians for the correct interpretation, from the imaging, of anatomy and radionuclide biodistribution, in order to simulate with maximum realism the system under investigation, i.e., the patient with a radiopharmaceutical biodistributed within his/her body.

6.2 Aim of the study

Even if direct Monte Carlo (MC) simulation is in principle the gold standard method for patient-specific dosimetry, that holds true if the simulated system modeled from imaging reproduces precisely the real system. In carrying out MC simulations of radionuclide diagnostics and therapies, by default there must be made multiple assumptions in modeling the system of interest, which is the patient's body with a radionuclide distribution within it. The main assumptions are:

- taking CT scans, which can be seen as a 3D "snapshots" of the body (a complete scan lasts few seconds), as representative of the patient body (or part of it) at certain "time points", approximating in this way its dynamic behaviour;
- assigning materials to voxels on the basis of average chemical compositions of organs and tissues;
- modeling the dynamic radiopharmaceutical biodistribution from 3D "snapshots" of it at certain time points, i.e. SPECT or PET scans, which by the way usually last at least 15-20 minutes, and therefore are more like "long exposure photographs", "averages" along that time interval.

Such assumptions are considered acceptable and are moreover unavoidable, since tomographic imaging at a finite number of "time points" is the best that can be done experimentally with the available resources in a nuclear medicine department. However, non-negligible mismatches with respect to the real system can be caused by tomography reconstruction noise, background noise and motion blurring, especially affecting functional scans, also due to their longer duration with respect to CTs. Such artefacts can result in inaccuracy in the absorbed dose estimation, as pointed out in Chapter 3 for ^{18}F-choline diagnostic imaging dosimetry, with the production of absorbed dose artefacts in low density regions, in particular lungs. Therefore, just using the native tomographic scans as they are as input data for MC simulations may not be the most realistic choice. The aim of the present study was to check if similar absorbed dose artefacts are produced in MC dosimetry for TARE treatments with ^{90}Y-loaded microspheres, in particular in lungs, by observing the effect of using different filtering techniques on the input SPECTs. Such techniques could be in case used to correct for the mentioned artefacts, given that minimizing inaccuracies in the absorbed dose estimation has a major importance, especially dealing with therapeutic activities as in TAREs.

6.3 Pre-simulation settings

6.3.1 Input scans and VOIs segmentations

The input data employed for this study were the same native CT and ^{99}Tc-MAA SPECT scans used in Chapter 5 (some projections are shown in Fig. 5.4), referring to three clinical ^{90}Y TARE cases. For all the patients a negligible shunt fraction was attested by the physicians, indicating that eventual signal blurring out of the liver should be ascribed solely to image noise and/or to patients' motion during the SPECT acquisition.

The VOIs which it was decided to examine were exactly the same defined in Sec. 5.3.2 (and shown in Fig. 5.5) as concerns liver, while lungs segmentations were additionally defined on CTs with 3D Slicer version 4.11, taking advantage of its module *Segment editor*. Separate segmentations were made for right lungs and left lungs, with three different variants for each:

a) Firstly, "standard" segmentations of the visible sections of the lungs in the Field of View (FoV) of the CT were performed, with the combined use of *Threshold* and *Isle* tools of *Segment editor*, selecting only voxels with HU values $<$

-200, and excluding manually, with the *Paint* tool, bronchi and trachea, when present in the FoV.

b) Secondly, alternative segmentations were defined subtracting from the previous "standard" segmentations the very low-density voxels corresponding to air, setting a threshold excluding HU < -855; this value is the upper limit of HU corresponding to air (Tab. 3.5) for the HU intervals and HU-density calibrations defined in Sec. 3.4.4 of Chapter 5, and also adopted in Chapter 4

c) Thirdly, further alternative segmentations were produced with the same logic of b) but setting a threshold of HU < -900 for excluding air-related voxels, a little less stringent requirement than exactly -855 HU.

Graphical representations of the various lungs segmentations are shown in Fig. 6.1. The purpose of the two alternative segmentations using a threshold to remove low-density voxels was obviously to exclude from the VOIs the areas that should correspond to air. The motivation behind this is to ascertain if significant differences in dosimetric results are observed between the three different segmentation choices, given that air regions are more subject to high-dose artefacts because of their very low masses.

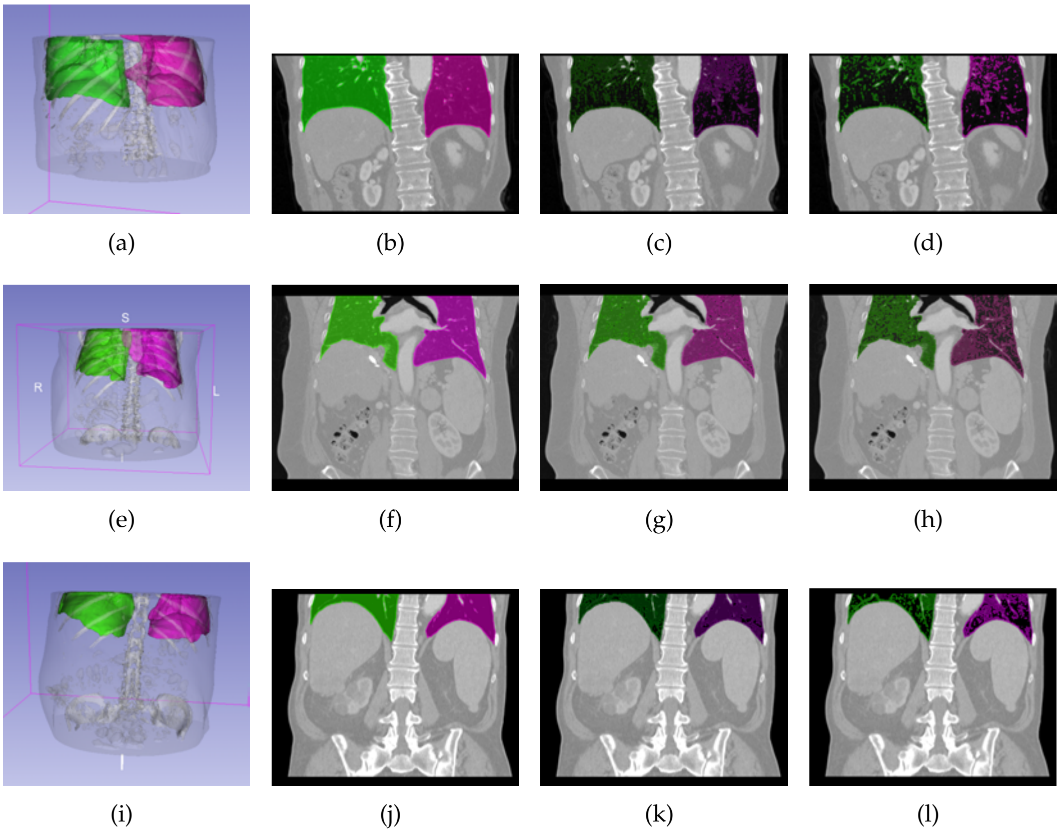

(a) (b) (c) (d)

(e) (f) (g) (h)

(i) (j) (k) (l)

FIGURE 6.1: Depictions of right lung (green) and left lung (magenta) segmentations for the three examined cases. The first row (a, b, c, d) refers to patient 1, 2nd row to pat. 2, 3rd row to pat. 3. For each row, starting from left, it is reported a 3D representation of the "standard" segmentations, and coronal slices of the "standard" segmentations, of the segmentations with air removal using -900 HU threshold, and of the segmentation with air removal using -855 HU threshold.

6.3.2 SPECT filtering techniques

To accomplish the objective of studying the effect of SPECT artefacts and/or noise on dosimetric outcomes, SPECT filtering procedures were implemented with 3D Slicer, in particular using its module *Segment editor* and the option *Mask volume*, that allows thresholding and logical operations on segmentations, adopting a zero-order interpolation in case of operations between images with different voxel dimensions and resolutions. The following four filtering procedures were adopted:

A) Set to zero SPECT voxels corresponding to CT voxels having HU < -855. The aim was minimizing the event decay probability in air regions, by zeroing the activity concentration (or SPECT count concentrations) within them, exactly as done in Sec. 3.6.1. These kind of filter has a general validity, since its logic is to prevent the simulation of decay events in unrealistic positions in which, in the phantom, there is air and not perfused tissue.

B) The same procedure and motivations as A), but with HU < -900 threshold instead of HU < -855.

C) Apply B) and in addition set to zero the voxels within the "standard" VOIs segmentations of the right lung and left lungs. The application of B) served mainly to remove eventual non-zero SPECT values in the air outside patient's body. The overall aim was minimizing as much as possible the decay probability within lung VOIs. This scenario would be suitable for cases in which eventual activity concentration in lungs is attributable with confidence to motion blurring and background noise only, excluding even a minimal pulmonary shunt (i.e., a real spill out of radiopharmaceutical in lungs).

D) Set to zero all the SPECT voxels outside liver VOI segmentation, in order to have non-zero decay probability only inside liver. This choice represents the situation in which the radioembolization takes places exclusively within liver, without any spill out. This situation describes adequately the patient cases examined in this study, for which negligible shunt fractions were attested.

Each of the described filtering procedures was applied alone and independently on each native SPECT of the three TARE cases: starting from the native SPECT of a patient, four filtered SPECTs, each adopting one different filtering method among A, B, C and D, were produced. In Fig. 6.2 are reported, as an illustrative example, slices of the various filtered SPECTs for patient 2, together with logical difference images between native and filtered SPECTs, to better appreciate the areas where the filters had more effect in removing SPECT counts. In panels (c), (e) and (g) can be visualized the reduction of SPECT counts within lungs produced by filter A, B and C respectively, while in panel (i) the reduction is forced everywhere outside the liver by filter D, with evident effect nearby the border of the liver VOI.

6.3.3 Geometry and physics settings

To conduct the study, GATE version 8.2 relying on GEANT4 version 10.05.p01 was used, and GAMOS version 6.0.0, relying on GEANT4 10.02, was also used, only for a single case, as it will be described.

For each patient case, independent GATE simulations were carried out for native SPECT and for each filtered SPECT described, using always the native CT as the starting point to build the morphological phantom. For patient 2, which among the

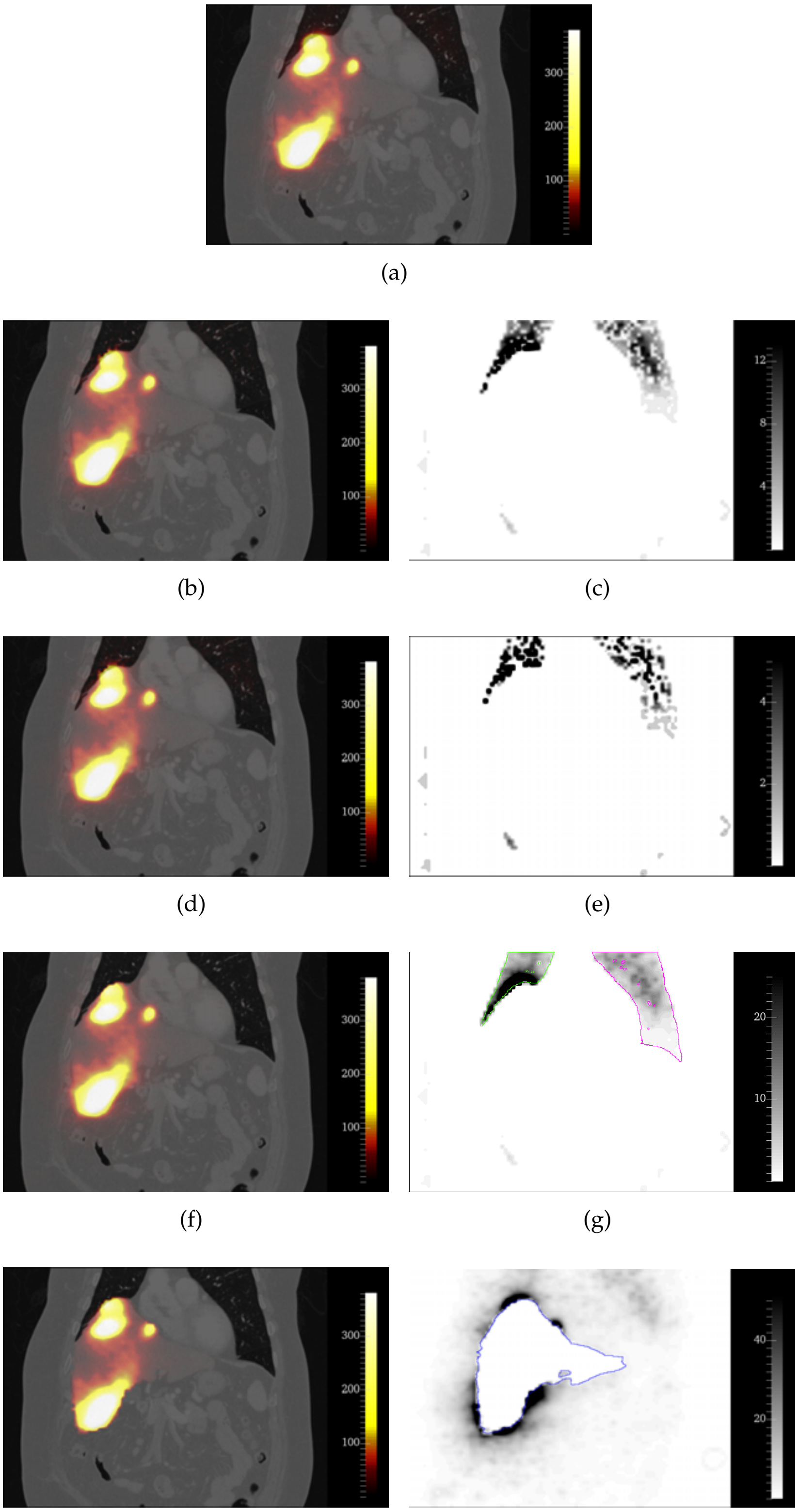

(a)

(b) (c)

(d) (e)

(f) (g)

(h) (i)

FIGURE 6.2: Pat. 2 coronal fusion slices of CT and SPECTs (counts), native (a) and filtered via A (b), B (d), C (f) and D (h) (Sec. 6.3.2), each accompanied on its right by the corresponding difference image between native and filtered SPECTs (e.g., (c) = (a) - (b)).

three patients has lesions in the upper part of liver, just at the interface with right lung (as visible in Fig. 5.4(c)), independent GAMOS simulations for native SPECT and each filtered SPECT were also carried out, to compare the results of the two toolkits in this more particular situation.

Given a patient, to build the corresponding voxelized phantom reproducing the body in the FoV of the CT, the *Automated HU stoichiometric calibration* was employed on the CT, with the same materials, HU intervals and HU-density calibration described in Sec. 3.4.4; the density tolerance was set 0.1 g/cm^3, as advisable from the results obtained in Chapter 4. In the case of GAMOS for patient 2, the procedure followed is the same described in Sec. 3.4.4.

For each different Tc-MAA SPECT (either the native one or one of the filtered ones), the functional scan was imported into GATE (and GAMOS for patient 2) to define the voxelized source reproducing the ^{90}Y spatial distribution, as explained in Sec. 3.4.5. ^{90}Y nuclei at rest were obviously set as ion type primary radiation, activating their decay with the *G4RadioactiveDecay* module. To simulate the interactions of their daughters with matter, the *G4EmStandardPhysics_option3* physics list was set.

For each simulation executed, the absorbed doses at voxel level D^{ijk}_{out} and their respective standard deviation of the mean absorbed dose δ^{ijk}, as described in Sec. 3.4.7 and in [117], were scored with *DoseActor* employing the *MassWeighting* algorithm in GATE, and with *GmPSPrinter3ddose* scorer in GAMOS, setting in both cases the scoring grid dimensions and resolutions equal to the ones of the CT.

All the simulations were run simulating $2{\cdot}10^8$ primary events, a value which ensured an average value of the standard deviation of the mean absorbed dose ($\langle\delta^{ijk}\rangle_{VOI}$) below 4% in lesions and below 6% in liver perfused and healthy liver perfused, for all the three patient cases.

6.4 Post-simulation dosimetric calculations

The correct absorbed dose values at voxel level for each simulation, D^{ijk}, were calculated as in Equation 4.2, with the cumulated-activity $\tilde{A}$ calculated exactly as in Eq. 4.3 and $A(0)$ being the actual administered activities during the TARE treatments of the considered patients, reported in Tab. 5.3. After producing the correct absorbed dose maps for each simulation, average absorbed doses within the examined VOIs, $\langle D\rangle_{VOI}$ defined as in Eq. 4.4, were evaluated with the *Segment Statistics* module of 3D Slicer; the same was done with the maps of standard deviation of the mean absorbed dose, to evaluate the average values within VOIs, $\langle\delta\rangle_{VOI}$ defined as in Eq. 4.5. An additional absorbed dose calculation was performed weighting the native-SPECT results for the factor b defined in Eq. 5.2, which is thought for background correction outside liver (it basically has the same objective of the SPECT filter D (Sec. 6.3.2), but it is a post-simulation correction rather than a pre-simulation correction). This additional calculation was done for liver VOIs only, since the background correction factor b is thought specifically for liver, and it would not make sense applied to lungs.

The average absorbed doses in VOIs obtained with the various filtered SPECTs (X) were compared in terms of relative percent differences $\kappa_{VOI,X\,filter}$ (%) with respect to the average absorbed doses obtained with native-SPECT (not-background-corrected) simulations:

$$\kappa_{VOI,\,X\,filter} = 100 \cdot \frac{\langle D_{\,X\,filter}\rangle_{VOI} - \langle D_{\,native}\rangle_{VOI}}{\langle D_{\,native}\rangle_{VOI}} \tag{6.1}$$

In addition, for each type of filtered-SPECT simulation and each VOI, the average value of these relative percent differences over the three patients, $\langle \kappa_{VOI,\, X\, filter} \rangle$ (%), were calculated:

$$\langle \kappa_{VOI,\, X\, filter} \rangle = \frac{\kappa^{pat1}_{VOI,\, X\, filter} + \kappa^{pat2}_{VOI,\, X\, filter} + \kappa^{pat3}_{VOI,\, X\, filter}}{3} \tag{6.2}$$

together with the standard deviations of these averages, $\sigma_{VOI,\, X\, filter}$.
For the simulations relative to patient 2, done both with GATE and GAMOS, the average absorbed dose results of the two toolkits were compared, for each SPECT type, as relative percent differences ε_{VOI}, taking GATE as a reference:

$$\varepsilon_{VOI} = 100 \cdot \frac{\langle D_{\text{ GAMOS}} \rangle_{VOI} - \langle D_{\text{ GATE}} \rangle_{VOI}}{\langle D_{\text{ GATE}} \rangle_{VOI}} \tag{6.3}$$

Dose Volume Histograms (DVHs) within VOIs for each simulation were also calculated, using Slicer's *Dose Volume Histogram* module.

6.5 Results and discussion

The average absorbed doses $\langle D \rangle_{VOI}$ in the defined VOIs for all the GATE simulations performed and their relative percent differences κ_{VOI} (%) with respect to the absorbed doses obtained with native-SPECT simulations are reported in histogram form in Fig. 6.3 and Fig. 6.4 for patient 1, in Fig. 6.5 and Fig. 6.6 for patient 2, in Fig. 6.7 and Fig. 6.8 for patient 3. The error bars in each of those histograms' bins are actually the average values of the standard deviation of mean absorbed dose within VOIs, $\langle \delta \rangle_{VOI}$, that were defined in Eq. 4.5 and correspond to the maximum statistical uncertainty associated to each average absorbed dose value. In Fig. 6.9 are reported the average values $\langle \kappa_{VOI} \rangle$ (Eq. 6.2) of these relative percent differences over the three patients, for each type of simulation and VOI, with error bars representing in this case the standard deviations σ_{VOI} of the averages. All the DVHs are instead reported in Appendix B, in Fig. B.1-B.6

6.5.1 Liver-related VOIs

Considering the average absorbed dose results in all the liver-related VOIs, for all patients emerge slight increases of absorbed dose with respect to the native-SPECT simulation for the simulations adopting the filters removing activity in air (A and B in Sec. 6.3.2) and lungs (C), represented as red, purple and dark blue bins in histograms, respectively. These increases are on average smaller than 5% in terms of $\langle \kappa_{VOI} \rangle$. The increase becomes instead significant, between about 30% and 40%, for the filter removing activity outside liver (D in Sec. 6.3.2, represented as light-blue bins in histograms), and on average of 50% in the case the native results rescaled for the background correction factor b (aqua green in histograms). Relative percent differences κ_{VOI}s show similar values in each VOI for each given simulation. The native background corrected results show exactly equal κ_{VOI}s in all the liver-related VOIs for each patient, following simply from this calculation algorithm, applying the same factor b to all the voxels of the native absorbed dose maps (Eq. 5.4). In particular, the increase produced by the factor b is of about 35% for patient 2 and 3, and about 75% for patient 1, thus depending strongly on the specific case. The use of this background correction factor on MC native-SPECT results can be considered as a standard and simple technique to avoid the effect of SPECT fictitious activity spill-out, due to noise and blurring, in cases when real shunts are recognized as absent or negligible, as in [48] and in the present study. In fact, as also observed in Chapter 5, first of all, without applying it, the native-SPECT Monte Carlo results happen to be significantly lower than all the other dosimetry approaches of *OpenDose Dosimetry 3D*. The results of the present chapter, using the same datasets, confirm this trend with the Monte Carlo filtered-SPECT simulations, since the filter returning closer results to the native background-corrected ones is the D filter, removing all the SPECT activity outside the liver VOI. Filter D is the most reasonable for the TARE cases examined, since the eventual spill-outs and artefacts present in the imaging should be ascribed entirely to residual reconstruction noise, background noise and motion blurring, and the corresponding activity has to be considered as liver activity. Thus the post-simulation correction through the b factor confirms to be a sufficiently effective alternative to account for the mentioned fictitious activity spill-outs in SPECTs. Changing point of view, it is reasonable to deduce that the native-SPECT results alone underestimate absorbed doses in liver-related VOIs. Filters A, B and C also underestimate liver absorbed doses, being not able to return results close to filter D and to the native background corrected ones.

An isolated exception is observed for the D-filter simulation absorbed dose in healthy liver perfused VOI of patient 3, which is lower than the native simulation absorbed dose. The cause of this behaviour can be identified simply in the definition of the segmentation of this VOI, obtained as volume difference between liver perfused, segmented on SPECT via a threshold based technique, and lesion VOI, segmented on CT (as described in Sec. 5.3.2). In the specific case of patient 3, liver perfused segmentation, because of some spill out ascribable to motion blurring and background noise, and because of the threshold-based nature of this segmentation, extends outside the liver VOI in some high-perfused areas near the liver borders, and so does also the healthy liver perfused VOI, as it can be noticed in panels (i)-(l) of Fig. 5.5. As a consequence, the D filter, by zeroing all the activity outside liver VOI, is in all likelihood the motive of the mentioned isolated reduction of absorbed dose in healty liver perfused.

The comparison between GATE and GAMOS simulation results, made only for patient 2, is reported in Fig. 6.10(a) for liver-related VOIs, and shows excellent agreement in all of them, with relative differences ε_{VOI} always below 0.4%.

6.5.2 Lungs-related VOIs

Considering the average absorbed dose results in the "standard" lungs VOIs (Sec. 6.3.1), it can be observed how filters reduce even a lot the average absorbed dose with respect to native-SPECT simulations. On average (Fig. 6.9), filter A, removing activity in air using a threshold of -855 HU, produces a reduction of 35-40% in both lungs; filter B - same as A but with -900 HU threshold - a reduction of 15-20%; filter C, removing entirely the activity in "standard" lungs VOIs, a reduction of 75% in right lung and 65% in left lung; filter D, removing all the activity outside the liver VOI, a reduction of about 90% in right lung and even of 99-100% in left lung, practically zeroing its absorbed dose.

Looking at the results in the other two alternative segmentations for each lung, with air voxels removed from segmentations, no significant differences are observed with respect to the "standard" segmentations for each lung, independently form the considered patient. This suggests that a post-simulation air "correction", based on executing the average absorbed dose evaluation on the absorbed dose maps using lungs VOIs with air voxels removed, is not actually effective in excluding possible absorbed dose overestimation and artefacts in lungs. As a matter of fact, in the native-SPECT simulations decay events can be anyways produced also from those air voxels if non-zero activity is found in them, and even excluding those voxels in the segmentations used for the average calculations, the energy depositions (and consequent absorbed doses) caused by them in the surrounding actual lung voxels are practically unchanged. In the various filtered-SPECT simulations the insensitivity to the three alternative lungs segmentations is motivated even more by the fact that decay events in air and lungs are reduced or totally cleared, depending on the filter.

Pre-simulation correction applied via SPECT-filtering techniques proves instead to have a strong effect on lungs dosimetric outcomes, and appeared to have the potential for being an effective tool for the correction of dose artefacts caused by different types of noise present in functional input scans. Based on the same consideration made for liver-related VOIs regarding SPECT artefacts due to motion blurring and background noise, depending on how much they cause unrealistic activity distributions in air and lungs, we can conclude that native-SPECT MC simulations can highly overestimate absorbed doses in lungs, especially because of their low densities and their nearness to liver perfused, the - ideally - only source in TARE. A careful choice and implementation of the filters is essential, requiring the help and opinion of physicians, in particular specialists of nuclear medicine and radiology, in order to recognize, based on their experience, blurring and noise caused by patient movement, tomographic reconstruction and background, distinguish them from actual shunts or leakages from the target organ, and select accordingly the most suitable filter. Filters like A and B can be in principle applied in any case, since they minimize the simulation of decays in correspondence to air regions, irrespective of the presence of shunts. Filters like C and D can be applied when no pulmonary shunts or no shunts at all are attested by the physicians, respectively.

The obtained results confirm the potential utility and benefit of using filtering methods of the functional scans to try obtaining more accurate absorbed dose results in lungs but also in liver, as seen in the previous paragraph, and as already suggested from the results of Chapter 3. In the case of TARE, differently from ^{18}F-choline PET imaging having to deal with the systemic biodistribution of choline, the selective distribution of ^{90}Y-loaded microspheres (or the similar ^{99m}Tc-MAA distribution in pre-therapy data, like ours) ensures much less indeterminacy in recognizing liver activity blurring and noise, giving a safer proof of lung absorbed doses overestimation when simply using native functional scan as input data.

The comparison between GATE and GAMOS simulation results, made only for patient 2, is reported in Fig. 6.10(b) for liver-related VOIs, and shows good agreement in all of them, both "standard" and alternative with air voxels removed; the relative differences ε_{VOI} are in all cases below 4%. GAMOS results appear systematically the ones little larger than GATE ones, an effect imputable, being equal all the other geometry and physics setting, to the different density assignment procedure of the two toolkits (similarly to what noticed in Chapter 3), to which low-density and poorly-perfused regions are more sensible; evidently, for this specific case, GAMOS has assigned on average little lower densities to voxels with respect to GATE.

All the discussed evidences, both for liver-related VOIs and lungs-related VOIs, can be deducted also in terms of voxel-level behaviours, made clear by DVHs in Appendix B. For liver-related VOIs, The DVHs representing the filter D, zeroing activity outside the liver, and the ones representing native background corrected results, are the ones deviating the most toward larger values with respect to the remaining simulations, which instead show close DVHs. For lungs VOIs, the DVHs corresponding to the various filtered-SPECT simulations show the respective decreases of lungs absorbed doses, and the invariance of results when using "standard" lungs VOIs and alternative lungs VOIs with air voxels removed, since almost identical DVHs for each triplet of VOI choice are obtained. For patient 2, for which also GAMOS simulations were carried out, GATE and GAMOS DVHs are practically superimposed for each type of simulation in each VOI, confirming their optimal agreement.

The mentioned evidences can also be visually appreciated directly from absorbed dose maps, for example looking at the coronal slices reported in Fig. 6.11, referring to patient 2 GATE simulations. Already comparing the filtered-SPECT absorbed dose slices in colored scale of panels (b), (d), (f) and (h) with the native-SPECT one of panel (a), it is evident the absorbed dose lowering in lungs, more or less pronounced depending on the filter. From the difference images in grayscale in panels (c), (e), (g) and (i), the lungs absorbed dose reduction appears more clear, and also the increase of liver absorbed dose for filtered-SPECT results is evident, especially for C and D filters in correspondence to lesions.

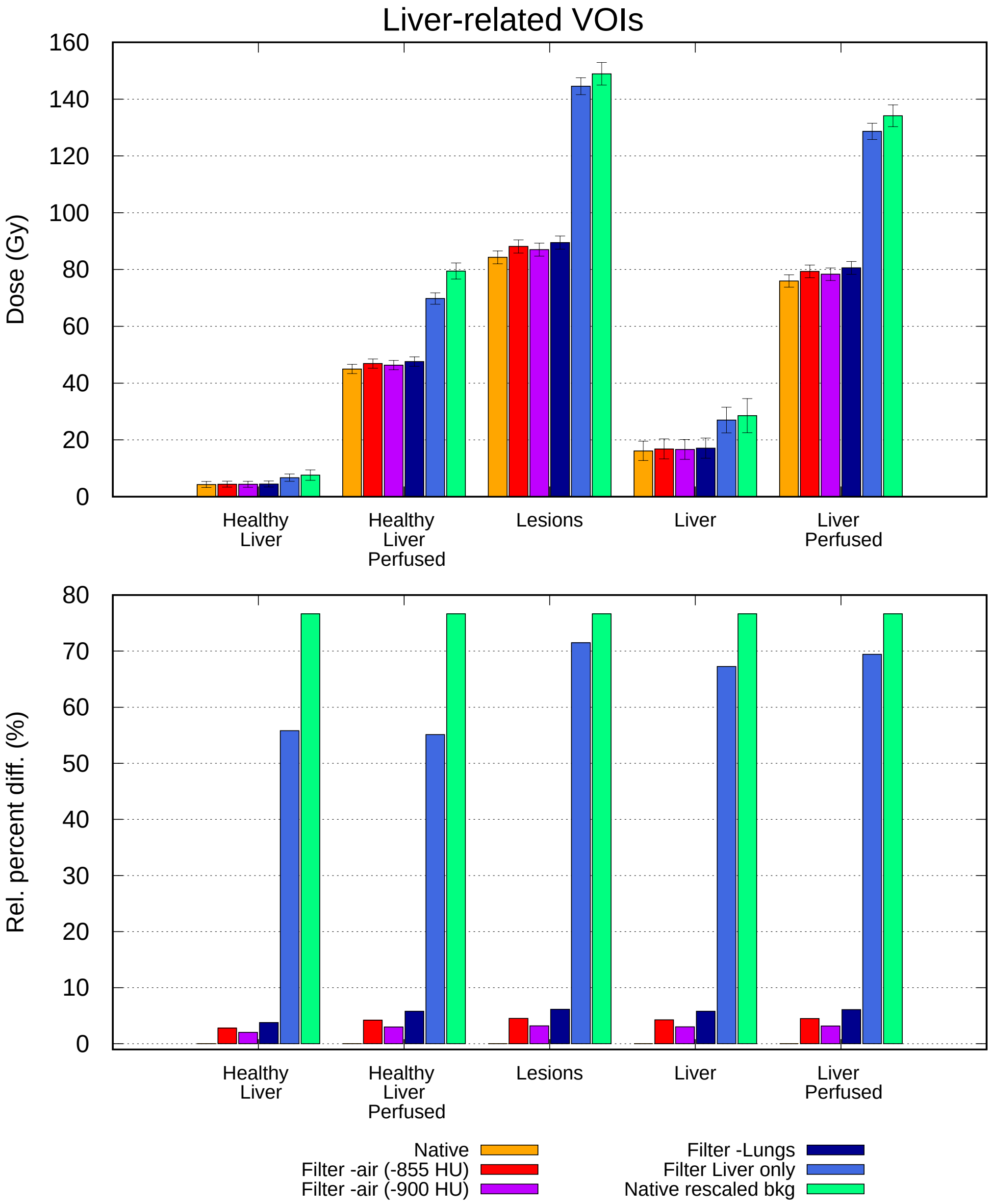

FIGURE 6.3: GATE average absorbed doses $\langle D \rangle_{VOI}$ in liver-related VOIs and corresponding relative percent differences κ_{VOI} with respect native-SPECT simulation for patient 1; the error bars are the average values of standard deviation of mean absorbed dose within VOIs, $\langle \delta \rangle_{VOI}$ (Eq. 4.5).

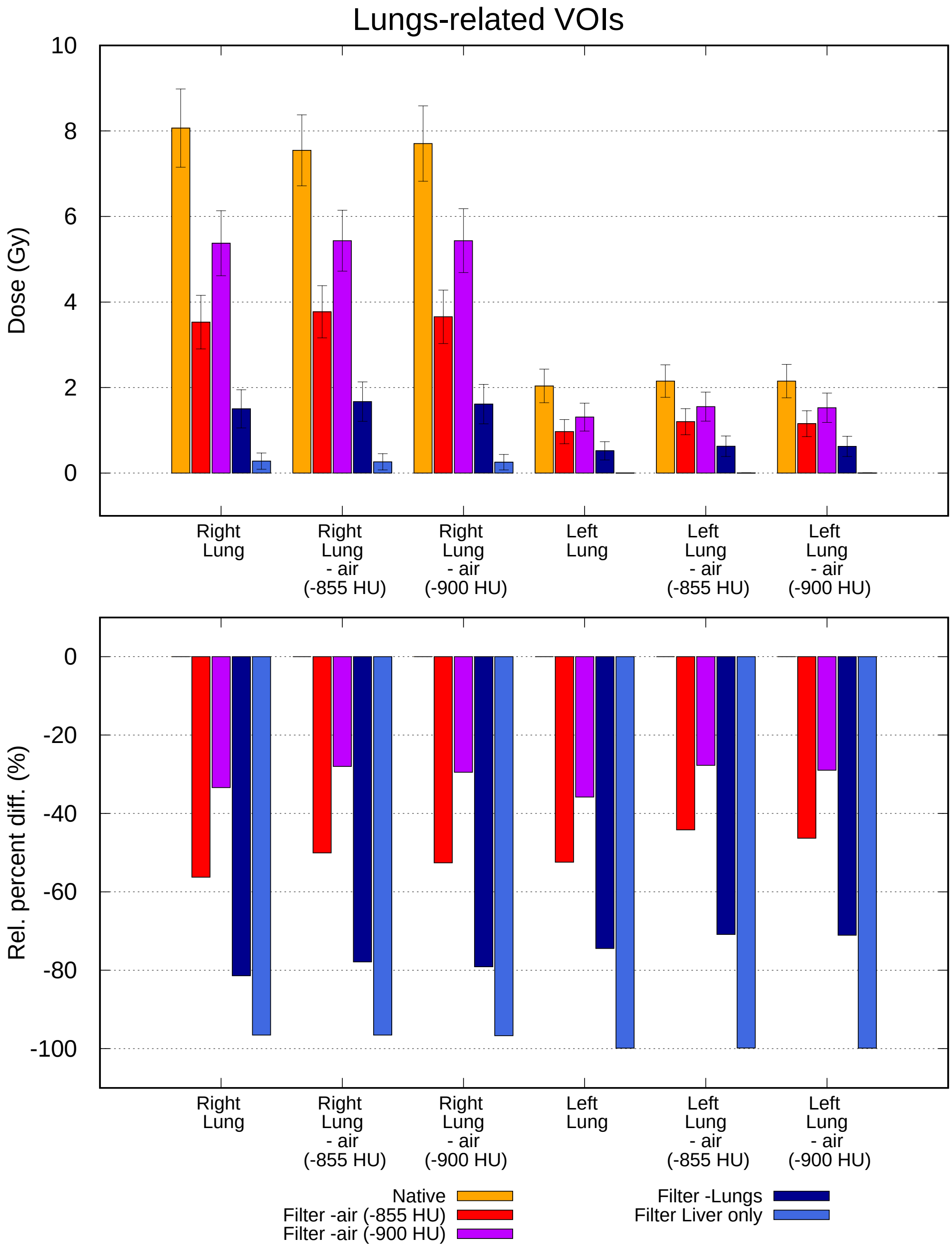

FIGURE 6.4: GATE average absorbed doses $\langle D\rangle_{VOI}$ in lungs-related VOIs and corresponding relative percent differences κ_{VOI} with respect native-SPECT simulation for patient 1; the error bars are the average values of standard deviation of mean absorbed dose within VOIs, $\langle\delta\rangle_{VOI}$ (Eq. 4.5).

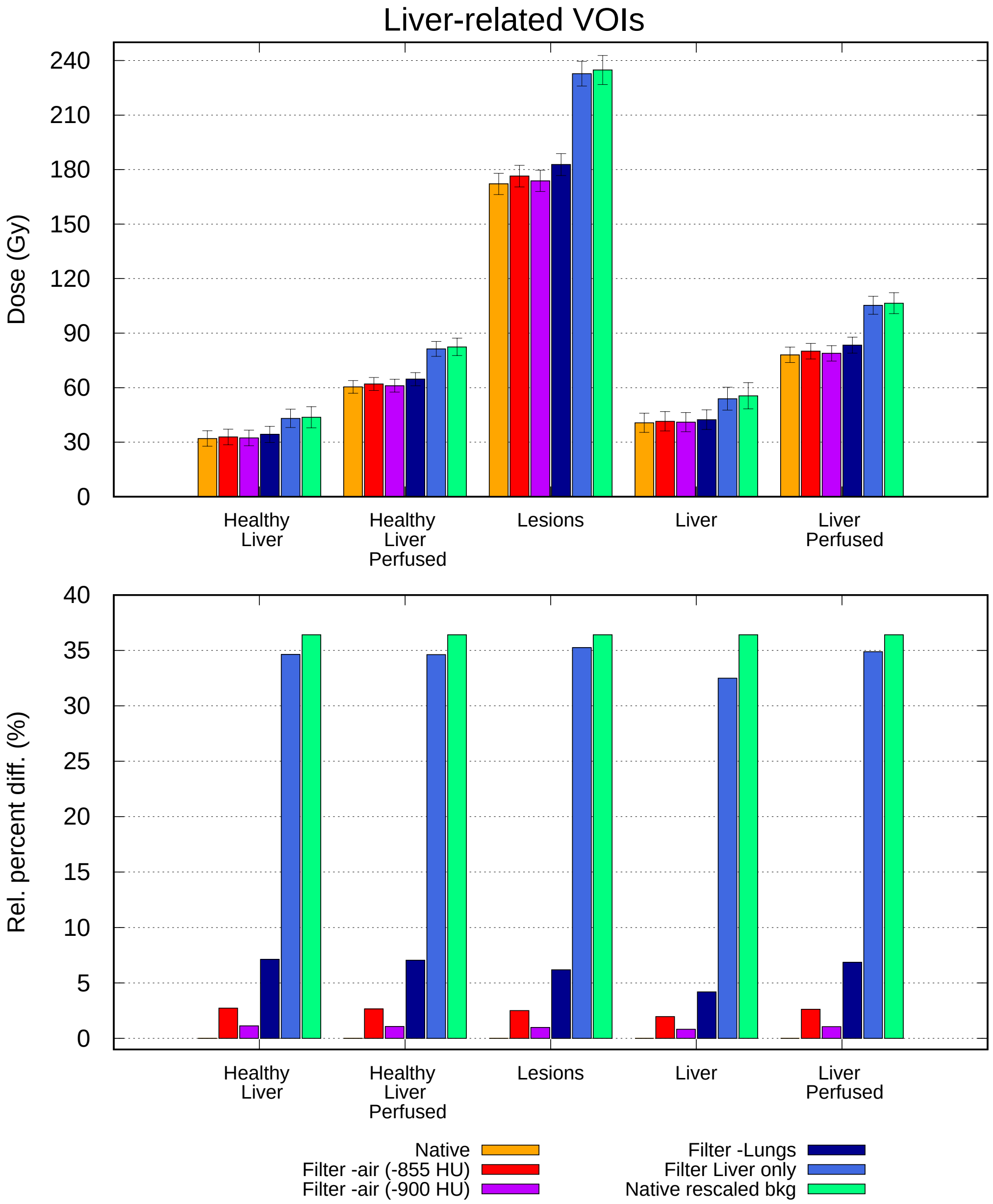

FIGURE 6.5: GATE average absorbed doses $\langle D \rangle_{VOI}$ in liver-related VOIs and corresponding relative percent differences κ_{VOI} with respect native-SPECT simulation for patient 2; the error bars are the average values of standard deviation of mean absorbed dose within VOIs, $\langle \delta \rangle_{VOI}$ (Eq. 4.5).

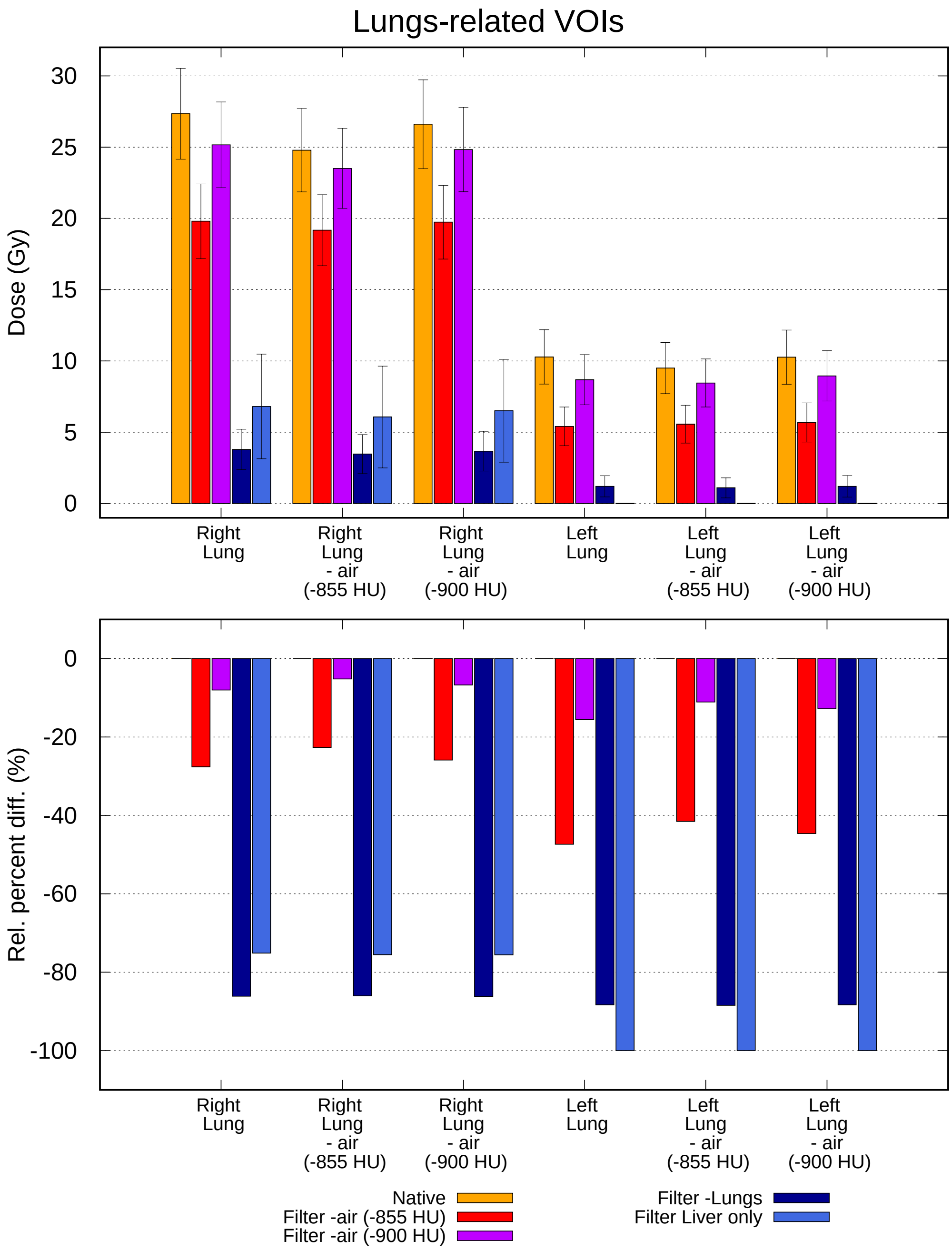

FIGURE 6.6: GATE average absorbed doses $\langle D \rangle_{VOI}$ in lungs-related VOIs and corresponding relative percent differences κ_{VOI} with respect native-SPECT simulation for patient 2; the error bars are the average values of standard deviation of mean absorbed dose within VOIs, $\langle \delta \rangle_{VOI}$ (Eq. 4.5).

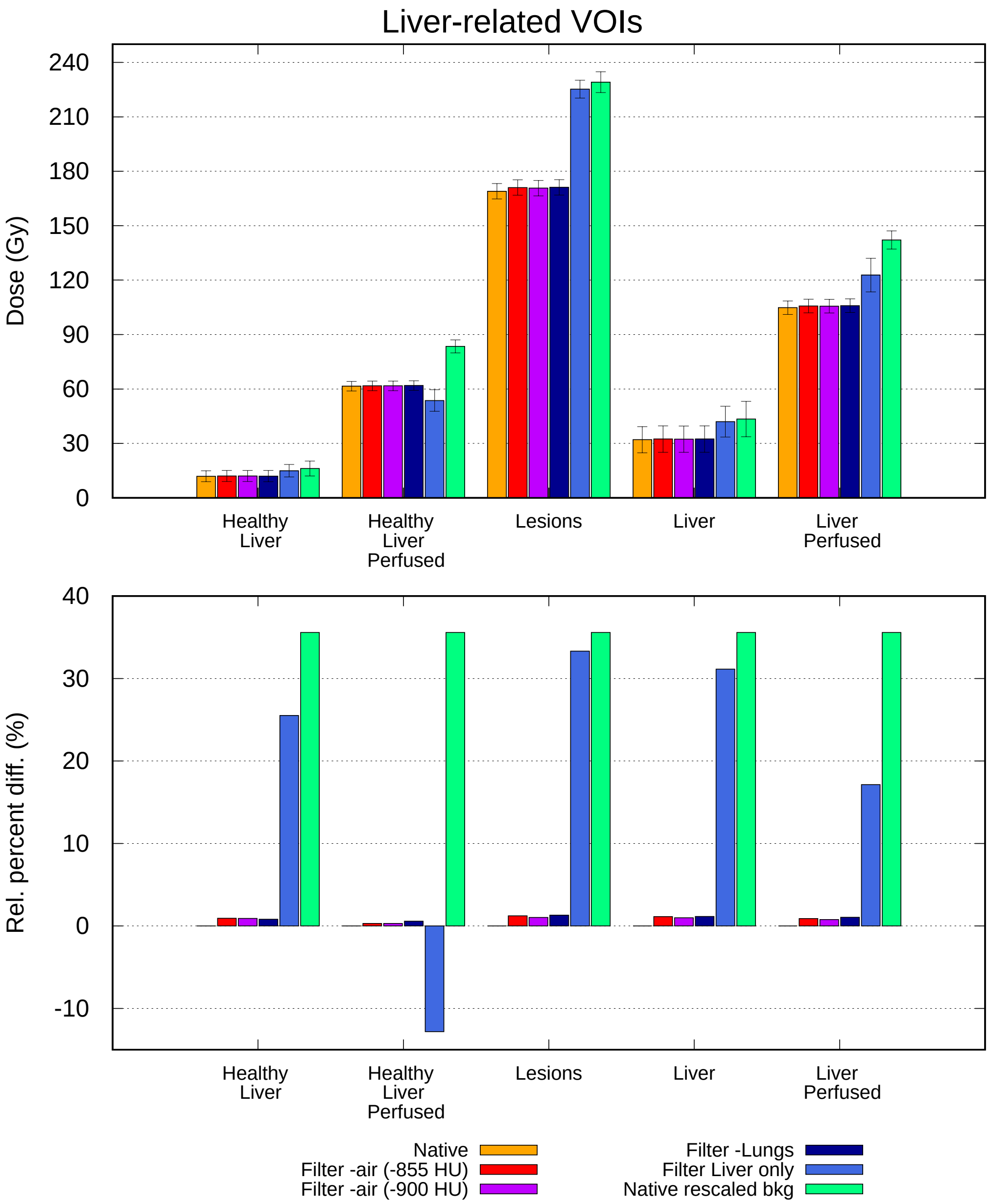

FIGURE 6.7: GATE average absorbed doses $\langle D \rangle_{VOI}$ in liver-related VOIs and corresponding relative percent differences κ_{VOI} with respect native-SPECT simulation for patient 3; the error bars are the average values of standard deviation of mean absorbed dose within VOIs, $\langle \delta \rangle_{VOI}$ (Eq. 4.5).

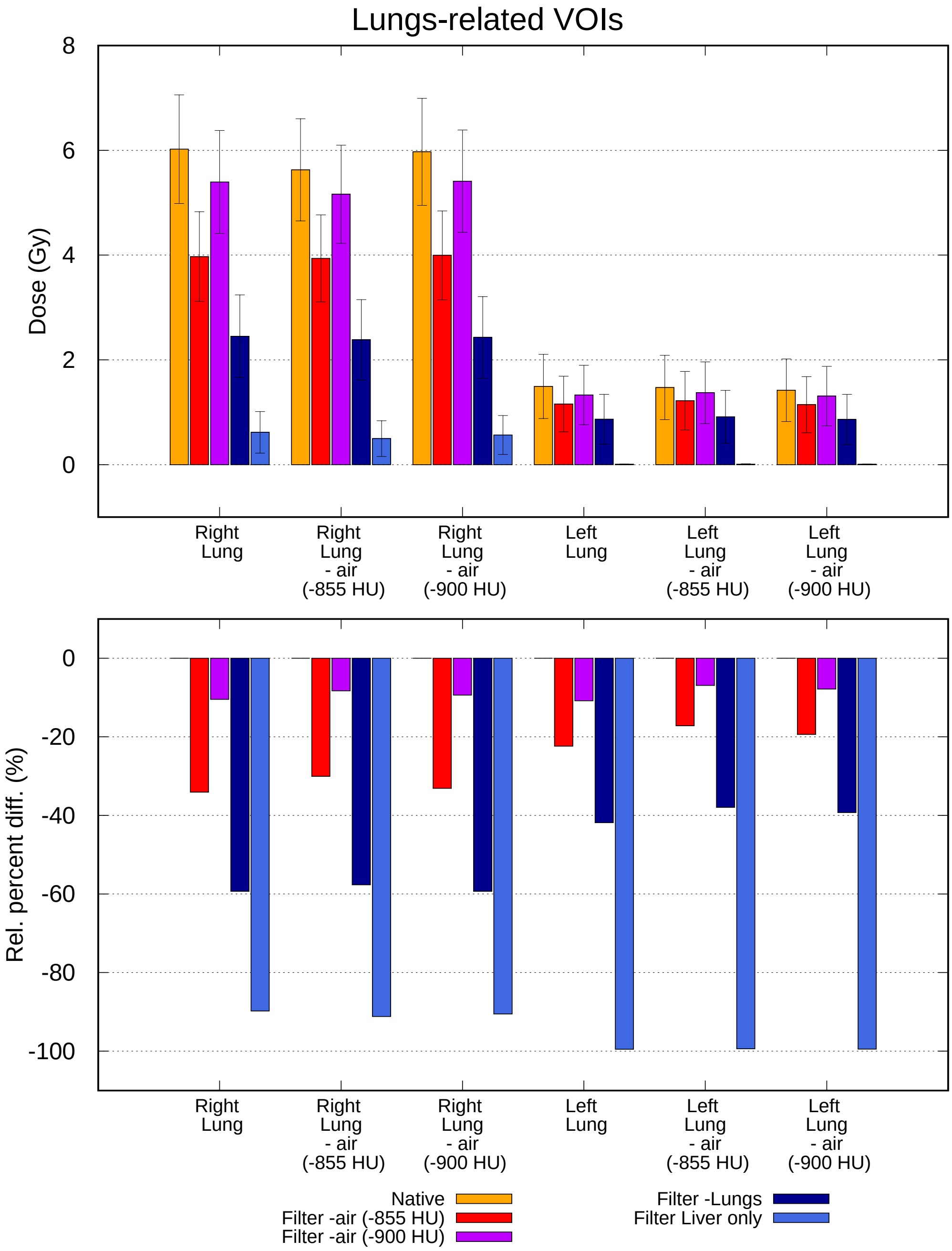

FIGURE 6.8: GATE average absorbed doses $\langle D \rangle_{VOI}$ in lungs-related VOIs and corresponding relative percent differences κ_{VOI} with respect native-SPECT simulation for patient 3; the error bars are the average values of standard deviation of mean absorbed dose within VOIs, $\langle \delta \rangle_{VOI}$ (Eq. 4.5).

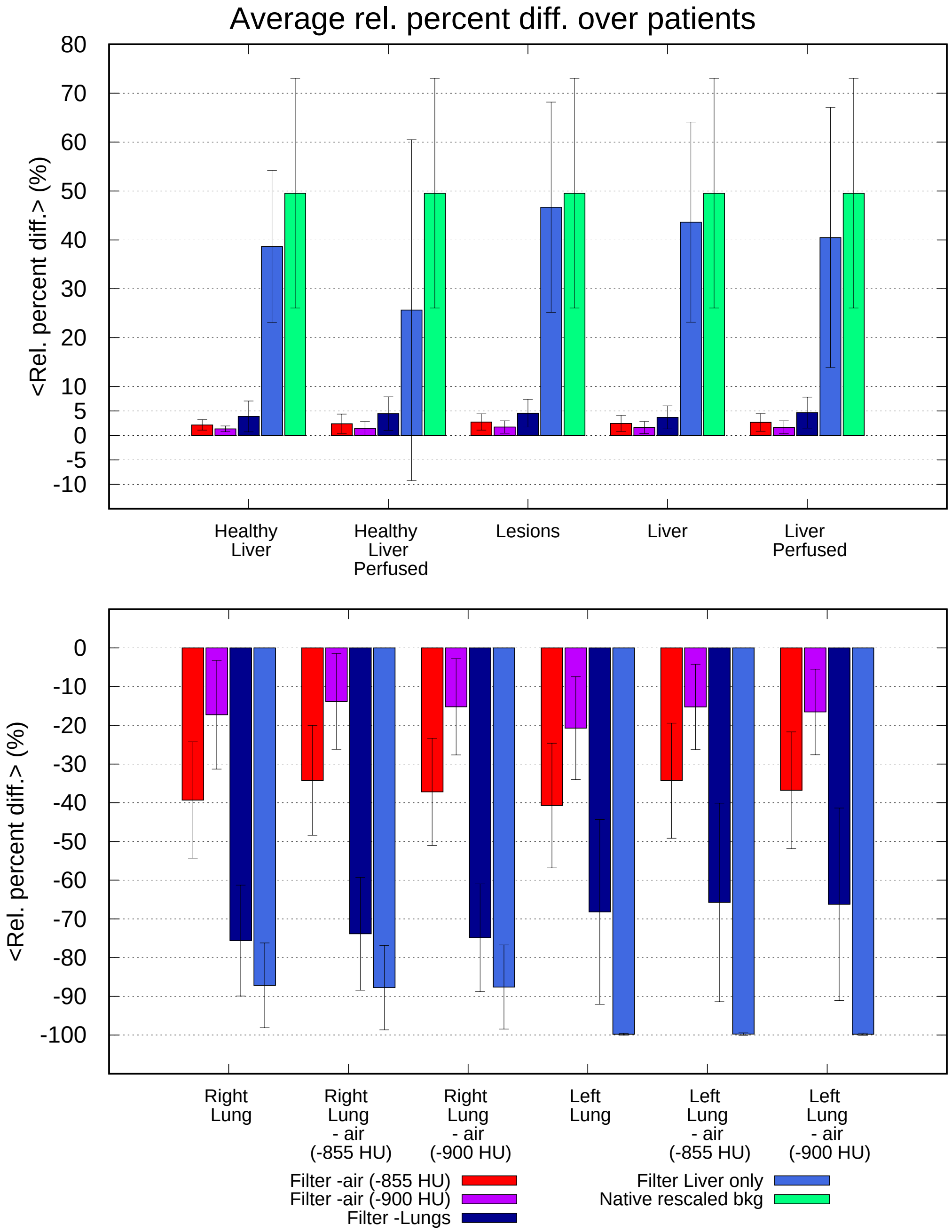

FIGURE 6.9: GATE average values of relative percent differences $\langle\kappa_{VOI}\rangle$ (Eq. 6.2) over the three patients in each type of VOI; the error bars here represent the standard deviations of the averages, σ_{VOI}.

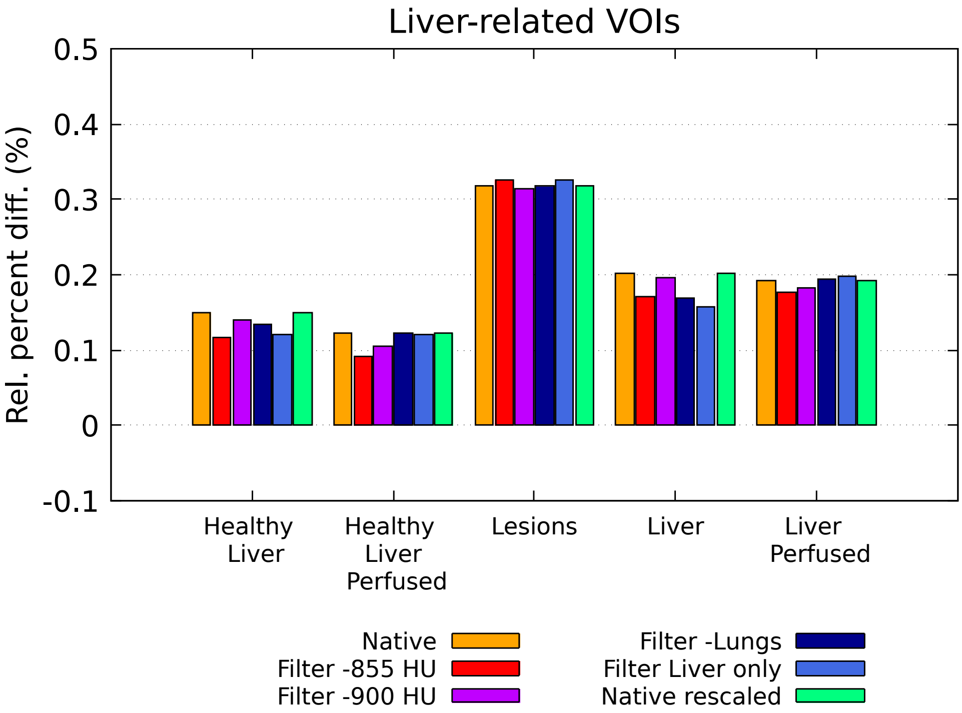

(a)

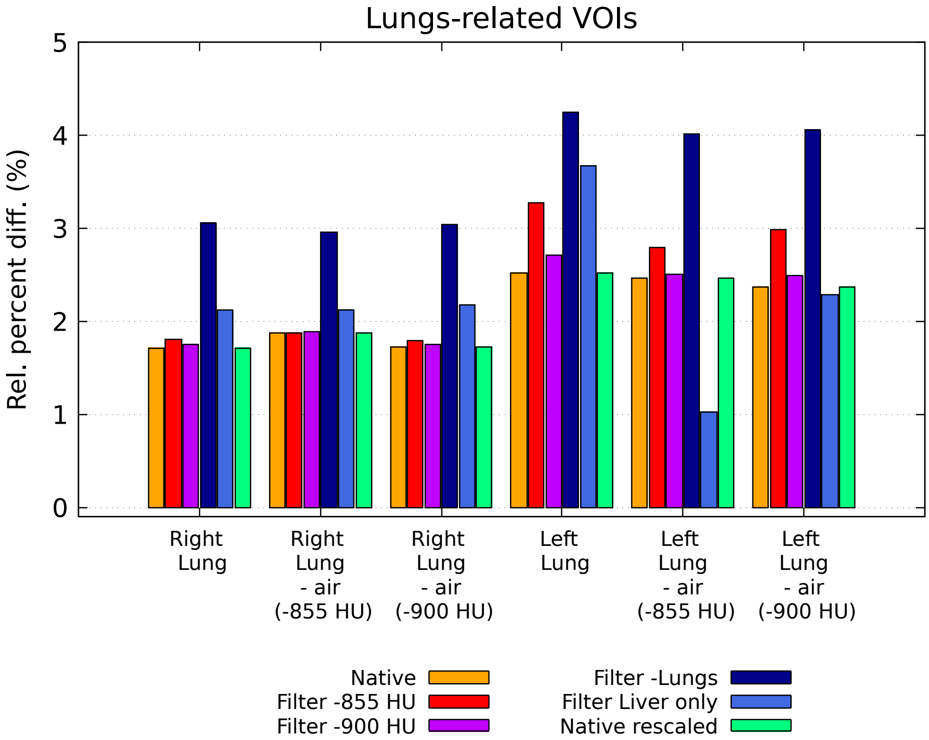

(b)

FIGURE 6.10: Comparison between GATE and GAMOS simulations average absorbed dose results for patient 2, in terms of relative percent differences ε_{VOI} (Eq. 6.3).

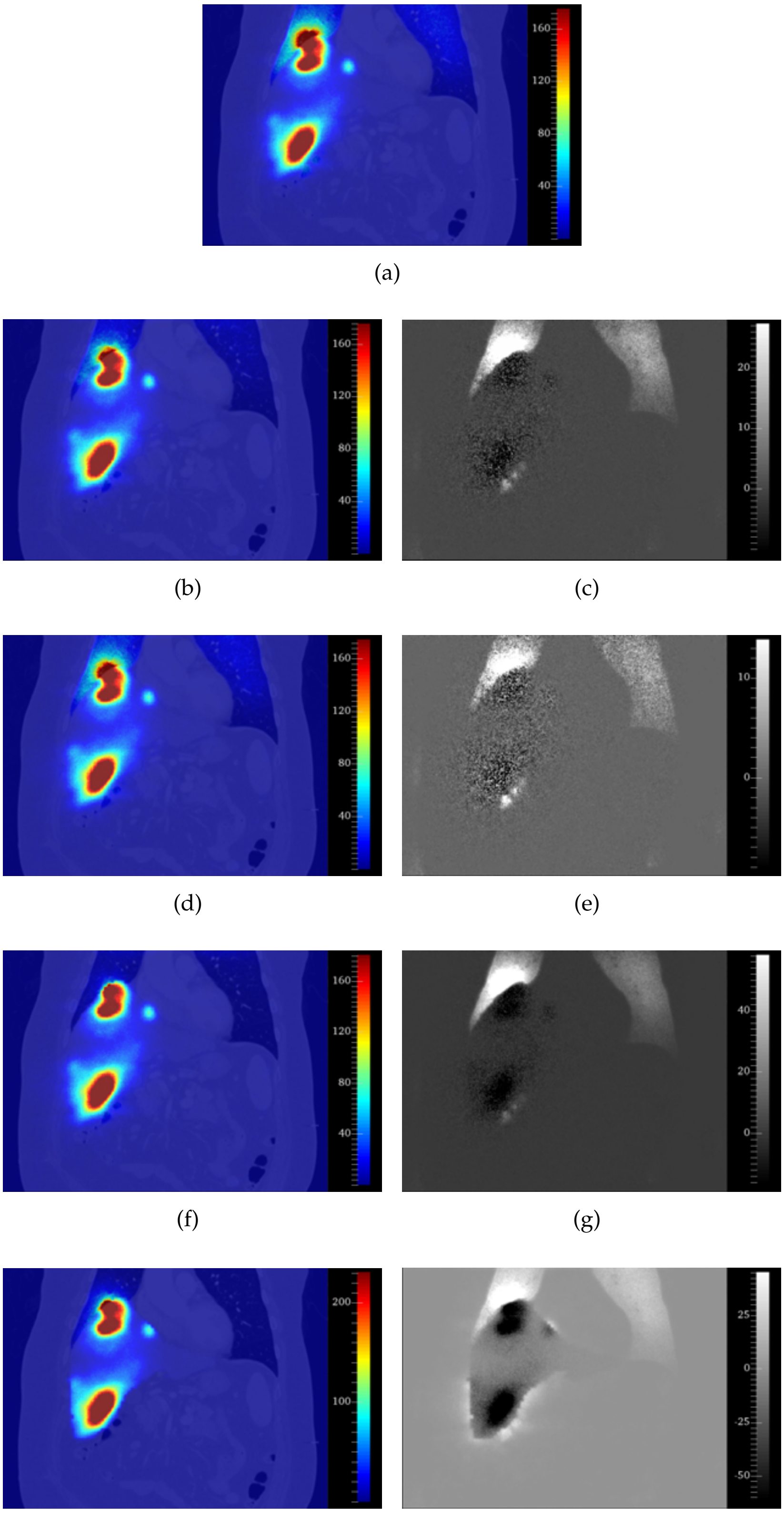
160
120
80
40
160
120
80
40
20
10
0
160
120
80
40
10
0
160
120
80
40
40
20
0
200
100
25
0
-25
-50

(a)

(b) (c)

(d) (e)

(f) (g)

(h) (i)

FIGURE 6.11: Coronal fusion slices for patient 2 of CT and GATE absorbed dose maps (Gy) obtained with native- (a) and filtered-SPECT A (b), B (d), C (f) and D (h) (Sec. 6.3.2), each accompanied on its right by the corresponding difference image (Gy) between native- and filtered-SPECT absorbed dose maps.

Chapter 7

A simplified kidney dosimetry protocol for ^{177}Lu-PRRT

7.1 Introduction

Imaging-based patient-specific kidney dosimetry provides a valuable contribution to the optimization of the activity administration in ^{177}Lu Peptide Receptor Radionuclide Therapy (PRRT) of NeuroEndocrine Tumors (NETs). However, the need of multiple SPECT/CT acquisitions and the subsequent dosimetric workflow imply a remarkable resource effort. In this Chapter, after a brief outline on NETs and PRRT, an original simplified personalized kidney dosimetry protocol for ^{177}Lu therapies will be presented. The protocol relies on a single quantitative SPECT/CT and multiple radiometric measurements executed with a collimated external probe, properly directed on kidneys. To introduce this protocol, a proof-of-concept study composed of three steps was carried out. First, an experimental phantom study characterized by external count-rate measurements in an abdominal phantom setup filled with activity concentrations of ^{99m}Tc, reproducing relevant organ effective half-lives occurring in ^{177}Lu PRRT, was conducted. The kidney half-life estimated through the external measurements resulted compatible within 3% with the expected value. Secondly, GATE Monte Carlo (MC) simulations reproducing the experiment, using ^{99m}Tc and ^{177}Lu as sources, were performed, confirming a similar level of accuracy. Thirdly, the proposed method was tested via MC simulations on a clinical case of ^{177}Lu-DOTATATE PRRT, with a dataset made of SPECT/CT images at three time points, comparing a simplified kidney dosimetry, employing a single SPECT/CT and probe measurements simulated at three time points, with the full image-based MC dosimetry. The simplified dosimetric method led to a kidney absorbed dose estimation compatible with the complete MC dosimetry within about 6%, 12% and 1%, using respectively the SPECT/CT at 2, 20 and 70 hours. The favourable aspects characterizing the proposed protocol, as well as the perspectives opened by it, will be finally discussed.

7.2 ^{177}Lu Peptide Receptor Radionuclide Therapy (PRRT) for NeuroEndocrine Tumors (NETs)

NeuroEndocrine Tumors (NETs) are a very diverse group of neoplasms arising from cells of the endocrine (hormonal) and nervous systems, whose primary site usually originates in gastrointestinal and bronchopulmonary tracts. However, all of them usually share the common feature of expressing somatostatin receptors (SSTRs). Therefore, somatostatin analogs (SSAs) are used for symptom relief and treatment, as well as for molecular imaging to localize the malignancies [131, 132]. Among

the therapeutic options available for NETs, Peptide Receptor Radionuclide Therapy (PRRT) has shown to be very promising, especially for the patients who suffer metastasized disease and require systemic treatment, which are about 40% of the total. PRRT consists in administering radiolabeled SSAs, so that they bind SSTRs on tumor cells, are internalized and later stored in lysosomes, thereby delivering the radioisotope to the tumor cells, that are finally targeted this way.
In 2018 the Food and Drug Administration (FDA) approved the therapeutic use for gastroenteropancreatic NETs (GEP-NETs) of ^{177}Lu-DOTATATE (also named ^{177}Lu-oxodotreotide, trade name LUTATHERA®), a chelated complex of ^{177}Lu with (Tyr3)-octreotide SSA through the DOTA chelator [132]. ^{177}Lu is a beta-emitting isotope of lutetium, decaying with 100% Branching Ratio and with an half-life of $T_{\frac{1}{2}} = 6.6443$ days into Hafnium ground state (79.44% of the time) [111]:

$$^{177}_{71}\text{Lu} \rightarrow {}^{177}_{72}\text{Hf} + \beta^- + \bar{\nu} \tag{7.1}$$

or into one of Hafnium's excited states, rapidly de-exciting by emitting gamma photons:

$$^{177}_{71}\text{Lu} \rightarrow {}^{177}_{72}\text{Hf}^* + \beta^- + \bar{\nu} \rightarrow {}^{177}_{72}\text{Hf} + \gamma + \beta^- + \bar{\nu} \tag{7.2}$$

The emission of such gammas makes the use of ^{177}Lu useful also for monitoring tumor response via functional imaging. The beta-emission spectrum of ^{177}Lu is reported in Fig. 7.1, and it is characterized by an overall end-point of $E_{\beta^- max}$ = 496.8 keV, and an overall average beta-emission energy of $\langle E_{\beta^-} \rangle$ = 133.644 keV [111].

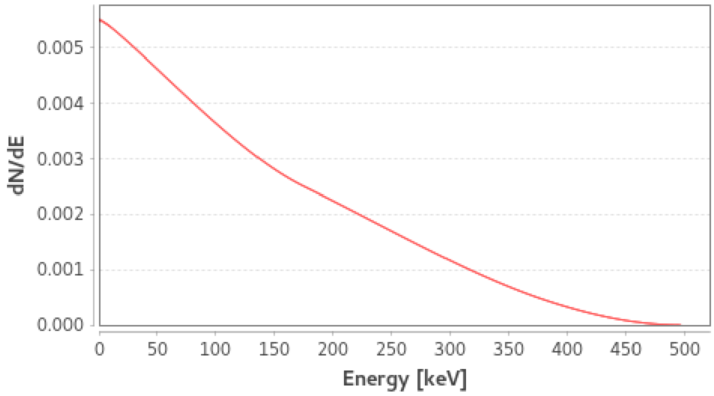

FIGURE 7.1: β^--emission energy spectrum of ^{177}Lu [111].

This lower energy and consequent lower range of ^{177}Lu's beta particles with respect to other radionuclides used in PRRT, such as ^{90}Y, are suitable for smaller lesion volumes, such as metastatic NETs, while the higher-energetic betas of ^{90}Y are more suitable for large tumors. For example, ^{177}Lu-DOTATATE for patients with SSTR-positive NETs has been shown to have comparable efficacy but a better hematological toxicity profile than ^{90}Y-DOTATOC [131]. In many studies, ^{177}Lu-DOTATATE, and in general ^{177}Lu in combination with SSAs, has proven efficacy in treating GEP-NETs in candidates with SSTR-positive advanced tumors and normal renal function, with good response in terms of decrease of tumor size, improvement of symptoms and of the quality of life. Adverse effects associated with ^{177}Lu-PRRT include myelotoxicity, due to irradiation of the bone marrow, and nephrotoxicity, as the radiopeptides are reabsorbed in the proximal tubule of kidneys and can accumulate in the renal interstitium. This last side effect can be partially reduced by administering a positively charged amino acid infusion [132].

7.3 Motivations and aims

Nephrotoxicity in one of the main dose-limiting factors for ^{177}Lu-PRRT, given also that kidneys are among the most irradiated organs in these treatments. Therefore, patient-specific kidney dosimetry provides valuable information to optimize the activity administration, in order to determine the maximum tolerable total activity administration along treatment cycles for a given patient [133, 134]. In External Beam RadioTherapy (EBRT), a total absorbed dose of 23 Gy along all the treatment cycles is adopted as a threshold to limit the risk of nephrotoxicity [135]. In absence of specific kidney absorbed dose limits for ^{177}Lu-PRRT, this value can be equally assumed for safety.

Treatment optimization relying on image-based dosimetry, as required by the EC Directive 2013/59/Euratom [136], would potentially lead to a significantly improved response in patients [134]. Even in a scheme employing fixed activity administration per cycle, typically 7.4 GBq, the optimal number of cycles a given patient should undergo to reach the limit kidney absorbed dose, and in parallel the highest absorbed dose to lesions, could be determined [137]. However, dosimetry-based optimization is not currently applied in most of the centers performing ^{177}Lu therapy, mainly because of the complexity of the dosimetry workflows in terms of cost, time and resources [138, 139].

Imaging-based post-treatment kidney dosimetry studies for ^{177}Lu-PRRT have been reported by many groups, with absorbed dose estimations obtained from quantitative imaging at successive time points after radiopharmaceutical administration. Dosimetry protocols employing sequential planar imaging, hybrid imaging and full tomographic (SPECT/CT) imaging have been examined; the latter have in principle the potential for the best accuracy and reproducibility, thanks to their full 3D information [134, 137, 140, 141]; on the other hand, the need of multiple SPECT/CT acquisitions and the subsequent dosimetric workflow imply a remarkable resource burden and represent a limiting-factor. Excluding research studies, imaging at no more than three time points are typically acquired in most clinical dosimetry protocols. Some studies investigated the possibility to employ only one or two SPECT/CT acquisitions [142–144], but such a choice inevitably reduces the amount of information available to model the patient-specific renal bio-kinetics. It is true that from cohort information it is known the usual kidney bio-kinetics, characterized by a rapid uptake followed first by a rapid excretion (plasma washout) and then by a slow clearance, and typically the whole behaviour is fitted with a single mono-exponential model. These cohort information can be used to compensate the use of a single SPECT/CT acquisition, but this involves a loss of patient specificity in the estimated dosimetric information, leading to possible losses in accuracy and indeed in the level of treatment optimization [145].

The aim of this study was to present a proof-of-concept for a simplified patient-specific renal dosimetry workflow for ^{177}Lu-PRRT, based on a single quantitative SPECT/CT acquisition of the abdominal region and multiple external probe measurements at the level of kidneys, performed at different time points. At this scope, firstly an experimental study on an abdominal phantom including kidney compartments was conducted, by performing sequential external count-rate measurements; secondly, Monte Carlo (MC) simulations reproducing the experiment were carried out; thirdly, the proposed dosimetric protocol was tested via MC simulation on a real patient ^{177}Lu-PRRT dataset, consisting in three consecutive SPECT/CTs, calculating and comparing the kidney absorbed dose obtained using full tomographic data with the one estimated following the proposed simplified protocol.

7.4 Phantom-based experimental study

The proposed simplified kidney dosimetry methodology was tested in an experimental phantom study, providing a controlled geometry with known activities in abdominal organ compartments. To perform the experiment, it was used an abdominal phantom (commercial Kyoto Liver/Kidney phantom, Nuclemed, Roeselare, Belgium [1]) having a main volume of 15 L and containing a liver insert of 1760 mL and two kidney inserts (left and right) with volumes of 155 and 160 mL, respectively. A photo showing a view from backside of the employed phantom, with the organ inserts visible, is shown in Fig. 7.2(a). The main phantom volume was filled with water, to reproduce photon attenuation typical of soft tissues. The organ inserts representing liver and the two kidneys were filled with specific activity concentrations (AC) of radionuclide in water, that will be detailed in the following. The liver insert also contained three spherical inserts (visible in Fig. 7.2(a)), having 48 mL of total volume, that in all the configurations of the study were filled with water and no radioactivity concentration. In absence of a specific insert within the main phantom volume representing the intestines, a 200-mL bottle containing a specific AC of radionuclide in water was positioned outside the phantom in some configurations of the experiment, as it will be explained below.

The aim of the study was to retrieve the kidney effective half-live "simulated" through experiment realizations, by performing multiple count-rate measurements with a collimated probe from outside of the phantom, while the organ inserts were filled with ACs of ^{99m}Tc, reproducing cohort-derived ACs of ^{177}Lu in organs of interest typical of ^{177}Lu-PRRT. The choice of using ^{99m}Tc was made for ease of accessibility, cost concerns and radioprotection reasons related to the need of voiding and filling the phantom inserts at each experimental realization (ER).

The phantom inserts were filled four times, so as to reproduce the relative uptakes of liver, kidneys and intestines at four time points after administration: 24, 48, 72 and 168 hours. Each Experimental Realization (referred to as ER1, ER2, ER3 and ER4) reproduced relative organ activities at the considered time points compatible with the median effective ^{177}Lu-DOTATATE organ half-lives listed in [146], namely 55 hrs for kidneys, 79 hrs for liver and 85 hrs for intestines. The latter value for intestines was assumed in absence of more specific information, taking the effective half-life of the remainder of the body (precisely 85 hrs). The activity concentration in each organ compartment was set to have an initial ratio of three to one between the kidneys and the liver and six to one between the kidneys and the intestine. As the bottle for the intestinal activity could not be placed inside of the phantom, its initial AC was chosen in order to compensate for the $\sim$10 cm of attenuation in water present between the center of the 200 mL external bottle and the ideal intestine position inside the main phantom volume. The total activities and activity concentrations used for each of the ERs are listed in Tab. 7.1. The adopted relative AC ratios between organs were based on the experience maturated in the center where the measurements were executed, the Institute of Radiation Physics (IRA) at Lausanne University Hospital (Switzerland); the adopted values also correlate with values extrapolated from published data [147–149].

The ^{99m}Tc activities in the syringes used to fill the different compartments for the different ERs were all measured in a Veenstra activimeter (Veenstra VDC-405. COMECER Netherlands [2]) available at the IRA in Lausanne. The calibration of the activimeter is periodically verified by a reference national metrology service from the

---

[1] `https://www.nuclemed.be/product.php?cat=37&prod=326`

[2] `https://www.comecer.com/it/vdc-505-calibratore-dose/`

TABLE 7.1: Experimentally set total activities TA (MBq) and activity concentrations AC (kBq/mL) in the different compartments, and experimental effective half-lives ($T_{\mathrm{eff\,exp}}$) characterizing their time evolution reproduced through ERs, deduced by fitting the TA (or AC) points.

	Compartment	L. Kidney	R. Kidney	Liver	Intestines
	Volume (mL)	155	160	1760	200
TA/AC	ER1 (24h)	115.6/745.8	111.7/698.1	426.6/242	114.3/571.5
	ER2 (48h)	85.7/552.8	81.9/512.1	344.5/195.7	96.5/482.4
	ER3 (72h)	64.7/417.7	62.2/389	281.9/160.2	80.7/403.6
	ER4 (168h)	18.8/121.3	17.5/109.4	123.4/70.1	35.5/177.6
	$T_{\mathrm{eff\,exp}}$ (hrs)	54.9	53.8	80.6	84.5
	T_{eff} [146] (hrs)	55	55	79	85

IRA. The uncertainty of the activity determination by the adopted activimeter is within 5% of the measured value.

For each ER, it was measured from the posterior side of the phantom the count-rate (CR) from two different locations pointing towards the left kidney, located 2 cm above and 2 cm below the kidney midplane (positions L-UP and L-DN respectively, as indicated in Fig. 7.2(a)). For each ER and acquisition location (L-UP and L-DN), three consecutive measurements were performed, and the average value of CR between them was considered. Left kidney was chosen as the most favourable location for the measurements, because of the general reduced overlap with other organs (liver in the first place) compared to the right kidney. In parallel to the collimated measures on the left kidney, up and down CR measurements in correspondence of the middle-point between the two kidneys (M-UP and M-DN positions, as indicated in Fig. 7.2(a)) were performed. These latter measurements were used to evaluate the background count-rate contribution (CR_{bg}) to be subtracted from the respective (left) kidney CR, in order to obtain background corrected count-rate (CR_{corr}). All the listed measurements for all the ERs were done both in presence and in absence of the bottle representing intestine compartment, and as a consequence of the activity source constituted by it. The bottle, when included in the set up, was always positioned along the collimated line of sight of the detector, as it is represented in Fig. 7.5.

All the count-rate measurements were performed using an Automess 6150 AD-6 dose rate meter equipped with the contamination probe (Automess 6150 AD-17 [3]). The probe was shielded against stray irradiation using a cylindrical cap collimator made of lead, expressly machined to host the AD-17 probe inside. The lead collimator had and inner cylinder diameter of 40 mm, an outer diameter of 70 mm, and a total length 90 mm. The front wall of the cylinder was 20-mm thick, with a circular hole of 10-mm diameter at its center, defining the cone of view of the measurement (see Fig. 7.5 for a detailed depiction).

From the CR probe measurements for the four ERs, the measured effective half-life (T_{eff}) of the left kidney was estimated by fitting with a mono-exponential function the mean values of CRs, separately using CRs corrected for background and CRs without background correction. Full details about the statistical analysis employed

---

[3] `https://www.automess.de/en/products/productfamily-6150ad/contamination-detection-probes`

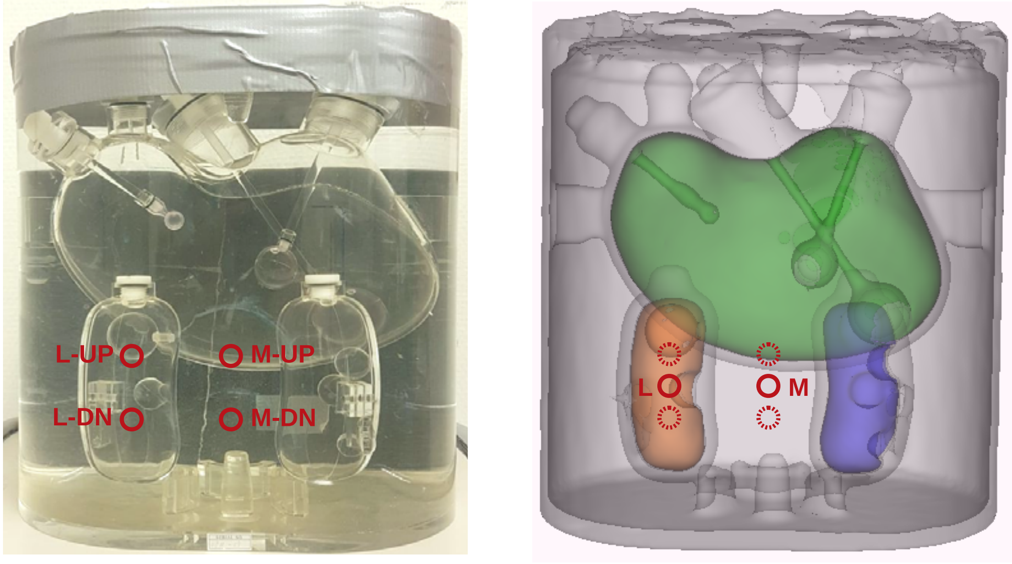

(a) (b)

FIGURE 7.2: (a) The abdominal phantom employed for the study, with depicted the positions (red circles) for both left kidney and background subtraction measurements. (b) Voxelized phantom defined for MC simulations, with segmentations of the regions of interest for this study: left kidney (orange), right kidney (blue) and liver (green). The positions of the simulated measurements are depicted with full red circles; dashed circles are the experimental positions as shown in panel (a)

are provided in Appendix C.

7.5 Monte Carlo simulations of the phantom set-up

Monte Carlo simulations were implemented to reproduce the phantom experiment with $^{99\mathrm{m}}$Tc, described in the previous paragraph. The simulations were then extended simulating ^{177}Lu instead of $^{99\mathrm{m}}$Tc, while maintaining the same set-up. For these purposes GATE version 9.0 [104], relying on GEANT4 version 10.05.p01 [94], was used.
The experimental set up was implemented into the MC as a composition of a voxelized volume, representing the abdominal phantom with liver and kidneys inserts, and multiple geometric volumes, to reproduce the collimated probe and the bottle representing intestines.

7.5.1 Geometry of the phantom set-up

Voxelized phantom volume

In order to define the computational voxelized phantom, first of all a CT scan of the abdominal experimental phantom filled with water was performed (resolution 256×256×201, voxel dimensions 1.95×1.95×1.95 mm^3). This CT image was resized and resampled using 3D Slicer version 4.11 [107], employing the *ResampleImageFilter* module with Lanczos interpolation [114], setting the volume borders in such a way as to restrict the field of view as much as possible to phantom only, which is the volume of interest for the study. The final image obtained, whose projections are shown in Fig. 7.3, had a resolution of 156×157×101 voxels, with voxel sizes of 2.0×2.0×2.0 mm^3.

To give GATE this last CT as input and build a corresponding computational phantom, the *Automated HU stoichiometric calibration* algorithm was used (described in Sec.s 2.5.2 and 3.4.4), setting a density tolerance value of 0.01 g/cm^3. In our case a problem arises: the HU scale of CTs is optimized for human tissues, and ranges approximately from -1000 (air) to 3000 (bone), saturating at 3071 HU on typical images [150]. In our CT, the metal screws contained in the employed phantom, some of which visible in Fig. 7.2(a) and (c) on the top section of the phantom, exhibit this kind of saturation. To overcome this evidence and perform a correct material and density assignment to voxels with GATE, first of all we extrapolated to HUs larger than 3000 the HU-density calibration points to be used, by fitting the calibration points in the conventional HU interval. The calibration points used are reported in Tab. 7.2, and were taken the same as the ones employed by the macros of *OpenDose Dosimetry 3D* module when using Monte Carlo "Generate GATE" method (Chapter 5), taken in turn from [105]. The bi-linear fit (with the same function reported in Eq. 3.2) performed on the calibration points is shown in Fig. 7.4 as solid blue line, and fit parameters are reported in Tab. 7.3.

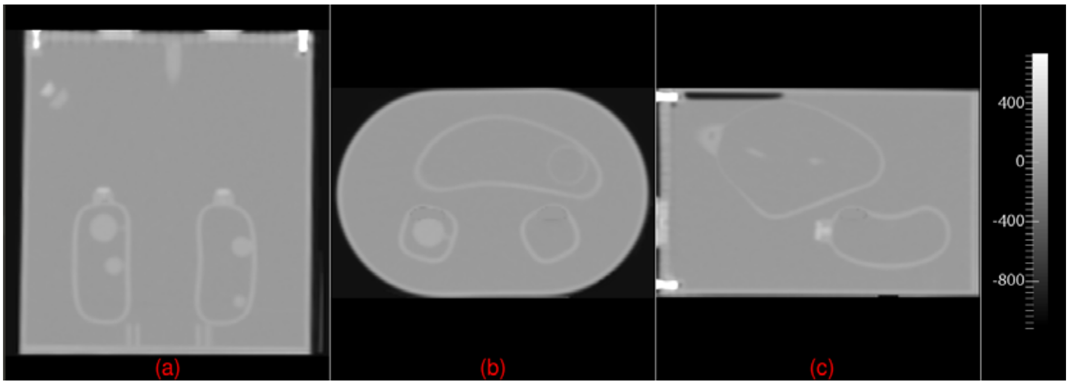

FIGURE 7.3: Axial (a), coronal (b) and sagittal (c) views of the phantom CT scan (the phantom was positioned standing on the CT bed), resampled and resized as described in Sec. 7.5.1.

TABLE 7.2: HU-density calibration values used for the density assignment to phantom's voxels, as described in Sec. 7.5.1.

HU	-1000	-750	-500	-250	0	150
ρ (g/cm^3)	0.0012	0.2512	0.5012	0.7512	1.0012	1.0767
HU	520	890	1260	1630	2000	
ρ (g/cm^3)	1.2661	1.4554	1.6447	1.8340	2.0233	

After having done the fit, knowing from the phantom constructor information that its screws are made of steel, we took 7.60 g/cm^3 as stainless steel average density, and deduced through the fit function the corresponding HU extrapolated value, which resulted being 12900 HU. This value was therefore set into CT voxels having originally HU values falling in the interval between 2500 and the maximum value

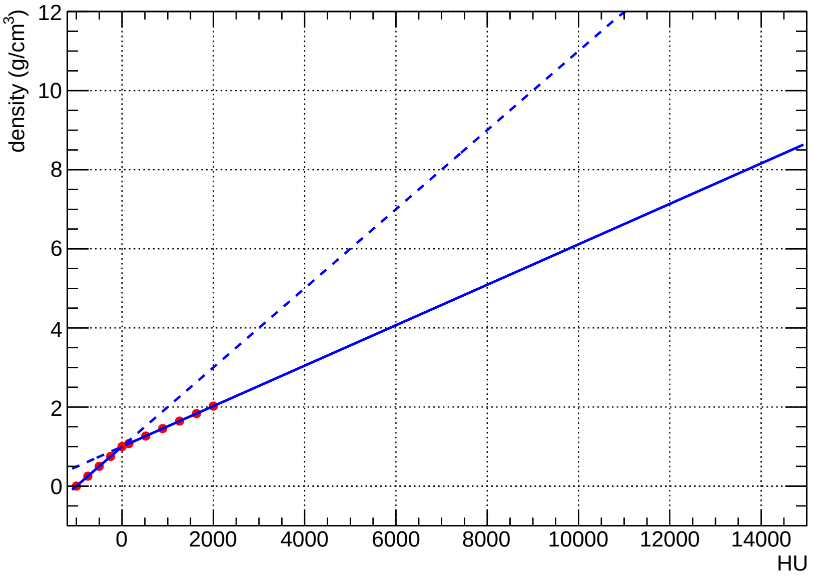

FIGURE 7.4: Bi-linear fit (solid blue line) of the calibration points (red circles) in Tab. 7.2, whose parameters are reported in Tab. 7.3.

TABLE 7.3: Fit parameters (defined in Eq. 3.2) and χ^2 of the bi-linear fit in Fig. 7.4 performed on HU-density calibration values of Tab. 7.2.

a	0.001 ± 3.007e-17
b	1.0012 ± 1.84e-14
χ^2/ndf (x < 0)	1.69e-27
a′	0.00051 ± 2.28e-07
b′	1.00047 ± 0.00026
χ^2/ndf (x ≥ 0)	8.80e-07

of the image, showing to correspond to the steel screws, taking advantage of the threshold masking section of 3D Slicer's *Segment editor*. The resized and resampled CT, with this additional editing applied, was used as the actual input for GATE. The materials set and their respective density and HU intervals used in the simulations via the *Automated HU stoichiometric calibration* algorithm, in order to reproduce accurately the main compositions and density variations within the phantom, are reported in Tab. 7.4.

Geometrical-shaped volumes

The objects external to the abdominal phantom were defined as geometrical-shaped volumes. The bottle used to represent the intestines was defined as a hollow cylinder of PMMA with 2.5-mm thick walls, containing 200 mL of water. The collimator shielding surrounding the Automess probe was defined combining cylindrical volumes, setting lead as their material. The probe volume was modelled as a water cylinder with diameter equal to the Automess 6150 AD-6 external diameter, placed inside the collimator according to the experimental position. The electrodes of the

TABLE 7.4: HU intervals and corresponding density (ρ) intervals set to identify the materials used for the phantom study simulations (Sec. 7.5.1); materials compositions were taken from the GEANT4 database [115], except for PMMA (not present), defined with the following elements and mass fractions, according to its chemical formula $(C_5O_2H_8)_n$: H 8.0541 %, C 59.9846 %, O 31.9613 %.

Material	**HU interval**	**ρ (g/cm^3)**
Air	$HU \leq -600.0$	$\rho \leq 0.40$
Polyethylene	$-600.0 < HU \leq -80.0$	$0.40 < \rho \leq 0.92$
Water	$-80.0 < HU \leq 30.0$	$0.92 < \rho \leq 1.05$
PMMA (polymethyl methacrylate)	$30.0 < HU \leq 2000.0$	$1.05 < \rho \leq 2.02$
Aluminium	$2000.0 < HU \leq 10000.0$	$2.02 < \rho \leq 6.11$
Stainless steel	$HU > 10000.0$	$\rho > 6.11$

dose rate meter were modelled as a cylindrical plate of aluminium with small lateral walls, whose dimensions and position in detector volume were deduced from a dedicated CT scan of the probe. The active volume of the detector was defined with their actual dimensions and position inside the instrument (27.2 mm of diameter, 0.8 mm of height), deduced also in this case from the dedicated CT scan.

For each ER, only two detector positions were simulated, namely one with the detector centered on the left kidney, in a vertical position at the midpoint between L-UP and L-DN, and one with the detector centered between kidneys, in a vertical position at the midpoint between M-UP and M-DN. Hereafter these two positions will be referred to as simply L and M configurations, respectively, as shown in Fig. 7.2(b). Details of the implemented geometry for the two configurations are reported and represented graphically in Fig. 7.5.

7.5.2 Primary sources and simulations settings

For both L and M configurations, four activity source regions were defined, corresponding to liver, right kidney, left kidney and bottle. These sources were used each alone in separate simulations, to properly account for their individual contributions to the energy deposited in the detector active volume and related uncertainties.

Liver and kidneys, being inside the abdominal phantom, were defined as voxelized sources, properly segmented with 3D Slicer's *Segment editor*; the segmentations are visible in Fig. 7.2(b) as colored volumes. Uniform distributions of activity were set inside these regions in GATE.

The bottle resembling intestines was instead defined as a geometric cylindrical source with uniform activity distributed within its walls.

Separate sets of simulations were performed using ^{99m}Tc and ^{177}Lu as radionuclides. In particular, ^{99m}Tc was simulated as a 140.511-keV source of gamma photons, since this is its main and practically only contributing decay channel to the probe signal. ^{177}Lu was simulated as an ion source using GEANT4's *RadioactiveDecay* module, which includes the full emission spectrum of beta and mono-energetic electrons, as well as gamma photons and characteristic X-rays of the radionuclide.

For each source, radionuclide and detector configuration, the simulation was split into two steps:

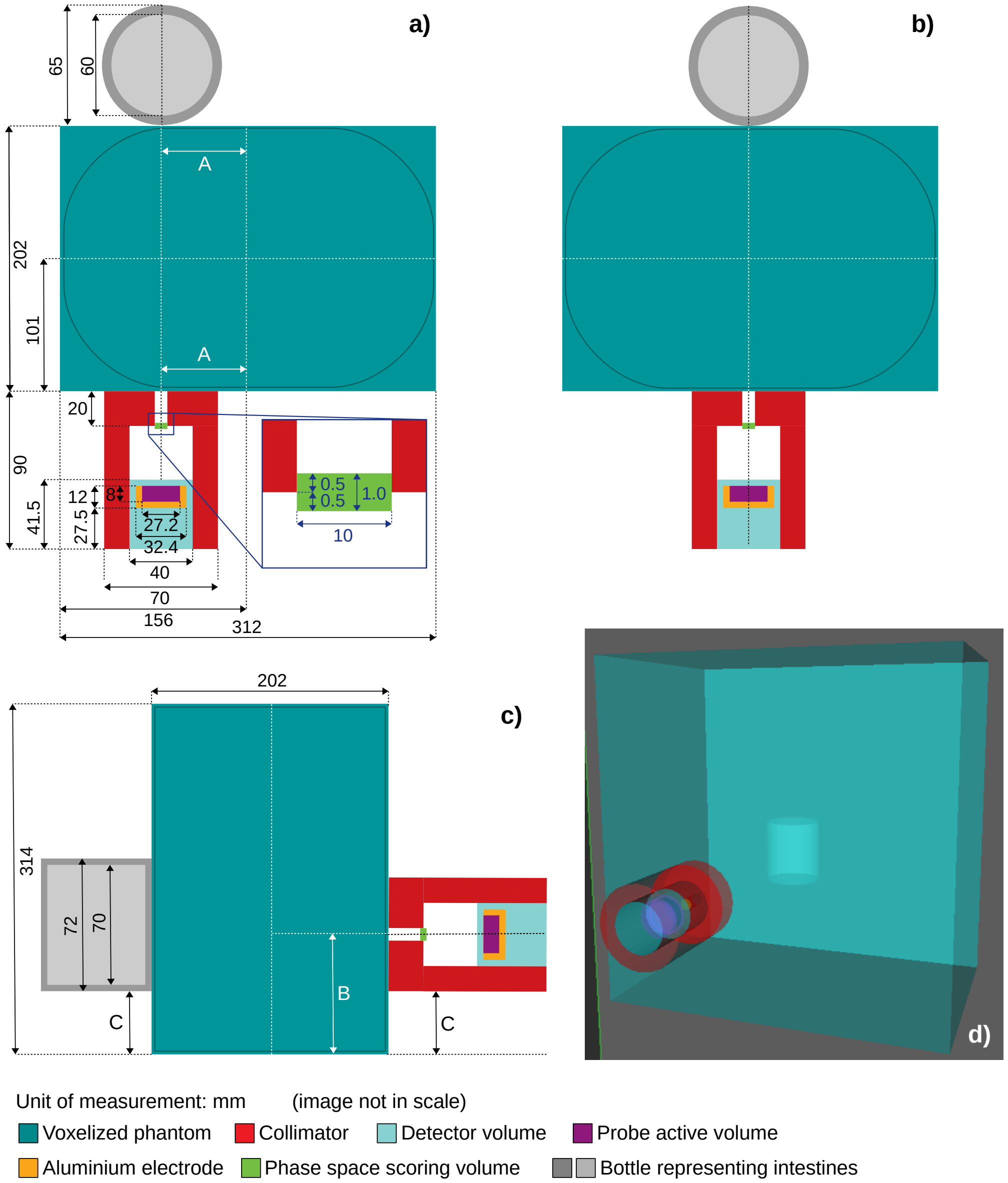
a)
b)
c)
d)
65
60
202
101
A
A
20
90
41.5
12
8
27.5
27.2
32.4
40
70
156
312
0.5
0.5
1.0
10
202
314
72
70
B
C
C
Unit of measurement: mm
(image not in scale)
Voxelized phantom
Collimator
Detector volume
Probe active volume
Aluminium electrode
Phase space scoring volume
Bottle representing intestines

FIGURE 7.5: Axial view of L (a) and M (b) configurations implemented in the MC geometry, sagittal view (c) referred to both configurations, and a 3D representation of the system in L configuration (d). In MC, A = 62 mm for L, A = 0 mm for M; B = 90 mm for both M and L, since in the experiment L-UP and M-UP had B = 110 mm, L-DN and M-DN had B = 70 mm; C = 55 mm in MC for both L and M.

1. In the first step, the complete geometry of the experimental measurement was set, namely: voxelized phantom, detector, collimator and bottle. The decay of radionuclides, uniformly distributed inside the selected source organ, and the transport and interaction of daughters in the whole *World* were simulated, using *G4EmStandardPhysics_option3* GEANT4's physics list. The *Phase Space* of particles passing through the collimator hole was scored (in particular, within the green volume shown in Fig. 7.5) and saved as a ROOT file [104].

2. In the second step, the geometries of detector and collimator only were set, and the *Phase Space* file produced in step 1. was used as the source to simulate, with high statistics, the photons collimated through the hole. The energy deposited in the detector active volume was scored with GATE's *DoseActor*.

Two independent simulations were performed for each source, radionuclide and configuration, to take into account in the uncertainties the effect of the phase space scoring on the deposited energy outcome, as explained in Appendix C, given that the collimated particles reaching the detector's active volume are "rare events" with respect to the total events in such simulations.

7.5.3 Simulations output analysis and kidney half-life estimation

The outcomes reproducing all the four ERs for the two considered radionuclides were deduced in terms of deposited energies per event (ε), and were obtained according to the procedure described as follows. Indicating with "s" the source region, with "c" the detector configuration (L or M), with "t" the ER (since ERs correspond to the four time points indicated in Sec. 7.4), with $E_{s,c}(t)$ the energy deposited in the probe active volume in a simulation employing $N_{s,c}(t)$ primary events in the first step and $K_{s,c}(t)$ events in the second step, the energy deposited per event in the probe active volume, $\varepsilon_{s,c}(t)$, was deduced as:

$$\varepsilon_{s,c}(t) = \frac{E_{s,c}(t) \cdot PE_{s,c}(t) \cdot AF_s(t)}{K_{s,c}(t)} \tag{7.3}$$

where $PE_{s,c}(t)$ is the number of phase space entries (that will be indicated as $P_{s,c}(t)$) per event in the first step,

$$PE_{s,c}(t) = \frac{P_{s,c}(t)}{N_{s,c}(t)} \tag{7.4}$$

and $AF_s(t)$ denotes the activity fraction, intended as the ratio between the activity $A_s(t)$ in the source region s for a specific ER (reported in Tab. 7.1) and the sum of the activities of all the four regions for ER1 (i.e. for t = 24 hrs):

$$AF_s(t) = \frac{A_s(t)}{\sum_s A_s(24\,\text{hrs})} \tag{7.5}$$

$N_{s,c}(t)$, both for $^{99\text{m}}$Tc and ^{177}Lu, was set equal to $2{\cdot}10^8$ for the simulations having left kidney as the source, and equal to 10^9 in the case the other sources; these values guaranteed at least 8000 $P_{s,c}(t)$ entries in the sampled phase space for all the first step simulations. $K_{s,c}(t)$ was instead set equal to $2{\cdot}10^8$ in all the simulations using $^{99\text{m}}$Tc, and equal to $5{\cdot}10^8$ in all the simulations using ^{177}Lu, in order to obtain $\varepsilon_{s,c}(t)$ values with relative statistical uncertainties below 0.2%.

In the case of simulations with $^{99\text{m}}$Tc, simulated as a source of 140.511-keV gammas, the $\varepsilon_{s,c}(t)$ was in addition weighted for the Branching Ratio (B.R.) of the 140.511-keV gamma emission channel, B.R. = 0.89 [111].

For both L and M detector configurations, the total energy deposited in the probe sensitive volume at time t, $\varepsilon_c(t)$, was obtained adding the deposited energies due to each source organ at time t:

$$\varepsilon_c(t) = \sum_s \varepsilon_{s,c}(t) \tag{7.6}$$

For each time point, the background-corrected total energy deposited per event, $\varepsilon_{\text{corr}}(t)$, was calculated as the difference between energy deposited per event in L configuration and M configuration:

$$\varepsilon_{\mathrm{corr}}(t) = \varepsilon_{\mathrm{L}}(t) - \varepsilon_{\mathrm{M}}(t) \tag{7.7}$$

The effective half-life (T_{eff}) in the left kidney was estimated by fitting with a mono-exponential function of the type written below the four $\varepsilon_{\mathrm{corr}}(t)$s obtained at t = 24, 48, 72 and 162 hrs:

$$f(t) = \varepsilon_0 \cdot e^{-ln(2) \cdot t/T_{\mathrm{eff}}} \tag{7.8}$$

where ε_0 and T_{eff} are fit parameters. The calculation of T_{eff} was moreover done also fitting $\varepsilon_{\mathrm{L}}(t)$s, i.e. the values without background correction, at the four mentioned times.

As stated in Sec. 7.5.2, two independent simulations were performed for each source, radionuclide and configuration. Therefore the fit procedure was applied to multiple combinations of $\varepsilon_{\mathrm{corr}}(t)$s - or $\varepsilon_{\mathrm{L}}(t)$s when considering background uncorrected energies - as detailed more extensively in Appendix C. Given all the T_{eff}s obtained as fit parameters, from them was deduced the average effective half-life $\langle T_{\mathrm{eff}} \rangle$ and the corresponding Standard Deviation ($\mathrm{SD}_{\mathrm{MC}}$). Furthermore, in order to test the accuracy of simpler measurement protocols, fits of the following combinations of three among the four time points were done:

- 3a: 24 hrs and 168 hrs fixed, and one time point between 48 hrs and 72 hrs;
- 3b: 168 hrs fixed and two time points between 24 hrs, 48 hrs and 72 hrs;
- 3c: no fixed time point.

For each of these three combination types, the corresponding $\langle T_{\mathrm{eff}} \rangle$s were calculated and compared. Finally, we repeated the aforementioned analysis by excluding in the $\varepsilon_c(t)$ calculations the contribution from the bottle source resembling intestines, to simulate the case of a negligible uptake in them.

7.6 Monte Carlo test on a ^{177}Lu-DOTATATE PRRT clinical case

The proposed simplified patient-specific method for ^{177}Lu renal dosimetry was testes on a clinical case of ^{177}Lu-DOTATATE PRRT cycle, whose dataset consisted of three SPECT/CT scans acquired at 2, 20 and 70 hours after the therapeutic administration. The CT and SPECT scans, after some pre-processing steps performed on 3D Slicer, were used as input for GATE 9.0 MC simulations to build, respectively, phantoms representing patient's body and radiopharmaceutical biodistributions at the three time points. The collimated detector was also implemented in the geometry. The goal of simulations was to score absorbed dose rate values inside kidneys and deposited energies in the detector probe following from ^{177}Lu decays. The probe signal was scored with the same methodology adopted in the MC simulations of the phantom study, with simulations in L and M configurations at each SPECT time point. Patient-specific MC outcomes were used to derive and compare absorbed doses to the kidneys, using a full image-based dosimetry workflow employing all the three available SPECT/CTs, and the proposed simplified kidney dosimetry, based on external probe measurements and only one quantitative SPECT/CT.

7.6.1 Simulations settings

The complete setup of a simulation consisted of the detector with collimator, defined as in Sec. 7.5.1, and of a voxelized volume representing the patient's abdomen, defined from a CT scan. For each time point, a voxelized activity source map was defined from the corresponding SPECT scan.
The three couples of SPECT/CT images were mutually registered with the help 3D Slicer *Transformation* module, taking the scans at 2 hrs as a reference. Rigid linear transforms only were used, centered on left kidney to have the best registration for this organ of interest. All the registered images have been resized and resampled in order to restrict the volume size to the patient's body only. The resampling was carried out using 3D Slicer *ResampleImageFilter* module adopting Lanczos interpolation. The resolution set for all the SPECT and CT images was 420×285×112, with voxel size 1.0×1.0×3.5 mm^3. Subsequently, each resampled CT and SPECT image was "corrected" in the regions outside the patient's body: for CTs, in order to remove residual parts of patient's bed anyways falling in the field of view of the resampled images (this was done because bed would not be present during a probe measurement); for SPECTs, to remove possible activity background noise outside the body. A filtering was applied in both cases using 3D Slicer masking offered by its *Segment editor* module, according the following procedure: for each time point, a segmentation of the whole CT scan and a segmentation the body were performed (threshold based, HU $>$ -500 + voxel "islands" editing), and a segmentation of the air outside the body (S in the following) was deduced via logical subtraction of the previous two (+ "islands" editing); at this point, CTs voxel values inside S were put to -1000, in order to represent air, SPECTs voxel values inside S were put to 0, to cancel eventual noise-due activity concentrations outside the body. The CTs and SPECTs processed with all the described procedures were used as input for simulations; projections of the mentioned images at the three time points are shown in Fig. 7.6.

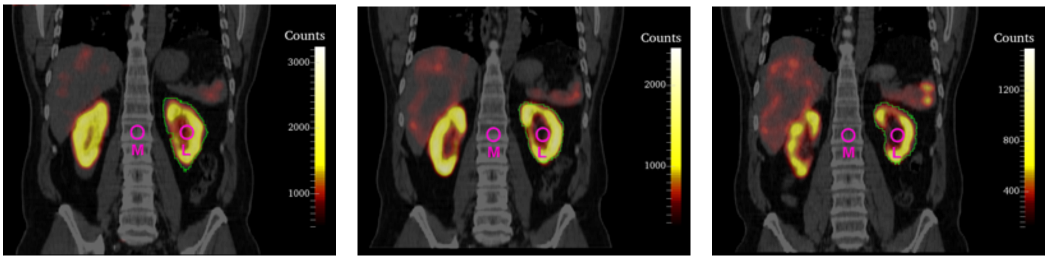

(a) (b) (c)

FIGURE 7.6: Coronal fusion slices of the resampled and corrected CTs and SPECTs at t = 2 hrs (a), 20 hrs (b) and 70 hrs (c); green lines represent the left kidney VOIs borders at the different time-points, magenta circles indicate the L and M positions of the detector in the simulations (pointing at the body from the posterior side)

For each CT, the respective voxelized volume representing patient's body was defined in GATE in the same way described in Sec. 7.5.1, but with no need to extrapolate HU-density calibration (since in the present case we deal with standard CTs of human body) and setting the materials reported in Tab. 7.5 for the indicated HU and density intervals; the intervals were selected analyzing the CT values distributions of the three CTs, in order to reproduce the transitions between the main tissue classes of the thoraco-abdominal district in terms of density inhomogeneities. The positions of the detector and collimator volumes with respect to the voxelized phantom for L

TABLE 7.5: HU intervals and corresponding density (ρ) intervals (through the fit in Fig. 7.4) set to identify the materials used for the clinical test simulations (Sec. 7.6); materials compositions were taken from the GEANT4 database, using ICRP compounds for tissues [115].

Material	**HU intervals**	**ρ (g/cm^3)**
Air	HU $\leq$ -900.0	$\rho \leq 0.10$
Lung tissue	-900.0 $<$ HU $\leq$ -150.0	$0.10 < \rho \leq 0.85$
Adipose tissue	-150.0 $<$ HU $\leq$ -60.0	$0.85 < \rho \leq 0.95$
Soft tissue	-60.0 $<$ HU $\leq$ 290.0	$0.95 < \rho \leq 1.15$
Cortical bone	HU $>$ 290.0	$\rho > 1.15$

and M configurations were chosen coherently to the phantom study settings, i.e., for L, detector pointing the midpoint of the left kidney, for M, detector pointing the midpoint between kidneys, from back as well, as depicted in the slices of Fig. 7.6 (and, analogously to the phantom study, with the same geometry of Fig. 7.5, but with no bottle and with voxelized volume size and distances A, B, C adapted to the present case).
A voxelized activity source was defined for each time point from the corresponding SPECT scan, with the usual GATE procedure for voxelized sources, described in Sec. 3.4.5. ^{177}Lu was selected as the radionuclide of the source, defined as in Sec. 7.5.2.
For each time point and configuration, the simulation performed was split into two steps, similarly to the phantom study:

1. In the first step the complete geometry was set, consisting in the voxelized patient phantom, the detector and the collimator. The decay of ^{177}Lu distributed according to the SPECT, and the transport and interaction of its daughters in the *World*, were simulated with the same settings of Sec. 7.5.2, scoring also in this case the *Phase Space* of particles passing through the collimator hole. The absorbed dose map (and dose squared map for the statistical uncertainty evaluation, as detailed in Appendix C) within the patient's body voxelized volume was also scored, with a spatial sampling equal to the resolution of the CT, using GATE's *DoseActor*.

2. The second step was analogous to the one of Sec. 7.5.2.

Three independent simulations for each time point and configuration were performed, for uncertainties calculation purpose (additional explanations are furnished in Appendix C). On each resampled and corrected CT, a volume of interest (VOI) representing left kidney was manually segmented with 3D Slicer (projections are visible in Fig. 7.6 for all the three time points), to be used for the half-life estimation and the dosimetric calculations.

7.6.2 Kidney half-life estimation and dosimetric calculations

For each simulation performed, the energy deposited per event in the probe active volume, $\varepsilon_c(t)$, was deduced in the same way reported in Eq. 7.3, considering that in this patient study the subscript "s", and therefore also Eq. 7.6, are unnecessary, given that the radionuclide decays are distributed according to one entire SPECT image, constituting a single unique source for each simulation. Moreover, instead of

$AF_s(t)$ (Eq. 7.5), it is used simply an $AF(t)$, which now represents the ratio between the total activity $A(t)$ in the SPECT at time t and the total activity in the SPECT at the first time point, $A(t = 2\,\text{hrs})$:

$$AF(t) = \frac{A(t)}{A(2\,\text{hrs})} \tag{7.9}$$

The number of primary events in all the first step simulations was set equal to $2{\cdot}10^8$, a value that ensured at least $3{\cdot}10^4$ phase space entries in all the simulations, and average relative statistical uncertainties on the dose map voxels ($\sigma_{v,i}(t)/D_{v,i}(t)$ in the Appendix C) within left kidney VOI below 9% in all the simulations. The number of primary events in all the second step simulations was set equal to $2{\cdot}10^8$, guaranteeing an estimation of $\varepsilon_c(t)$ values with relative statistical uncertainties below 0.3%.
The effective half-life in the left kidney, T_{eff}, was estimated by fitting the background-corrected energies deposited per event, $\varepsilon_{\text{corr}}(t)$s, at the three time points, t = 2, 20 and 70 hrs. The $\varepsilon_{\text{corr}}(t)$s were calculated as in Eq. 7.7. The estimation of T_{eff}s was in addition carried out by fitting the energies deposited without background correction, $\varepsilon_{\text{L}}(t)$s. Three time-points fits were made using all the possible combinations of simulations outcomes performed at each time point, deducing the average effective half-life $\langle T_{\text{eff}} \rangle$ and its Standard Deviation SD_{MC}, as further described in Appendix C.
As anticipated, two kinds of kidney dosimetry workflows were implemented: a full 3D image-based direct MC dosimetry, assumed as a reference, and a simplified dosimetry protocol based on a unique image-based MC calculation at a single time-point and on the external detector measurements done at multiple time-points proposed in the present study.

Full image-based MC dosimetry

In the full MC dosimetry workflow, the absorbed dose to left kidney, D_{full}, was evaluated integrating with a mono-exponential fit function the average absorbed dose rates $\langle \dot{D}(t) \rangle$ inside the left kidney VOI at the three time points of the SPECT/CTs, deduced from the absorbed dose maps obtained from step 1) MC simulations (described in Sec. 7.6.1). Indicating with $\langle D(t) \rangle$ the average absorbed dose in the left kidney VOI at time t in a simulation employing $N(t)$ events in the first step, $\langle \dot{D}(t) \rangle$ was deduced as:

$$\langle \dot{D}(t) \rangle = \frac{\langle D(t) \rangle \cdot A(t)}{N(t))} \tag{7.10}$$

where $A(t)$ is the total activity in the SPECT at time t. D_{full} was calculated analytically as follows:

$$D_{\text{full}} = D_0 \int_0^{+\infty} e^{-\frac{ln(2)\cdot t}{T_{\text{full}}}} dt = \frac{D_0 \cdot T_{\text{full}}}{ln(2)} \tag{7.11}$$

with T_{full} and D_0 as fit parameters.

Simplified MC dosimetry

The simplified dosimetry workflow was based on the assumption of selecting a single SPECT/CT at a time T, one of the three considered time points, and absorbed dose rate external probe measurements on the patient at all the three considered time points, to deduce the ^{177}Lu effective half-life in left kidney. For T = 2, 20 and 70 hrs, the kidney average absorbed dose, $D_{\text{simpl},T}$, was evaluated from the average absorbed dose rate $\langle \dot{D}(t = T) \rangle$ and from the T_{eff} deduced from the simulated probe measurements:

$$D_{\text{simpl},T} = \frac{\langle \dot{D}(T) \rangle}{e^{-\frac{ln(2)\cdot T}{\langle T_{\text{eff}} \rangle}}} \int_0^{+\infty} e^{-\frac{ln(2)\cdot t}{\langle T_{\text{eff}} \rangle}} dt = \frac{\langle \dot{D}(T) \rangle \cdot \langle T_{\text{eff}} \rangle}{ln(2) \cdot e^{-\frac{ln(2)\cdot t}{\langle T_{\text{eff}} \rangle}}} \tag{7.12}$$

7.7 Results

7.7.1 Phantom study: experimental results

The effective half-lives obtained from the mono-exponential fits of CRs, acquired through the four sets of measurements reproducing the ERs, according to the procedure described in Sec. 7.4, are reported in Tab. 7.6. The fits were done for the measurements in L-UP and L-DN positions, with and without the bottle resembling the intestines and with and without background correction. The Standard Errors (SE$_{\text{fit}}$) of the T_{eff}s values were evaluated according to the procedure detailed in Appendix C. The times spent to carry out the CR measurements used to derive T_{eff} estimates lasted from a minimum of 90 s, for ER1, to a maximum of 200 s, for ER4.

TABLE 7.6: Effective kidney half-lives T_{eff} calculated in the experimental phantom study from four-time-points fits of the average of the consecutive count-rates, their corresponding standard errors and the relative differences κ (%) with respect to reference (54.9 hrs) in Tab. 7.1.

	Sources:	No intestines			With intestines		
CRs		T_{eff} (hrs)	SE$_{\text{fit}}$ (hrs)	κ (%)	T_{eff} (hrs)	SE$_{\text{fit}}$ (hrs)	κ (%)
No bkg. corr.	UP	56.9	0.9	+3.6	60.0	0.8	+9.2
	DN	56.1	0.9	+2.1	58.8	0.9	+7.1
Bkg. corr.	UP	53.4	2.5	-2.7	56.0	2.0	+2.0
	DN	53.9	2.2	-1.8	55.9	1.8	+1.8

The T_{eff}s deduced from CRs without background correction differ for less than 9% with respect to the expected value set in the left kidney insert (54.9 hrs, reported in Tab. 7.1) in the case including intestines, less than 4% in the case excluding intestines. For T_{eff}s deduced from background corrected CRs, the differences with the reference come down below 2% in the case including intestines, below 3% excluding intestines. Therefore, the background correction appears to improve the agreement between estimated and expected values, according to their uncertainties, irrespective of UP and DN configuration of detector and of intestines contribution. In general, background uncorrected results tend to overestimate a bit the effective half-life, especially in the cases including intestines.

7.7.2 Phantom study: MC simulations results

The average effective half-lives in the left kidney were deduced from the Monte Carlo outcomes of the phantom experiment simulation, both for $^{99\text{m}}$Tc and ^{177}Lu sources simulated. Four time-points mono-exponential fits combinations, plus the three types of combinations of three time-points fits explained in Sec. 7.5.3, were analyzed according to the methodology described in Appendix C. The results in terms $\langle T_{\text{eff}} \rangle$s and T_{eff}s distributions, for all the configurations simulated, are reported in

Tab. 7.7 and in Fig. 7.7, respectively.

TABLE 7.7: Average effective kidney half-lives $\langle T_{\text{eff}} \rangle$ for the phantom study MC simulations, evaluated for the reported nuclides, *CR*s types, time-points choice (*TP*) and simulated sources, as explained in Sec. 7.5.3 and Appendix C.

	Sources:		No intestines		With intestines	
Nuclide	*CR*s	*TP*	$\langle T_{\text{eff}} \rangle$ (hrs)	SD_{MC} (hrs)	$\langle T_{\text{eff}} \rangle$ (hrs)	SD_{MC} (hrs)
$^{99\text{m}}$Tc	No bkg. corr.	4	60.14	0.17	61.08	0.17
		3a	60.10	0.19	61.05	0.19
		3b	60.08	0.20	61.02	0.20
		3c	60.43	0.70	61.38	0.72
	Bkg. corr.	4	54.33	0.33	54.29	0.33
		3a	54.33	0.34	54.29	0.34
		3b	54.21	0.40	54.17	0.40
		3c	54.9	1.4	54.9	1.4
^{177}Lu	No bkg. corr.	4	57.7	0.6	58.6	0.5
		3a	57.6	0.6	58.5	0.6
		3b	57.6	0.6	58.5	0.6
		3c	58.1	1.4	59.0	1.4
	Bkg. corr.	4	53.1	1.1	53.1	1.1
		3a	53.1	1.1	53.1	1.1
		3b	53.0	1.2	53.0	1.2
		3c	53.8	2.4	53.8	2.4

The effective kidney half-lives calculated via MC simulating $^{99\text{m}}$Tc sources show an agreement within 2% with respect to the expected value of Tab. 7.1 when using background corrected energies deposited, while the agreement falls within 11% when background uncorrected results are considered, without significant differences between the cases including and excluding the contribution of intestines. This behaviour is in line with the one exhibited by the experimental measurements.
Comparing MC simulations results with the corresponding experimental results of Tab. 7.6, an agreement within 4% is found in the case background corrected data including intestines, within 5% in the case without background correction including intestines, within 3% in the case with background correction excluding intestines, within 8% in the case without background correction excluding intestines.
For all the different cases examined, no relevant differences emerge between the $\langle T_{\text{eff}} \rangle$s deduced from four time-point fits and the different choices of three time-point fits, while their respective Standard Deviations (SD_{MC}) vary on the basis of the employed sample of time-points. MC results for $^{99\text{m}}$Tc using background corrected energies deposited are therefore in agreement with both the expected value and the experimentally-derived values, according to their respective uncertainties, and irrespective to the presence of uptaking intestines.
Concerning simulations with ^{177}Lu sources, the agreement of $\langle T_{\text{eff}} \rangle$s with the expected value of Tab. 7.1 is within 4% using background corrected results, within 7% using background uncorrected results, irrespective of intestines contribution. The comparisons of ^{177}Lu MC results with experimental results of Tab. 7.6 show agreements in line (and even better, concerning the background uncorrected cases) with the comparison between $^{99\text{m}}$Tc MC results and Tab. 7.6. This evidence indicates the

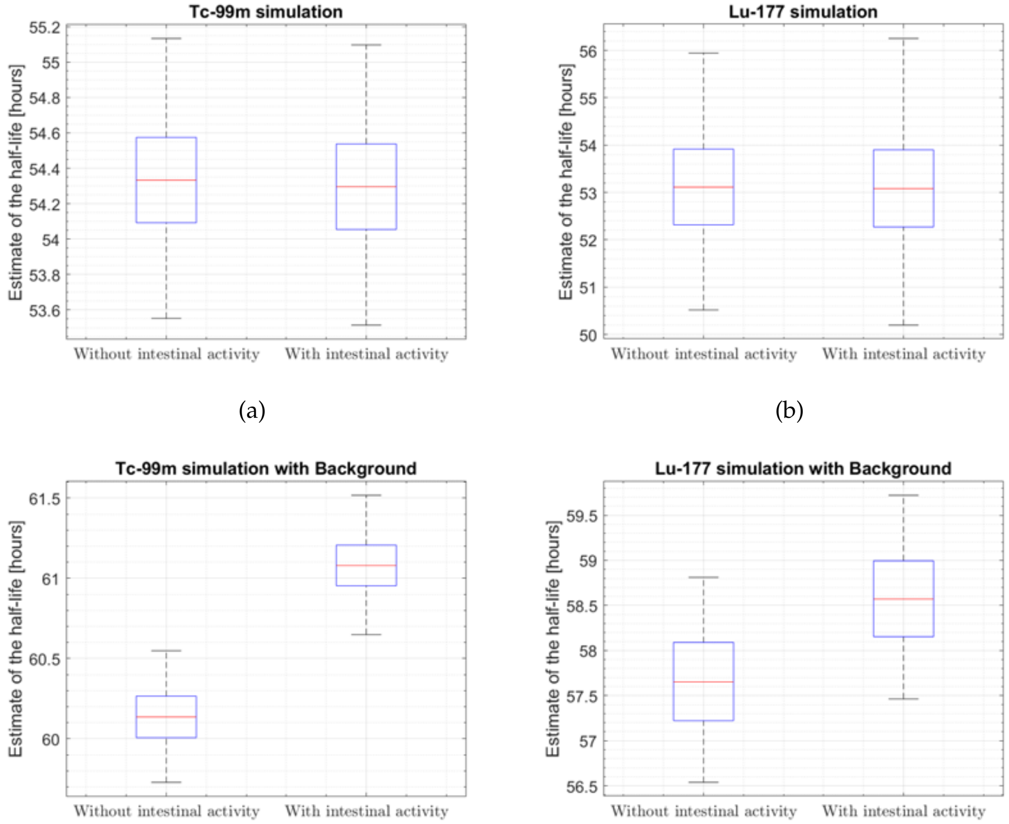

(a) (b)

(c) (d)

FIGURE 7.7: Box-plots of the left kidney half-lives T_{eff} estimated from MC simulations employing $^{99\text{m}}$Tc and ^{177}Lu, deduced from four-time-points fit combinations as explained in Sec. 7.5.3 and Appendix C. In (a) and (b) the results from fits performed on with count-rates corrected for the background, in (c) and (d) without background correction.

reliability of extending the adopted count-rate method, experimentally tested on a phantom filled with activity concentrations of $^{99\text{m}}$Tc, to ^{177}Lu, the radionuclide of interest for this study, without significant differences in accuracy.

7.7.3 Dosimetry workflows on ^{177}Lu-DOTATATE PRRT clinical case: MC simulations results

The effective half-life in the left kidney retrieved from the full image-based MC dosimetry workflow, T_{full}, and the average effective half-life retrieved from the simulated probe measurements to test the simplified dosimetry workflows, $\langle T_{\text{eff}} \rangle$, both defined in Sec. 7.6.2, are reported and compared in Tab. 7.8.
Coronal slices of absorbed dose rate maps evaluated through simulations (step 1. described in Sec. 7.6.1) at the three time points are shown in Fig. 7.8.
T_{full} and $\langle T_{\text{eff}} \rangle$ deduced from simulations with background correction applied have an agreement within 10%, which however is within the estimated statistical uncertainties of the values. Comparing the T_{full} with the $\langle T_{\text{eff}} \rangle$ deduced without background correction, the discrepancy arises to a value within 20%, which instead falls outside of the statistical uncertainty intervals of the two compared values.

TABLE 7.8: Effective kidney half-lives for the PRRT patient study obtained for the full image-based and simplified dosimetry workflows, as described in Sec. 7.6.

Probe signal	Dosimetry method	Eff. half-life (hrs)	Stat. unc. (hrs)
/	full image-based (3 SPECT/CTs)	$T_{\text{full}} = 45.08$	$\text{SE}_{\text{fit}} = 0.15$
Bkg. corr.	simplified (1 SPECT/CT + 3 probe meas.)	$\langle T_{\text{eff}} \rangle = 50$	$\text{SD}_{\text{MC}} = 7$
No bkg. corr.	simplified (1 SPECT/CT + 3 probe meas.)	$\langle T_{\text{eff}} \rangle = 36$	$\text{SD}_{\text{MC}} = 3$

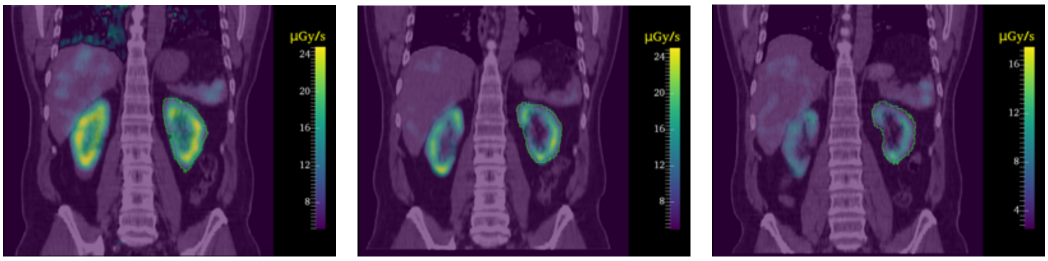

(a) (b) (c)

FIGURE 7.8: Coronal slices of the absorbed dose rate maps estimated with MC simulations, fused with respective CTs, at $t = 2$ hrs (a), 20 hrs (b) and 70 hrs (c); green lines represent the left kidney VOIs borders at each time point.

In Fig. 7.9 are shown the functions integrated to deduce the absorbed dose values to left kidney: the mono-exponential fit function of the three absorbed dose rate points estimated in the full image-based MC workflow, returning T_{full} as fit parameter (Fig. 7.9(a)), and the analytical mono-exponential functions of Eq. 7.12 adopted for the simplified dosimetry workflows, employing a single SPECT scan at 2 hrs (Fig. 7.9(b)), 20 hrs (Fig. 7.9(c)) or 70 hrs (Fig. 7.9(d)), and using the value of $\langle T_{\text{eff}} \rangle$ deduced from background corrected results. The values of the left kidney absorbed doses obtained with the full MC dosimetry procedure and the simplified dosimetry procedures are reported in Tab. 7.9.

The absorbed doses obtained with the simplified protocol using probe measurements to estimate the effective renal half-life, in the case of employing background corrected results, exhibit an agreement within about 6%, 12% and 1% with respect to the result of the fully image-based MC dosimetric procedure, respectively if the single SPECT/CT scan employed for the calculation was performed at time $T = 2$, 20 and 70 hours after administration. In the case of employing background uncorrected results, the agreement between absorbed doses deduced with the simplified and full method falls within 23%, 10% and 4%, using respectively the SPECT/CT scan performed at time $T = 2$, 20 and 70 hours.

The background corrected results show a better agreement with full MC image-based results with respect to the background uncorrected ones in the case of $T = 2$ hrs and $T = 70$ hrs. The best agreement in terms of relative percent difference between absorbed dose average values is observed when using $T = 70$ hrs, but in parallel it

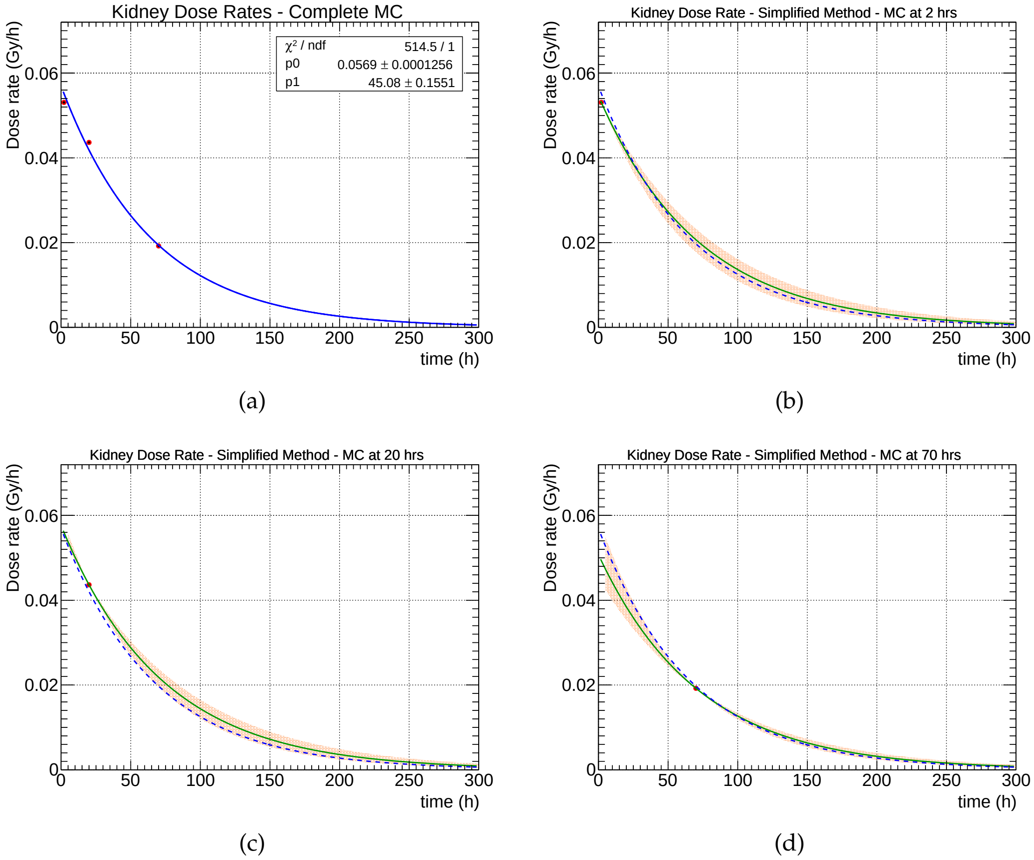

(a) (b)

(c) (d)

FIGURE 7.9: In (a), the red points are the $\langle \dot{D}(t) \rangle$s, the solid blue line is the mono-exponential fit function integrated in Eq. 7.11 for the full image-based MC dosimetry. In (b), (c) and (d), the single red point is the average absorbed dose rate evaluated at time T = 2, 20, and 70 hrs, respectively, employed for the simplified dosimetry; the solid green line is the analytical mono-exponential function integrated in Eq. 7.12; the orange shaded region represents the absolute uncertainties on the function's values; the dashed blue line is the same function represented as solid blue line in a), plotted to compare full and simplified dosimetry functions.

has also to be taken into account that each $D_{\mathrm{simpl},T}$ value has a non negligible statistical uncertainty, which is within 14% in the cases of absorbed doses deduced using background corrected data.

7.8 Discussion

In the present study was presented an original simplified methodology for the assessment of the absorbed dose in kidneys, that could be applicable for patients undergoing ^{177}Lu PRRT treatments. The proposed methodology would provide for the deduction of patient-specific renal radiopharmaceutical biokinetics by means of multiple consecutive measurements of count-rates (or alternatively dose-rates) with external probe pointing on left kidney, feasible using radioprotection detectors commonly available in nuclear medicine departments. A count-rate (or dose-rate) curve

TABLE 7.9: Left kidney average absorbed doses $\langle D \rangle$, also expressed per unit of administered activity as $\langle D \rangle / A_{\mathrm{adm}}$, evaluated with the full and simplified dosimetry protocols, and the relative percent differences δ (%) with respect to the full dosimetry value.

Probe signal	Dosimetry	T (hrs) of SPECT/CT	$\langle D \rangle$ (Gy)	$\langle D \rangle / A_{\mathrm{adm}}$ (Gy/GBq)	Stat. Unc. on $\langle D \rangle$ (Gy)	δ (%)
/	full	2, 20, 70	3.700	0.66	0.006	/
Bkg. corr.	simpl.	2	3.94	0.71	0.54	+6.4
	simpl.	20	4.15	0.74	0.57	+12.1
	simpl.	70	3.66	0.66	0.51	-1.1
No bkg. corr.	simpl.	2	2.87	0.51	0.23	-22.5
	simpl.	20	3.33	0.60	0.27	-10.0
	simpl.	70	3.84	0.69	0.31	+3.8

as a function of time retrieved in such a way, representative of the organ patient-specific biokinetics, would be used to complement a 3D absorbed dose rate calculation at a single time point, deduced from a quantitative SPECT/CT acquisition; by converting the curve into an absorbed dose rate curve, fixing for it the deduced absorbed dose rate point and integrating with respect to time, an estimate of the absorbed dose to kidneys along a treatment cycle is obtained. This dosimetry workflow presents a direct analogy with hybrid dosimetry methods already present in literature, employing a single quantitative functional tomographic acquisition plus multiple planar acquisitions [71]. In terms of time consumption, the proposed workflow would further reduce the demand in terms of gamma camera occupation with respect to hybrid approach, exploiting only the single 3D SPECT/CT acquisition, without any 2D scan.

The described workflow was subjected to a proof-of-concept, in first place developed as a phantom experiment reproducing a simplified abdominal configuration of a patient, with liver, kidneys (and eventually intestines) compartments filled with specific activity concentrations of $^{99\mathrm{m}}$Tc. The possibility of estimating the actual renal effective half-life from external count-rate measurements in the presence of activity from other organ compartments, characterized by different half-lives, was successfully tested. In fact, the obtained experimental estimates for the kidney T_{eff} were in a reasonably good agreement (within 3%) with the expected value, known from the experiment construction.

The T_{eff} measurement was assessed in two different positions (L-UP and L-DN), one 4-cm apart from the other in the craniocaudal direction, obtaining comparable results; this evidence reassures on the robustness of the methodology against the particular positioning of the collimated external probe for the measurement.

In the performed experiment, we examined probe measurements at four time-points ranging from 24 hours until one week after the therapeutic administration, reproduced as ERs by adequately adapting the activity concentrations (and consequently total activities) in the phantom compartments. However, nothing prevents to examine more time points to provide a more reliable time-evolution information all along the measurement period, convenient for appropriately fitting with mono-exponential function - and in case also with more complex functions - the count-rates, and better model the renal slow excretion phase. In this respect, it is also encouraging to notice that the time required to obtain sufficient count statistics with the collimated external probe configurations used in the presented study was between 90 s (ER1) and 200 s (ER4), considerably shorter compared to typical acquisition duration for gamma camera imaging.

In a second step of the proof-of-concept, we compared the phantom experiment to MC simulations replicating the experimental set-up, and additional simulations were also performed replacing the ^{99m}Tc source, actually used in the experiment, with ^{177}Lu, the main radioisotope of interest for the therapeutic application in PRRT. All the MC simulations provided promising results in view of a possible application of the proposed methodology to a real patient case; in fact, all the $\langle T_{\mathrm{eff}} \rangle$ estimates employing background corrected data presented deviations within 4% at maximum from the expected values known from the experiment construction.

A third step of the proof-of-concept aimed at illustrating the potential applicability of the workflow to real patient cases, obviously taking into consideration that a definitive demonstration of robustness of the methodology in patients will require experimental studies on patients, with an extensive application and validation in a sufficiently large cohort, steps that were beyond the scope of the presented initial proof-of-concept. Nevertheless, the promising results reported for the single ^{177}Lu-DOTATATE PRRT case examined could hopefully contribute to pave the way to the clinical application of the proposed renal dosimetry methodology.

Both in the phantom study and in the patient case test emerged the benefit of executing also count-rate measurements between kidneys, for background estimation and subsequent correction to left kidney measurements, since the background corrected data exhibit a better agreement with the expected values of kidney effective half-life, and in the patient case also in the estimation of the average absorbed dose to the kidney.

An aspect that should be investigated deeper in future studies, in particular experimental studies on patient cohorts, is the choice of the time-point in which to acquire the single SPECT/CT for the simplified dosimetry protocol. The results of the present work showed the best agreement (within about 1 %) with the full image-based dosimetry for the latest time-point among the three examined, 70 hrs, but the MC simulations results for a single patient case cycle is not sufficient to deduce a general conclusion that a late point is the best choice. By the way, an early acquisition, within 1-2 days after administration, would be more suitable for patient's comfort, since he/she would be already at the hospital, and in addition an early scan benefits from the higher activity bio-distributed in patient's body with respect to late scans, which guarantee poorer statistics. In addition, the result obtained using the SPECT/CT at 2 hrs for the simplified dosimetry is not bad, with an agreement within about 6% with the full dosimetry result. Ultimately, at the moment there are not enough elements to establish with confidence a specific choice.

The proposed dosimetry method presents a number of favourable aspects in perspective. Multiple consecutive external acquisitions using a collimated count-rate probe, as the one described in this work, should not represent a problem in a clinical application. In reason for the common availability and the relative low cost in terms equipment and measurement time, along with the positive impact in terms of patient comfort, as stated before it would be potentially possible to perform measurements even at more than three or four time-point, enabling a potential improvement of the fit-conditioning and of the accuracy of the kidney T_{eff} estimate on a full patient-specific base.

It is also worth noting that count-rate measurements could be performed not only at the hospital but also at the patient's home by a trained technologist or nurse, if convenient. This fact would have particular relevance in the case the patients that, for any reason, cannot come back to the hospital for late time-points measurements (i.e., around one week post-therapy), that are considered key for a reliable dosimetry [144, 145, 151]. Reducing patient's transfer is not only a benefit in terms of comfort, but also in terms of radioprotection, minimizing the exposure of both the staff and the public.

Care should be put in the reproducibility of the measurement geometry. In this respect, a mark could be drawn directly on the skin of the patient to leave a fixed reference for the subsequent re-positioning of the collimated probe. Identifying the most favourable location for the detector window on patient's back should not represent a problem, since patients undergoing ^{177}Lu PRRT procedures routinely occur pre-treatment SPECT/CT imaging that can be used for this purpose. Otherwise, ultrasonography could used to identify the appropriate positioning in an alternative way, and it would constitute a non-ionizing imaging option.

Finally, it can be argued that patients with important tumour volumes overlapping the collimated cone of view across the kidney region could not be appropriate for the applicability of the proposed protocol. This aspect should be investigated more in detail in future studies on clinical cases. Diagnostic pre-therapy imaging, such as ^{68}Ga-DOTATOC, could be nevertheless employed in the selection of patients that could benefit or not from the proposed renal dosimetry method. Pre-therapy imaging would be desirable also for evaluating the relative renal functionality of the two kidneys. The proposed methodology, indeed, actually permits to calculate the absorbed absorbed dose in the left kidney, by performing the count-rate measurements pointing towards it; but in order to extend realistically the results obtained to the right kidney, avoiding the simple assumption of taking the same result for both kidneys, it is needed an indication of how much the biokinetics of the two kidneys are similar or different. For this purpose, pre-therapy dynamic planar imaging could be quite helpful.

General conclusion

In this brief final chapter are summarized the main contributions and findings of this work of thesis, and also some perspectives for future studies are mentioned.

The first two chapters gave an overview on internal dosimetry in nuclear medicine and on Monte Carlo (MC) methods, respectively. In particular, Chapter 1 presented an up to date literature review on dosimetric concepts and quantities, radiobiological effects, radionuclide therapies, nuclear medicine imaging techniques and, above all, internal dosimetry models. Chapter 2 did the same regarding the basics of MC calculations, their applications in radiation physics and nuclear medicine, and the simulation software packages employed in this thesis: GEANT4, GATE and GAMOS. Part of the contents of these first two chapters will contribute to a book chapter in the upcoming Encyclopedia of Nuclear Medicine and Molecular Imaging edited by Elsevier, entitled "Monte Carlo Methods in Nuclear Medicine", to whose writing I had the privilege to contribute as a co-author and which is currently undergoing the review process.

Chapter 3 described a comparative study of voxel-level patient-specific MC internal dosimetry for ^{18}F-choline PET diagnostics, carried out independently with GATE and GAMOS and focused on the effect on dosimetric results of background noise affecting PET scans used as input data. A threshold-based and segmentation-based filtering procedure was implemented and applied to the considered PET scan, aiming at minimizing the activity concentration in areas corresponding to unrealistic uptaking locations with respect to the CT - primarily air -, in order to identify and correct noise-induced absorbed dose artefacts. The latter ones showed to occur especially in lungs and other air-rich organs and sections of the body, as expectable, and proved to be non-negligible, with filtered-PET average absorbed dose rate estimations being smaller than native-PET ones by approximately 40-50%. The native-PET results obtained with GATE and GAMOS showed acceptable agreement between each other, with only some higher differences in low-density and poorly-perfused voxels, imputable to the density-assignment procedure differing a bit in the two toolkits and having more impact on the mentioned areas. The agreement showed to improve in the case of filtered-PET results.

Partial results of this study were presented at the Scientific meeting of the "Accademia Peloritana dei Pericolanti, Classe di Scienze Fisiche, Matematiche e Naturali", held in Messina in December 2019 [152], and were also part of the following conference paper [153]; final results were presented at the "106° Congresso Nazionale SIF" held on-line in September 2020 [154], and were published in the following journal article [155].

The applied filtering procedure appeared reasonable and valid as a correction method, but the application to a larger cohort of cases would be advisable to establish a more solid evidence of the observed effects. In addition, an experimental and simulative study on a thoracic phantom containing realistic lungs inserts could be a useful complement to verify *ab initio* the effectiveness of the filtering method implemented.

A noticeable aspect of the employed filtering method is its independence on the radiopharmaceutical, on the type of 3D tomographic imaging type used and even on the absorbed dose calculation method, potentially enabling its application to voxel-level dosimetry of any diagnostic and therapeutic procedure and not limiting to calculations done with MC simulations, since the filters act on the input imaging data, that can be equally used in LED and voxelized DPKs convolution approaches.

Chapter 4 dealt with the optimization of computation times in voxel-level patient-specific MC simulations for internal dosimetry of ^{90}Y TARE cases, performed using as input data pre-therapy ^{99m}Tc-MAA SPECT/CTs. For this purpose, the behavior of the computation time as a function of two parameters was investigated, running multiple simulations by varying: the input CT scan resolution – through resamplings of the native scan – and the cuts on the production of secondary particles. Taking as a reference the simulation employing the native CT and the smallest among the production cuts examined (0.01 mm), the best combination of parameters resulted being the choice of a CT resampling with voxel volume 8 times larger than the native one (that was $0.89\times0.89\times2.00$ mm^3), and production cuts between 0.1 and 0.5 mm; this combination guaranteed the maintenance of an excellent dosimetric accuracy, with differences of average absorbed doses with respect to the reference within 1% in liver-related VOI, within 4% in lungs and within 2% in kidneys, while reducing simulation time to the 45% of the reference one. Other combinations of parameters, speeding up the simulation times even to the 25-30 % of the reference at the expense of slightly lower dosimetric accuracies, can also be considered on the basis of the required accuracy.
Preliminary results of the study were presented at the Virtual Scientific meeting of the "Accademia Peloritana dei Pericolanti, Classe di Scienze Fisiche, Matematiche e Naturali", held in November 2020 [156]; final results will be presented at the "107° Congresso Nazionale SIF" as an invited talk, to be communicated on-line in September 2021 [157], and were also submitted to a journal as a research article, which is currently under review.
The results of the reported study can be used as a starting-point guideline for the simulations settings of ^{90}Y TARE MC studies, and the achievable time savings, even if not of order of magnitudes, can be highly beneficial both for single cases and local computing resources, and also in studies carried out on computing grids or supercomputers, with multiple cases or multiple configurations to be investigated.

In Chapter 5 were first described the features of the *OpenDose Dosimetry 3D* free module of the imaging computing software 3D Slicer, a module developed within the *OpenDose* international collaboration for the easy and user-friendly implementation of patient-specific internal dosimetry workflows with multiple algorithms: time integration of activities or of absorbed dose rates, calculated with LED or voxelized DPK convolution or MC simulation. Then it was reported the testing and validation of the module for the dosimetry of ^{90}Y TARE cases, performed by completing dosimetric workflows with all the available algorithms and comparing their results - in terms of average absorbed doses in liver-related VOIs - with literature results obtained with direct GAMOS MC simulations using the same imaging input data. The validation was concluded successfully, given the good agreement found with published results for all the dosimetric algorithms, exhibiting relative differences within 6% for almost all the VOIs and patients considered, and with the few larger discrepancies remaining in any case within 12% and being expected because of the intrinsic differences between the various algorithms.
Preliminary results of this work were communicated by a colleague at the 33rd Annual Congress of the European Association of Nuclear Medicine Congress (EANM20), held on-line in October 2020 [158], and an article regarding the validation of the

OpenDose Dosimetry 3D module, containing also the final results reported in this thesis, is being written.

In Chapter 6 was treated the investigation and possible correction of absorbed dose artefacts caused by background noise and motion blurring present in input SPECTs in the frame of voxel-level patient-specific MC dosimetry of ^{90}Y TARE. Similarly to the study of Chapter 3, this goal was achieved by developing threshold-based and segmentation-based filtering techniques to be applied to the SPECT scans exploiting the co-registered input CT scans, in this case particularly to minimize the unrealistic simulation of radionuclide decays respectively in air, in lungs VOIs or in all the voxels outside liver VOI. Comparing the results of the various filtered-SPECT simulations with the native-SPECT ones, significant differences emerged: native-SPECT average absorbed doses showed underestimation with respect to filtered-SPECT ones in liver-related VOIs, with relative percent differences up to 40% for some of the adopted filters, while in lungs-related VOIs overestimation was found, with relative percent differences ranging from 20% to even 99%, strongly depending on the employed filter. Also in this case the filtering techniques of the functional scans appear to have the potential for being an effective tool for the correction of absorbed dose artefacts caused by different types of noise, but a careful choice and implementation of them is essential, requiring the fundamental help of physicians in defining segmentation-based algorithms, since they rely on the correct interpretation of body's anatomy in CT scans and of the nature of the spatial distribution of activity in the corresponding SPECT scans.
Partial results of the mentioned work were presented at the 3rd European Congress of Medical Physics (ECMP 2020), held on-line in June 2021 [159], and updated results will be presented at the "107° Congresso Nazionale SIF" in September 2021 [157]. The submission to a journal of an article based on these results in under consideration.

In Chapter 7 was presented a novel simplified protocol for renal patient-specific dosimetry of ^{177}Lu PRRTs, based on a single SPECT/CT and multiple collimated probe measurements executed properly pointing towards kidneys to deduce the information on the radiopharmecautical biokinetics in them. A proof of concept of this original method was carried out by firstly performing an abdominal phantom experiment, aimed at retrieving from external count-rate measurements the correct effective half-life in kidneys inserts in presence of other emitting organ inserts; this result was successfully achieved, with agreement within 3% with the value expected from the experiment construction. Then GATE MC simulations reproducing the experiment were developed, producing a similar level of agreement and verifying the correct implementation of the set-up in the simulation environment. Finally, the method was tested via MC on a patient imaging dataset of a ^{177}Lu-DOTATATE cycle, composed of three SPECT/CTs (respectively at 2, 20 and 70 hours), by simulating the external probe measurements on the reconstructed patient's abdomen with ^{177}Lu distribution within it, and comparing the results of the simplified dosimetry workflow with a complete imaging-based workflow employing all the SPECT/CTs of the dataset. The simplified workflow led to kidney average absorbed dose estimations compatible with the complete ones within about 6%, 12% and 1%, using respectively the SPECT/CT at 2, 20 and 70 hours, a promising result especially when using the earliest and latest time point among the three.
The results of this study were submitted to a journal as an article, which is currently under review, and will be presented at the 34th Annual Congress of the European Association of Nuclear Medicine (EANM21), that will take place on-line in October 2021 [160].

The robustness of the proposed protocol and the best choice of the time point for the single SPECT/CT should be deeply investigated in future experimental studies, performing the collimated probe measurements on actual ^{177}Lu PRRT patients and for a larger number of time points. The conducted proof of concept encourages to follow this path, since if good results will be confirmed in a cohort, it will open for the clinical applicability of the method, that would bring the highly favourable aspects of reducing the needed tomographic imaging to a single scan, minimizing the occupation time of scanners and improving patient comfort, and thus being more feasible in hospitals still not performing dosimetry-based personalized activity adjustment for ^{177}Lu therapies.

In conclusion, all the results obtained in this thesis point out the inestimable utility of MC simulation in the field of internal dosimetry in nuclear medicine, from the performing of patient-specific dosimetric case studies, also constituting a reference for all the simplified dosimetric methods, to the possibility of testing novel approaches for such simplified methods, and also new diagnostic and therapeutic procedures. Nevertheless, they also showed the possible limits of MC approach, highlighting the need of extreme attention in implementing imaging-based MC simulations, since, even if MC is in principle the gold standard for internal dosimetry, this holds true if an excellent correspondence between the real system investigated and its modeled counterpart in the simulation environment is realized. Noise and artefacts affecting the input scans, almost inevitably because of their nature of reconstruction tomographic images, negatively influences the mentioned correspondence, and have proven to have the possibility of producing non-negligible misestimation in absorbed dose calculations, especially in organs and regions with substantial presence of air. Pre-simulation filtering procedures of the functional scans, implemented with high care and rationality, configure themselves as a viable tool for the correction of such possible misestimations, and therefore to overcome the possible limits of MC calculations for internal dosimetry based on imaging data. These improvements would contribute to estimate with the maximum possible accuracy the absorbed dose in organs and tissues of interest for diagnostic and therapeutic procedures. From a better dosimetric accuracy consequently benefit the accuracy of patient-specific optimization of treatments and also of the deduction of dose-effect correlations, which in turns would contribute to the ultimate the goal of nuclear medicine treatments: the improvement of life expectation and quality of life for patients affected by diseases.

Appendix A

^{90}Y-TARE MC dosimetry: optimization of simulation times

In the present Appendix Chapter additional results relative to Chapter 4 of this dissertation are reported.

A.1 Average absorbed doses tables

Average absorbed doses $\langle D\rangle_{VOI}$'s, relative percent differences ε_{VOI}'s, and average standard deviation of mean absorbed doses $\langle\delta\rangle_{VOI}$, as defined in Sec. 4.5 of Chapter 4, are reported in Tables A.1-A.5.

A.2 DVHs

DVHs within VOIs, relative to all the simulations of Chapter 4, are reported in Figures A.1-A.12, each compared with the corresponding DVH obtained from the reference simulation (N CT and 0.01 mm production cut) in terms of relative per cent difference σ between volume percentages, defined in Eq. 4.8.

TABLE A.1: $\langle D \rangle_{VOI}$ (Gy), $\langle \delta \rangle_{VOI}$ (%) and ε_{VOI} (Eq. 4.7 in Chapter 4) for N CT in the considered VOIs, respectively reported as the upper, middle and lower value in column for each box, i.e. for each combination of range cut and VOI.

	VOI	Li.	Le.	Li.P.	H.Li.	H.Li.P.	R.K.	L.K.	R.L.	L.L.
CT	**Cut**									
N	0.01	31.032 22.466 /	168.844 2.500 /	104.761 3.550 /	11.914 25.394 /	61.540 4.259 /	0.6476 42.075 /	0.3219 63.671 /	6.084 17.108 /	1.501 40.927 /
	0.05	32.032 22.436 -1.81E-05	168.850 2.498 3.43E-05	104.765 3.548 3.56E-05	11.912 25.360 -1.25E-04	61.543 4.256 4.04E-05	0.6489 41.958 1.94E-03	0.3229 63.570 3.29E-03	6.063 17.111 -3.53E-03	1.501 40.997 -5.32E-04
	0.1	32.033 22.448 2.46E-05	168.860 2.498 9.32E-05	104.751 3.549 -9.88E-05	11.912 25.374 -1.43E-04	61.512 4.258 -4.58E-04	0.6497 41.992 3.29E-03	0.3235 63.522 4.95E-03	6.0017 17.234 -1.36E-02	1.491 41.074 -7.08E-03
	0.5	32.032 22.522 -1.29E-06	168.836 2.507 -4.66E-05	104.748 3.561 -1.27E-04	11.914 25.457 4.87E-05	61.523 4.272 -2.76E-04	0.6498 42.157 3.36E-03	0.3213 63.828 -1.94E-03	5.958 17.290 -2.08E-02	1.485 41.092 -1.10E-02
	1.0	32.032 22.588 -1.03E-05	168.852 2.517 4.91E-05	104.745 3.576 -1.62E-04	11.912 25.532 -1.53E-04	61.507 4.290 -5.52E-04	0.6505 42.075 4.46E-03	0.3240 63.826 6.14E-03	5.9674 17.491 -1.92E-02	1.4849 41.439 -1.10E-02

TABLE A.2: $\langle D \rangle_{VOI}$ (Gy), $\langle \delta \rangle_{VOI}$ (%) and ε_{VOI} (Eq. 4.7 in Chapter 4) for R2 CT in the considered VOIs, respectively reported as the upper, middle and lower value in column for each box, i.e. for each combination of range cut and VOI.

	VOI	Li.	Le.	Li.P.	H.Li.	H.Li.P.	R.K.	L.K.	R.L.	L.L.
CT	**Cut**									
R2	0.01	32.054	167.762	104.999	11.814	61.715	0.6481	0.3247	5.843	1.449
		16.530	1.842	2.603	18.716	3.128	30.782	52.228	12.985	33.527
		6.59E-04	-6.41E-03	2.27E-03	-8.40E-03	2.83E-03	7.55E-04	8.68E-03	-3.97E-02	-3.53E-02
	0.05	32.051	167.738	104.988	11.814	61.712	0.6506	0.3242	5.846	1.446
		16.520	1.840	2.601	18.704	3.125	30.689	52.264	12.962	33.482
		5.62E-04	-6.55E-03	2.16E-03	-8.38E-03	2.79E-03	4.70E-03	6.95E-03	-3.92E-02	-3.69E-02
	0.1	32.052	167.760	104.986	11.813	61.692	0.6525	0.3225	5.825	1.433
		16.510	1.840	2.601	18.693	3.126	30.675	52.276	12.991	33.574
		6.18E-04	-6.42E-03	2.14E-03	-8.48E-03	2.47E-03	7.63E-03	1.79E-03	-4.26E-02	-4.54E-02
	0.5	32.051	167.736	104.992	11.814	61.720	0.6521	0.3232	5.786	1.428
		16.570	1.844	2.606	18.761	3.132	30.736	52.317	13.008	33.752
		5.56E-04	-6.56E-03	2.20E-03	-8.42E-03	2.91E-03	6.95E-03	4.15E-03	-4.91E-02	-4.88E-02
	1.5	32.050	167.744	104.979	11.812	61.692	0.6511	0.3245	5.759	1.430
		16.618	1.852	2.619	18.814	3.147	30.872	52.370	13.227	33.922
		5.39E-04	-6.51E-03	2.07E-03	-8.53E-03	2.46E-03	5.41E-03	7.96E-03	-5.36E-02	-4.78E-02

TABLE A.3: $\langle D \rangle_{VOI}$ (Gy), $\langle \delta \rangle_{VOI}$ (%) and ε_{VOI} (Eq. 4.7 in Chapter 4) for R8 CT in the considered VOIs, respectively reported as the upper, middle and lower value in column for each box, i.e. for each combination of range cut and VOI.

	VOI	Li.	Le.	Li.P.	H.Li.	H.Li.P.	R.K.	L.K.	R.L.	L.L.
CT	**Cut**									
R8	0.01	31.907 10.555 -3.91E-03	168.390 1.170 -2.69E-03	104.693 1.662 -6.52E-04	11.813 11.930 -8.47E-03	61.696 1.994 2.52E-03	0.6511 19.348 5.37E-03	0.3282 37.034 1.96E-02	5.841 8.452 -3.99E-02	1.458 22.390 -2.92E-02
	0.05	31.909 10.542 -3.85E-03	168.389 1.169 -2.69E-03	104.685 1.660 -6.56E-04	11.814 11.916 -8.28E-03	61.696 1.992 2.52E-03	0.6469 19.385 -1.14E-03	0.3269 37.096 1.56E-02	5.840 8.429 -4.02E-02	1.456 22.372 -2.99E-02
	0.1	31.906 10.540 -3.95E-03	168.375 1.169 -2.78E-03	104.685 1.660 -7.27E-04	11.814 11.913 -8.38E-03	61.693 1.992 2.48E-03	0.6481 19.384 7.48E-04	0.3277 36.853 1.80E-02	5.816 8.461 -4.41E-02	1.450 22.470 -3.40E-02
	0.5	31.905 10.552 -3.98E-03	138.379 1.170 -2.75E-03	104.679 1.662 -7.87E-04	11.812 11.926 -8.54E-03	61.680 1.994 2.26E-03	0.6478 19.371 3.33E-04	0.3271 36.991 1.63E-02	5.777 8.469 -5.06E-02	1.444 22.417 -3.79E-02
	2.0	31.907 10.568 -3.91E-03	168.395 1.174 -2.66E-03	104.682 1.667 -7.63E-04	11.812 11.944 -8.53E-03	61.673 2.001 2.15E-03	0.6510 19.446 5.30E-03	0.3287 37.139 2.11E-02	5.744 8.585 -5.60E-02	1.436 22.541 -4.36E-02

TABLE A.4: $\langle D \rangle_{VOI}$ (Gy), $\langle \delta \rangle_{VOI}$ (%) and ε_{VOI} (Eq. 4.7 in Chapter 4) for R64 CT in the considered VOIs, respectively reported as the upper, middle and lower value in column for each box, i.e. for each combination of range cut and VOI.

	VOI	Li.	Le.	Li.P.	H.Li.	H.Li.P.	R.K.	L.K.	R.L.	L.L.
CT	**Cut**									
R64	0.01	31.635	164.539	105.779	12.141	64.918	0.6406	0.3301	5.331	1.367
		4.583	0.527	0.735	5.176	0.879	8.478	16.708	4.236	11.708
		-1.24E-02	-2.55E-02	9.71E-03	1.91E-02	5.49E-02	-1.08E-02	2.54E-02	-1.24E-01	-8.98E-02
	0.05	31.634	164.520	105.772	12.142	64.920	0.6395	0.3327	5.345	1.375
		4.582	0.526	0.734	5.175	0.878	8.486	16.722	4.234	11.735
		-1.24E-02	-2.56E-02	9.65E-03	1.91E-02	5.49E-02	-1.25E-02	3.35E-02	-1.22E-01	-8.40E-02
	0.1	31.631	164.528	105.771	12.138	64.912	0.6391	0.3308	5.340	1.371
		4.582	0.526	0.734	5.175	0.878	8.483	16.612	4.226	11.663
		-1.25E-02	-2.56E-02	9.63E-03	1.88E-02	5.48E-02	-1.32E-02	2.77E-02	-1.23E-01	-8.71E-02
	0.5	31.631	164.514	105.758	12.140	64.900	0.6407	0.3322	5.314	1.362
		4.589	0.526	0.734	5.182	0.878	8.465	16.604	4.217	11.715
		-1.25E-02	-2.56E-02	9.51E-03	1.90E-02	5.46E-02	-1.07E-02	3.19E-029	-1.27E-01	-9.28E-02
	4.0	31.633	164.532	105.760	12.139	64.891	0.642	0.332	5.263	1.360
		4.593	0.527	0.735	5.188	0.880	8.485	16.654	4.269	8.484
		-1.25E-02	-2.55E-02	9.53E-03	1.89E-02	5.44E-02	-8.21E-03	3.08E-02	-1.35E-01	-9.44E-02

TABLE A.5: $\langle D \rangle_{VOI}$ (Gy), $\langle \delta \rangle_{VOI}$ (%) and ε_{VOI} (Eq. 4.7 in Chapter 4) for RS CT in the considered VOIs, respectively reported as the upper, middle and lower value in column for each box, i.e. for each combination of range cut and VOI.

	VOI	Li.	Le.	Li.P.	H.Li.	H.Li.P.	R.K.	L.K.	R.L.	L.L.
CT	**Cut**									
RS	0.01	31.956	169.278	105.165	11.510	61.618	0.6497	0.3235	5.613	1.349
		4.858	0.530	0.752	5.502	0.903	8.887	18.333	4.289	12.823
		-2.39E-03	2.57E-03	3.85E-03	-3.39E-02	1.26E-03	3.24E-03	4.82E-03	-7.75E-02	-1.02E-01
	0.05	31.954	169.270	105.155	11.509	61.607	0.6505	0.3240	5.607	1.352
		4.846	0.529	0.751	5.490	0.902	8.863	18.094	4.283	12.786
		-2.44E-03	2.52E-03	3.76E-03	-3.39E-02	1.08E-03	4.48E-03	6.45E-03	-7.85E-02	-9.98E-02
	0.1	31.953	169.266	105.147	11.509	61.596	0.6521	0.3238	5.598	1.348
		4.848	0.529	0.751	5.491	0.902	8.883	18.256	4.287	12.787
		-2.47E-03	2.50E-03	3.68E-03	-3.40E-02	9.02E-04	6.88E-03	5.72E-03	-8.00E-02	-1.02E-01
	0.5	31.954	169.265	105.153	11.510	61.607	0.6537	0.3234	5.673	1.344
		4.847	0.529	0.751	5.490	0.902	8.849	18.430	4.286	12.616
		-2.45E-03	2.49E-03	3.74E-03	-3.39E-02	1.08E-03	9.45E-03	7.44E-03	-8.41E-02	-1.05E-01
	4.0	31.953	169.278	105.150	11.507	61.592	0.6471	0.3225	5.45	1.335
		4.858	0.530	0.752	5.502	0.903	8.998	18.441	4.336	12.730
		-2.47E-03	2.57E-03	3.71E-03	-3.41E-02	8.48E-04	-7.80E-04	1.87E-03	-8.87E-02	-1.11E-01

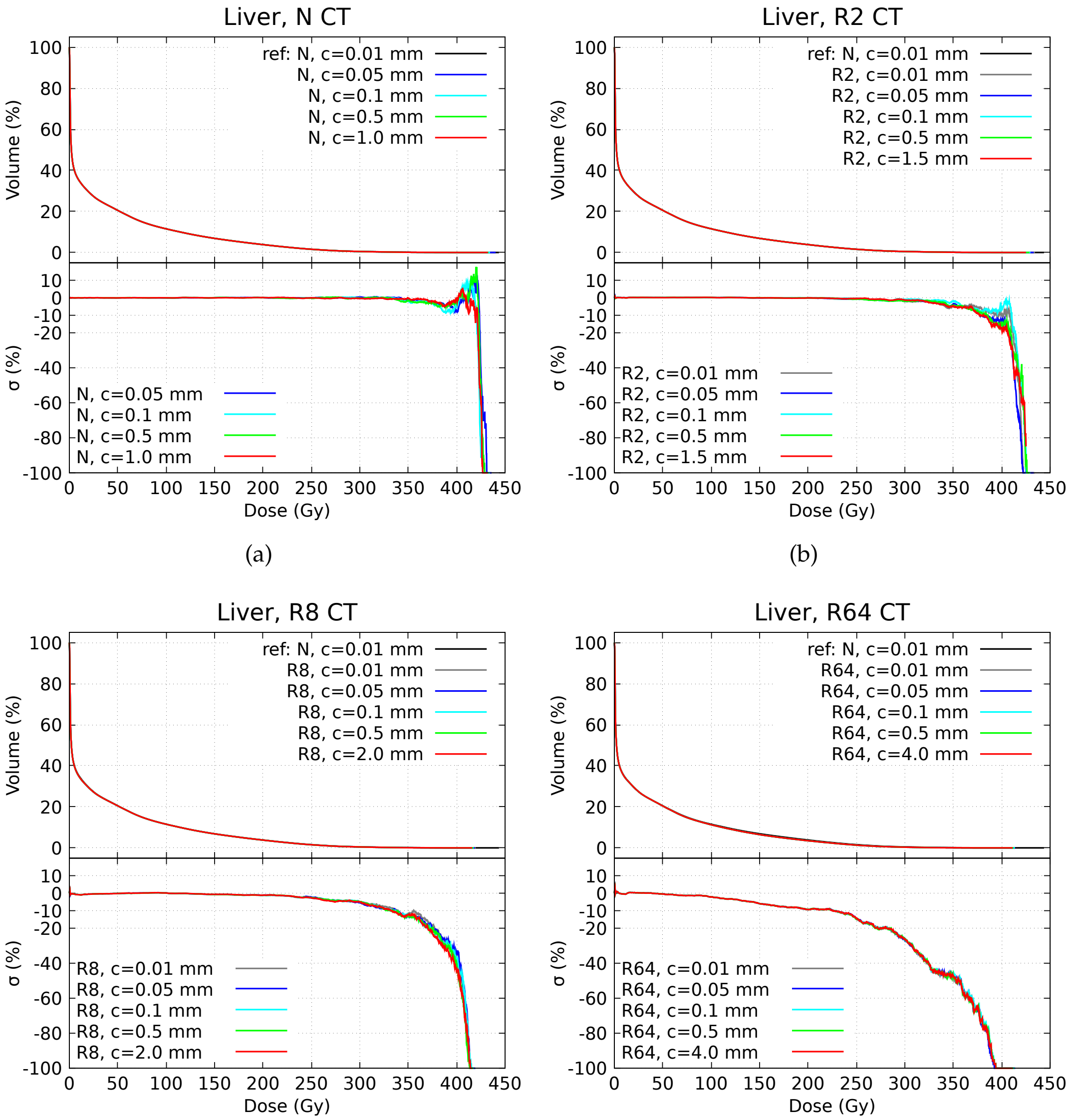

(a) (b)

(c) (d)

FIGURE A.1: DVHs and σs (%) in liver VOI for N, R2, R8 and R64 CTs, relative to Chapter 4.

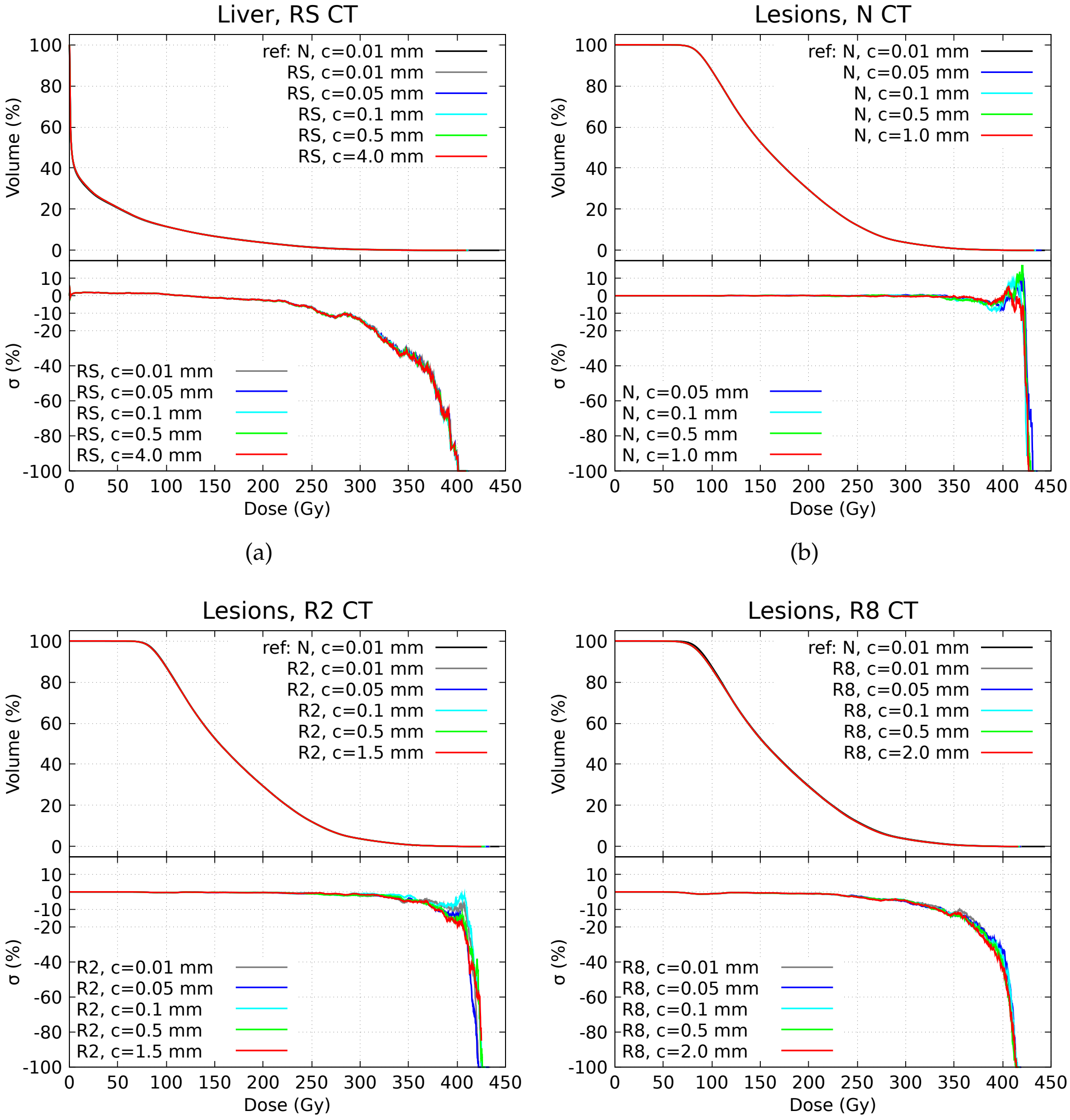

(a) (b)

(c) (d)

FIGURE A.2: DVHs and σs (%) in liver VOI for RS CT, and in lesions VOI for N, R2 and R8 CTs, relative to Chapter 4.

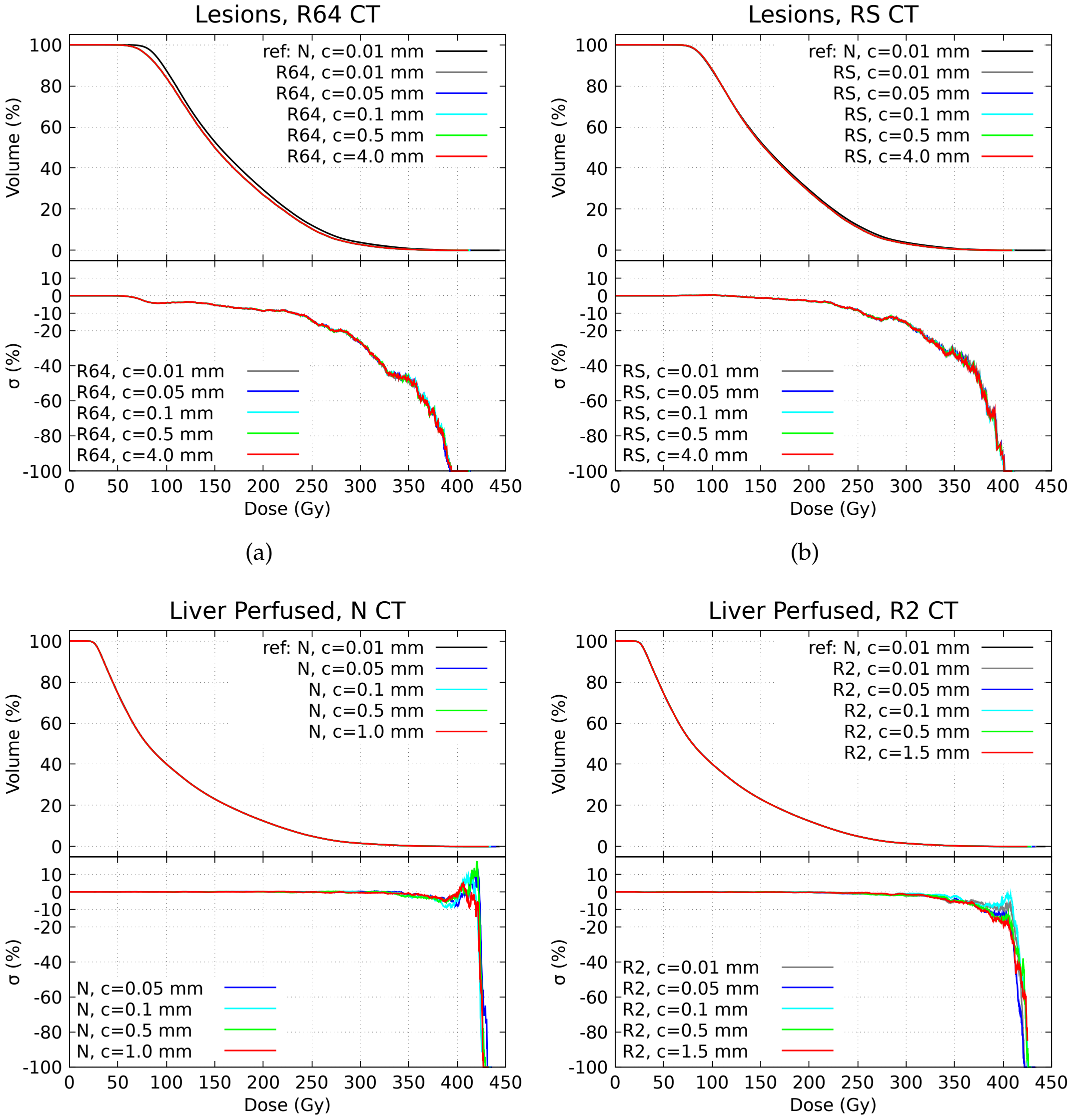
Lesions, R64 CT

Lesions, RS CT

Liver Perfused, N CT

Liver Perfused, R2 CT

(a)

(b)

(c)

(d)

FIGURE A.3: DVHs and σs (%) in lesions VOI for R64 and RS CTs, and in liver perfused VOI for N and R2 CTs, relative to Chapter 4.

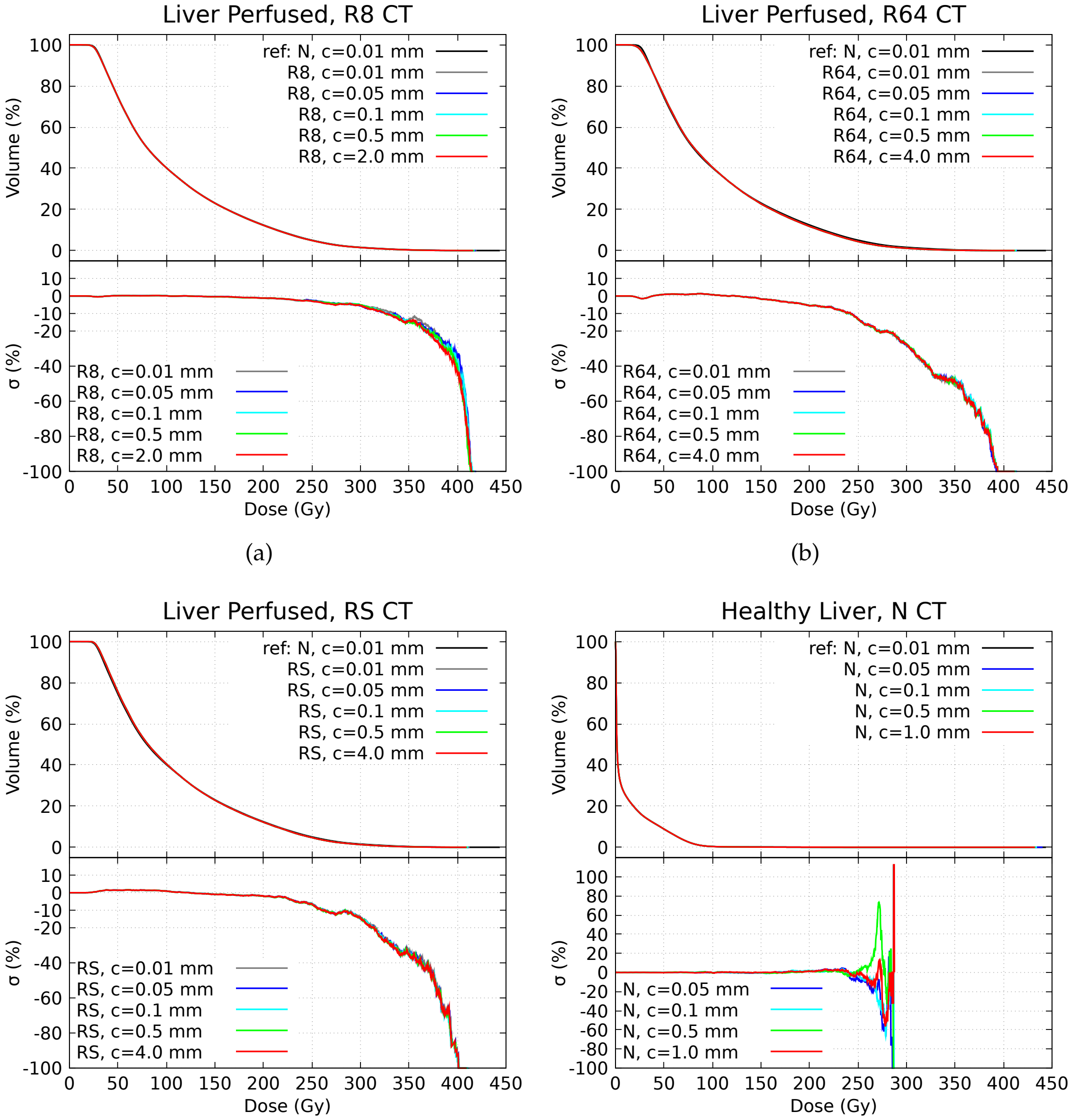

(a) (b)

(c) (d)

FIGURE A.4: DVHs and σs (%) in liver perfused VOIs for R8, R64 and RS CTs, and in healthy liver VOI for N CT, relative to Chapter 4.

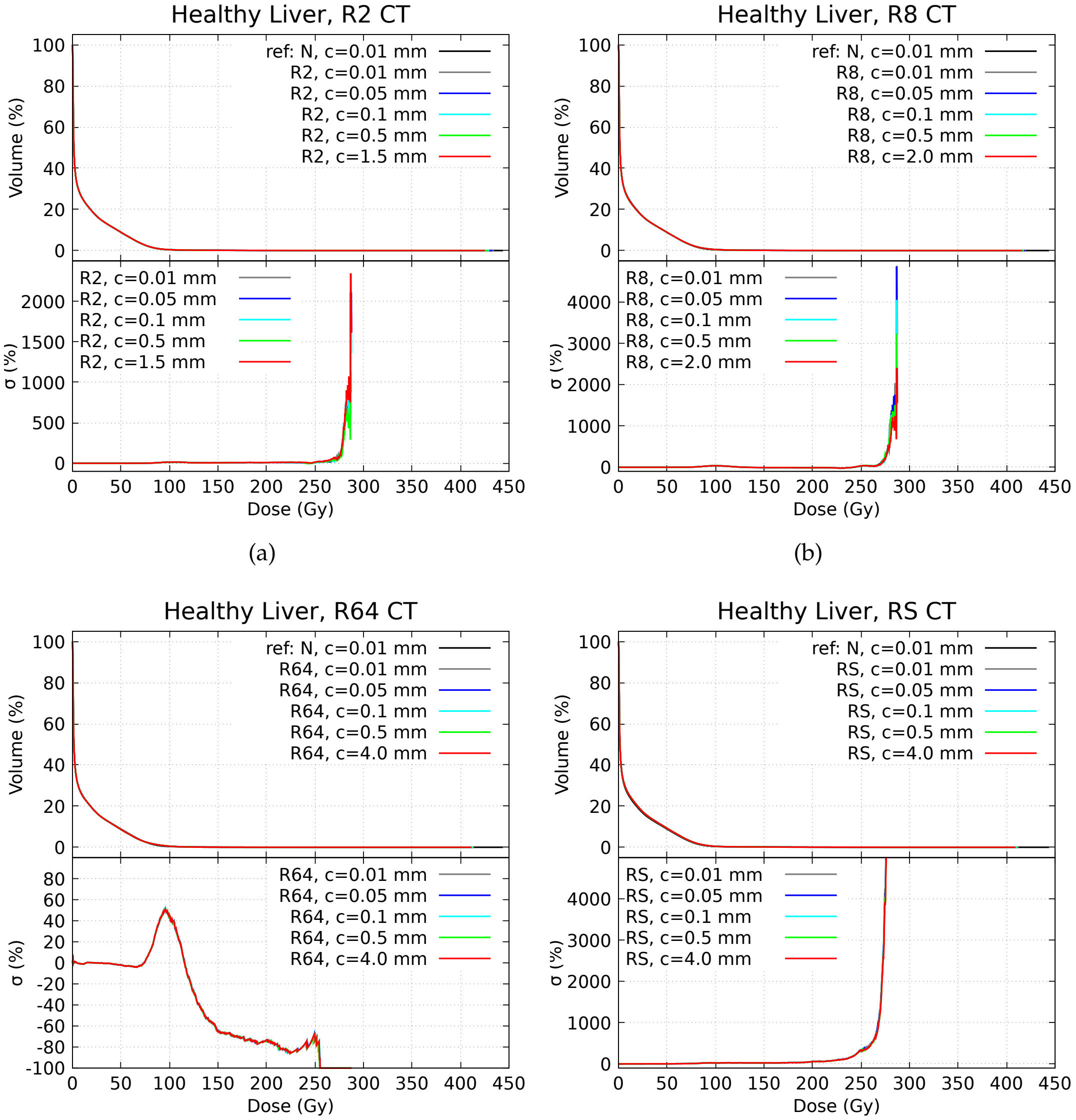

(a)

(b)

(c)

(d)

FIGURE A.5: DVHs and σs (%) in healthy liver VOI for R2, R8, R64 and RS CTs, relative to Chapter 4.

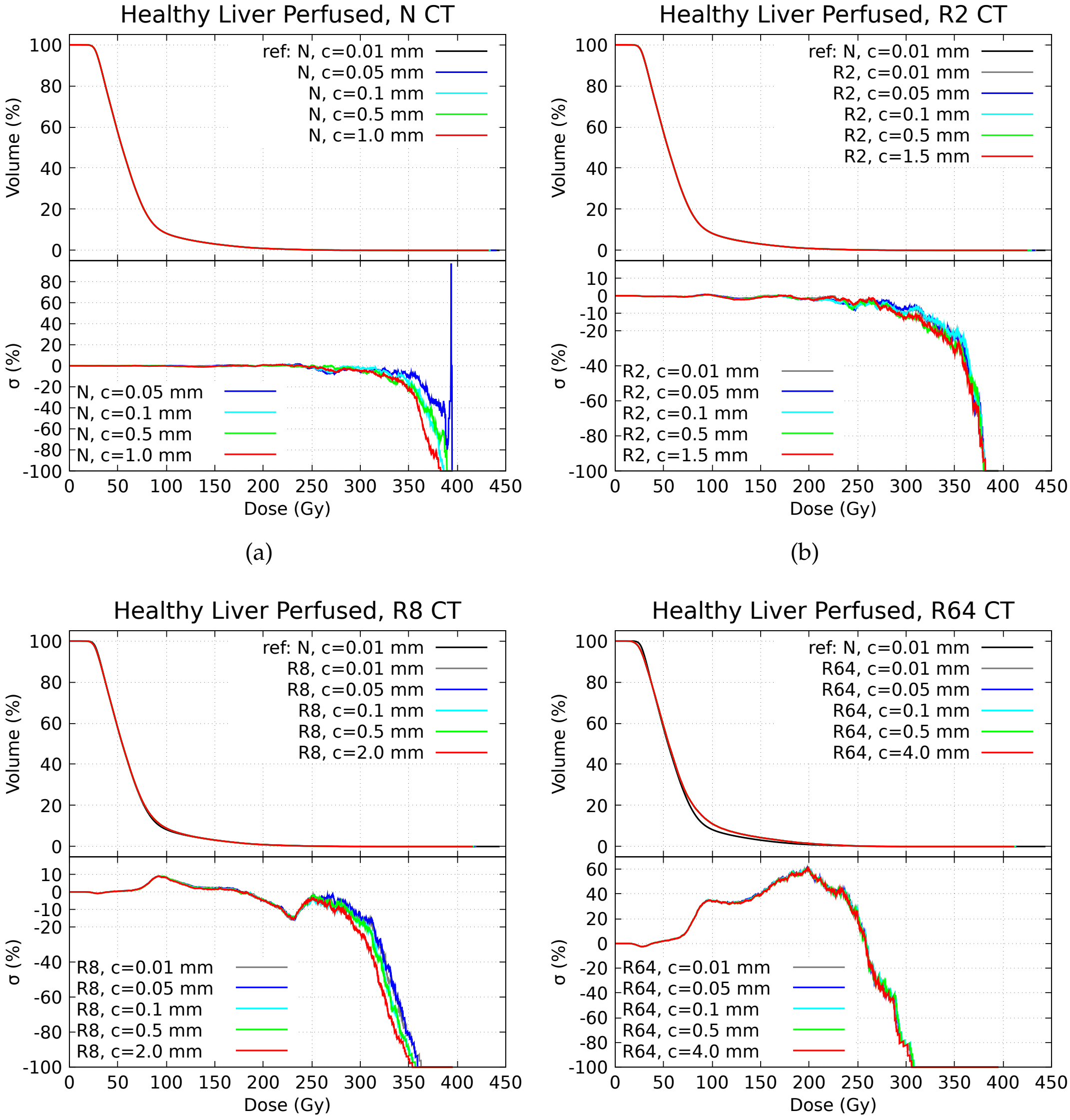

(a) (b) (c) (d)

FIGURE A.6: DVHs and σs (%) in healthy liver perfused VOI for N, R2, R8 and R64 CTs, relative to Chapter 4.

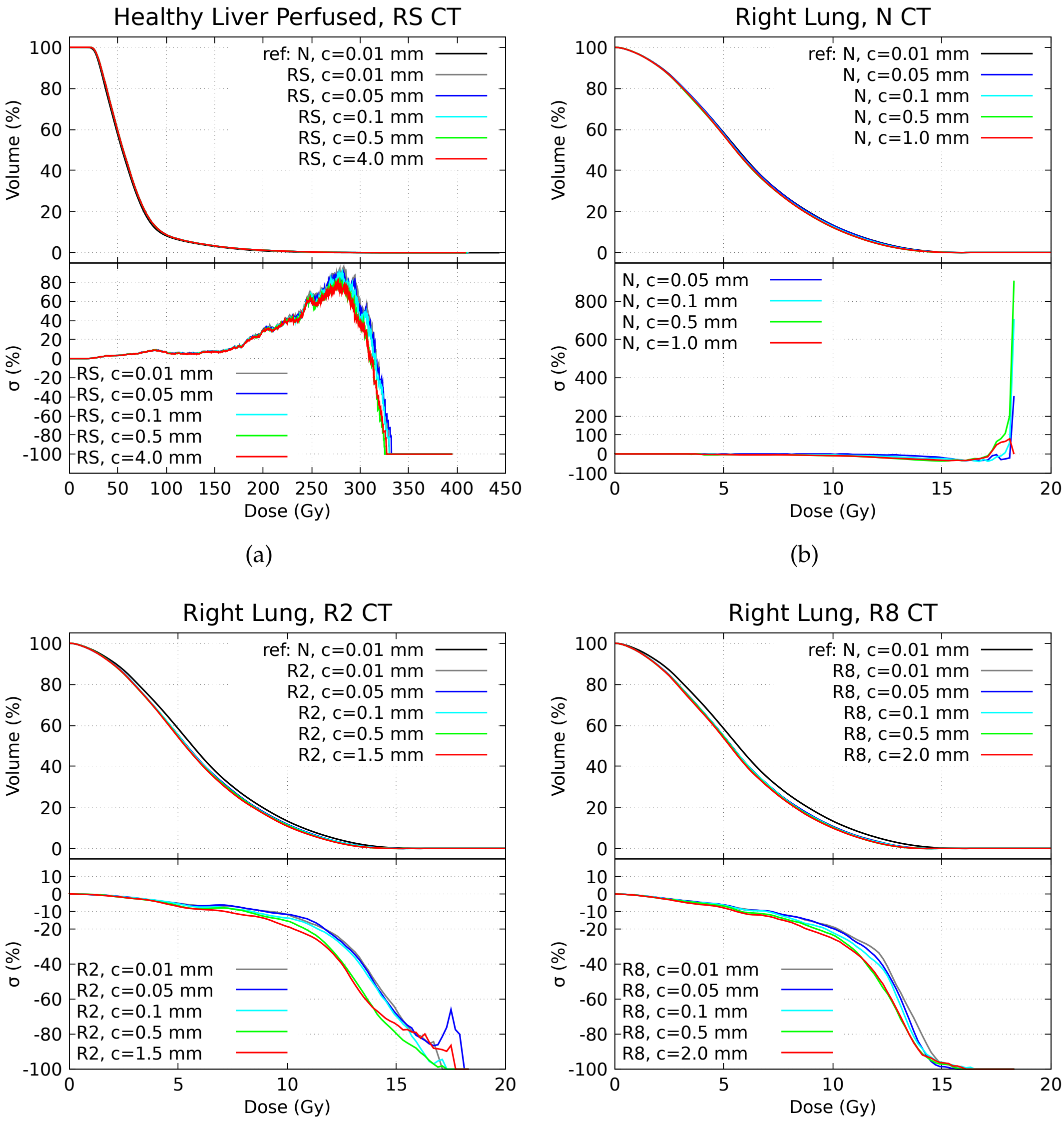

(a) (b)

(c) (d)

FIGURE A.7: DVHs and σs (%) in healthy liver perfused VOI for RS CT, and in right lung VOI for N, R2 and R8 CTs, relative to Chapter 4.

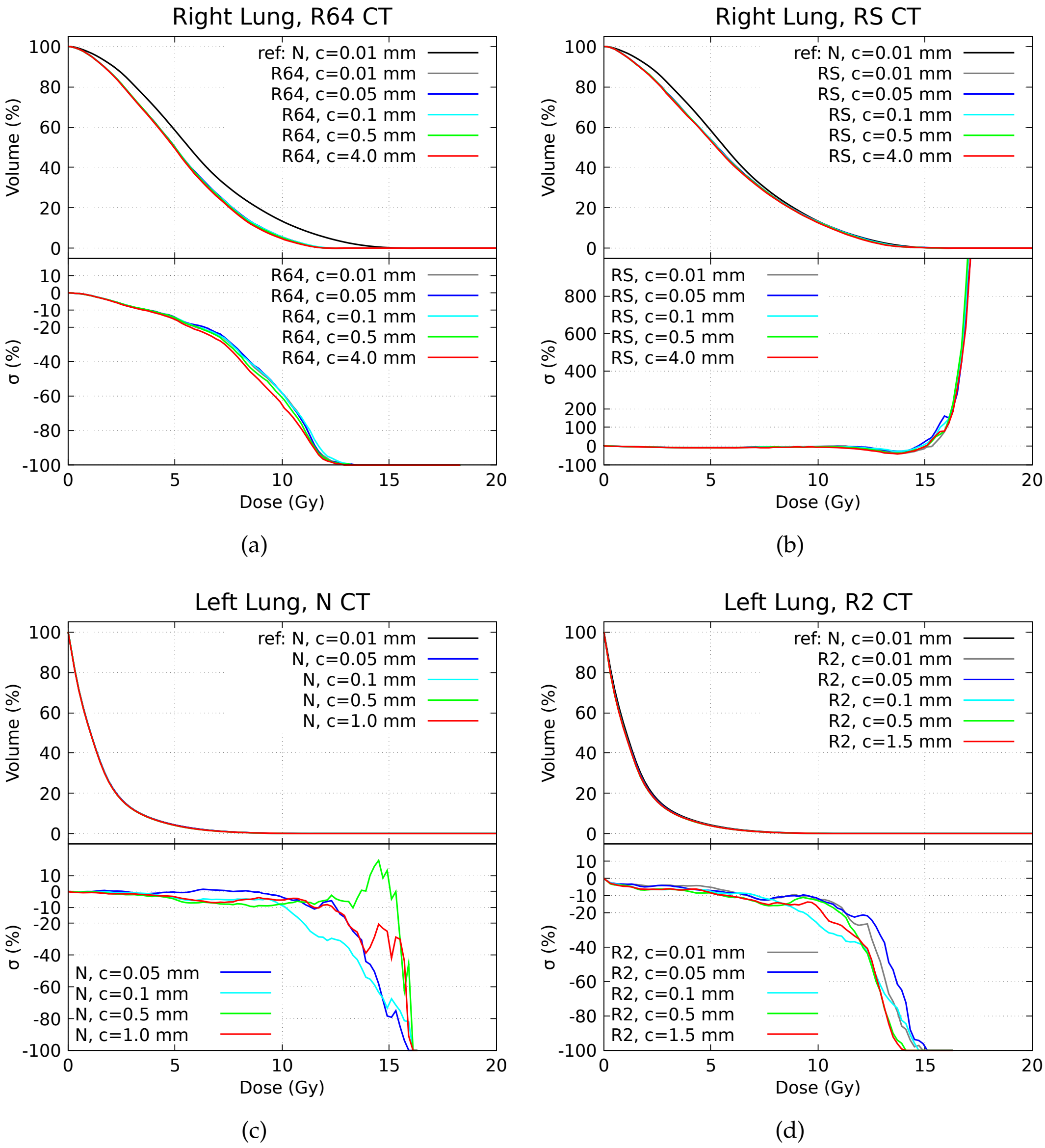

(a) (b)

(c) (d)

FIGURE A.8: DVHs and σs (%) in right lung VOI for R64 and RS CTs, and in left lung VOI for N and R2 CTs, relative to Chapter 4.

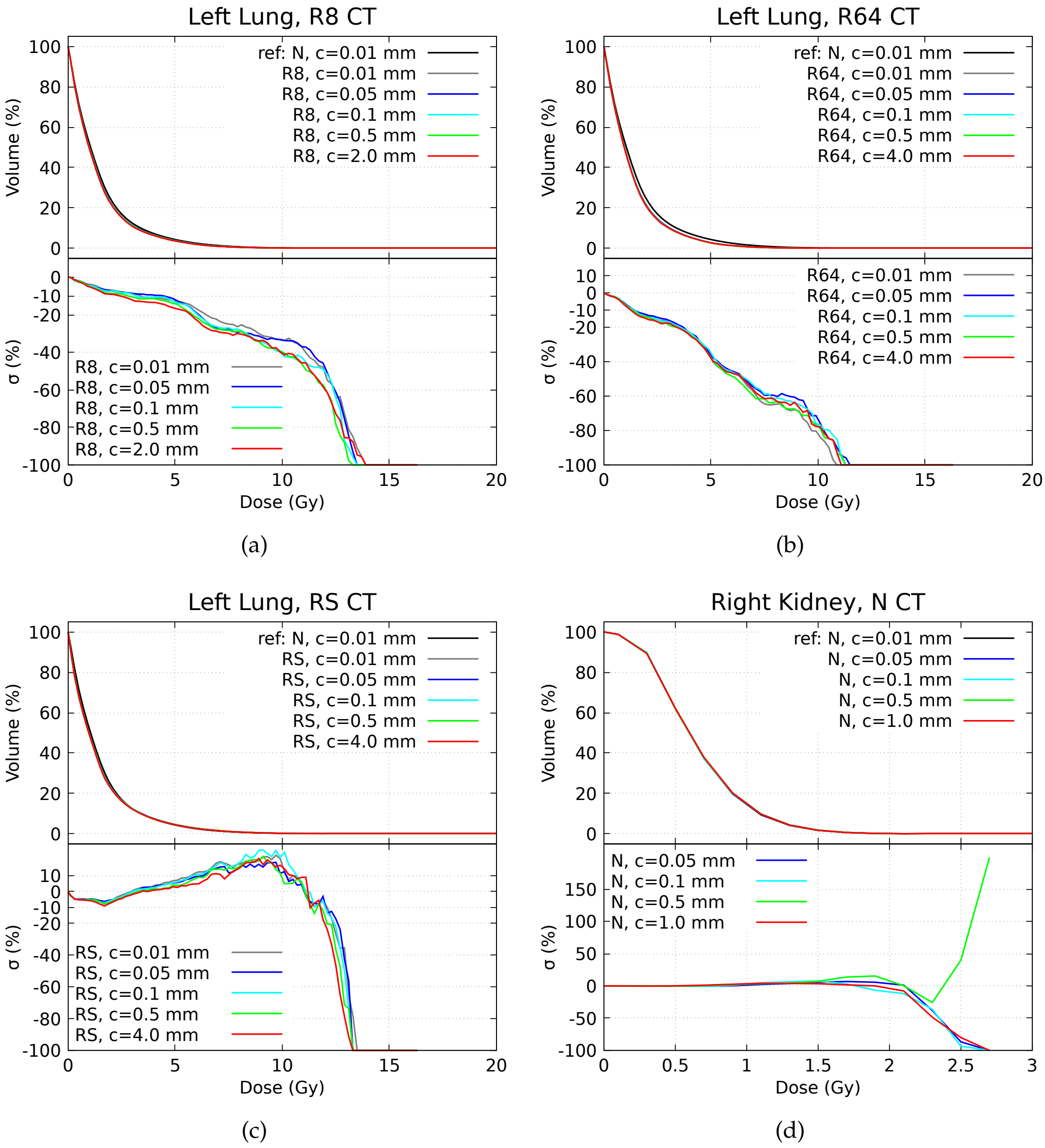

(a) (b)

(c) (d)

FIGURE A.9: DVHs and σs (%) in left lung VOI for R8, R64 and RS CT, and in right kidney VOI for N CT, relative to Chapter 4.

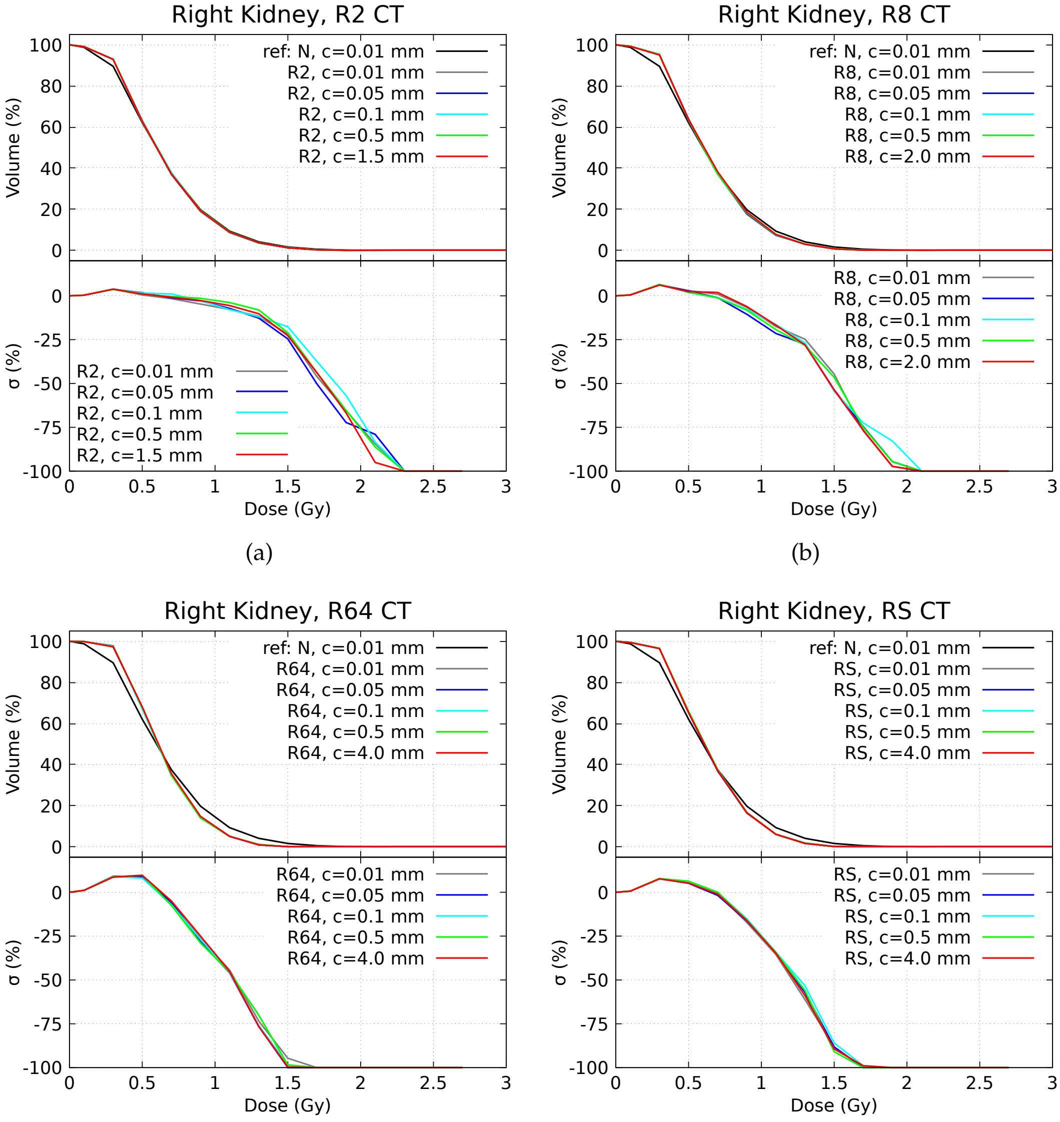

(a) (b)

(c) (d)

FIGURE A.10: DVHs and σs (%) in right kidney VOI for R2, R8, R64 and RS CTs, relative to Chapter 4.

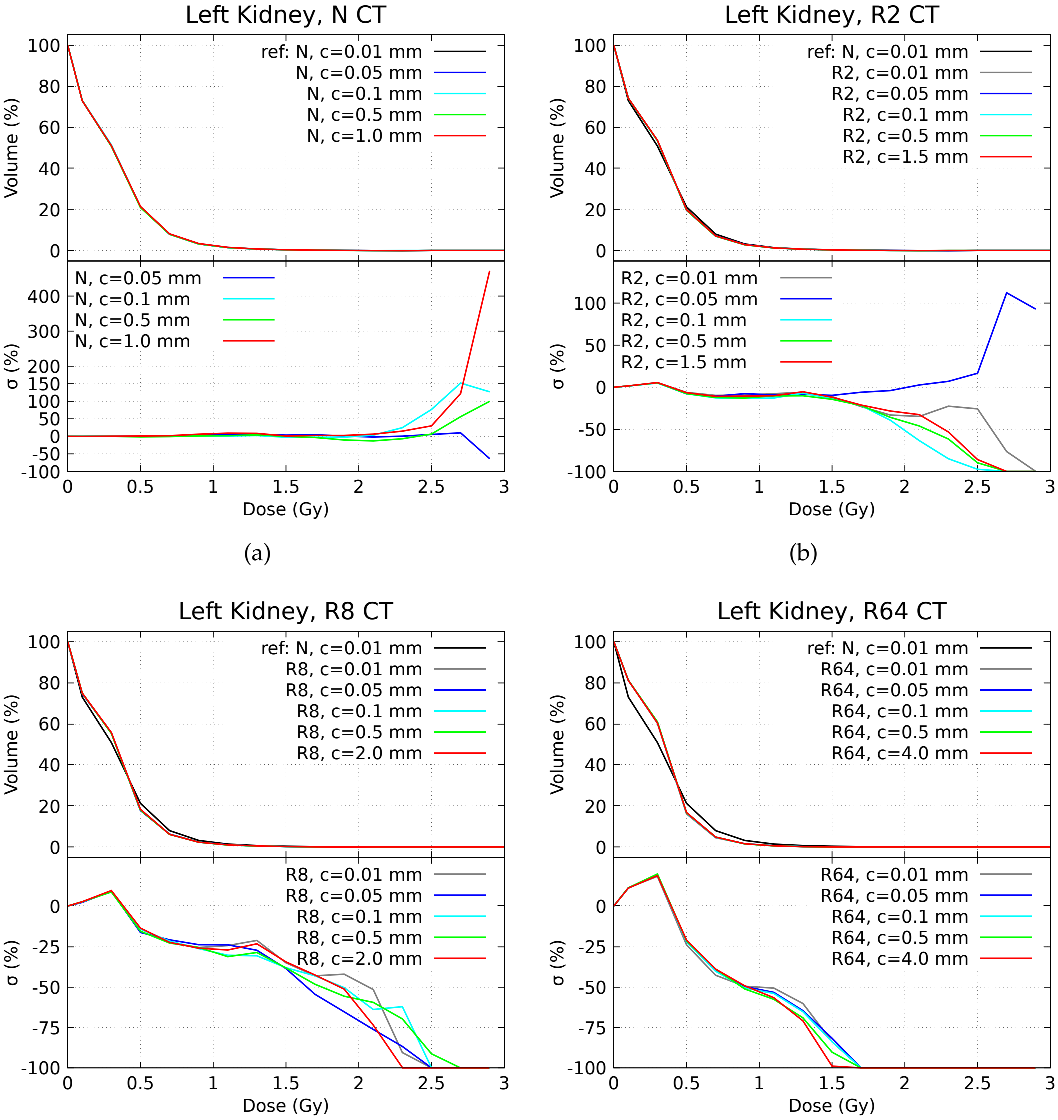

(a)

(b)

(c)

(d)

FIGURE A.11: DVHs and σs (%) in left kidney VOI for N, R2, R8 and R64 CTs, relative to Chapter 4.

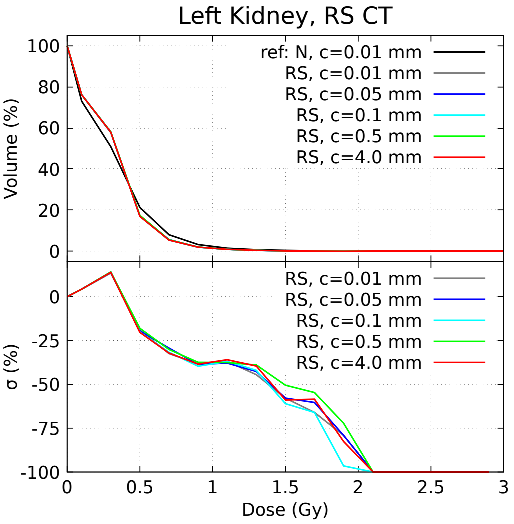

(a)

FIGURE A.12: DVHs and σs (%) in left kidney VOI for RS CT, relative to Chapter 4.

Appendix B

^{90}Y-TARE MC dosimetry: effects of SPECT artefacts and noise

In the present Appendix Chapter additional results relative to Chapter 6 of this dissertation are reported.

B.1 DVHs

The DVHs within VOIs relative to all the simulations of Chapter 6 are reported in Figures B.1 and B.2 for patient 1, in Figures B.3 and B.4 for patient 2, in Figures B.5 and B.6 for patient 3.

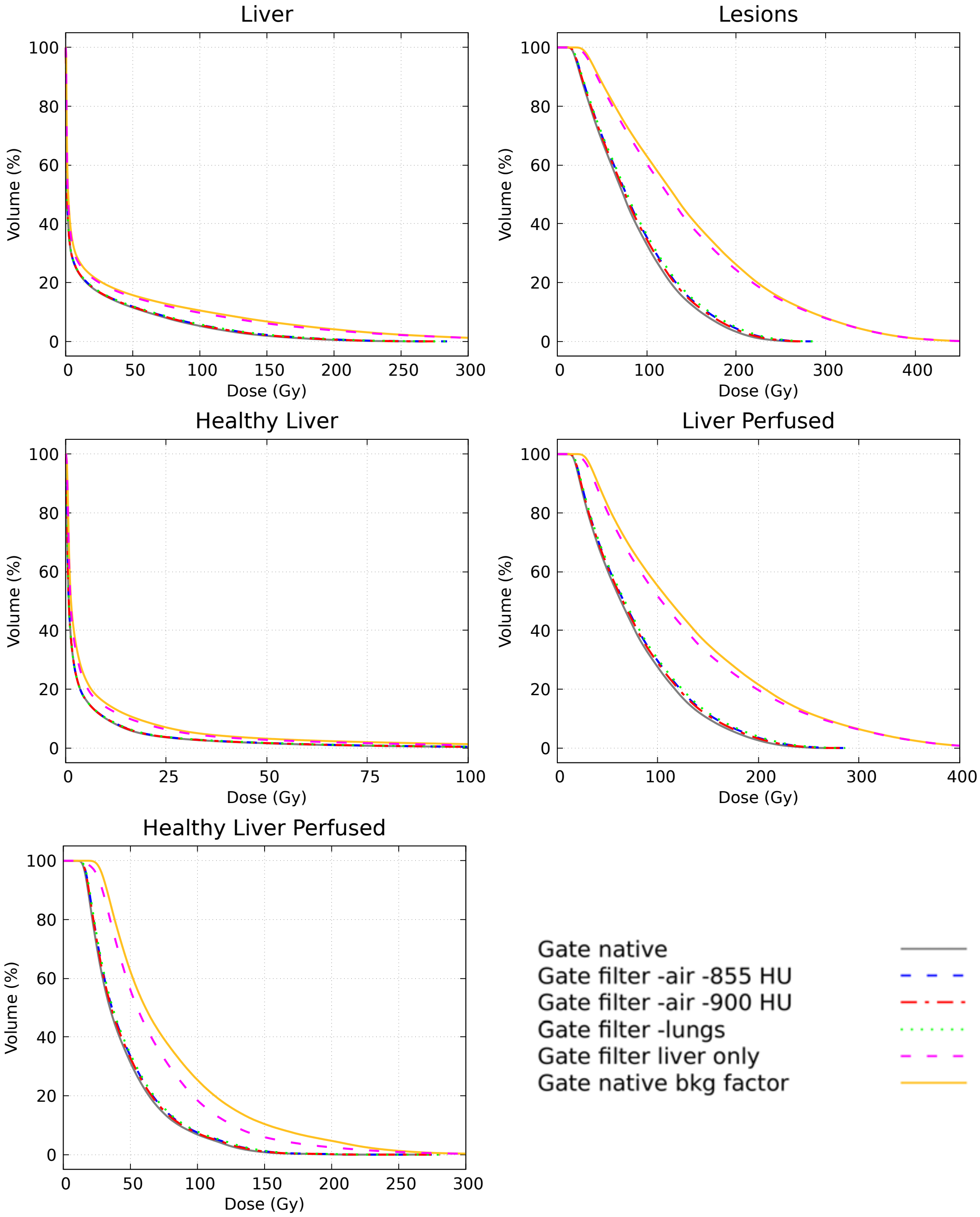

FIGURE B.1: DVHs in liver-related VOIs of patient 1 obtained with all the types of GATE simulations described in Chapter 6.

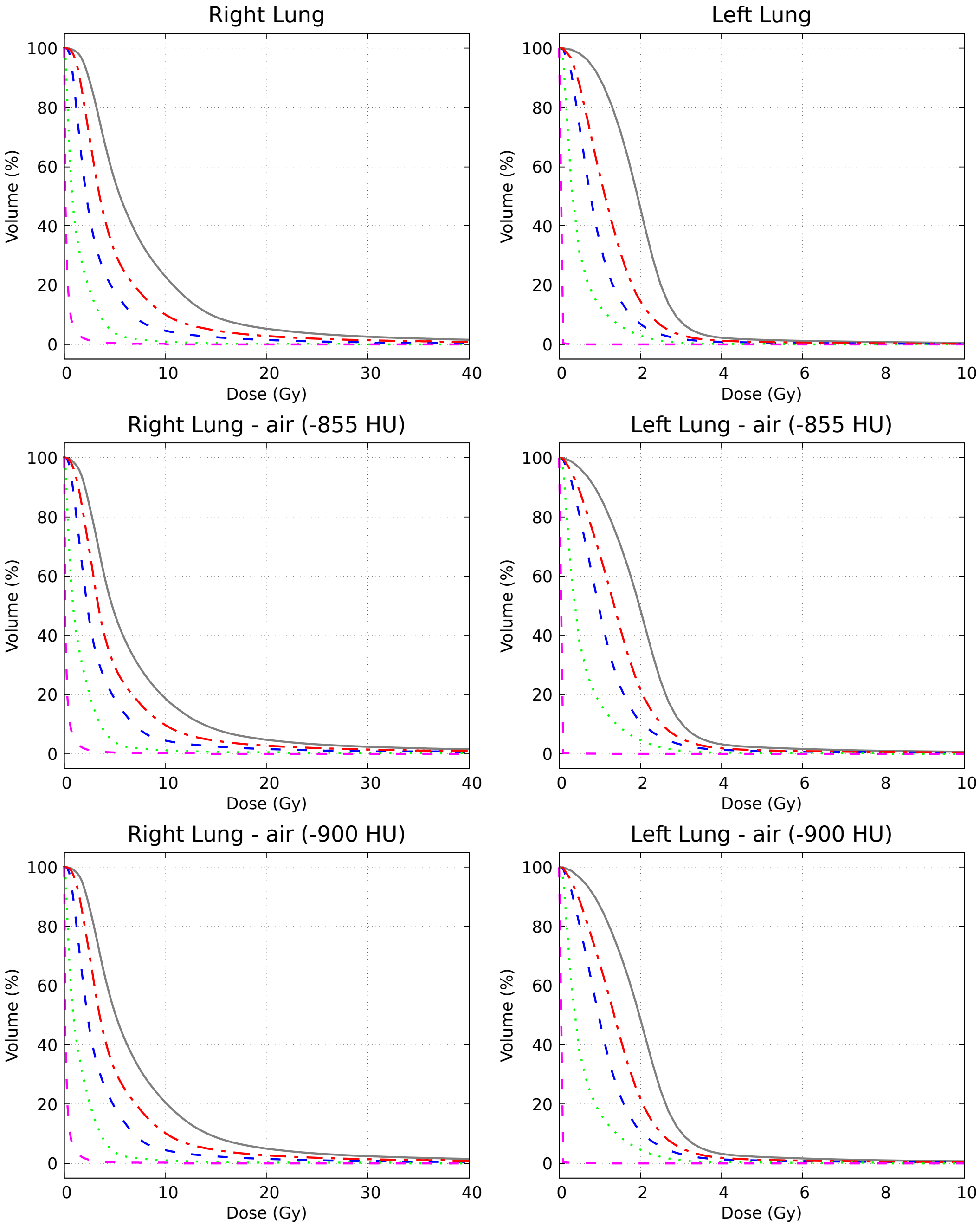

FIGURE B.2: DVHs in lungs-related VOIs of patient 1 obtained with all the types of GATE simulations described in Chapter 6; the color key is the same as in Fig. B.1

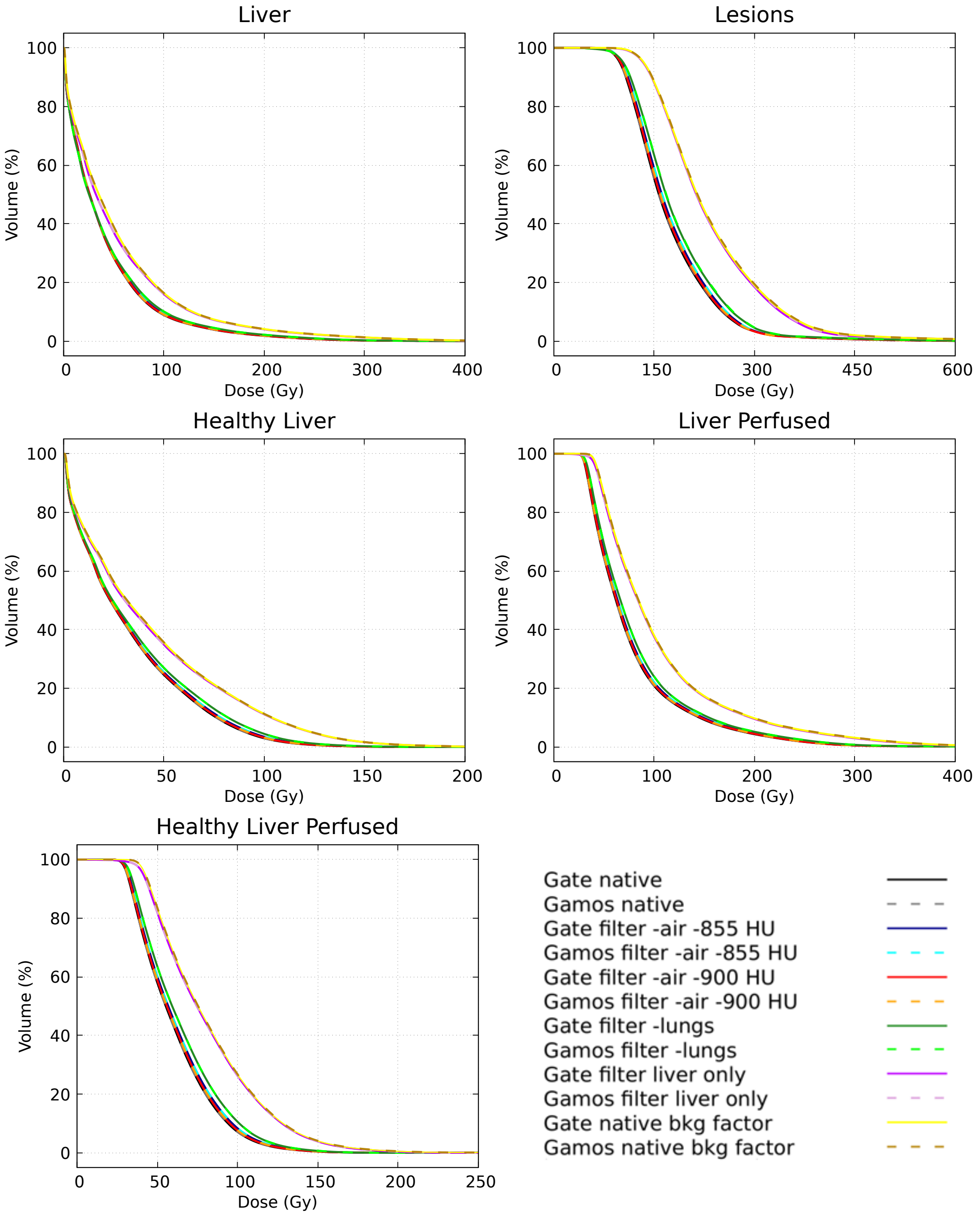

FIGURE B.3: DVHs in liver-related VOIs of patient 2 obtained with all the types of GATE and GAMOS simulations described in Chapter 6.

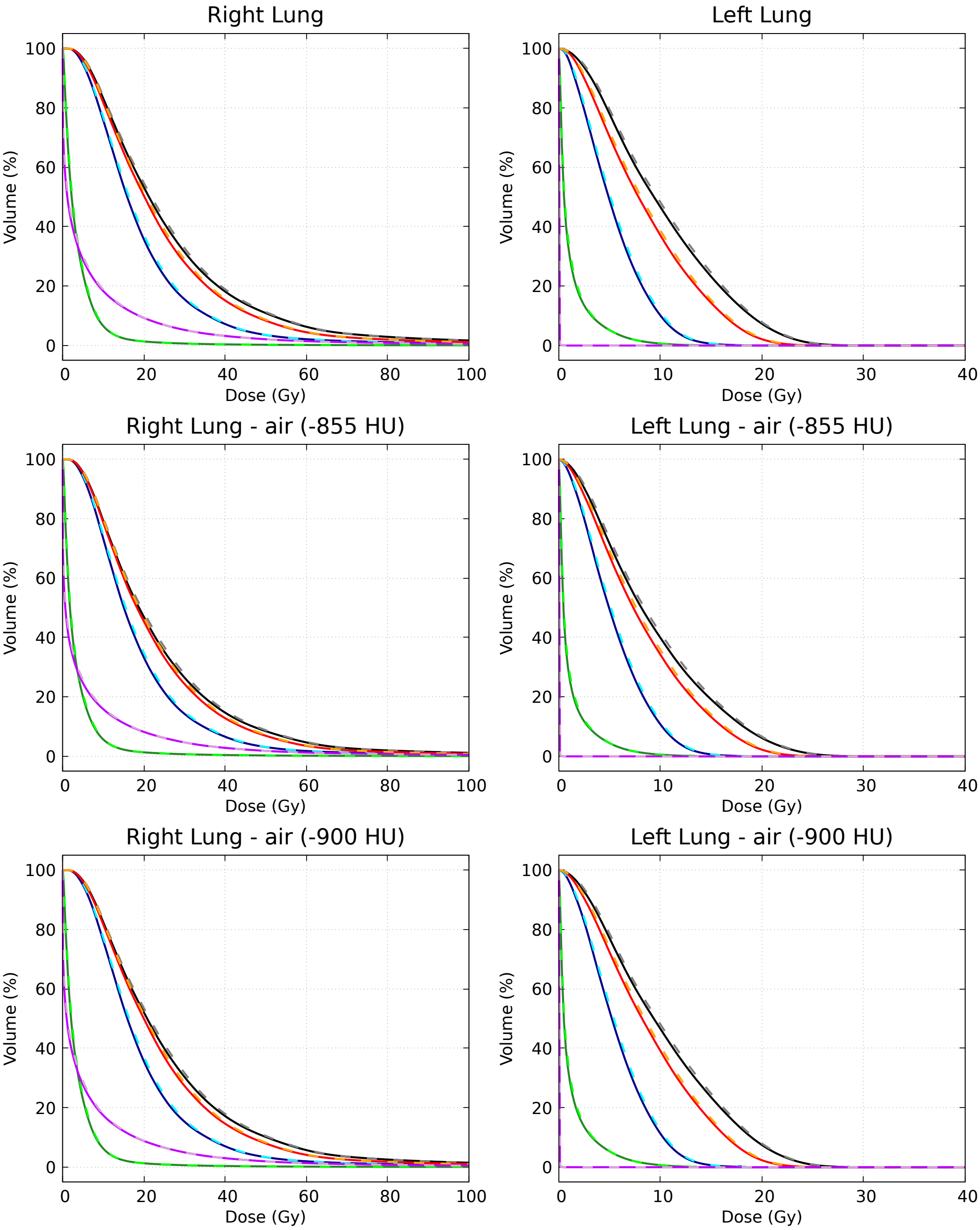

FIGURE B.4: DVHs in lungs-related VOIs of patient 2 obtained with all the types of GATE and GAMOS simulations described in Chapter 6; the color key is the same as in Fig. B.3

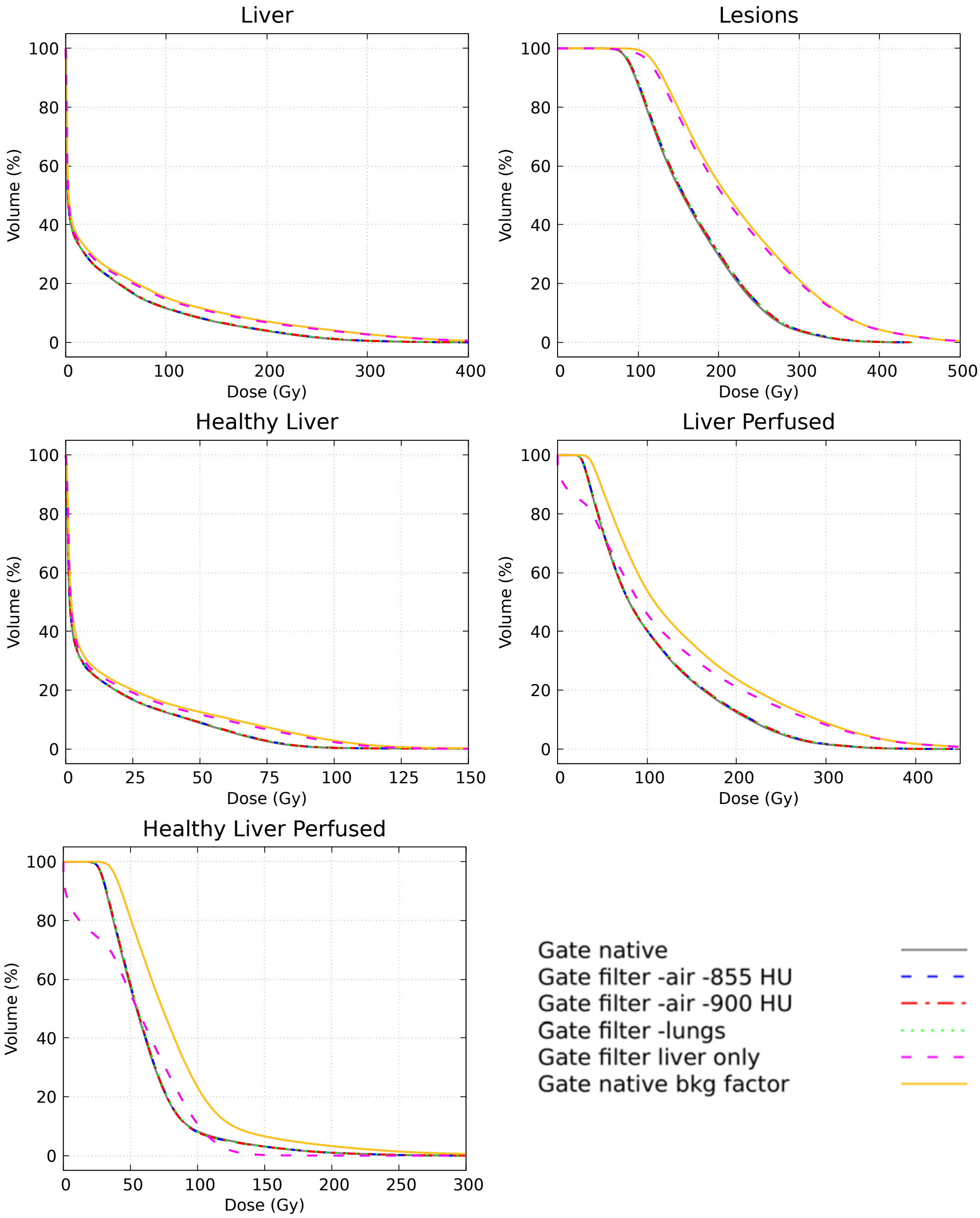

FIGURE B.5: DVHs in liver-related VOIs of patient 3 obtained with all the types of GATE simulations described in Chapter 6.

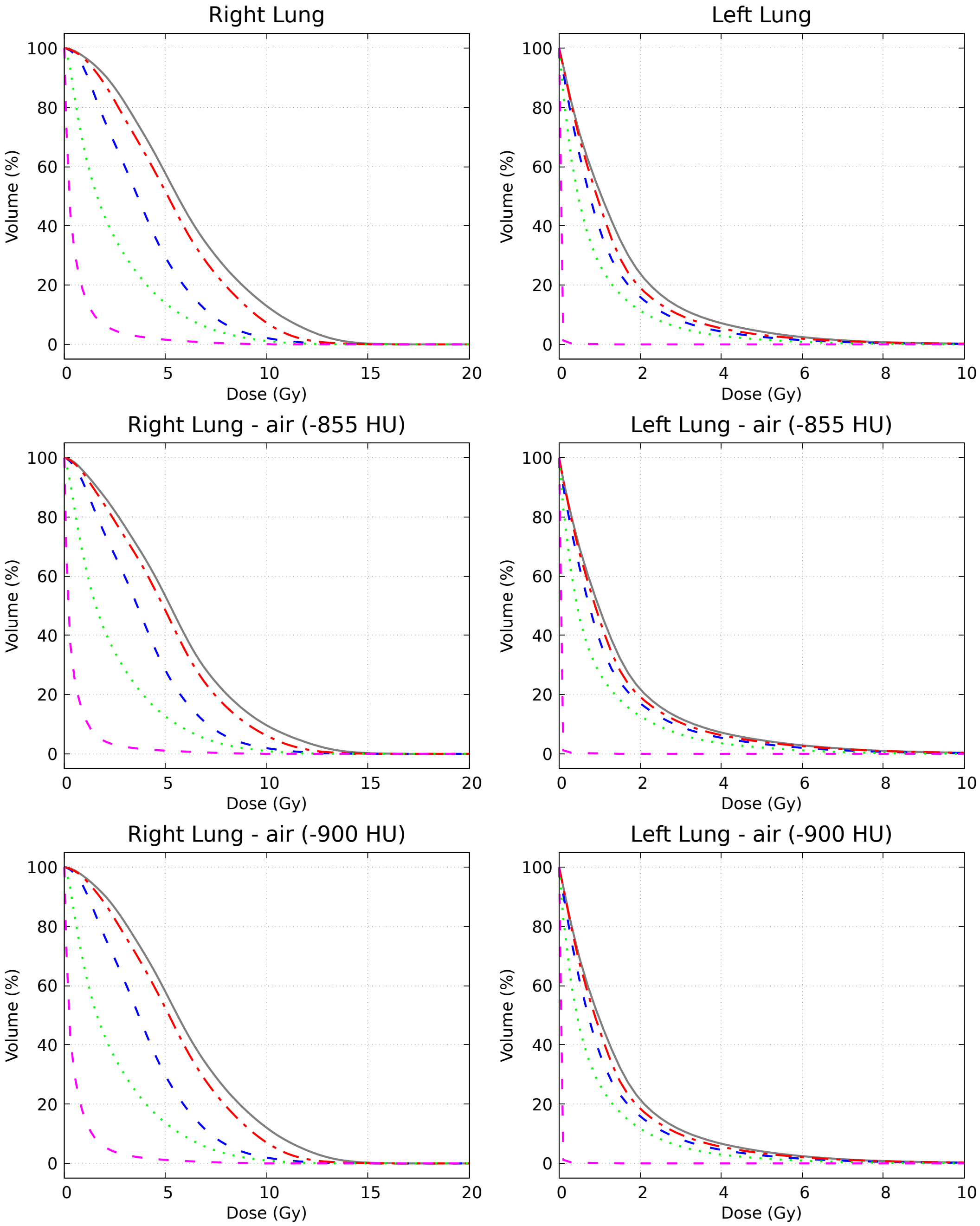

FIGURE B.6: DVHs in lungs-related VOIs of patient 3 obtained with all the types of GATE simulations described in Chapter 6; the color key is the same as in Fig. B.5

Appendix C

^{177}Lu-PRRT simplified kidney dosimetry protocol: uncertainties analysis

In the present Appendix Chapter additional details about the calculation procedures adopted in Chapter 7 of this dissertation are given, with particular focus on the uncertainties analysis for the quantities evaluated and presented in the results.

C.1 Statistics and uncertainties evaluation in experimental measurements

As it was described in Sec. 7.4, the measurements-derived effective half-life values in the (left) kidney, T_{eff}s, were estimated by fitting with a mono-exponential function the mean values of count rates obtained from measurements with the detector in L positions (L-UP and L-DN) in the four ERs, corrected for background (CR_{corr}) and also without background correction (CR). The fits were performed with the data analysis software ROOT [106, 161] v5.34.38, using its *TGraphErrors* class with standard settings. The uncertainties on CRs and CR_{bg}s (the latter are the count rates measured with detector in M-UP or M-DN positions, for background subtraction purpose) were calculated as the standard deviations of the count rate averages for the considered ER (among t = 24, 48, 72 and 168 hrs), hereafter indicated as $\mathrm{SD}_{\mathrm{CR}}$ and $\mathrm{SD}_{\mathrm{bg}}$, respectively. $\mathrm{SD}_{\mathrm{CR}}$s and $\mathrm{SD}_{\mathrm{bg}}$s were calculated with the uncertainty propagation from the standard deviation on the integral count N, which is derived from the Poisson law, as $\mathrm{SD}_{\mathrm{CR}} = \mathrm{SD}_{N/t_{\mathrm{acq}}} = \sqrt{N}/t_{\mathrm{acq}}$ (the same is valid for $\mathrm{SD}_{\mathrm{bg}}$), where t_{acq} is the duration of the corresponding count rate measurement in seconds; t_{acq}s were adjusted to guarantee relative uncertainties lower than 5% on the estimate of N (which had values $N > 400$ counts).
The uncertainties on the average values of CR_{corr}s, $\mathrm{SD}_{\mathrm{corr}}$, were computed as:

$$\mathrm{SD}_{\mathrm{corr}} = \sqrt{\left(\mathrm{SD}_{\mathrm{CR}}\right)^2 + \left(\mathrm{SD}_{\mathrm{bg}}\right)^2} \tag{C.1}$$

since CR_{corr}s were obtained, for each ER, subtracting the average CR_{bg} from the average CR, which are independent values.
The uncertainty on T_{eff} was retrieved by the software used, ROOT, as the standard error on the fit parameter, $\mathrm{SE}_{\mathrm{fit}}$, taking into account the uncertainties on the CRs or CR_{corr}s, depending on the case considered, in the calculation.

C.2 Statistics and uncertainties evaluation for MC simulations

C.2.1 Uncertainties on half-lives

The uncertainties on the estimates of kidney average effective half-lives calculated from simulations, $\langle T_{\mathrm{eff}} \rangle$s, were computed as standard deviations on the employed set of T_{eff}s, indicated as $\mathrm{SD_{MC}}$. $\mathrm{SD_{MC}}$s take into account the phase space scoring in the first step of simulations (see Sec. 7.5.2 and 7.6.1), thanks to the fact that multiple simulations with different seeds, therefore independent between each other, were performed for each configuration and source organ. In fact, both for the MC phantom study and the MC patient study, a set of estimated kidney effective half-lives T_{eff}s was obtained by setting combinations of the simulated deposited energies $\varepsilon_{s,c}(t)$s (Eq. 7.3), obtained from different simulations, to evaluate $\varepsilon_c(t)$s and $\varepsilon_{\mathrm{corr}}(t)$s (Eq. 7.6 and 7.7, respectively), and fitting the latter ones with mono-exponential functions. The average effective half-lives $\langle T_{\mathrm{eff}} \rangle$s and the standard deviations $\mathrm{SE_{MC}}$s of each set of fits were consequently computed.

With reference to the MC simulations carried out for the phantom study, two independent simulations were performed for each source organ in configuration L, and the same was done in configuration M, with L and M simulations being also independent between each other. In the case of a four time-point fit of background corrected energies $\varepsilon_{\mathrm{corr}}(t)$s, the total number of possible combinations, resulting from the choice of one of the two simulated deposited energies for each source organ, time-point and configuration, would result in more than 4 billion combinations. In fact, there are 24 ways of combining the deposited energies of the four sources at a time t to obtain a $\varepsilon_c(t)$, $24 \cdot 2$ ways of combining between L and M configurations for background subtraction to obtain a $\varepsilon_{\mathrm{corr}}(t)$, and a total of $24 \cdot 2 \cdot 4 = 232$ choices when combining them between the 4 time points. To reduce this number to a processable one of $65536 (= 2 \cdot 16)$, it was decided to use only one combination, randomly selected, for subtracting L and M simulations to obtain the $\varepsilon_{\mathrm{corr}}(t)$s. In the case of three time-point fits of background corrected energies, the same logic was followed, as well as in the cases excluding the bottle resembling intestines, obviously having, in these cases, fewer total combinations with respect to the four time-points and four sources case.

In the case of four time-points fits and three time-points fits of background uncorrected energies $\varepsilon_c(t)$s, the total number of combinations is computationally sustainable and all of the available combinations were employed in the calculations.

For the simulations carried out for the ^{177}Lu-PRRT patient clinical case, the number of time-points was three, the number of independent simulations executed for each time point was three for the L configuration, and three as well for the M configuration, and the simulated deposited energy is due to a single global source for each time, modelled on an entire SPECT scan. The total number of available combinations of $\varepsilon_{\mathrm{corr}}(t)$s to fit is thus $729 (= 32 \cdot 3)$, computationally sustainable and therefore not requiring a reduction of the number of combinations as in the phantom study. All the available combinations of $\varepsilon(t)$s to fit were as well used in the case of background uncorrected analysis.

The relative statistical uncertainties on the deposited energies scored in the second steps of the simulations (Sec. 7.5.2 and 7.6.1) were lower than 0.2% in all the cases, and were therefore considered negligible in the calculations.

C.2.2 Uncertainties on absorbed dose rates

The evaluation of the uncertainties on the left kidney average absorbed dose rates $\langle \dot{D}(t) \rangle$s for the clinical case (Eq. 7.10) was obtained step by step starting from the uncertainties on the absorbed doses in each voxel for each simulation considered. Considering a single step 1. simulation "i" (Sec. 7.6.1), the absorbed dose $D_{v,i}(t)$ in each voxel "v" is computed by GATE as the sum of the absorbed doses deposited for each primary event simulated N_i:

$$D_{v,i}(t) = \sum_{j=1}^{N_i} D_{v,i,j}(t) \tag{C.2}$$

where $D_{v,i,j}(t)$ is the absorbed dose in voxel v during the j-th history of the i-th simulation.
The absolute uncertainty $\sigma_{v,i}(t)$ on $D_{v,i}(t)$ was calculated as the standard deviation of the mean absorbed dose on the number of primary events N_i simulated [117]:

$$\sigma_{v,i}(t) = \sqrt{\frac{1}{N_i - 1}\left(\frac{d_{v,i}(t)}{N_i} - \left(\frac{D_{v,i}(t)}{N_i}\right)^2\right)} \tag{C.3}$$

where $d_{v,i}(t)$ indicates the sum of squared absorbed doses in voxel v in a simulation i for each primary event N_i simulated, computed by GATE as stated in Sec. 7.6.1:

$$d_{v,i}(t) = \sum_{j=1}^{N_i} D^2_{v,i,j}(t) \tag{C.4}$$

In our study we merged the absorbed dose maps of all the available step 1. simulations referred to a time t, to obtain the absorbed dose $D_v(t)$ in each voxel for the overall sample of independent simulations. For each time point, six absorbed dose maps in total were merged, three from L simulations and three from M simulations. The corresponding absorbed dose squared maps were analogously merged, in order to evaluate, for each voxel, the standard deviation $\sigma_v(t)$ of the mean absorbed dose on the overall number of primary events N of the merged sample [103]:

$$\sigma_v(t) = \sqrt{\frac{1}{N-1}\left(\frac{\sum_{i=1}^{6} d_{v,i}(t)}{N} - \left(\frac{\sum_{i=1}^{6} D_{v,i}(t)}{N}\right)^2\right)} \tag{C.5}$$

with:

$$N = \sum_{i=1}^{6} N_i \tag{C.6}$$

The renal average absorbed doses $\langle D(t) \rangle$ were evaluated averaging, for each time point t, the $D_v(t)$s of all the voxels within the left kidney VOI segmented for that t (Sec. 7.6.1 and 7.6.2). The uncertainties $\sigma(t)$s on $\langle D(t) \rangle$s were deduced from the uncertainty propagation for a function of multiple variables [162], assuming the total absorbed doses in each voxel as independent variables and their standard deviations on means as independent random errors. This led to:

$$\sigma(t) = \frac{1}{W}\sqrt{\sum_{v=1}^{W} \sigma_v^2(t)} \tag{C.7}$$

where W indicates the number of voxels composing the considered VOI.
Kidney average absorbed dose rates $\langle \dot{D}(t) \rangle$s were evaluated according to Eq. 7.10. The uncertainties on $\langle \dot{D}(t) \rangle$s were considered equal to the uncertainties on kidney average absorbed doses $\langle D(t) \rangle$s, since, referring to Eq. 7.10, $N(t)$s are exact simulation settings values without uncertainty, and the uncertainties on $A(t)$s are not considered in this work, and, in any case, they affect in the same way full image-based dosimetry and simplified dosimetry, given that they both use the same $\langle \dot{D}(t) \rangle$s.

C.2.3 Uncertainties on total absorbed doses

The uncertainties on kidney absorbed doses D_{full} and $D_{\text{simpl},T}$ were evaluated through the uncertainty propagation on the quantities used in the analytical expressions employed in Eq. 7.11 and Eq. 7.12, respectively. Regarding D_{full}, the standard error on the fit parameters (SE_{fit}) returned from the fit software used (ROOT v5.34.38 using *TGraphErrors* class with standard settings) were considered in the uncertainty propagation. Considering the SE_{fit} on D_0 to have some degree of correlation with the SE_{fit} on T_{full}, since being both deduced from the same fit procedure, the uncertainty on D_{full}, σD_{full}, was calculated through the propagation of errors including the covariance term [162], finally returning:

$$\begin{aligned}
&\delta D_{\text{full}} = \\
&= \sqrt{(\partial_{D_0})^2 \cdot \text{SE}^2_{\text{fit}}(D_0) + (\partial_{T_{\text{full}}})^2 \cdot \text{SE}^2_{\text{fit}}(D_0) + 2\partial_{D_0}\partial_{T_{\text{full}}} Cov(D_0, T_{\text{full}})} = \\
&= \sqrt{(T_{\text{full}})^2 \cdot \text{SE}^2_{\text{fit}}(D_0) + (D_0)^2 \cdot \text{SE}^2_{\text{fit}}(D_0) + 2T_{\text{full}} D_0 Cov(D_0, T_{\text{full}})}
\end{aligned} \tag{C.8}$$

in which ∂_{D_0} and $\partial_{T_{\text{full}}}$ indicate the following partial derivatives:

$$\partial_{D_0} = \frac{\partial D_{\text{full}}}{\partial D_0} \tag{C.9}$$

$$\partial_{T_{\text{full}}} = \frac{\partial D_{\text{full}}}{\partial T_{\text{full}}} \tag{C.10}$$

and where $Cov(T_{\text{full}}, D_0)$ indicates the covariance of the variables T_{full} and D_0.
In the case of $D_{\text{simpl},T}$, the SD_{MC} on $\langle T_{\text{eff}} \rangle$ (introduced in Sec. C.2.1) and the $\sigma(t)$ on $\langle \dot{D}(t) \rangle$ were considered in the uncertainty propagation. $\langle T_{\text{eff}} \rangle$ and $\langle \dot{D}(t) \rangle$ can be reasonably assumed as uncorrelated variables, therefore the uncertainty on $D_{\text{simpl},T}$, $\delta D_{\text{simpl},T}$, was calculated with the error propagation of a function of uncorrelated

variables [162], finally returning:

$$\begin{aligned}
&\delta D_{\text{simpl},T} = \\
&= \sqrt{\left(\frac{\partial D_{\text{simpl},T}}{\partial D_0}\right)^2 \cdot \sigma^2(t) + \left(\frac{\partial D_{\text{simpl},T}}{\partial \langle T_{\text{eff}}\rangle}\right)^2 \cdot (\text{SD}_{\text{MC}})^2} = \\
&= \sqrt{\left(\frac{\langle T_{\text{eff}}\rangle}{ln(2)e^{-\frac{ln(2)T}{T_{\text{eff}}}}}\right)^2 \cdot \sigma^2(t) + \left(\frac{\langle \dot{D}(T)\rangle}{ln(2)} e^{-\frac{ln(2)T}{T_{\text{eff}}}} \left(1 - \frac{ln(2)T}{\langle T_{\text{eff}}\rangle}\right)\right)^2 \cdot (\text{SD}_{\text{MC}})^2}
\end{aligned} \tag{C.11}$$

Bibliography

[1] F. H. Attix. *Introduction to Radiological Physics and Radiation Dosimetry*. New York: John Wiley & Sons, Ltd, 1986. eprint: `https://onlinelibrary.wiley.com/doi/pdf/10.1002/9783527617135`. URL: `https://doi.org/10.1002/9783527617135`.

[2] H. Zaidi and G. Sgouros, eds. *Therapeutic Applications of Monte Carlo Calculations in Nuclear Medicine (1st ed.)* Boca Raton: CRC Press., 2002. URL: `https://doi.org/10.1201/9781420033250`.

[3] E.B. Podgorsak, ed. *Radiation Oncology Physics: A Handbook for Teachers and Students*. Vienna: International Atomic Energy Agency (IAEA), 2005. ISBN: 92-0-107304-6. URL: `https://www.iaea.org/publications/7086/radiation-oncology-physics`.

[4] International Commission on Radiation Units and Measurements (ICRU). "ICRU Report No.85". In: *Journal of the ICRU* 11.1 (Apr. 2011), NP–NP. ISSN: 1473-6691. DOI: `10.1093/jicru/ndr012`. eprint: `https://academic.oup.com/jicru/article-pdf/11/1/NP/2440176/ndr012.pdf`. URL: `https://doi.org/10.1093/jicru/ndr012`.

[5] J.F. Ward. "DNA Damage Produced by Ionizing Radiation in Mammalian Cells: Identities, Mechanisms of Formation, and Reparability". In: ed. by W.E. Cohn and K. Moldave. Vol. 35. Progress in Nucleic Acid Research and Molecular Biology. Academic Press, 1988, pp. 95–125. DOI: `https://doi.org/10.1016/S0079-6603(08)60611-X`. URL: `https://www.sciencedirect.com/science/article/pii/S007966030860611X`.

[6] E. Amato et al. "Internal Radiation Dosimetry: Models and Applications". In: *12 Chapters on Nuclear Medicine*. Ed. by A. Gholamrezanezhad. InTech, 2011. Chap. 2, pp. 25–46. URL: `https://www.intechopen.com/chapters/25566`.

[7] S.J. McMahon. "The linear quadratic model: Usage, interpretation and challenges". In: *Physics in Medicine and Biology* 64.1 (2019). DOI: `10.1088/1361-6560/aaf26a`. URL: `https://www.scopus.com/inward/record.uri?eid=2-s2.0-85058876408&doi=10.1088$%5C%$2f1361-6560$%5C%$2faaf26a&partnerID=40&md5=2ccce8d054a6905cfa175b4654a81fb9`.

[8] R.G. Dale and B. Jones. "The assessment of RBE effects using the concept of biologically effective dose". In: *International Journal of Radiation Oncology*Biology*Physics* 43.3 (1999), pp. 639–645. ISSN: 0360-3016. DOI: `https://doi.org/10.1016/S0360-3016(98)00364-2`. URL: `https://www.sciencedirect.com/science/article/pii/S0360301698003642`.

[9] C.A. Tobias. "The repair-misrepair model in radiobiology: comparison to other models". In: *Radiation research. Supplement* 8 (1985), S77–95. ISSN: 0485-8611. DOI: `10.2307/3583515`. URL: `https://doi.org/10.2307/3583515`.

[10] S.B. Curtis. “Lethal and Potentially Lethal Lesions Induced by Radiation — A Unified Repair Model”. In: *Radiation Research* 106.2 (May 1986), pp. 252–270. ISSN: 0033-7587. DOI: 10.2307/3576798. eprint: https://meridian.allenpress.com/radiation-research/article-pdf/106/2/252/2120215/3576798.pdf. URL: https://doi.org/10.2307/3576798.

[11] D.T. Goodhead. “Saturable Repair Models of Radiation Action in Mammalian Cells”. In: *Radiation Research* 104.2s (Nov. 1985), S58–S67. ISSN: 0033-7587. DOI: 10.2307/3576633. eprint: https://meridian.allenpress.com/radiation-research/article-pdf/104/2s/S58/2118815/3576633.pdf. URL: https://doi.org/10.2307/3576633.

[12] D.J. Carlson et al. “Combined Use of Monte Carlo DNA Damage Simulations and Deterministic Repair Models to Examine Putative Mechanisms of Cell Killing”. In: *Radiation Research* 169.4 (2008), pp. 447–459. DOI: 10.1667/RR1046.1. URL: https://doi.org/10.1667/RR1046.1.

[13] M. Guerrero and M. Carlone. “Mechanistic formulation of a lineal-quadratic-linear (LQL) model: Split-dose experiments and exponentially decaying sources”. In: *Medical Physics* 37.8 (2010), pp. 4173–4181. DOI: 10.1118/1.3456927. eprint: https://aapm.onlinelibrary.wiley.com/doi/pdf/10.1118/1.3456927. URL: https://aapm.onlinelibrary.wiley.com/doi/abs/10.1118/1.3456927.

[14] L. Zhao et al. “A generalized target theory and its applications”. In: *Scientific Reports* 5 (Sept. 2015), p. 14568. DOI: 10.1038/srep14568.

[15] L. Bodgi and N. Foray. “The nucleo-shuttling of the ATM protein as a basis for a novel theory of radiation response: resolution of the linear-quadratic model*”. In: *International Journal of Radiation Biology* 92.3 (2016). PMID: 26907628, pp. 117–131. DOI: 10.3109/09553002.2016.1135260. eprint: https://doi.org/10.3109/09553002.2016.1135260. URL: https://doi.org/10.3109/09553002.2016.1135260.

[16] E. Rørvik et al. “Exploration and application of phenomenological RBE models for proton therapy”. In: *Physics in Medicine and Biology* 63 (Aug. 2018). DOI: 10.1088/1361-6560/aad9db.

[17] M. Joiner et al. “Low-dose hypersensitivity: Current status and possible mechanisms”. In: *International journal of radiation oncology, biology, physics* 49 (Feb. 2001), pp. 379–89. DOI: 10.1016/S0360-3016(00)01471-1.

[18] M. Astrahan. “Some implications of linear-quadratic-linear radiation dose-response with regard to hypofractionation”. In: *Medical Physics* 35.9 (2008), pp. 4161–4172. DOI: https://doi.org/10.1118/1.2969065. eprint: https://aapm.onlinelibrary.wiley.com/doi/pdf/10.1118/1.2969065. URL: https://aapm.onlinelibrary.wiley.com/doi/abs/10.1118/1.2969065.

[19] C. Park et al. “Universal Survival Curve and Single Fraction Equivalent Dose: Useful Tools in Understanding Potency of Ablative Radiotherapy”. In: *International Journal of Radiation Oncology*Biology*Physics* 70.3 (2008), pp. 847–852. ISSN: 0360-3016. DOI: https://doi.org/10.1016/j.ijrobp.2007.10.059. URL: https://www.sciencedirect.com/science/article/pii/S0360301607044604.

[20] J.Z. Wang et al. “A Generalized Linear-Quadratic Model for Radiosurgery, Stereotactic Body Radiation Therapy, and High–Dose Rate Brachytherapy”. In: *Science Translational Medicine* 2.39 (2010), 39ra48–39ra48. ISSN: 1946-6234. DOI: 10.1126/scitranslmed.3000864. eprint: https://stm.sciencemag.org/content/2/39/39ra48.full.pdf. URL: https://stm.sciencemag.org/content/2/39/39ra48.

[21] David J. Brenner. “The Linear-Quadratic Model Is an Appropriate Methodology for Determining Isoeffective Doses at Large Doses Per Fraction”. In: *Seminars in Radiation Oncology* 18.4 (2008). Hypofractionation, pp. 234–239. ISSN: 1053-4296. DOI: https://doi.org/10.1016/j.semradonc.2008.04.004. URL: https://www.sciencedirect.com/science/article/pii/S1053429608000337.

[22] “The 2007 Recommendations of the International Commission on Radiological Protection. ICRP publication 103”. In: *Annals of the ICRP* 37.2-4 (2007), pp. 1–332. DOI: 10.1016/j.icrp.2007.10.003. eprint: https://doi.org/10.1016/j.icrp.2007.10.003. URL: https://doi.org/10.1016/j.icrp.2007.10.003.

[23] B. Jones et al. “The Role of Biologically Effective Dose (BED) in Clinical Oncology”. In: *Clinical Oncology* 13.2 (2001), pp. 71–81. ISSN: 0936-6555. DOI: https://doi.org/10.1053/clon.2001.9221. URL: https://www.sciencedirect.com/science/article/pii/S0936655501992210.

[24] A. Niemierko. “Reporting and analyzing dose distributions: A concept of equivalent uniform dose”. In: *Medical Physics* 24.1 (1997), pp. 103–110. DOI: https://doi.org/10.1118/1.598063. eprint: https://aapm.onlinelibrary.wiley.com/doi/pdf/10.1118/1.598063. URL: https://aapm.onlinelibrary.wiley.com/doi/abs/10.1118/1.598063.

[25] M. Chan and C. Chiang. “Revisiting the formalism of equivalent uniform dose based on the linear-quadratic and universal survival curve models in high-dose stereotactic body radiotherapy”. In: *Strahlentherapie und Onkologie* (Nov. 2020). DOI: 10.1007/s00066-020-01713-w.

[26] Francisco. Henríquez and Silvia. Castrillón. “A quality index for equivalent uniform dose”. In: *Journal of Medical Physics* 36.3 (2011), pp. 126–132. DOI: 10.4103/0971-6203.83466. eprint: https://www.jmp.org.in/article.asp?issn=0971-6203;year=2011;volume=36;issue=3;spage=126;epage=132;aulast=Henr$\%$EDquez;t=6. URL: https://www.jmp.org.in/article.asp?issn=0971-6203;year=2011;volume=36;issue=3;spage=126;epage=132;aulast=Henr$%5C%$EDquez;t=6.

[27] A. Wambersie et al. “The RBE issues in ion-beam therapy: Conclusions of a joint IAEA/ICRU working group regarding quantities and units”. In: *Radiation protection dosimetry* 122 (Feb. 2006), pp. 463–70. DOI: 10.1093/rpd/ncl447.

[28] S. Bentzen et al. “Bioeffect modeling and equieffective dose concepts in radiation oncology Terminology, quantities and units”. In: *Radiotherapy and oncology : journal of the European Society for Therapeutic Radiology and Oncology* 105 (Nov. 2012). DOI: 10.1016/j.radonc.2012.10.006.

[29] H. Rodney Withers, Howard D. Thames, and Lester J. Peters. “A new isoeffect curve for change in dose per fraction”. In: *Radiotherapy and Oncology* 1.2 (1983), pp. 187–191. ISSN: 0167-8140. DOI: `https://doi.org/10.1016/S0167-8140(83)80021-8`. URL: `https://www.sciencedirect.com/science/article/pii/S0167814083800218`.

[30] R. Hobbs et al. “Redefining Relative Biological Effectiveness in the Context of the EQDX Formalism: Implications for Alpha-Particle Emitter Therapy”. In: *Radiation research* 181 (Feb. 2014), pp. 90–8. DOI: `10.1667/RR13483.1`.

[31] W.E. Bolch et al. “MIRD pamphlet No. 21: A generalized schema for radiopharmaceutical dosimetry-standardization of nomenclature”. In: *Journal of Nuclear Medicine* 50.3 (2009), pp. 477–484. DOI: `10.2967/jnumed.108.056036`. URL: `https://www.scopus.com/inward/record.uri?eid=2-s2.0-62449175592&doi=10.2967$%5C%$2fjnumed.108.056036&partnerID=40&md5=4c6c3ee342bcc03a2a17e3fe45d03ea1`.

[32] Pat B. Zanzonico. “Internal Radionuclide Radiation Dosimetry: A Review of Basic Concepts and Recent Developments”. In: *Journal of Nuclear Medicine* 41.2 (2000), pp. 297–308. ISSN: 0161-5505. eprint: `https://jnm.snmjournals.org/content/41/2/297.full.pdf`. URL: `https://jnm.snmjournals.org/content/41/2/297`.

[33] D.M.V. Huizing et al. “Dosimetry methods and clinical applications in peptide receptor radionuclide therapy for neuroendocrine tumours: a literature review”. In: *EJNMMI Research* 8 (2018). DOI: `10.1186/s13550-018-0443-z`. URL: `https://www.scopus.com/inward/record.uri?eid=2-s2.0-85052697625&doi=10.1186$%5C%$2fs13550-018-0443-z&partnerID=40&md5=9ca050066559bb98fe0c1cd9c18b5722`.

[34] R. Baskar et al. “Cancer and Radiation Therapy: Current Advances and Future Directions”. In: *International journal of medical sciences* 9 (Feb. 2012), pp. 193–9. DOI: `10.7150/ijms.3635`.

[35] J. Skowronek. “Current status of brachytherapy in cancer treatment – short overview”. In: *Journal of Contemporary Brachytherapy* 9 (Dec. 2017), pp. 581–589. DOI: `10.5114/jcb.2017.72607`.

[36] G. Sgouros et al. “Radiopharmaceutical therapy in cancer: clinical advances and challenges”. In: *Nature Reviews Drug Discovery* 19 (July 2020). DOI: `10.1038/s41573-020-0073-9`.

[37] R. Stubbs and S. Wickremesekera. “Selective internal radiation therapy (SIRT): A new modality for treating patients with colorectal liver metastases”. In: *HPB : the official journal of the International Hepato Pancreato Biliary Association* 6 (Feb. 2004), pp. 133–9. DOI: `10.1080/13651820410025084`.

[38] V. McCready. “Radioiodine – the success story of Nuclear Medicine: 75th Anniversary of the first use of Iodine-131 in humans”. In: *European Journal of Nuclear Medicine and Molecular Imaging* 44 (Oct. 2016). DOI: `10.1007/s00259-016-3548-5`.

[39] E. Amato et al. “Internal dosimetry in nuclear medicine”. In: *Medical Physics* (2013), pp. 115–134. URL: `https://www.scopus.com/inward/record.uri?eid=2-s2.0-84892789551&partnerID=40&md5=f10777f975a662465c12d964aeee83b0`.

[40] S.R. Cherry, J. Sorenson, and M. Phelps. *Physics in Nuclear Medicine*. Elsevier Inc., 2012. ISBN: 9781416051985. DOI: `10.1016/C2009-0-51635-2`.

[41] *Quality Assurance for SPECT Systems*. Human Health Series 6. Vienna: INTERNATIONAL ATOMIC ENERGY AGENCY, 2009. ISBN: 978-92-0-103709-1. URL: `https://www.iaea.org/publications/8119/quality-assurance-for-spect-systems`.

[42] *Quality Assurance for PET and PET/CT Systems*. Human Health Series 1. Vienna: INTERNATIONAL ATOMIC ENERGY AGENCY, 2009. ISBN: 978-92-0-103609-4. URL: `https://www.iaea.org/publications/8002/quality-assurance-for-pet-and-pet/ct-systems`.

[43] Withers, P. J. and Bouman, C. and Carmignato, S. and Cnudde, V. and Grimaldi, D. and Hagen, C. K. and Maire, E. and Manley, M. and Du Plessis, A. and Stock, S. R. "X-ray computed tomography". eng. In: *NATURE REVIEWS METHODS PRIMERS* 1.1 (2021), p. 21. ISSN: 2662-8449. URL: `%7Bhttp://dx.doi.org/10.1038/s43586-021-00015-4%7D`.

[44] M. D. Farwell, D. A. Pryma, and D. A. Mankoff. "PET/CT imaging in cancer: Current applications and future directions". In: *Cancer* 120.22 (2014), pp. 3433–3445. DOI: `10.1002/cncr.28860`. eprint: `https://acsjournals.onlinelibrary.wiley.com/doi/pdf/10.1002/cncr.28860`. URL: `https://acsjournals.onlinelibrary.wiley.com/doi/abs/10.1002/cncr.28860`.

[45] O. Israel et al. "Two decades of SPECT/CT – the coming of age of a technology: An updated review of literature evidence". In: *European Journal of Nuclear Medicine and Molecular Imaging* 46 (Sept. 2019). DOI: `10.1007/s00259-019-04404-6`.

[46] W.E. Bolch et al. "MIRD pamphlet no. 17: The dosimetry of nonuniform activity distributions - Radionuclide S values at the voxel level". In: *Journal of Nuclear Medicine* 40.1 (1999), 11S–36S. URL: `https://www.scopus.com/inward/record.uri?eid=2-s2.0-0032898060&partnerID=40&md5=6439484b4420f9589e41fb9c47c1031e`.

[47] P. Kletting et al. "Molecular radiotherapy: The NUKFIT software for calculating the time-integrated activity coefficient". In: *Medical Physics* 40.10 (2013). DOI: `10.1118/1.4820367`. URL: `https://www.scopus.com/inward/record.uri?eid=2-s2.0-84885751261&doi=10.1118$%5C%$2f1.4820367&partnerID=40&md5=2b0ca8af8163abe91d517e338904dbfc`.

[48] L. Auditore et al. "Internal dosimetry for TARE therapies by means of GAMOS Monte Carlo simulations". In: *Physica Medica* 64 (2019), pp. 245–251. ISSN: 1120-1797. DOI: `10.1016/j.ejmp.2019.07.024`. URL: `https://www.sciencedirect.com/science/article/pii/S1120179719301772`.

[49] W.S. Snyder et al. ""S"Absorbed Dose Per Unit Cumulated Activity for Selected Radionuclides and Organs". In: *MIRD Pamphlet No. 11* (1975). URL: `https://ci.nii.ac.jp/naid/10008539831/en/`.

[50] X.G. Xu and K.F. Eckerman, eds. *Handbook of Anatomical Models for Radiation Dosimetry (1st ed.)* Boca Raton: CRC Press., 2009. URL: `https://doi.org/10.1201/EBK1420059793`.

[51] M. Bardies and J.-F. Chatal. "Absorbed doses for internal radiotherapy from 22 beta-emitting radionuclides: Beta dosimetry of small spheres". In: *Physics in Medicine and Biology* 39.6 (1994), pp. 961–981. DOI: `10.1088/0031-9155/39/6/004`. URL: `https://www.scopus.com/inward/record.uri?eid=2-s2.0-0028246532&doi=10.1088$%5C%$2f0031-9155$%5C%$2f39$%5C%$2f6$%5C%$2f004&partnerID=40&md5=28c80b52c0ee3dbdff5530b8a11e47f4`.

[52] E. Amato, A. Italiano, and S. Baldari. “An analytical model to calculate absorbed fractions for internal dosimetry with alpha, beta and gamma emitters”. In: *AAPP Atti della Accademia Peloritana dei Pericolanti, Classe di Scienze Fisiche, Matematiche e Naturali* 92.1 (2014). DOI: `10.1478/AAPP.921A1`. URL: `https://www.scopus.com/inward/record.uri?eid=2-s2.0-84896354053&doi=10.1478$%5C%$2fAAPP.921A1&partnerID=40&md5=92fec2ef5d656550e4a5ed9d4ff506f7`.

[53] Richard E. Toohey, Michael G. Stabin, and Evelyn E. Watson. “The AAPM/RSNA Physics Tutorial for Residents”. In: *RadioGraphics* 20.2 (2000). PMID: 10715348, pp. 533–546. DOI: `10.1148/radiographics.20.2.g00mc33533`. eprint: `https://doi.org/10.1148/radiographics.20.2.g00mc33533`. URL: `https://doi.org/10.1148/radiographics.20.2.g00mc33533`.

[54] A.C. Traino, M. Piccinno, and C. Avigo. “Dosimetry of non-uniform activity distribution: possibility to use the local energy deposition approach at the voxel level in radionuclide therapy”. In: *Biomedical Physics & Engineering Express* 2.6 (Nov. 2016), p. 065001. DOI: `10.1088/2057-1976/2/6/065001`. URL: `https://doi.org/10.1088/2057-1976/2/6/065001`.

[55] E. Hippeläinen, M. Tenhunen, and A. Sohlberg. “Fast voxel-level dosimetry for 177 Lu labelled peptide treatments”. In: *Physics in medicine and biology* 60 (Aug. 2015), pp. 6685–6700. DOI: `10.1088/0031-9155/60/17/6685`.

[56] S.A. Graves, R.T. Flynn, and D.E. Hyer. “Dose point kernels for 2,174 radionuclides”. In: *Medical Physics* 46.11 (2019), pp. 5284–5293. DOI: `https://doi.org/10.1002/mp.13789`. eprint: `https://aapm.onlinelibrary.wiley.com/doi/pdf/10.1002/mp.13789`. URL: `https://aapm.onlinelibrary.wiley.com/doi/abs/10.1002/mp.13789`.

[57] B.M. Mendes et al. “Calculation of dose point kernel values for monoenergetic electrons and beta emitting radionuclides: Intercomparison of Monte Carlo codes”. In: *Radiation Physics and Chemistry* 181, 109327 (Apr. 2021), p. 109327. DOI: `10.1016/j.radphyschem.2020.109327`.

[58] H.B. Giap et al. “Validation of a dose-point kernel convolution technique for internal dosimetry”. In: *Physics in medicine and biology* 40.3 (Mar. 1995), pp. 365–381. ISSN: 0031-9155. DOI: `10.1088/0031-9155/40/3/003`. URL: `https://doi.org/10.1088/0031-9155/40/3/003`.

[59] A. Dieudonné et al. “Study of the impact of tissue density heterogeneities on 3-dimensional abdominal dosimetry: Comparison between dose kernel convolution and direct monte carlo methods”. In: *Journal of Nuclear Medicine* 54.2 (Feb. 2013), pp. 236–243. ISSN: 0161-5505. DOI: `10.2967/jnumed.112.105825`.

[60] M. Pacilio et al. “Differences among Monte Carlo codes in the calculations of voxel values for radionuclide targeted therapy and analysis of their impact on absorbed dose evaluations”. In: *Medical Physics* 36.5 (2009), pp. 1543–1552. DOI: `https://doi.org/10.1118/1.3103401`. eprint: `https://aapm.onlinelibrary.wiley.com/doi/pdf/10.1118/1.3103401`. URL: `https://aapm.onlinelibrary.wiley.com/doi/abs/10.1118/1.3103401`.

[61] E. Amato et al. “Use of the GEANT4 Monte Carlo to determine three-dimensional dose factors for radionuclide dosimetry”. In: *Nuclear Instruments and Methods in Physics Research Section A: Accelerators, Spectrometers, Detectors and Associated Equipment* 708 (Apr. 2013), pp. 15–18. DOI: `10.1016/j.nima.2013.01.014`.

[62] E. Amato, A. Italiano, and S. Baldari. “Monte Carlo study of voxel S factor dependence on tissue density and atomic composition”. In: *Nuclear Instruments and Methods in Physics Research A* 729 (Nov. 2013), pp. 870–876. DOI: 10.1016/j.nima.2013.08.059.

[63] A. Dieudonné et al. “Fine-Resolution Voxel S Values for Constructing Absorbed Dose Distributions at Variable Voxel Size”. In: *Journal of nuclear medicine : official publication, Society of Nuclear Medicine* 51 (Oct. 2010), pp. 1600–7. DOI: 10.2967/jnumed.110.077149.

[64] N. Lanconelli et al. “A free database of radionuclide voxel S values for the dosimetry of nonuniform activity distributions”. In: *Physics in Medicine and Biology* 57.2 (Jan. 2012), pp. 517–533. ISSN: 0031-9155. DOI: 10.1088/0031-9155/57/2/517.

[65] M. Pacilio et al. “Differences in 3D dose distributions due to calculation method of voxel S-values and the influence of image blurring in SPECT”. In: *Physics in medicine and biology* 60 (Feb. 2015), pp. 1945–1964. DOI: 10.1088/0031-9155/60/5/1945.

[66] S. Berenato et al. “Influence of voxel S factors on three-dimensional internal dosimetry calculations.” In: *Physica medica* 32 10 (2016), pp. 1259–1262. DOI: 10.1016/j.ejmp.2016.09.012.

[67] D. Villoing et al. “Internal dosimetry with the Monte Carlo code GATE: Validation using the ICRP/ICRU female reference computational model”. In: *Physics in Medicine and Biology* 62 (Mar. 2017), pp. 1885–1904. DOI: 10.1088/1361-6560/62/5/1885.

[68] H.G. Menzel, C. Clement, and P. DeLuca. “Realistic reference phantoms: an ICRP/ICRU joint effort. A report of adult reference computational phantoms. ICRP publication 110”. In: *Annals of the ICRP* 39.2 (2009), pp. 1–164. DOI: 10.1016/j.icrp.2009.09.001. URL: https://doi.org/10.1016/j.icrp.2009.09.001.

[69] M. Chauvin et al. “OpenDose: Open-Access Resource for Nuclear Medicine Dosimetry”. In: *Journal of Nuclear Medicine* 61 (Mar. 2020), jnumed.119.240366. DOI: 10.2967/jnumed.119.240366.

[70] J. Grimes and A. Celler. “Comparison of internal dose estimates obtained using organ-level, voxel S value, and Monte Carlo techniques”. In: *Medical Physics* 41.9 (2014), p. 092501. DOI: 10.1118/1.4892606. eprint: https://aapm.onlinelibrary.wiley.com/doi/pdf/10.1118/1.4892606. URL: https://aapm.onlinelibrary.wiley.com/doi/abs/10.1118/1.4892606.

[71] Y.K. Dewaraja et al. “MIRD pamphlet no. 23: Quantitative SPECT for patient-specific 3-dimensional dosimetry in internal radionuclide therapy”. In: *Journal of Nuclear Medicine* 53.8 (2012), pp. 1310–1325. DOI: 10.2967/jnumed.111.100123. URL: https://www.scopus.com/inward/record.uri?eid=2-s2.0-84864751150&doi=10.2967$%5C%$2fjnumed.111.100123&partnerID=40&md5=8107e541e546cd784269e4220ba1aa6e.

[72] E. Amato, D. Lizio, and S. Baldari. *Applications of the Monte Carlo method in medical physics*. 2013, pp. 105–113. URL: https://www.scopus.com/inward/record.uri?eid=2-s2.0-84892813754&partnerID=40&md5=5e2b21d34ad265df02d8bf2579a72615.

[73] I. Tsougos et al. “Patient-specific internal radionuclide dosimetry”. In: *Nuclear medicine communications* 31 (Feb. 2010), pp. 97–106. DOI: 10.1097/MNM.0b013e328330626f.

[74] S. Mattsson. "Patient dosimetry in nuclear medicine". In: *Radiation Protection Dosimetry* 165.1-4 (2015), pp. 416–423. ISSN: 1742-3406. DOI: `10.1093/rpd/ncv061`.

[75] M. Ljungberg and K. Sjogreen Gleisner. "The accuracy of absorbed dose estimates in tumours determined by Quantitative SPECT: A Monte Carlo study". In: *Acta oncologica (Stockholm, Sweden)* 50 (Aug. 2011), pp. 981–9. DOI: `10.3109/0284186X.2011.584559`.

[76] W. Ai-dong et al. "Effect of CT Image-Based Voxel Size On Monte Carlo Dose Calculation". In: *2005 IEEE Engineering in Medicine and Biology 27th Annual Conference*. 2005, pp. 6449–6451. DOI: `10.1109/IEMBS.2005.1615975`.

[77] P. Ziegenhein et al. "Fast CPU-based Monte Carlo simulation for radiotherapy dose calculation". In: *Physics in Medicine and Biology* 60.15 (July 2015), pp. 6097–6111. DOI: `10.1088/0031-9155/60/15/6097`. URL: `https://doi.org/10.1088/0031-9155/60/15/6097`.

[78] M. Ljungberg, S.-E. Strand, and M.A. King, eds. *Monte Carlo Calculations in Nuclear Medicine: Applications in Diagnostic Imaging*. 2nd Edition. Series in Nuclear Medicine and Biomedical Engeneering. Boca Raton: CRC Press, 2012. ISBN: 9780429151163. DOI: `10.1201/b13073`. URL: `https://www.taylorfrancis.com/books/edit/10.1201/b13073/monte-carlo-calculations-nuclear-medicine-michael-ljungberg-sven-erik-strand-michael-king`.

[79] H. Chi-Ok et al. "Buffon's Needle Algorithm to Estimate ". In: *Applied Mathematics* 08 (Jan. 2017), pp. 275–279. DOI: `10.4236/am.2017.83022`.

[80] R. Marks. "Monte Carlo". In: Jan. 2016, pp. 1–4. DOI: `10.1057/978-1-349-94848-2_709-1`.

[81] F. Coccetti. "The Fermiac or Fermi's Trolley". In: *Il Nuovo Cimento C* 08.296 (2 2016). DOI: `10.1393/ncc/i2016-16296-7`.

[82] A. Rotondi, P. Pedroni, and A. Pievatolo. *Probabilità, Statistica e Simulazione*. 3rd Edition. Collana di Statistica e Probabilità Applicata. Milan: Springer, 2012. ISBN: 978-88-470-2364-2. DOI: `10.1007/978-88-470-2364-2`. URL: `https://link.springer.com/book/10.1007/978-88-470-2364-2`.

[83] I. Vattulainen et al. "A Comparative Study of Some Pseudorandom Number Generators". In: *Computer Physics Communications* 86 (Apr. 1993), pp. 209–226. DOI: `10.1016/0010-4655(95)00015-8`.

[84] S. Agostinelli et al. "Geant4 - a simulation toolkit". In: *Nuclear Instruments and Methods in Physics Research Section A* 506.3 (2003), pp. 250–303. DOI: `10.1016/S0168-9002(03)01368-8`.

[85] A. Ferrari et al. *FLUKA: A Multi-Particle Transport Code*. Tech. rep. SLAC-R-773. SLAC National Accelerator Lab., Menlo Park, CA (United States)s, 2005. DOI: `10.2172/877507`. URL: `https://www.osti.gov/biblio/877507`.

[86] T. Goorley et al. "Initial MCNP6 Release Overview". In: *Nuclear Technology* 180.3 (2012), pp. 298–315. DOI: `10.13182/NT11-135`. eprint: `https://doi.org/10.13182/NT11-135`. URL: `https://doi.org/10.13182/NT11-135`.

[87] *EGS5 Webpage*. URL: `https://rcwww.kek.jp/research/egs/egs5.html`. last accessed on 2021-07-20.

[88] *EGSnrc Webpage - Canada, Government of Canada. "EGSnrc: software tool to model radiation transport - National Research Council Canada"*. URL: https://nrc.canada.ca/en/research-development/products-services/software-applications/egsnrc-software-tool-model-radiation-transport. last accessed on 2021-07-20.

[89] J. Sempau et al. "Experimental benchmarks of the Monte Carlo code penelope". In: *Nuclear Instruments and Methods in Physics Research Section B: Beam Interactions with Materials and Atoms* 207.2 (2003), pp. 107–123. ISSN: 0168-583X. DOI: 10.1016/S0168-583X(03)00453-1. URL: https://www.sciencedirect.com/science/article/pii/S0168583X03004531.

[90] S. Incerti et al. "THE GEANT4-DNA PROJECT". In: *International Journal of Modeling, Simulation, and Scientific Computing* 01.02 (2010), pp. 157–178. DOI: 10.1142/S1793962310000122. eprint: https://doi.org/10.1142/S1793962310000122. URL: https://doi.org/10.1142/S1793962310000122.

[91] S. Incerti et al. "Review of Geant4-DNA applications for micro and nanoscale simulations". In: *Physica Medica* 32.10 (2016), pp. 1187–1200. ISSN: 1120-1797. DOI: 10.1016/j.ejmp.2016.09.007. URL: https://www.sciencedirect.com/science/article/pii/S1120179716309279.

[92] S. Jan et al. "GATE: a simulation toolkit for PET and SPECT". In: *Physics in Medicine & Biology* 49.19 (2004), pp. 4543–4561. DOI: 10.1088/0031-9155/49/19/007.

[93] P. Arce et al. "GAMOS: A framework to do GEANT4 simulations in different physics fields with an user-friendly interface". In: *Nuclear Instruments and Methods in Physics Research Section A Accelerators Spectrometers Detectors and Associated Equipment* (Jan. 2014). DOI: 10.1016/j.nima.2013.09.036.

[94] *GEANT4 website*. URL: https://geant4.web.cern.ch/node/1. last accessed on 2021-08-30.

[95] J. Allison et al. "Geant4 developments and applications". In: *IEEE Transactions on Nuclear Science* 53.1 (2006), pp. 270–278. DOI: 10.1109/TNS.2006.869826.

[96] J. Allison et al. "Recent developments in Geant4". In: *Nuclear Instruments and Methods in Physics Research Section A: Accelerators, Spectrometers, Detectors and Associated Equipment* 835 (2016), pp. 186–225. ISSN: 0168-9002. DOI: 10.1016/j.nima.2016.06.125. URL: https://www.sciencedirect.com/science/article/pii/S0168900216306957.

[97] J. Apostolakis and D.H. Wright. "An Overview of the Geant4 Toolkit". In: *AIP Conference Proceedings* 896.1 (2007), pp. 1–10. DOI: 10.1063/1.2720452. eprint: https://aip.scitation.org/doi/pdf/10.1063/1.2720452. URL: https://aip.scitation.org/doi/abs/10.1063/1.2720452.

[98] K. Amako et al. "Geant4 and its validation". In: *Nuclear Physics B - Proceedings Supplements* 150 (2006). Proceedings of the 9th Topical Seminar on Innovative Particle and Radiation Detectors, pp. 44–49. ISSN: 0920-5632. DOI: 10.1016/j.nuclphysbps.2004.10.083. URL: https://www.sciencedirect.com/science/article/pii/S0920563205008066.

[99] Geant4 Collaboration. *Geant4 Guide for Physics Lists, version 10.5*. URL: https://geant4-userdoc.web.cern.ch/UsersGuides/PhysicsListGuide/BackupVersions/V10.5-2.0/html/index.html. last accessed on 2021-08-30.

[100] J.K. Tuli. “Evaluated nuclear structure data file”. In: *Nuclear Instruments and Methods in Physics Research Section A: Accelerators, Spectrometers, Detectors and Associated Equipment* 369.2 (1996), pp. 506–510. ISSN: 0168-9002. DOI: `https://doi.org/10.1016/S0168-9002(96)80040-4`. URL: `https://www.sciencedirect.com/science/article/pii/S0168900296800404`.

[101] *GATE website*. URL: `http://www.opengatecollaboration.org/`. last accessed on 2021-08-30.

[102] S. Jan et al. “GATE V6: a major enhancement of the GATE simulation platform enabling modelling of CT and radiotherapy”. In: *Physics in Medicine and Biology* 56.4 (Jan. 2011), pp. 881–901. DOI: `10.1088/0031-9155/56/4/001`. URL: `https://doi.org/10.1088/0031-9155/56/4/001`.

[103] D. Sarrut et al. “A review of the use and potential of the GATE Monte Carlo simulation code for radiation therapy and dosimetry applications”. In: *Medical Physics* 41.6 (2014), p. 064301. DOI: `10.1118/1.4871617`.

[104] *GATE Documentation, Version 9.1*. URL: `https://opengate.readthedocs.io/en/latest/`. last accessed on 2021-08-30.

[105] W. Schneider, T. Bortfeld, and W. Schlegel. “Correlation between CT numbers and tissue parameters needed for Monte Carlo simulations of clinical dose distributions”. In: *Physics in Medicine and Biology* 45.2 (Jan. 2000), pp. 459–478. DOI: `10.1088/0031-9155/45/2/314`. URL: `https://doi.org/10.1088/0031-9155/45/2/314`.

[106] *ROOT Data Analysis Framework website*. URL: `https://root.cern/`. last accessed on 2021-08-30.

[107] *3D Slicer website*. URL: `https://www.slicer.org/`. last accessed on 2021-08-30.

[108] *GAMOS website*. URL: `http://fismed.ciemat.es/GAMOS/gamos.php`. last accessed on 2021-08-30.

[109] P. Arce et al. “GAMOS: A Geant4-based easy and flexible framework for nuclear medicine applications”. In: *2008 IEEE Nuclear Science Symposium Conference Record* (2008), pp. 3162–3168. DOI: `10.1109/NSSMIC.2008.4775023`.

[110] *GAMOS User's Guide, version 6.0.0*. URL: `http://fismed.ciemat.es/GAMOS/GAMOS_doc/GAMOS.6.0.0/GamosUsersGuide_V6.0.0.html`. last accessed on 2021-08-30.

[111] *International Atomic Energy Agency - Nuclear Data Service website*. URL: `https://www-nds.iaea.org/`. last accessed on 2021-08-30.

[112] H. Jadvar. “Molecular imaging of prostate cancer: PET radiotracers”. In: *American Journal of Roentgenology* 199.2 (2012), pp. 278–291. DOI: `10.2214/AJR.12.8816`.

[113] O. Schillaci et al. “18F-choline PET/CT physiological distribution and pitfalls in image interpretation: Experience in 80 patients with prostate cancer”. In: *Nuclear Medicine Communications* 31.1 (2010), pp. 39–45. ISSN: 0143-3636. DOI: `10.1097/MNM.0b013e328330adc5`.

[114] Slicer Wiki contributors. *3D Slicer User Manual Documentation/4.10*. URL: `https://www.slicer.org/wiki/Documentation/4.10`. last accessed on 2021-08-30.

[115] Geant4 Collaboration. *Geant4 Physics Reference Manual, version 10.5*. URL: `https://geant4-userdoc.web.cern.ch/UsersGuides/PhysicsReferenceManual/BackupVersions/V10.5-2.0/html/index.html`. last accessed on 2021-08-30.

[116] U. Schneider, E. Pedroni, and A. Lomax. “The calibration of CT Hounsfield units for radiotherapy treatment planning”. In: *Physics in Medicine and Biology* 41.1 (Jan. 1996), pp. 111–124. DOI: `10.1088/0031-9155/41/1/009`. URL: `https://doi.org/10.1088/0031-9155/41/1/009`.

[117] I. J. Chetty et al. “Reporting and analyzing statistical uncertainties in Monte Carlo–based treatment planning”. In: *International Journal of Radiation Oncology*Biology*Physics* 65.4 (2006), pp. 1249–1259. ISSN: 0360-3016. DOI: `https://doi.org/10.1016/j.ijrobp.2006.03.039`. URL: `https://www.sciencedirect.com/science/article/pii/S0360301606005311`.

[118] A. Pépin et al. “Management of respiratory motion in PET/computed tomography: the state of the art”. In: *Nuclear Medicine Communications* 35.2 (2014), pp. 113–122. DOI: `10.1097/MNM.0000000000000048`.

[119] R. Sacco et al. “Transarterial radioembolization for hepatocellular carcinoma: An update and perspectives”. In: *World Journal of Gastroenterology* 21.21 (2015), pp. 6518–25. DOI: `10.3748/wjg.v21.i21.6518`. URL: `https://doi.org/10.3748/wjg.v21.i21.6518`.

[120] C. Rognoni et al. “Trans-arterial radioembolization for intermediate-advanced hepatocellular carcinoma: a budget impact analysis”. In: *BMC Cancer* 18.1 (July 2018), p. 715. ISSN: 1471-2407. DOI: `10.1186/s12885-018-4636-7`.

[121] E. Garin et al. “Personalised versus standard dosimetry approach of selective internal radiation therapy in patients with locally advanced hepatocellular carcinoma (DOSISPHERE-01): a randomised, multicentre, open-label phase 2 trial”. In: *The Lancet Gastroenterology & Hepatology* 6.1 (2021), pp. 17–29. ISSN: 2468-1253. DOI: `https://doi.org/10.1016/S2468-1253(20)30290-9`. URL: `https://www.sciencedirect.com/science/article/pii/S2468125320302909`.

[122] V. Mazzaferro et al. “Yttrium-90 radioembolization for intermediate-advanced hepatocellular carcinoma: A phase 2 study”. In: *Hepatology* 57.5 (2013), pp. 1826–1837. DOI: `https://doi.org/10.1002/hep.26014`. eprint: `https://aasldpubs.onlinelibrary.wiley.com/doi/pdf/10.1002/hep.26014`. URL: `https://aasldpubs.onlinelibrary.wiley.com/doi/abs/10.1002/hep.26014`.

[123] C. Chiesa et al. “Radioembolization of hepatocarcinoma with (90)Y glass microspheres: development of an individualized treatment planning strategy based on dosimetry and radiobiology”. In: *European journal of nuclear medicine and molecular imaging* 42.11 (Oct. 2015), pp. 1718–1738. ISSN: 1619-7070. DOI: `10.1007/s00259-015-3068-8`. URL: `https://doi.org/10.1007/s00259-015-3068-8`.

[124] L. Auditore et al. “Monte Carlo 90Y PET/CT dosimetry of unexpected focal radiation-induced lung damage after hepatic radioembolisation”. In: *Physics in Medicine & Biology* 65.23 (Nov. 2020), p. 235014. DOI: `10.1088/1361-6560/abbc80`. URL: `https://doi.org/10.1088/1361-6560/abbc80`.

[125] A. Milano et al. “In silico validation of MCID platform for Monte Carlo-based voxel dosimetry applied to 90Y-radioembolization of liver malignancies”. In: *Applied Sciences (Switzerland)* 11.4 (2021), pp. 1–16. DOI: `10.3390/app11041939`.

[126] T. Moraes et al. “Medical image interpolation based on 3D Lanczos filtering”. In: *Computer Methods in Biomechanics and Biomedical Engineering: Imaging & Visualization* 8.3 (2020), pp. 294–300. DOI: `10.1080/21681163.2019.1683469`. eprint: `https://doi.org/10.1080/21681163.2019.1683469`. URL: `https://doi.org/10.1080/21681163.2019.1683469`.

[127] Geant4 Collaboration. *Geant4 Book for Application Developers, version 10.5*. URL: `https://geant4-userdoc.web.cern.ch/UsersGuides/ForApplicationDeveloper/BackupVersions/V10.5-2.0/html/index.html`. last accessed on 2021-08-30.

[128] A. Petitguillaume et al. “Three-Dimensional Personalized Monte Carlo Dosimetry in Y-90 Resin Microspheres Therapy of Hepatic Metastases: Nontumoral Liver and Lungs Radiation Protection Considerations and Treatment Planning Optimization”. In: *Journal of nuclear medicine : official publication, Society of Nuclear Medicine* 55 (Feb. 2014). DOI: `10.2967/jnumed.113.120444`.

[129] *OpenDose collaboration website*. URL: `https://opendose.org/home`. last accessed on 2021-08-30.

[130] *SlicerOpenDose3D GitLab webpage*. URL: `https://gitlab.com/opendose/opendose3d`. last accessed on 2021-08-30.

[131] H. Desai, S. Borges-Neto, and Z. Wong. “Molecular Imaging and Therapy for Neuroendocrine Tumors”. In: *Current Treatment Options in Oncology* 20 (Aug. 2019). DOI: `10.1007/s11864-019-0678-6`.

[132] Muhammad Maqsood, Asim Tameez Ud Din, and Ameer Khan. “Neuroendocrine Tumor Therapy with Lutetium-177: A Literature Review”. In: *Cureus* 11 (Jan. 2019). DOI: `10.7759/cureus.3986`.

[133] M. Cremonesi et al. “Dosimetry in Peptide Radionuclide Receptor Therapy: A Review”. In: *Journal of Nuclear Medicine* 47.9 (2006), pp. 1467–1475. ISSN: 0161-5505. eprint: `https://jnm.snmjournals.org/content/47/9/1467.full.pdf`. URL: `https://jnm.snmjournals.org/content/47/9/1467`.

[134] U. Garske-Román et al. “Prospective observational study of 177Lu-DOTA-octreotate therapy in 200 patients with advanced metastasized neuroendocrine tumours (NETs): feasibility and impact of a dosimetry-guided study protocol on outcome and toxicity”. In: *European Journal of Nuclear Medicine and Molecular Imaging* 45 (June 2018). DOI: `10.1007/s00259-018-3945-z`.

[135] U. Eberlein, M. Cremonesi, and M. Lassmann. “Individualized Dosimetry for Theranostics: Necessary, Nice to Have, or Counterproductive?” In: *Journal of Nuclear Medicine* 58.Supplement 2 (2017), 97S–103S. ISSN: 0161-5505. DOI: `10.2967/jnumed.116.186841`. eprint: `https://jnm.snmjournals.org/content/58/Supplement_2/97S.full.pdf`. URL: `https://jnm.snmjournals.org/content/58/Supplement_2/97S`.

[136] European Society of Radiology (ESR). “Summary of the European Directive 2013/59/Euratom: essentials for health professionals in radiology”. In: *Insights into Imaging* 6 (Aug. 2015), pp. 411–417. DOI: `10.1007/s13244-015-0410-4`.

[137] A. Sundlöv et al. “Individualised 177Lu-DOTATATE treatment of neuroendocrine tumours based on kidney dosimetry”. In: *European Journal of Nuclear Medicine and Molecular Imaging* 44 (Aug. 2017). DOI: `10.1007/s00259-017-3678-4`.

[138] C. Stokke et al. "Dosimetry-based treatment planning for molecular radiotherapy: A summary of the 2017 report from the Internal Dosimetry Task Force". In: *EJNMMI Physics* 4 (Nov. 2017). DOI: `10.1186/s40658-017-0194-3`.

[139] K. Sjogreen-Gleisner et al. "Variations in the practice of molecular radiotherapy and implementation of dosimetry: results from a European survey". In: *EJNMMI Physics* 4 (Dec. 2017). DOI: `10.1186/s40658-017-0193-4`.

[140] M. Chalkia et al. "Patient-specific dosimetry in peptide receptor radionuclide therapy: a clinical review". In: *Australasian Physical & Engineering Sciences in Medicine* 38 (Nov. 2014). DOI: `10.1007/s13246-014-0312-7`.

[141] K. Willowson et al. "A comparison of 2D and 3D kidney absorbed dose measures in patients receiving 177Lu-DOTATATE". In: *Asia Oceania Journal of Nuclear Medicine and Biology* 6.2 (2018), pp. 113–119. ISSN: 2322-5718. DOI: `10.22038/aojnmb.2018.26105.1182`. eprint: `https://aojnmb.mums.ac.ir/article_10329_444f4ef7f5a36d93b731d54a47988a6a.pdf`. URL: `https://aojnmb.mums.ac.ir/article_10329.html`.

[142] H. Hänscheid et al. "Dose Mapping after Endoradiotherapy with 177Lu-DOTATATE/-TOC by One Single Measurement after Four Days". In: *Journal of Nuclear Medicine* (2017). ISSN: 0161-5505. DOI: `10.2967/jnumed.117.193706`. eprint: `https://jnm.snmjournals.org/content/early/2017/06/05/jnumed.117.193706.full.pdf`. URL: `https://jnm.snmjournals.org/content/early/2017/06/05/jnumed.117.193706`.

[143] M. Del Prete et al. "Accuracy and reproducibility of simplified QSPECT dosimetry for personalized 177Lu-octreotate PRRT". In: *EJNMMI Physics* 5 (Oct. 2018). DOI: `10.1186/s40658-018-0224-9`.

[144] A. Chicheportiche et al. "Dosimetry after peptide receptor radionuclide therapy: impact of reduced number of post-treatment studies on absorbed dose calculation and on patient management". In: *EJNMMI Physics* 7 (Jan. 2020). DOI: `10.1186/s40658-020-0273-8`.

[145] M. Sandström et al. "Kidney dosimetry in 777 patients during Lu-DOTATATE therapy: aspects on extrapolations and measurement time points". In: *EJNMMI Physics* 7 (Dec. 2020). DOI: `10.1186/s40658-020-00339-2`.

[146] G. Marin et al. "A dosimetry procedure for organs-at-risk in 177Lu peptide receptor radionuclide therapy of patients with neuroendocrine tumours". In: *Physica Medica* 56 (2018), pp. 41–49. ISSN: 1120-1797. DOI: `https://doi.org/10.1016/j.ejmp.2018.11.001`. URL: `https://www.sciencedirect.com/science/article/pii/S1120179718313139`.

[147] L. Bodei et al. "Peptide receptor radionuclide therapy with Lu-177-DOTATATE: the IEO phase I-II study". In: *European journal of nuclear medicine and molecular imaging* 38 (Sept. 2011), pp. 2125–35. DOI: `10.1007/s00259-011-1902-1`.

[148] M. Sandström et al. "Individualized dosimetry in patients undergoing therapy with Lu-177-DOTA-D-Phe(1)-Tyr(3)-octreotate". In: *European journal of nuclear medicine and molecular imaging* 37 (Oct. 2009), pp. 212–25. DOI: `10.1007/s00259-009-1216-8`.

[149] M. Sandström et al. “Individualized Dosimetry of Kidney and Bone Marrow in Patients Undergoing 177Lu-DOTA-Octreotate Treatment”. In: *Journal of Nuclear Medicine* 54.1 (2013), pp. 33–41. ISSN: 0161-5505. DOI: `10.2967/jnumed.112.107524`. eprint: `https://jnm.snmjournals.org/content/54/1/33.full.pdf`. URL: `https://jnm.snmjournals.org/content/54/1/33`.

[150] J.P. Mullins et al. “Treatment planning for metals using an extended CT number scale”. In: *Journal of Applied Clinical Medical Physics* 17.6 (2016), pp. 179–188. ISSN: 1526-9914. DOI: `10.1120/jacmp.v17i6.6153`.

[151] F. Guerriero et al. “Kidney Dosimetry in Lu and Y Peptide Receptor Radionuclide Therapy: Influence of Image Timing, Time-Activity Integration Method, and Risk Factors”. In: *BioMed research international* 2013 (June 2013), p. 935351. DOI: `10.1155/2013/935351`.

[152] D. Pistone et al. “Internal dosimetry of PET radio-pharmaceuticals through Monte Carlo simulations: a comparison between GATE and GAMOS code”. 2019. URL: `http://www.accademiapeloritana.it/Eventi2019/Documentazione/3%20dicembre%202019.pdf`. Conference talk communicated at the Scientific meeting of the “Accademia Peloritana dei Pericolanti, Classe di Scienze Fisiche, Matematiche e Naturali”, Messina (Italy), December 3, 2019.

[153] E. Amato et al. “Full Monte Carlo internal dosimetry in nuclear medicine by means of GAMOS”. In: *Journal of Physics: Conference Series* 1561 (2020), p. 012002. DOI: `10.1088/1742-6596/1561/1/012002`.

[154] D. Pistone et al. “Internal dosimetry in diagnostic and therapeutic nuclear medicine using GATE and GAMOS Monte Carlo simulations”. In: *Atti del 106° Congresso Nazionale SIF, 14-18 Settembre 2020*. 2020. ISBN: 978-88-7438-123-4. URL: `https://www.sif.it/static/SIF/resources/public/files/congr20/atti_congresso_106.pdf`.

[155] D. Pistone et al. “Monte Carlo based dose-rate assessment in ^{18}F-Choline PET examination: a comparison between GATE and GAMOS codes”. In: *Atti della Accademia Peloritana dei Pericolanti - Classe di Scienze Fisiche, Matematiche e Naturali* 98.1 (2020), p. 5. ISSN: 1825-1242. DOI: `10.1478/AAPP.981A5`. URL: `https://cab.unime.it/journals/index.php/AAPP/article/view/AAPP.981A5`.

[156] A. Italiano et al. “GATE Monte Carlo dosimetry in ^{90}Y TARE planning: influence of simulation parameters and image resampling on dosimetric accuracy and optimization of computational times”. 2020. URL: `http://www.accademiapeloritana.it/Eventi2020/Documentazione/26%20novembre%202020.pdf`. Conference talk communicated at the Virtual Scientific meeting of the “Accademia Peloritana dei Pericolanti, Classe di Scienze Fisiche, Matematiche e Naturali”, November 26, 2020.

[157] D. Pistone et al. “Advances in Monte Carlo patient-specific internal dosimetry for ^{90}Y-TARE treatments”. In: *Atti del 107° Congresso Nazionale SIF, 13-17 Settembre 2021*. 2021. ISBN: 978-88-7438-127-2. URL: `https://www.sif.it/static/SIF/resources/public/files/congr21/Atti_Congresso_107_2021.pdf`.

[158] A. Vergara Gil et al. “OpenDose3D: A free, collaborative 3D Slicer module for patient-specific dosimetry”. In: *European Association of Nuclear Medicine October 22 – 30, 2020 Virtual*. Vol. 47. Suppl 1. 2020, S314–S315. DOI: `10.1007/s00259-020-04988-4`.

[159] D. Pistone et al. "Internal dosimetry Monte Carlo study of TARE treatments. A comparison between GATE and GAMOS focused on lung dosimetry and background correction". 2021. URL: `https://www.symposium.it/files/eventi/101/ecmp-2020-909.pdf`. Conference talk communicated at the 3rd European Congress of Medical Physics (ECMP 2020), held on-line, June 16-19, 2021.

[160] D. Pistone et al. "A simplified method for kidney dosimetry in ^{177}Lu therapies based on single SPECT-CT and multiple external probe measurements". 2021. URL: `https://eanm21.eanm.org/`. Conference talk to be presented at the 34th Annual Congress of the European Association of Nuclear Medicine (EANM 2021), to be held on-line, October 20-23, 2021.

[161] R. Brun and F. Rademakers. "ROOT — An object oriented data analysis framework". In: *Nuclear Instruments and Methods in Physics Research Section A: Accelerators, Spectrometers, Detectors and Associated Equipment* 389.1 (1997). New Computing Techniques in Physics Research V, pp. 81–86. ISSN: 0168-9002. DOI: `https://doi.org/10.1016/S0168-9002(97)00048-X`. URL: `https://www.sciencedirect.com/science/article/pii/S016890029700048X`.

[162] J. R. Taylor. *An introduction to error analysis: The study of uncertainties in physical measurements*. Series of books in physics. Mill Valley, California: University Science Books, 1982. eprint: `https://www.niser.ac.in/sps/sites/default/files/basic_page/John%20R.%20Taylor%20-%20An%20Introduction%20to%20Error%20Analysis_%20The%20Study%20of%20Uncertainties%20in%20Physical%20Measurements-University%20Science%20Books%20(1997).pdf`. URL: `https://www.worldcat.org/title/introduction-to-error-analysis-the-study-of-uncertainties-in-physical-measurements/oclc/8568621`.